

Annual and Longitudinal Variations of the Pacific North Equatorial Countercurrent

Nina K. Lolk

Department of Atmospheric Sciences
University of California, Los Angeles

March 1992



National Aeronautics and
Space Administration

Jet Propulsion Laboratory
California Institute of Technology
Pasadena, California







NASA-CR-192805

JPL Publication 92-8

Annual and Longitudinal Variations of the Pacific North Equatorial Countercurrent

Nina K. Lolk

Department of Atmospheric Sciences
University of California, Los Angeles

(NASA-CR-192805) ANNUAL AND
LONGITUDINAL VARIATIONS OF THE
PACIFIC NORTH EQUATORIAL
COUNTERCURRENT (JPL) 224P

N93-23138

Unclass

63/48 0154692

494501

March 1992



National Aeronautics and
Space Administration

Jet Propulsion Laboratory
California Institute of Technology
Pasadena, California

(COVER PAGE)

PREFACE

This JPL publication is an unedited copy of a thesis prepared by Nina K. Lolk as a partial requirement to obtain the Master of Science degree from the Department of Atmospheric Sciences at the University of California, Los Angeles. The research was performed under Contract 958658 to UCLA from the Jet Propulsion Laboratory, California Institute of Technology, with funds from the National Aeronautics and Space Administration (UPN 578-22-26-40). The thorough presentation of the results of the climatological-mean monthly simulation of tropical Pacific oceanographic conditions was deemed of value to numerous ongoing programs, such as the Tropical Ocean Global Atmosphere (TOGA), Equatorial Pacific Ocean Climate Studies (EPOCS), Tropical Instability Wave Experiment (TIWE), and TOGA Program on Seasonal-to-Interannual Prediction (T-POP), to warrant additional distribution of the thesis as a JPL publication.

Reference herein to any specific commercial product, process, or service by trade name, trademark, manufacturer, or otherwise, does not constitute or imply its endorsement by the United States Government or the Jet Propulsion Laboratory, California Institute of Technology.

Contents

List of Figures	v
List of Tables	ix
Acknowledgments	x
Abstract of the Thesis	xi
Chapter 1. Introduction	1
Chapter 2. Observational and Theoretical Review	4
2.1 Observations of the annual cycle of the NECC	4
2.1.1 The thermal field	6
2.1.2 The motion field	8
2.2. Theoretical review	8
2.2.1 Ekman theory	8
2.2.2 Sverdrup balance	10
2.2.3 Ekman pumping	12
Chapter 3. Annual Variation of the Simulated NECC	13
3.1 Description of the GFDL-OGCM	13
3.2 Description of the climatological wind stress	14
3.3 The seasonal cycle of temperature and currents	17
3.3.1 The thermal field	17
3.3.2 The motion field	29
3.3.3 Transports	40
3.4 Comparison with observations	46
3.5 Discussion	48
Chapter 4. Degree of Geostrophy	50
4.1 Method	52

4.2 Results	54
4.3 Discussion	64
Chapter 5. Relationship Between Wind Stress Curl and Thermocline Depth	70
5.1 Motivation	70
5.2 Method	71
5.3 Results	73
5.3 Discussion	81
Chapter 6. Summary and Conclusions	87
Appendix A. Monthly Mean Wind Stress	93
A.1 Wind stress	94
A.2 Wind stress curl	100
Appendix B. Monthly Maps of Surface Temperature and Currents	107
B.1 Instantaneous sea surface temperature	108
B.2 Monthly mean sea surface temperature	114
B.3 Monthly mean surface currents	121
Appendix C. Monthly Mean Latitude-Depth Sections along 150°E, 180°, 160°W, 140°W, 125°W and 110°W	128
C.1 Zonal current	129
C.2 Meridional current	141
C.3 Geostrophic current	154
C.4 Dynamic height	179
C.5 Temperature	192
References	205

List of Figures

Figure 2.1 Annual mean cross-section along 150°-158°W observed during May 1979 - April 1980, a) temperature, b) dynamic height and c) zonal velocity in cm s ⁻¹ . From Wyrtki and Kilonsky 1984.	7
Figure 3.1 Hellerman and Rosenstein (1983) climatological wind stress for March and September. The zonal component is contoured with an interval 0.1 N m ⁻² and negative (westward) contours are dashed.	16
Figure 3.2 Monthly mean wind stress curl computed from Hellerman and Rosenstein (1983) climatological wind stress for March and September. The contour interval is 5 x 10 ⁻⁸ N m ⁻³ and negative curl is shaded	18
Figure 3.3 Monthly mean SST for February, June, and November.	19
Figure 3.4 Instantaneous monthly SST for February, June, and November.	21
Figure 3.5 Latitude-depth sections of annual mean temperature. The contour interval is 2°C.	23
Figure 3.6 Latitude-depth diagram of the monthly mean temperature along 160°W for January, April, July, and October. The contour interval is 2°C.	24
Figure 3.7 Latitude-depth diagram of the standard deviation of temperature. Contour interval is 0.5°C.	25
Figure 3.8 Time series of the depth of the 20°C isotherm in meters for 4.5°N and 9.2°N along 160°W.	27
Figure 3.9 Monthly averaged 5 m currents for January, April, July, and October. The zonal component is contoured with an interval of 50 cm s ⁻¹ and negative (westward) contours are dashed.	31

Figure 3.10 Hovmöller diagram of the zonal current component at 5 m and 7°N. The contour interval is 10 cm s ⁻¹ and negative (westward) currents are shaded.	32
Figure 3.11 Latitude-depth diagram of the annual mean zonal current component. The contour interval is 10 cm s ⁻¹ and negative (westward) currents are shaded.	35
Figure 3.12 Latitude-depth diagram of the zonal current component standard deviation. The contour interval is 5 cm s ⁻¹ .	36
Figure 3.13 Latitude-depth diagram of the annual mean meridional current component. The contour interval is 10 cm s ⁻¹ and negative (westward) currents are shaded.	37
Figure 3.14 Latitude-depth diagram of the meridional current component standard deviation. Contour interval is 2 cm s ⁻¹ .	39
Figure 3.15 Latitude-depth diagram of the monthly mean vertical velocity along 160°W for January, April, July, and October. The contour interval is 50 cm day ⁻¹ and shaded values indicate downwelling.	41
Figure 3.16.a Annual cycle of the latitudinal width of the NECC in degrees.	44
Figure 3.16.b Annual cycle of the thickness of the NECC in meters.	45
Figure 3.17 Annual cycle of the eastward transport of the NECC in Sv (1 Sv = 10 ⁶ m ³ s ⁻¹). The thin dotted line is the annual mean.	47
Figure 4.1 Latitude-depth diagram of the annual mean zonal geostrophic current component from 2.7°N to 15°N. The contour interval is 10 cm s ⁻¹ and negative (westward) currents are shaded.	56
Figure 4.2 Latitude-depth diagram of the zonal geostrophic current component from 2.7°N to 15°N for March and September. The contour interval is 10 cm s ⁻¹ and negative (westward) currents are shaded.	57

Figure 4.3 Latitude-depth diagram of the zonal current component from 15°S to 15°N for March and September. The contour interval is 10 cm s ⁻¹ and negative (westward) currents are shaded.	58
Figure 4.4 Profile of monthly mean surface dynamic height anomaly (in dyn cm) relative to 484 x 10 ⁴ Pa along 160°W for February, April, June, August, October, and December.	61
Figure 4.5 Comparison between the 5/484 x 10 ⁴ Pa geostrophic current, u_g , (thin dotted curve) and the 5 m model total zonal current, u_m , (thick curve) along 160°W for February, May, August, and November.	62
Figure 4.6 Latitude-depth maps of per cent explained variance (R^2) of u_m by u_g from 2.3°N to 15°N.	63
Figure 4.7 Annual mean of the zonal Coriolis acceleration terms, $f u_g$ 5/484 (thin dotted curve) and $f u_{5m}$ (crosses), and the meridional acceleration, $\partial v_{5m}/\partial t$, in 10 ⁻⁶ cm sec ⁻² from 3°N to 10°N. The curve of $\partial v_{5m}/\partial t$ overlies the zero line as the magnitude of $\partial v_{5m}/\partial t$ is small relative to the other two terms.	66
Figure 4.8 Standard deviations of the zonal Coriolis acceleration terms, $f u_g$ 5/484 (thin dotted curve) and $f u_{5m}$ (crosses), and the meridional acceleration, $\partial v_{5m}/\partial t$, in 10 ⁻⁶ cm sec ⁻² from 3°N to 10°N.	67
Figure 4.9 Time series of the zonal Coriolis acceleration terms, $f u_g$ 5/484 (thin dotted curve) and $f u_{5m}$ (crosses) and the meridional acceleration, $\partial v_{5m}/\partial t$, in 10 ⁻⁶ cm sec ⁻² at 4.5°N, 7°N and 9°N. The bottom row of figures represent the residual, defined as $\partial v_{5m}/\partial t + f(f u_{5m} - u_g$ 5/484).	69
Figure 5.1.a Comparison of monthly averaged Ekman pumping, w_E (thick curve) and vertical velocity of the 20°C isotherm, $\partial h_{20}/\partial t$ (thin curve) in cm day ⁻¹ at 4.5°N.	76
Figure 5.1.b Comparison of monthly averaged Ekman pumping, w_E (thick curve) and vertical velocity of the 20°C isotherm, $\partial h_{20}/\partial t$ (thin curve) in cm day ⁻¹ at 9.2°N.	77

Figure 5.2.a. Comparison of monthly averaged Ekman pumping, w_E (thick curve) and the model-simulated vertical velocity, w (diamonds), in cm day^{-1} at 4.5°N.	79
Figure 5.2.b Comparison of monthly averaged Ekman pumping, w_E (thick curve) and the model-simulated vertical velocity (diamonds) in cm day^{-1} at 9.2°N.	80
Figure 5.3.a Comparison of monthly mean vertical velocity of the 20°C isotherm, $\partial h_{20}/\partial t$ (thick curve) and model-simulated vertical velocity, w (diamonds), in cm day^{-1} at 4.5°N.	82
Figure 5.3.b Comparison of monthly mean vertical velocity of the 20°C isotherm, $\partial h_{20}/\partial t$ (thick curve) and model-simulated vertical velocity, w (diamonds), in cm day^{-1} at 9.2°N.	83

List of Tables

<p>Table 3.1 Monthly mean surface dynamic height anomaly (in dyn cm) of the countercurrent trough (near 10°N), the equatorial ridge (near 4°N), and the difference between the two across the NECC.</p> <p>Table 3.2 Monthly displacement (in dyn cm) about the annual mean of the countercurrent trough (near 10°N) and the equatorial ridge (near 4°N).</p> <p>Table 3.3 Monthly mean NECC boundaries. The missing values appear because the NECC is not defined according to the criteria stated in the text at certain longitudes and times of the year. *Subjectively determined as discussed in the text.</p> <p>Table 4.1 Example of a vertical integration of the dynamic height anomaly, ΔD. The profile is from January at a location of 150°W, 5°N. T is the temperature (°C) and S is salinity in Practical Salinity Unit (S).</p> <p>Table 4.2 Monthly mean zonal geostrophic velocity at 5 m relative to 484×10^4 Pa (u_g) and 5 m model velocity (u_m). Both u_m and u_g are averaged over the NECC region using the monthly mean boundaries in Table 3.3.</p> <p>Table 5.1 Annual mean and standard deviation (rms) of the movement of the 20°C isotherm ($\partial h_{20}/\partial t$), Ekman pumping ($w_E$) and the model-simulated vertical velocity (w) at 4.5°N (near the southern boundary of the NECC) and 9.2°N (near the northern boundary of the NECC) in cm day⁻¹. The correlation coefficient (R) is computed for $\partial h_{20}/\partial t$ and w_E in Case I, w_E and w in Case II, and $\partial h_{20}/\partial t$ and w in Case III. R values greater than 0.57 (or less than - 0.57) are significantly different from zero at 95% confidence.</p> <p>Table 5.2 Comparison of the values of the two terms determining the sign of the Ekman pumping velocity, w_E at 4.5°N. If $\text{curl}_z \tau > M_y^E \beta$, $w_E > 0$, or if $\text{curl}_z \tau$ $< M_y^E \beta$, $w_E < 0$.</p>	<p style="text-align: right;">28</p> <p style="text-align: right;">30</p> <p style="text-align: right;">33</p> <p style="text-align: right;">55</p> <p style="text-align: right;">59</p> <p style="text-align: right;">74</p> <p style="text-align: right;">84</p>
--	--

ACKNOWLEDGMENTS

Many people have offered their help in the preparation of this thesis. First, I would like to thank my advisor, Dr. David Halpern, whose patience is unsurpassed, for his guidance and support. I am grateful for valuable time he spent reading this thesis and for his suggestions for improvement. Second, I would like to acknowledge Professor Michael Ghil, Professor J. David Neelin, and the chair of my committee, Professor Carlos R. Mechoso, for reading this thesis and offering their constructive criticisms.

I also want to thank the computer programmers and analysts at UCLA, Louise Lee, William Weibel, Fabrice Cuq and Joseph Spahr for their help and the departmental staff, Wesley Radlein, "LV" Oliver, Michael Carr, and Rick Fort, for their unending support.

Dr. Yi Chao is acknowledged for sharing his expertise in ocean modelling, Tammy Weckwerth for her editing effort, Dr. Kuanman Xu for his help with the UCLA graphics software, Dr. Feifei Jin, Chichung Lin, Vladimir Ryshko, Dr. Victor Magaña, Michael Dettinger, Shi Jiang and Zheng Hao for helpful discussions.

This work was performed for the Jet Propulsion Laboratory, California Institute of Technology, sponsored by the National Aeronautics and Space Administration.

ABSTRACT OF THE THESIS

**Annual and Longitudinal Variations of the
Pacific North Equatorial Countercurrent**

by

Nina Kjaerbo Lolk

Master of Science in Atmospheric Science

University of California, Los Angeles, 1992

Professor Carlos R. Mechoso, Chair

The climatological annual cycle of the Pacific North Equatorial Countercurrent simulated by an ocean general circulation model (OGCM) was studied. Emphasis was placed on the longitudinal variation of transports, degree of geostrophy and the relationship between Ekman pumping and vertical displacement of the thermocline. The longitudinal variation was explored using six sections along 150°E, 180°, 160°W, 140°W, 125°W and 110°W.

A primitive equation OGCM of the Pacific ocean, developed at NOAA's Geophysical Fluid Dynamics Laboratory, was run for 3 years and the fields used were from the third year. The fields consisted of zonal, meridional and vertical current components and temperature and salinity averaged every three days. The model was forced with the Hellerman and Rosenstein (1983) climatological wind stress.

The mean annual eastward transport (19.9 Sv) was largest at 160°W. The month of maximum transport was September along 160°W. Annual mean (and standard deviation) current boundaries along 160°W were 9.2°N (1.0°), 5.1°N (1.1°) and 187 m (90.6 m). The amplitude of the annual cycle of the NECC was greatest between 160°W and 140°W. Although the NECC is geostrophic to the first order, deviations from geostrophy were found in the boreal spring and summer near the southern boundary and near the surface. Meridional local acceleration was found to play a role between 3°N-5°N.

The relationship between Ekman pumping, thermocline movement and the model-simulated vertical velocity was studied. Results indicate that thermocline movement is a poor indicator of both the vertical velocity and the Ekman pumping velocity. However, a weak relationship was found between Ekman pumping and the vertical velocity.

CHAPTER 1

Introduction

The North Equatorial Countercurrent (NECC) flows from west to east, counter to the prevailing winds in the latitude band from 5° to 10°N. Present knowledge of the NECC characterizes it as being in geostrophic balance to first order but yet possessing high variability on the intra-seasonal, annual and inter-annual time scales. Seasonal variations in the strength of the surface NECC were discussed as early as 1895 by Caesar Puls (Wyrtki and Kendall 1967). Much of the knowledge of the NECC is based on application of the geostrophic method as direct current measurements are scarce but widespread observations of sea level, temperature and salinity are taken routinely. Historically, the presence of the NECC was first explained by Sverdrup (1947) in terms of the wind stress curl.

A major difficulty in applying Sverdrup's geostrophic theory is the large uncertainty in estimating wind stress curl. Different estimates of wind stress curl vary greatly (Trenberth *et al.* 1989). Calculations of NECC transport (e.g. Spillane and Niiler 1975; Meyers 1980) have suggested that the theory of Sverdrup (1947) is inadequate in accounting for the NECC due to the assumptions that acceleration, advection and lateral mixing are negligible. Recent simulations of the equatorial currents

using an ocean general circulation model (OGCM) have yielded inconsistent descriptions of the NECC on the inter-annual time scale depending on the wind stress forcing applied at the surface (Harrison *et al.* 1989).

There is a need for 1) a spatially comprehensive description of the NECC, 2) an evaluation of the sensitivity of the NECC to the wind stress curl and 3) an assessment of the applicability of the geostrophic method to the NECC. The object of the thesis is thus to describe the longitudinal variation of the annual cycle of the NECC and to evaluate the mechanisms important in creating the variability. The investigation will focus on the relationship between wind stress curl, vertical motion and thermocline depth. The degree of geostrophy at various longitudes and times of the year is also investigated.

The study is carried out using fields from an OGCM developed at NOAA's Geophysical Fluid Dynamics Laboratory (GFDL) in Princeton, New Jersey. The model was run for three years. The results shown here are from the third year which represents the model equilibrium seasonal cycle. The application of a model to investigate Pacific equatorial currents which are almost all zonal and extend for ten to fifteen thousand kilometers is perhaps a necessity as high resolution observational studies are very expensive. Using the model fields allows for analyses that are unprecedented in spatial and temporal resolution.

The primary goal of this thesis is to describe a climatological annual cycle of the NECC which can serve as a benchmark for observations and simulations with the different wind stress products currently available. A secondary goal is to identify the regions of greatest variability of the NECC such that future efforts to monitor the variability of the current can be focused at particular longitudes. The subsequent sections of the thesis are organized as follows. A review of relevant observational studies and theory pertaining to the NECC will be presented in chapter 2. In chapter 3

the annual variation and spatial structure of the model countercurrent is described. The simulated characteristics of the NECC will be compared to observations. Chapters 4 and 5 contain analyses of the important linear dynamical mechanisms for variability of the current on the annual as well as monthly time scale. In chapter 4, the degree of geostrophy is discussed and in chapter 5 a comparison between the wind stress curl-induced Ekman pumping, the vertical movement of the thermocline and the model-simulated vertical velocity is made. Chapter 6 contains a summary and conclusions.

Appendix A contains maps of the Hellerman and Rosenstein (1983) climatological, monthly-averaged wind stress and wind stress curl, which is computed from the wind stress, for the Pacific ocean from 130°E to 70°W and 20°S to 20°N . Monthly maps of the model-simulated sea surface temperature and 5 m currents are shown in Appendix B. Appendix C contains monthly-mean, latitude-depth sections along 150°E , 180° , 160°W , 140°W , 125°W and 110°W of the zonal, meridional and zonal geostrophic current components, dynamic height and temperature.

CHAPTER 2

Observations and Theoretical Review

The first part of this chapter reviews some observational field experiments in which information on the amplitude of the seasonal cycle was obtained. To a first approximation, the flow of the eastward NECC is in geostrophic balance with the north-south sloping thermocline. Therefore, the discussion will focus on observations of the seasonal and longitudinal variation of 1) dynamic height variations across the current, 2) mass transport and 3) spatial extent. The second part of chapter 2 reviews theoretical aspects of the NECC. Topics included in this section are Ekman theory, Sverdrup theory and Ekman pumping.

2.1 Observations of the annual cycle of the NECC

Some of the earliest direct current measurements leading to a rough description of the current structure were described by Knauss (1961). In his work direct measurements of the vertical structure of the current were compared to geostrophic calculations based on temperature data and the NECC was found to be in geostrophic balance to a first approximation. That is, the meridional momentum balance can be

reduced to a balance between the meridional pressure gradient and the Coriolis acceleration caused by the zonal current component

$$f u_g = -\frac{1}{\rho} \frac{\partial p}{\partial y} \quad (2.1)$$

Here, f is the Coriolis parameter, ρ is density, p is hydrostatic pressure, u_g is zonal geostrophic velocity component and y is positive northward. In most cases Knauss (1961) found that the current measurements yielded velocities that were greater than the geostrophic velocities by 20 to 50%. Knauss (1961) suggested that the discrepancy was an indication that the flow contained a significant wind-driven Ekman transport.

Wyrtki and Kendall (1967) computed geostrophic transports per meridional width along meridians from 130°E across the Pacific to 80°W. The computations were based on 79 historical hydrographic sections. Wyrtki and Kendall (1967) concluded that the average NECC transport decreased linearly from west to east and speculated that flow is weakest from March to June and strongest in August and September.

The most comprehensive and most recent field experiment carried out in the equatorial Pacific NECC was the Hawaii-to-Tahiti Shuttle Experiment (HTSE) (Wyrtki *et al.* 1981). The experiment took place during 1979-80 and consisted of 43 transequatorial sections along 150°-158°W from 17°S to 20°N. Temperature, salinity and direct current measurements were obtained using a variety of instruments. Vertical profiles of temperature and salinity were obtained with conductivity-temperature-depth recorders (CTDs) at every degree of latitude (Wyrtki and Kilonsky 1984). Based on these data, geostrophic currents were computed and compared with direct, continuous current measurements taken by a Doppler acoustic log (DAL) (Johnson *et al.* 1988). In a study preliminary to the HTSE, Barnett and Patzert (1980) described the scales of thermal variability in the HTSE region based on measurements by airborne expendable

bathythermographs (AXBTs) dropped at weekly intervals during November 1977-January 1978. Also during that three month period, direct current measurements were obtained using moored current meters at 6°, 7° and 8°N along 150°W (Halpern 1991).

2.1.1 The thermal field

Figure 2.1.a shows the annual mean (April 1979-March 1980) temperature structure discussed by Wyrtki and Kilonsky (1984). Across the region of the NECC, from about 5°N to 10°N, the thermocline is defined by the 14°C and the 26°C isotherms. The thermocline is elevated near 10°N and depressed near 5°N. At 5°N and 10°N the thermocline is located between 105-170 m (thickness ≈ 65 m) and 40-110 m (thickness ≈ 70 m), respectively. The meridional temperature gradient across the NECC, $\partial T/\partial y$, from the surface to 50 m, is about 2°C/444 km (0.005°C km⁻¹). At 100 m it is 12°C/444 km (0.03°C km⁻¹) and at 150 m it is 6°C/444 km (0.01°C km⁻¹). Below 150 m $\partial T/\partial y$ is smaller. The meridional temperature gradient across the NECC is thus concentrated in the layer between 50-150 m.

The associated profile of the annual mean anomaly of surface dynamic height relative to 1000×10^4 Pa is shown in Fig. 2.1.b. The salinity, which also contributes to the surface dynamic height anomaly, ranges from 34.3 to 34.9 Practical Salinity Unit (PSU) from 5°-10°N and 0-150 m (not shown). The surface dynamic height anomaly across the NECC changes from 150 dynamic cm (dyn cm) at 9°N to 175 dyn cm at 5°N; a difference of 25 dyn cm. Using 1000×10^4 Pa as the reference level, Wyrtki and Kilonsky (1984) calculated annual mean zonal geostrophic transports.

2.1.2 The motion field

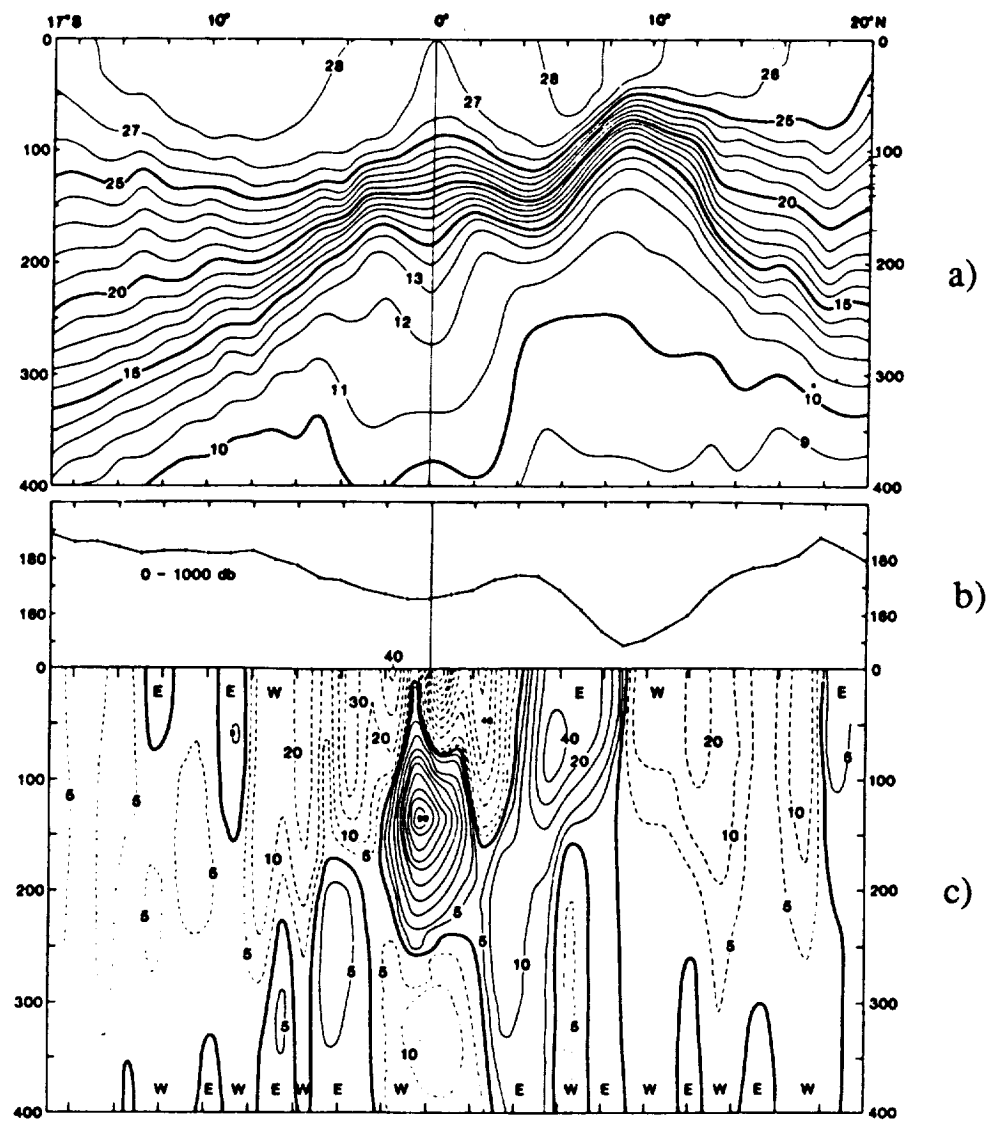


Figure 2.1 Annual mean cross-section along 150°-158°W observed during May 1979 - April 1980, a) temperature, b) dynamic height and c) zonal velocity in cm s^{-1} . From Wyrtki and Kilonsky 1984.

The zonal geostrophic flow is shown in Fig. 2.1.c. The horizontal boundaries of the NECC are clearly defined by the eastward flow between 4°-9°N. In the vertical, however, since boundaries are not as obvious, Wyrki and Kilonsky (1984) subjectively determined a dividing line at 170 m between the NECC and the sub-surface countercurrent located between 200-400 m. As a result, the NECC is defined as a shallow current confined within the upper 170 m. Other features characterizing the annual mean current are: 1) maximum current speed of near 40 cm s^{-1} , 2) current maximum located sub-surface between 40-100 m, and 3) eastward flow present at the surface layers between 4°-9°N. The geostrophic transport was calculated by integrating the zonal current over the area of the NECC defined by a bottom depth near 170 m and horizontal boundaries at 4° and 9°N. Mean annual eastward transport is thus estimated at 19.8 Sv ($1 \text{ Sv}=10^6 \text{ m}^3 \text{ s}^{-1}$).

2.2 Theoretical review of NECC Dynamics

The work of Ekman at the beginning of the century represents one of the earliest theoretical contributions to modern oceanography. Ekman (1905), inspired by observations at sea, wanted to isolate the effects of the winds on the generation of currents.

2.2.1 Ekman Theory

The Ekman equations, 2.2, were derived assuming no horizontal velocity gradients and steady motion and neglecting horizontal pressure gradients. In addition, the ocean was assumed to be infinitely deep such that friction at great depth is negligible

because the velocity approaches zero with increasing depth and lateral friction can be ignored. The Ekman currents are thus given by

$$fv_e + A_z \frac{\partial^2 u_e}{\partial z^2} = 0 \quad (2.2.a)$$

$$-fu_e + A_z \frac{\partial^2 v_e}{\partial z^2} = 0 \quad (2.2.b)$$

where u_e and v_e are the Ekman velocity components in the x (positive east) and the y (positive north) directions, A_z is the coefficient of vertical eddy viscosity and z is positive upward. The boundary conditions for Eq. 2.2 are constant wind stress at $z=0$ and $u_e=v_e=0$ in deep water. The vertical eddy viscosity, A_z , is assumed to be constant. For a wind blowing in the north-south direction only, the solutions to Eq. 2.2 are (Pond and Pickard 1987)

$$u_e(z) = V_o \cos\left(\frac{\pi}{4} + \frac{\pi}{D_E} z\right) \exp\left(-\frac{\pi}{D_E} z\right) \quad (2.3.a)$$

$$v_e(z) = V_o \sin\left(\frac{\pi}{4} + \frac{\pi}{D_E} z\right) \exp\left(-\frac{\pi}{D_E} z\right) \quad (2.3.b)$$

where $V_o = \frac{\sqrt{2} \pi \tau_y}{D_E \rho f}$ (2.4)

is the magnitude of the surface Ekman current and

$$D_E = \pi \left(\frac{2A_z}{|f|} \right)^{1/2} \quad (2.5)$$

is the Ekman depth or the depth of frictional influence. Ekman's equations are unique in the sense that they give the velocity components of a pure drift current as a function of depth. The surface currents are simply obtained by setting z equal to zero. At $z=-D_E$,

the Ekman depth, the current vector is exactly opposite to the surface vector and the current speed has decreased to $(1/e)V_0$.

If Eq. 2.2 is integrated from the surface to a level deep enough such that the integration includes the entire wind-driven layer, expressions for the Ekman mass transport per unit width can be obtained:

$$M_x^E = \frac{\tau_y}{f} \quad (2.6.a)$$

$$M_y^E = -\frac{\tau_x}{f} \quad (2.6.b)$$

The important implications of Ekman's work are that the purely wind-driven transports are 1) at right angles to the wind, 2) proportional to the wind stress, and 3) inversely proportional to sine of the latitude. Pure drift current vectors turn and decrease in magnitude with depth.

2.2.2 Sverdrup Balance

Sverdrup (1947) was interested in accounting for the observed features of the equatorial surface currents on the basis of wind stress forcing only. He was particularly motivated by the conspicuous presence of the equatorial countercurrent. The starting point was the linear, steady-state horizontal momentum equation including the effects due to the horizontal pressure gradients, rotation and vertical friction,

$$\frac{\partial p}{\partial x} = f \rho v + \frac{\partial \tau_x}{\partial z} \quad (2.7.a)$$

$$\frac{\partial p}{\partial y} = -f \rho u + \frac{\partial \tau_y}{\partial z} \quad (2.7.b)$$

Lateral frictional effects are ignored. The bottom boundary condition is zero currents at a depth d where the horizontal pressure gradients and horizontal velocities vanish, d is

sometimes called the "level of no motion." Integration of Eq. 2.7 from $z=0$ to $z=-d$ yields

$$\frac{\partial P}{\partial x} = f M_y + \tau_x(z=0) \quad (2.8.a)$$

$$\frac{\partial P}{\partial y} = -f M_x + \tau_y(z=0) \quad (2.8.b)$$

where τ_x and τ_y and M_x and M_y are the x-and y-components of the wind stress, τ , and the mass transport, M , which is defined as

$$M = \int_{z=-d}^{z=0} \rho V dz \quad (2.9)$$

After cross-differentiating Eq. (2.8), subtracting Eq.'s 2.8.a and 2.8.b, and using the integrated continuity equation between $z=0$ and $z=-d$, where $w(z=0) = w(z=-d) = 0$,

$$\frac{\partial M_x}{\partial x} + \frac{\partial M_y}{\partial y} = 0, \quad (2.10)$$

the "vorticity balance for the interior ocean" is obtained:

$$M_y \beta - \text{curl}_z \tau = 0 \quad (2.11)$$

where $\beta = df/dy = 2\omega \cos \theta / R$ is the meridional gradient of the planetary vorticity, f and $\text{curl}_z \tau$ is the vertical component of the curl of the wind stress at the sea surface, τ .

The implications of the vorticity balance Eq. 2.11 can be illustrated assuming a homogeneous ocean. For example if $\text{curl}_z \tau$ is positive, the vorticity of a fluid parcel will increase. This results in northward displacement such that the equation can be balanced by greater planetary vorticity on the left-hand-side of Eq. 2.11. In addition, when the curl of the wind stress is zero, the integrated north-south mass transport is also zero. This is in fact observed as lines of zero wind stress curl approximately coincides with the boundaries separating the circulation in major gyres.

2.2.3 Ekman Pumping

The flow in the layer between $z=0$ and $z=-d$ consists of both Ekman and geostrophic current components such that Eq. 2.10 may be written as

$$\nabla_h \cdot \mathbf{M} = \nabla_h (\mathbf{M}^E + \mathbf{M}^G) = 0. \quad (2.12)$$

The subscript h indicates horizontal divergence. The continuity equation for the Ekman layer, i.e., the layer from $z=0$ to $z=-D_E$ where $-D_E$ is the bottom of the layer of frictional influence defined above is thus given by (Stommel, 1965)

$$\nabla_h \cdot \mathbf{M}^E - \rho w_E = 0. \quad (2.13)$$

Here, w_E is the vertical velocity at the bottom of the Ekman layer associated with divergence and convergence in the Ekman layer. If $w_E \neq 0$ mass is transferred to or from the geostrophic layer below the Ekman layer leading to convergence and divergence of the mass transport in the geostrophic layer. This process is referred to as Ekman pumping.

An expression for the Ekman pumping velocity, w_E , in terms of the wind stress curl may be obtained by substituting Eq. 2.6, the definition of \mathbf{M}^E , into Eq. 2.13

$$\frac{\partial}{\partial x} \left(\frac{\tau_y}{f} \right) + \frac{\partial}{\partial y} \left(-\frac{\tau_x}{f} \right) - \rho w_E = 0. \quad (2.14)$$

On a β -plane ($f = f_0 + \beta y$), Eq. 2.14 becomes

$$w_E = \frac{1}{\rho f} (\text{curl}_z \boldsymbol{\tau} - M_y^E \beta). \quad (2.15)$$

Here ρ is the density of sea water and f is the Coriolis parameter. Equation 2.15 will be applied to investigate the relationship between the north-south slope of the NECC thermocline and the Ekman pumping velocity.

Chapter 3

Annual Variation of the Simulated NECC

3.1 Description of the model

The ocean general circulation model (OGCM) used in this study was developed at NOAA's Geophysical Fluid Dynamics Laboratory (GFDL). The GFDL OGCM is based on the primitive equations with the Boussinesq and hydrostatic approximations. The numerical method was developed by Bryan (1969) and the model physics is described in Cox (1984). Pacanowski and Philander (1981) modified the model to include parameterization of the mixing coefficients in terms of the Richardson number. Such a modification was believed to be necessary to achieve realistic simulations of the Equatorial Undercurrent (EUC) in light of new observations of highly variable eddy viscosity in the EUC (Halpern 1980). Currently the model is being run on a CRAY-YMP at NASA's Ames Research Center. Further details on the model, which generated the fields described herein, can be found in Chao *et al.* (1991).

The domain of the GFDL OGCM covers the equatorial Pacific from 130°E to 70°W and from 30°S to 50°N. The surface forcing is climatological monthly mean wind stress

(Hellerman and Rosenstein 1983) and the heat flux across the air-sea interface is calculated using the model-simulated sea surface temperature and the prescribed air temperature. The wind stress is made to vary smoothly from month to month by linear interpolation. The model is started from a state of rest and the initial temperature and salinity are the climatology for January (Levitus 1982). The model has 27 levels in the vertical; the upper 10 levels have a resolution of 10 m. The model ocean has a flat bottom at a depth of 4149 m. The latitudinal resolution is $1/3^{\circ}$ in the latitude band from 10°S to 10°N . Poleward of 10° , the grid spacing increases gradually to 2.5° latitude at 30°S and 50°N . The longitudinal resolution is 1° longitude. For a further description of the boundary conditions and model design, see Chao *et al.* (1991). This model has been successfully applied in simulations of the seasonal cycles of the tropical Pacific (Philander *et al.* 1987), the tropical Atlantic (Philander and Pacanowski 1986) and the El Niño of 1982-83 (Philander and Seigel 1985).

During the model run, values of the three current components u , v , w , and temperature and salinity, T and S , are averaged and stored every three days. A 1-hour snapshot on the 15th day of the month of all five variables is also stored. Since both of these products are used it is important to distinguish between them. Monthly averages are computed using the ten 3-day averages for every month.

3.2 Description of the climatological wind stress

The Hellerman and Rosenstein (1983) (H&R) wind stress data are based on 106 years of historical surface wind observations made over the world ocean. The wind data were processed at the National Climatic Center (the data set is commonly referred to as TDF-11). H&R calculated the stress components using a drag coefficient which was a function of the magnitude of the wind, $(u^2+v^2)^{1/2}$ and the difference between the air

temperature and sea surface temperature (SST). The functional relationship to these two parameters were based on the tabulated values of Bunker (1976).

The annual cycle is revealed by comparing March and September wind stress (Fig. 3.1). The climatological southeast trades are weak in March when the ITCZ is at its southernmost location near the equator. In September the ITCZ has moved to its northernmost position and the southeast trades are strong. Depending on the wind stress product used, hindcasts of the 1982-1983 El Niño with an OGCM yield substantially different simulations of the NECC (Harrison *et al.* 1989). This sensitivity to $\text{curl}_z \tau$ makes simulating the NECC a difficult task. The results described herein may therefore be somewhat specific to the H&R climatological wind stress. Several authors have suggested that the H&R wind stress is overestimated by 20-30%. For example, Harrison (1989) computed wind stress using the TDF-11 winds with the Large and Pond (1982) drag coefficient rather than the Bunker (1976) formulation used by H&R. The resulting wind stress was typically smaller by $2 \times 10^{-2} \text{ N m}^{-2}$ in the trades and $4 \times 10^{-2} \text{ N m}^{-2}$ in the middle latitudes. In another study, a comparison between the wind stress computed based on ECMWF analyses and the H&R wind stress was made (Trenberth *et al.* 1989). In contrast to the findings of Harrison (1989), the ECMWF wind stress is weaker than H&R only in the subtropics and northern middle latitudes. In the tropics, ECMWF is comparable or slightly stronger than the H&R wind stress (see Fig. 21 in Trenberth *et al.* 1989).

The curl of the wind stress, $\text{curl}_z \tau$, was computed from the H&R wind stress. The 1° latitude by 1° longitude wind stress was interpolated onto the model grid prior to the computation. Since Δx is uniform in the model grid and Δy is not, $\text{curl}_z \tau$ was approximated by the following finite difference equation:

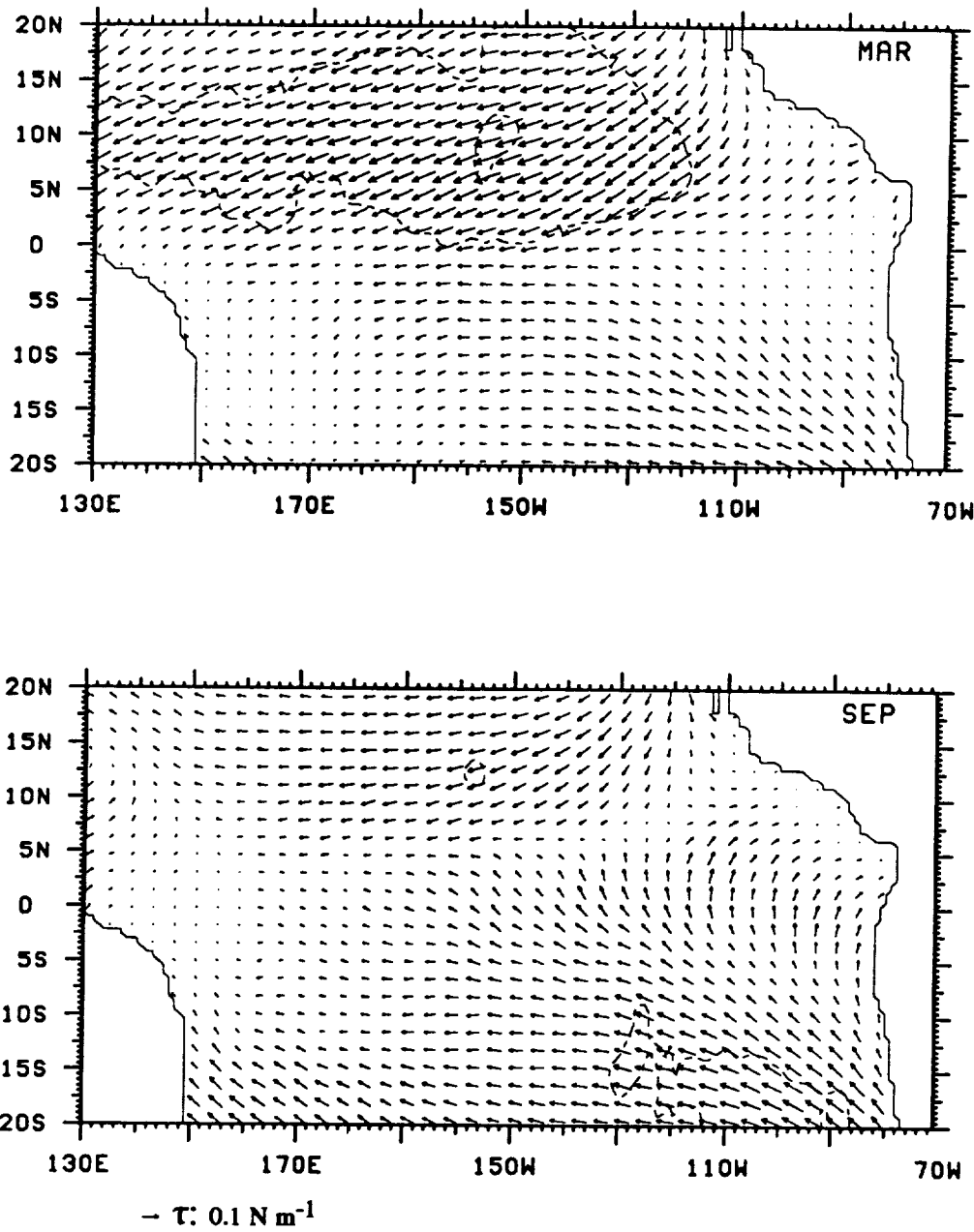


Figure 3.1 Hellerman and Rosenstein (1983) climatological wind stress for March and September. The zonal component is contoured with an interval 0.1 N m^{-2} and negative (westward) contours are dashed.

$$(\text{curl}_z \tau)_{i,j} = \frac{[(\tau_y)_{i+1,j} - (\tau_y)_{i-1,j}]}{2\Delta x} - 0.5 \left\{ \frac{[(\tau_x)_{i,j+1} - (\tau_x)_{i,j}]}{\Delta y_j} + \frac{[(\tau_x)_{i,j} - (\tau_x)_{i,j-1}]}{\Delta y_{j-1}} \right\}. \quad (3.1)$$

Here the longitudinal and latitudinal grid points are subscripted by i and j, respectively. The monthly mean $\text{curl}_z \tau$ for March and September are shown in Fig. 3.2. The structure of the curl in March is characterized by a region of positive curl between 10°N and the equator. In September the curl in this region is negative, at least from the equator to about $7^\circ\text{-}8^\circ\text{N}$, such that there is a large change in the magnitude and sign across the NECC region.

3.3 The seasonal cycle of temperature and currents

Monthly-mean maps of sea surface temperature (SST) and surface currents were produced to illustrate their respective annual cycles. In addition to the surface plots, the circulation in the y-z plane along various longitude lines is investigated. The choices of longitude sections are 150°E , 180° , 160°W , 140°W , 125°W and 110°W .

3.3.1 The thermal field

a. SST

Equatorial SST, in the Pacific peak in February with temperatures from 28°C to 30°C west of the date line and between $24\text{-}28^\circ\text{C}$ east of the date line (see Fig. 3.3). The development of the seasonal equatorial cold tongue in the eastern Pacific is evident in March with the appearance of 23°C water near 108°W . Equatorial SST continue to cool through August when the 24°C water extends from the coast of South America to near 135°W and the area covered by 21°C water reaches a maximum. The cycle is completed with gradual warming from November to February. In the western Pacific from

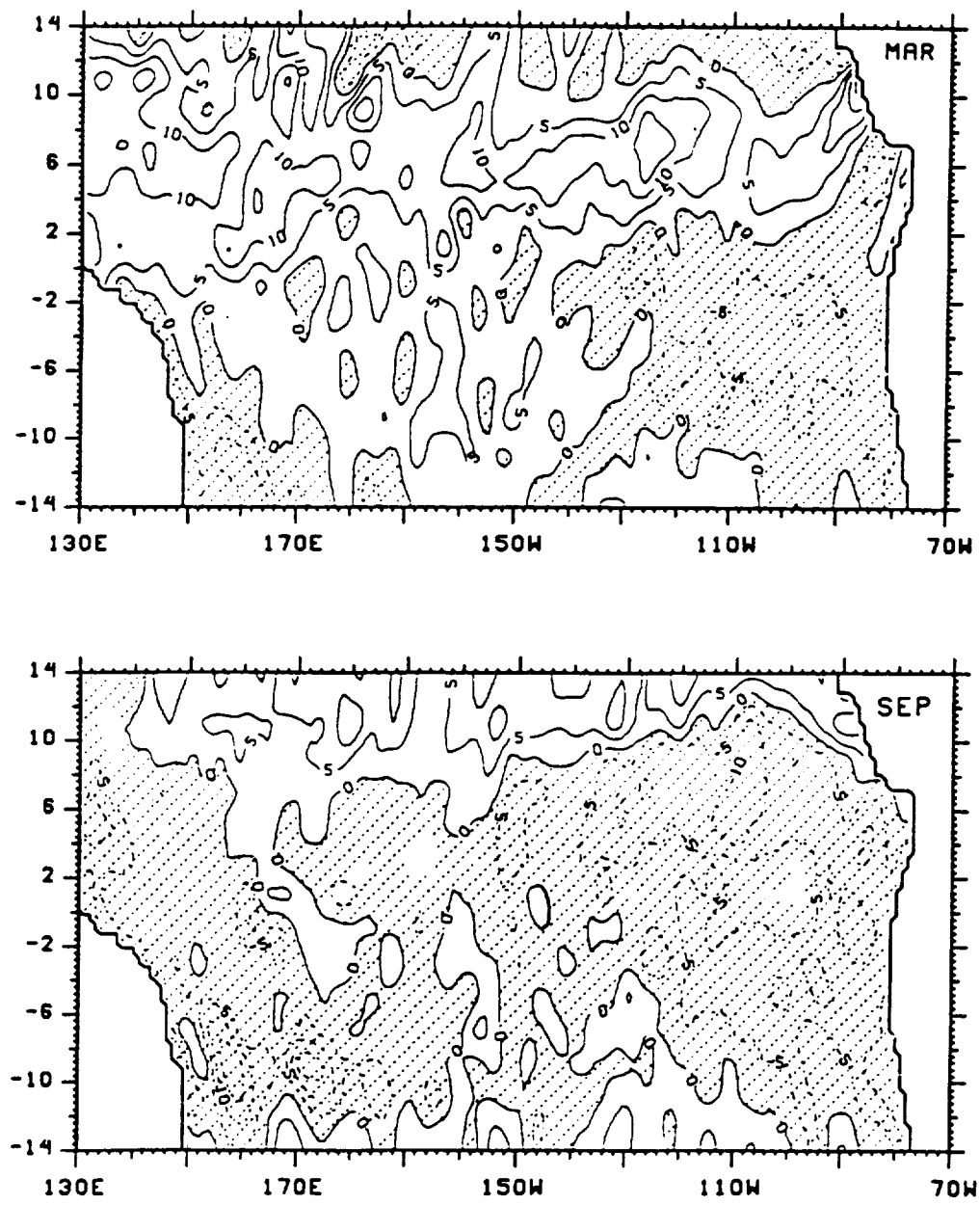


Figure 3.2 Monthly mean wind stress curl computed from Hellerman and Rosenstein (1983) climatological wind stress for March and September. The contour interval is $5 \times 10^{-8} \text{ N m}^{-3}$ and negative curl is shaded.

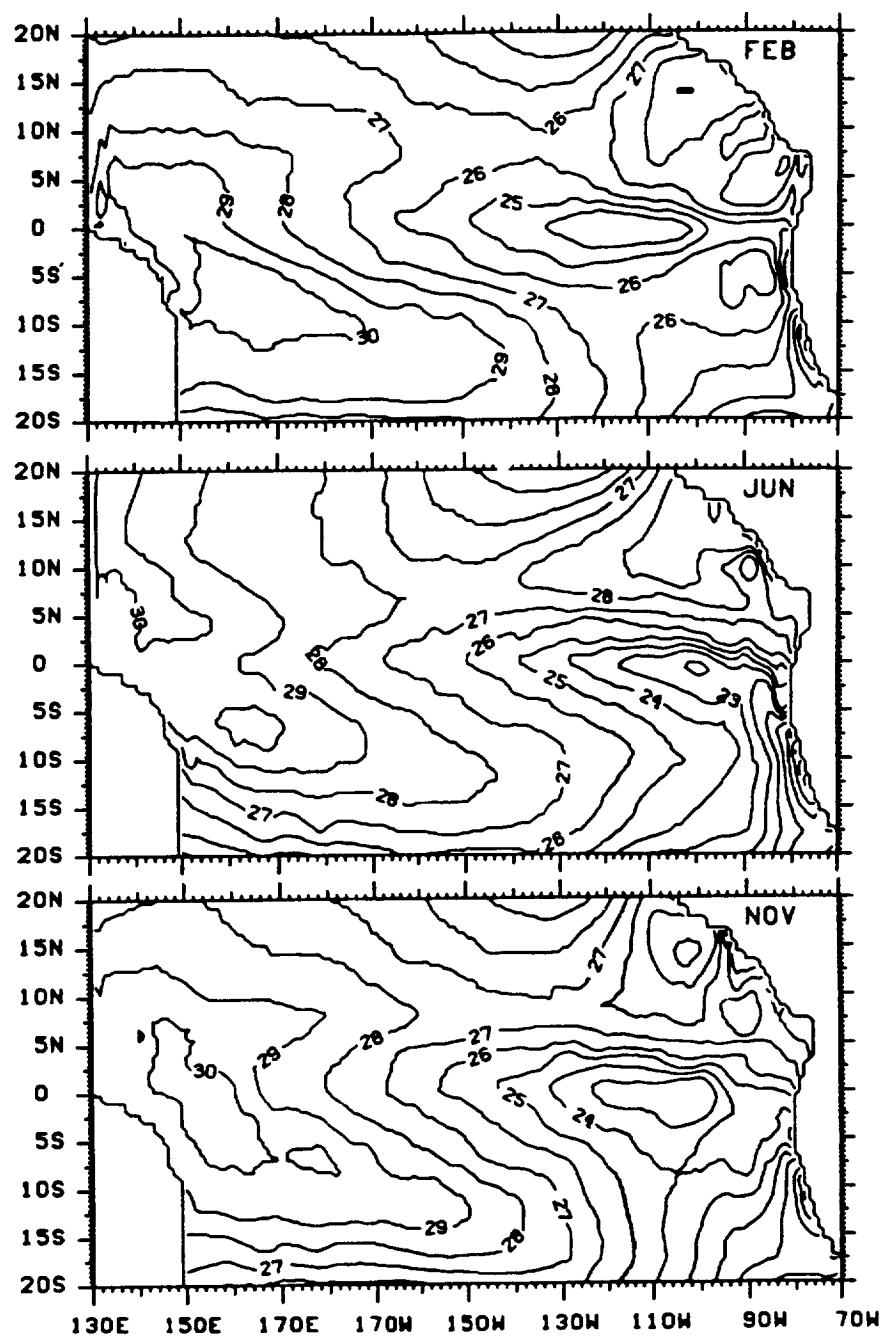


Figure 3.3 Monthly mean SST for February, June, and November.

November through March, warm water above 30°C is located on the equator and southward to near 10°S from 150°E to 175°W. From April through November most of the western Pacific is dominated by SSTs above 28°C and the 30°C water has expanded northward across the equator. In July, August and September this pool of warmest water has shifted north of the equator to cover an area from approximately 3-20°N and 135°E-160°E.

Based on the SST maps, the NECC is associated with warm temperatures relative to the South Equatorial Current (SEC) to the south and the North Equatorial Current (NEC) to the north. SSTs across the NECC are almost never less than 26°C. From June to October, 28°C waters are common across the entire basin as warm water is advected eastward in the NECC. From an interannual standpoint, variations in the strength of the NECC leading to increased (decreased) eastward advection of heat has been linked to cooling (warming) of the West Pacific warm pool (Meyers and Donguy 1984).

A prominent feature in the monthly *snapshot* SST maps (Fig. 3.4) is the wavy pattern in the eastern equatorial SST front near 3°N. The oscillations are due to equatorial unstable waves (Legeckis 1977; Philander 1978). The SST waves seem to be limited in both space and time. In the monthly *snapshot* SST maps, the waves are weak from February to May and strong from July to January. This is consistent with the findings of Legeckis (1986) who found SST waves in satellite imagery to be most pronounced from August to February.

Since the model-simulated unstable waves (Philander *et al.* 1986) have periods near 30 days, monthly averaging the 3-day values has a smoothing effect. It is therefore curious that the monthly mean maps show oscillations in the SST isotherms occurring only in March, April and May and not during the remainder of the year (see Appendix

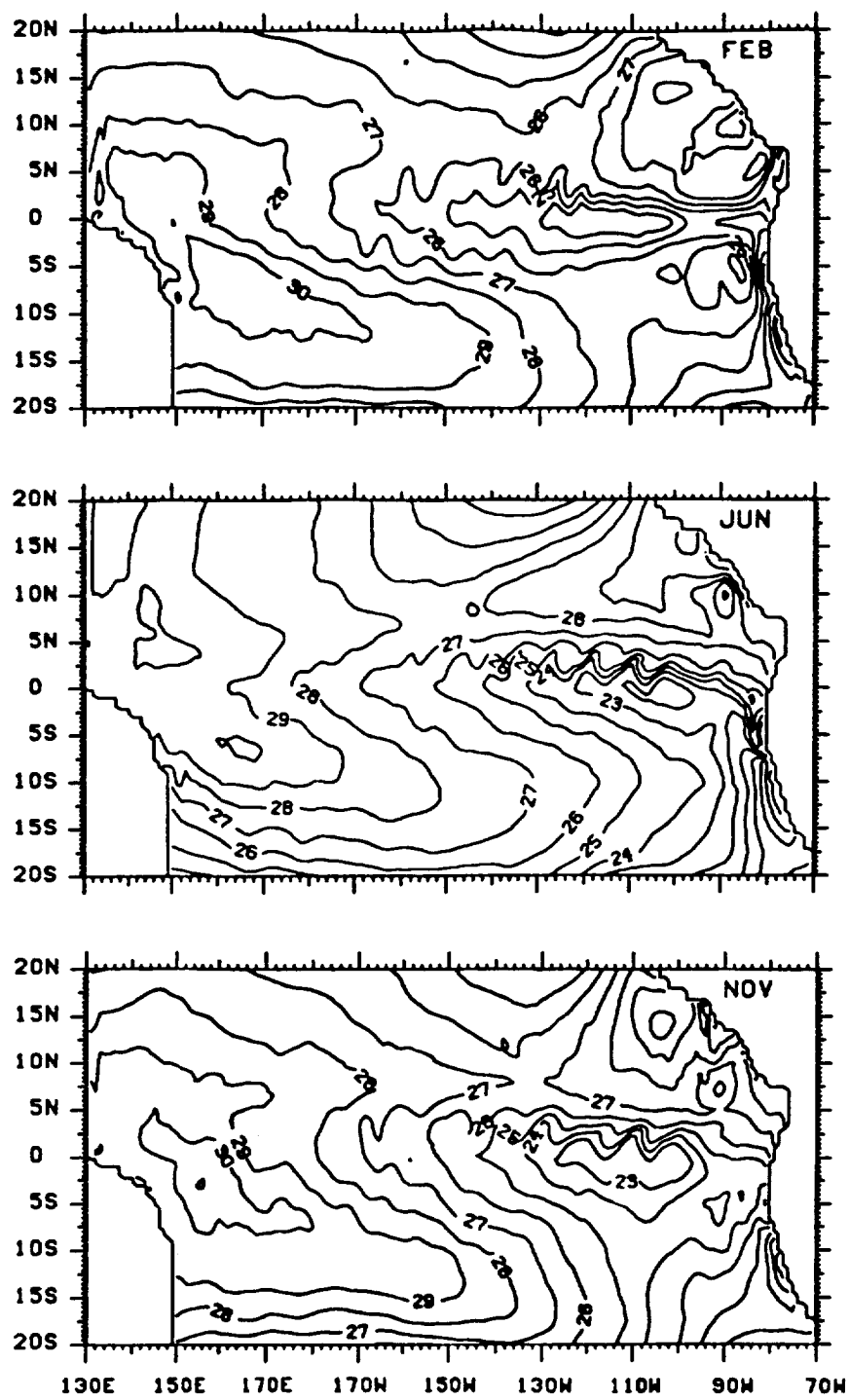


Figure 3.4 Instantaneous monthly SST for February, June, and November.

B.1), contrary to the results of Legeckis (1986) and Philander *et al.* (1986). The wavy pattern in the monthly averaged maps in March and April are probably not due the unstable waves described by Philander *et al.* (1986), since the wavelength appears smaller than the 1000 km characteristic of the unstable waves (Yi Chao, personal communication).

b. Vertical structure of temperature

The vertical structure of the annual mean temperature north of the equator is characterized by a north-south thermocline slope, a pattern which is evident across most of the basin (Fig. 3.5). At 150°E and 180° the thermocline is somewhat diffused compared to the central Pacific sections. The thickness of the 160°W thermocline (defined by the 14°C and the 26°C isotherms) at 5°N and 10°N is 90 m and 120 m, respectively. The 110°W section has a shallow thermocline and almost no north-south slope. Figure 3.6 illustrates the movement of the thermocline during the year along 160°W. The annual cycle of the north-south slope of the thermocline may be illustrated by the 20°C isotherm which approximately marks the center of the thermocline. The difference in the depth of the 20°C isotherm between 5°N and 10°N is 20 m in April, 50 m in July, 70 m in October, and 50 m in January.

The seasonal fluctuations of the thermocline are concentrated north of the equator in a well-defined subsurface latitude band. For instance, at 160°W a region of standard deviations greater than 2°C is located between 130-180 m and 2.5°-5°N (Fig. 3.7). The same is true at 140°W but at 125°W there are two regions of large standard deviations, one between 2.5°N-5°N, 80-120 m and another in the upper 40 m between 10-14°N. The annual variability at 110°W is greatest north of 10°N, which is outside the NECC region. At 150°E the area of greatest variation occupies the entire depth range of the

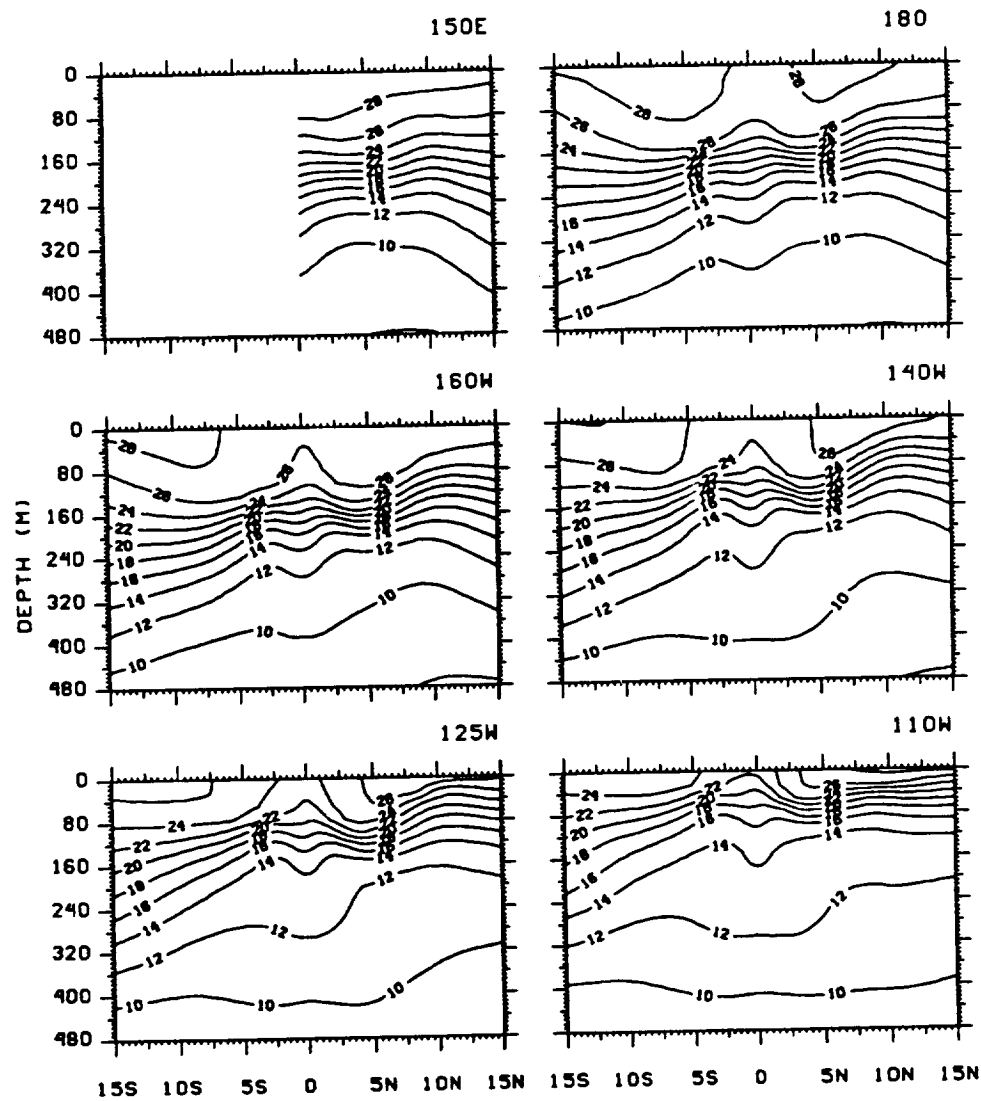


Figure 3.5 Latitude-depth sections of annual mean temperature. The contour interval is 2°C .

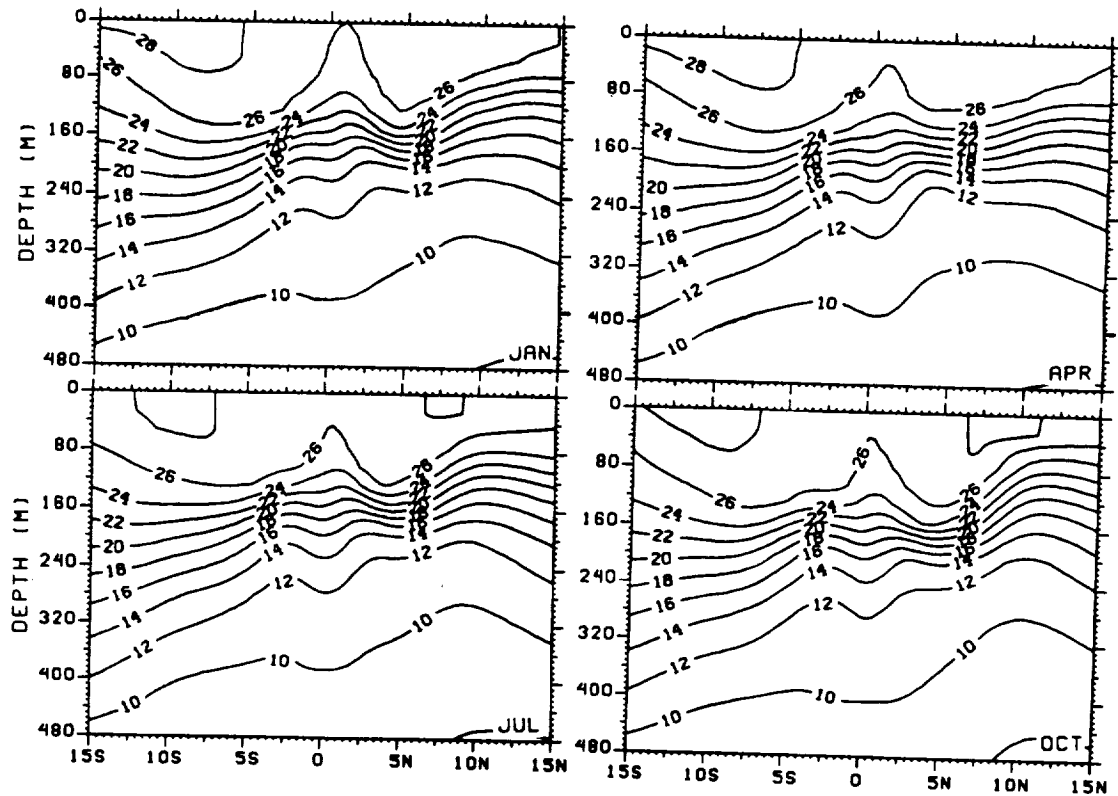
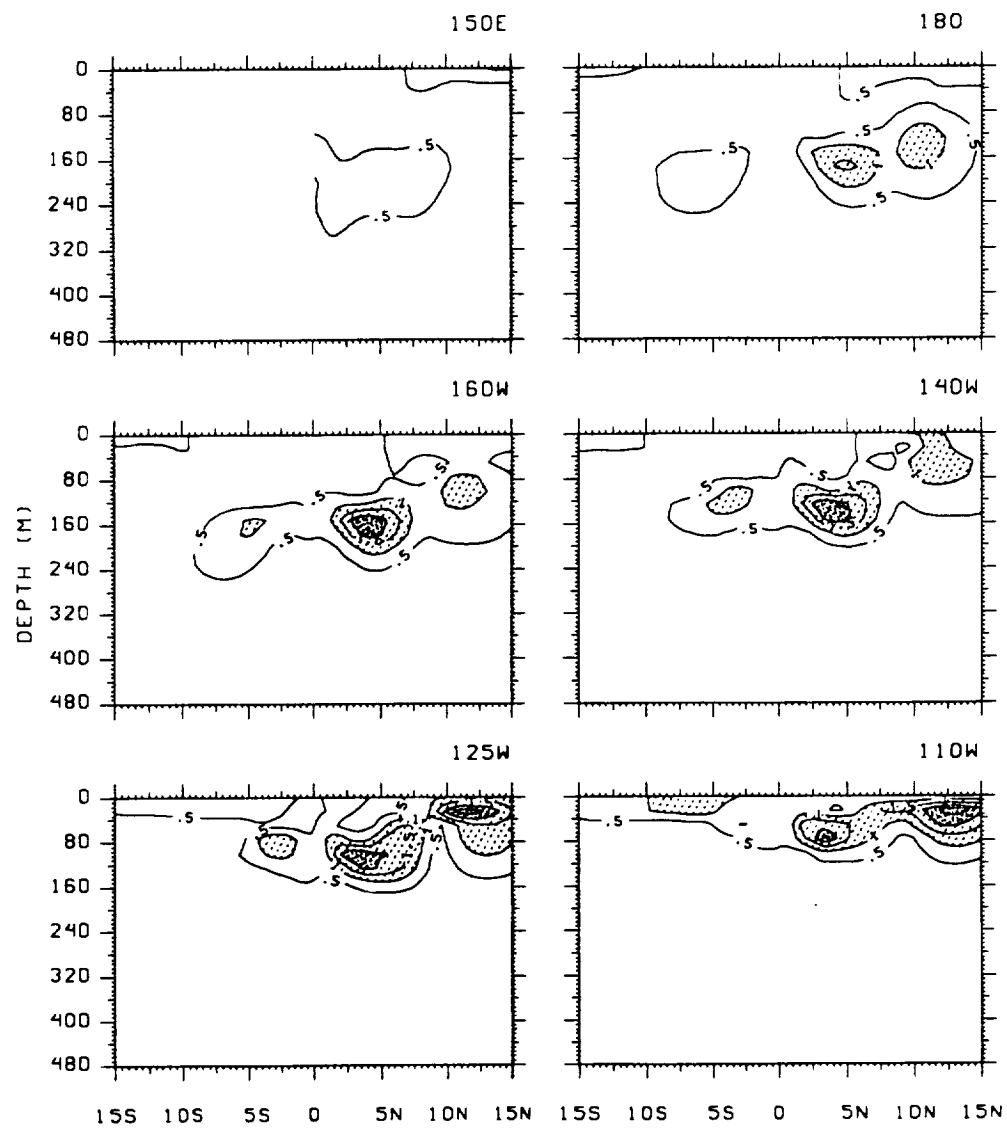


Figure 3.6 Latitude-depth diagram of the monthly mean temperature along 160°W for January, April, July, and October. The contour interval is 2°C.



**Figure 3.7 Latitude-depth diagram of the standard deviation of temperature.
Contour interval is 0.5°C.**

thermocline indicating that the thermocline moves up and down as a whole. In contrast in the 160°, 140° and 125°W sections, the vertical temperature changes are limited to a few isotherms in the center of the thermocline. The largest annual variations coincide with the location of the annual mean 20°C isotherm at those longitudes (compare Figs. 3.5 and 3.7). The 20°C isotherm will thus capture much of the seasonal variations in the depth of the thermocline.

Time series of the depth of the 20°C isotherm near the southern and northern boundaries of the NECC along 160°W are presented in Fig. 3.8. Vertical oscillations associated with the unstable waves are also clearly evident in the temperature field. As mentioned above, the north-south thermocline slope across the NECC is weak in April and strong in October. The difference between the depth of the 20°C isotherm at 9.2°N and at 4.5°N shown in Fig. 3.8 represents the north-south thermocline slope across the NECC. It appears that the transition from the weak north-south slope in April to the steep slope in October is marked by a rapid increase in the depth of the 20°C isotherm at 9.2°N during the month of July. Thereafter, the 20°C isotherm at 9.2°N remains near a depth of 160 m from August until November after which it gradually rises to 135 m in June. In contrast, the depth of the 20°C isotherm at 4.5°N changes gradually from June to November.

c. Density field

The dynamic height anomaly at 5 m relative to 484×10^4 Pa was computed from the vertical profiles of temperature and salinity. The method for computing the dynamic height anomaly is described in chapter 4. Table 3.1 summarizes the model-simulated annual changes in the surface dynamic height anomaly of the countercurrent trough near 10°N and the equatorial ridge near 4°N as a function of longitude. The north-south

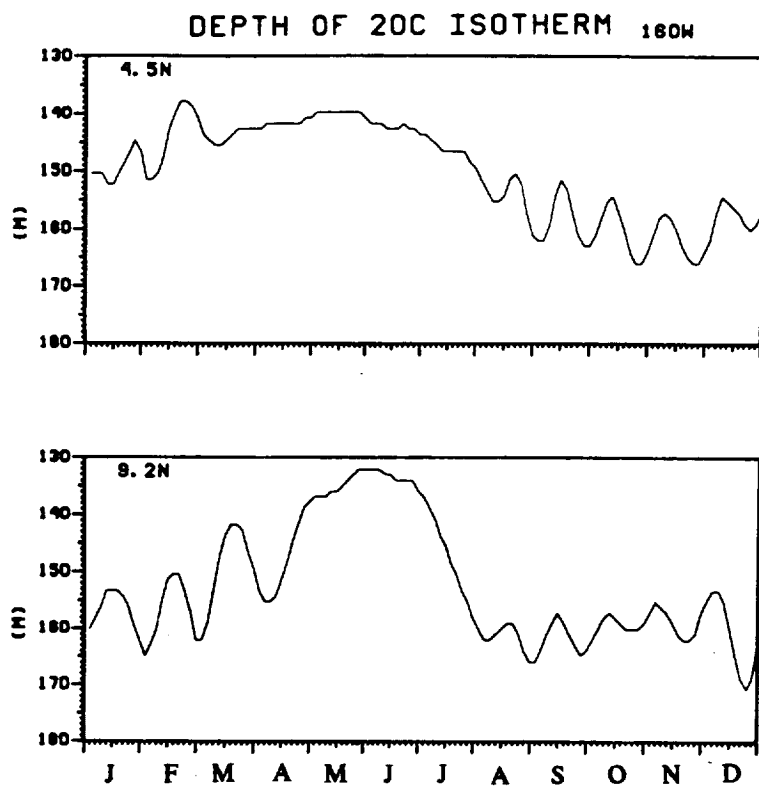


Figure 3.8 Time series of the depth of the 20°C isotherm in meters for 4.5°N and 9.2°N along 160°W.

Table 3.1. Monthly mean dynamic height anomaly at 5 m relative to 484×10^4 Pa (in dyn cm) of the equatorial ridge, the countercurrent trough and the difference between the two.

		JAN	FEB	MAR	APR	MAY	JUN	JUL	AUG	SEP	OCT	NOV	DEC	AVR.	S. D.
150°E	Trough	127.4	129.3	131.4	131.6	132.4	133.3	131.3	130.0	129.9	128.8	127.0	126.5	129.9	2.2
	Ridge	137.8	141.7	143.5	141.5	141.4	140.8	139.0	134.1	140.2	143.6	142.1	139.3	140.4	2.6
	ΔNECC	10.4	12.5	12.2	10.0	9.0	7.1	7.7	4.1	10.3	15.2	15.1	12.8	10.5	3.3
180°	Trough	119.0	122.3	124.6	127.0	127.9	124.9	123.7	122.3	119.5	117.6	117.6	118.8	122.4	3.6
	Ridge	137.6	138.6	134.9	133.0	129.4	130.6	131.5	138.2	141.1	139.9	138.6	137.5	135.9	3.9
	ΔNECC	18.5	16.3	10.2	5.8	1.5	5.7	7.8	15.0	21.6	22.2	21.0	18.7	13.7	7.2
160°W	Trough	119.7	114.1	113.8	115.0	113.4	111.8	110.9	110.0	107.9	105.8	105.7	108.5	111.4	4.1
	Ridge	128.0	124.8	121.1	120.5	118.3	121.2	127.0	132.7	132.2	131.3	130.7	130.9	126.6	5.2
	ΔNECC	16.0	10.7	7.3	5.5	4.9	9.4	16.1	22.7	24.3	25.5	25.3	22.4	15.8	8.1
140°W	Trough	97.0	99.5	101.7	103.0	101.4	98.7	97.9	96.1	94.7	93.9	93.9	95.6	97.8	3.1
	Ridge	116.8	113.0	108.9	108.7	110.8	114.5	121.1	121.3	121.4	121.0	121.5	120.3	116.6	5.2
	ΔNECC	19.8	13.5	7.1	5.2	9.4	15.8	23.2	25.0	26.7	27.4	27.6	24.7	18.8	8.3
125°W	Trough	88.2	92.6	94.9	93.8	93.4	92.5	93.3	92.3	91.2	89.3	87.4	87.6	91.4	2.3
	Ridge	107.9	104.8	101.0	102.4	105.3	110.1	113.4	113.3	112.6	113.2	113.2	110.8	109.0	4.6
	ΔNECC	19.7	12.1	6.1	8.7	11.9	18.6	20.2	21.1	21.4	24.0	25.7	23.4	17.7	6.4
110°W	Trough	92.2	93.8	93.5	94.0	95.1	96.5	96.9	94.6	92.6	91.6	92.3	90.7	93.6	1.9
	Ridge	99.2	95.8	95.0	100.1	103.2	104.4	104.0	103.0	103.4	103.6	102.0	100.7	101.2	3.2
	ΔNECC	7.0	2.0	1.5	6.0	8.0	7.9	7.0	9.6	10.8	12.0	9.8	10.0	7.6	3.2

difference in the surface dynamic height anomaly is an indicator of the strength of the zonal geostrophic current component. The largest annually averaged difference across the NECC is 18.8 dyn cm along 140°W. October is the month of seasonal maximum difference in the 150°E, 180°, 160°W and 110°W sections. Minima occur in August at 150°, May at 180° and 160°W, April at 140°W and March at 125° and 110°W.

There is no consistent pattern of trough displacement about the annual mean being larger or smaller than the ridge displacement (Table 3.2). In addition the maximum displacement of neither the trough nor the ridge is related to the occurrence of maximum difference across the NECC (compare Tables 3.1 and 3.2). This indicates that the annual cycles of the movement of the trough, the ridge and the difference between the two are out-of-phase. This is consistent with observations from sea level stations in the equatorial Pacific (Wyrtki 1974a).

3.3.2 The motion field

a. *Surface currents*

The character of the surface flow in the equatorial current system from 15°S to 15°N varies throughout the year in response to the changing winds (Wyrtki 1974b). Figure 3.9 illustrates the annual cycle of the equatorial surface currents. In April westward flow dominates the equatorial Pacific, except for a region of eastward flow in the eastern Pacific from 4°-7°N. The eastward flow appears to be part of a local anticyclonic circulation centered near 95°W and 3.5°N. Current speeds are fairly uniform equatorward of 5°. The divergence associated with poleward drift is clearly evident along the equator in the central Pacific throughout the year. By July, the branch of the SEC located north of the equator has intensified considerably and the eastward flow in the NECC is now extending westward to 150°W. As illustrated in Fig. 3.10 the

Table 3.2. Monthly displacement (in dyn cm) about the annual mean of the equatorial ridge and the countercurrent trough.

	JAN	FEB	MAR	APR	MAY	JUN	JUL	AUG	SEP	OCT	NOV	DEC
150°E	2.5	0.6	-1.5	-1.7	-2.5	-3.4	-1.4	-0.1	-0.0	1.1	2.9	3.4
	ΔTRF	2.7	-1.3	-3.1	-1.1	-1.0	-0.4	1.5	6.3	0.3	-3.2	-1.7
180°	ΔTRF	3.4	0.1	-2.2	-4.6	-5.5	-2.5	-1.3	0.1	2.9	4.8	3.6
	ΔRDG	-1.7	-2.7	1.0	2.9	6.6	5.3	4.4	-2.3	-5.2	-4.0	-2.7
160°W	ΔTRF	-8.3	-2.7	-2.4	-3.6	-2.0	-0.4	0.5	-6.2	-5.6	-4.8	-4.1
	ΔRDG	-1.4	1.8	5.5	6.1	8.3	5.3	-0.5	-6.2	-5.6	-4.8	-4.4
140°W	ΔTRF	0.8	-1.7	-4.0	-5.2	-3.7	-0.9	-0.1	1.7	3.1	3.9	2.2
	ΔRDG	-0.2	3.6	7.7	7.9	5.8	2.1	-4.5	-4.7	-4.8	-4.4	-4.9
125°W	ΔTRF	3.2	-1.3	-3.5	-2.4	-2.0	-1.2	-1.9	-0.9	0.2	2.1	4.0
	ΔRDG	1.1	4.3	8.0	6.6	3.7	-1.1	-4.4	-4.3	-3.6	-4.2	-4.2
110°W	ΔTRF	1.5	-0.2	0.2	-0.3	-1.4	-2.9	-3.3	-0.9	1.0	2.1	1.4
	ΔRDG	2.0	5.4	6.2	1.2	-2.0	-3.2	-2.8	-1.8	-2.2	-2.4	-0.9
												0.5

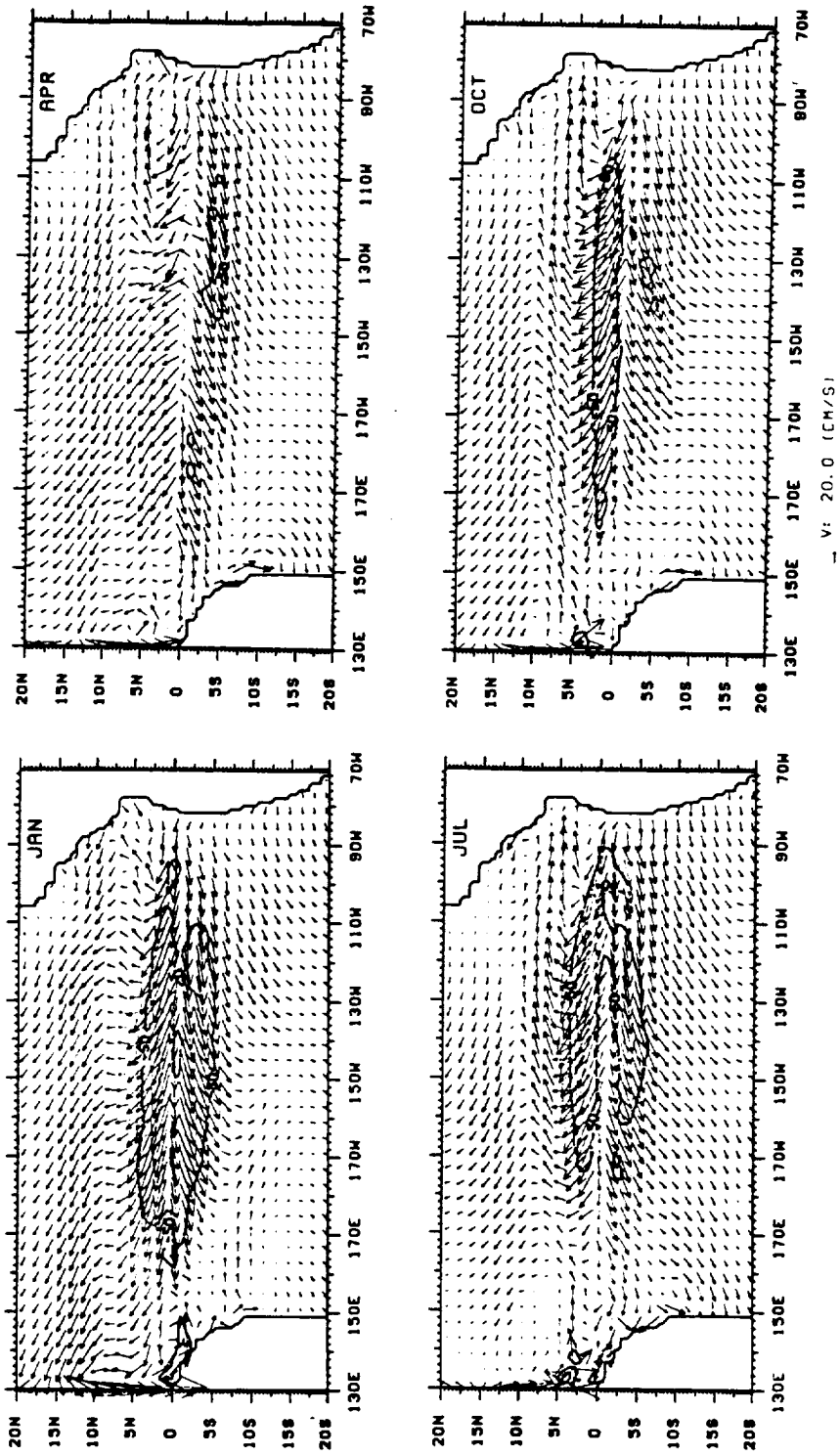


Figure 3.9 Monthly averaged 5 m currents for January, April, July, and October.
The zonal component is contoured with an interval of 50 cm s^{-1} and negative
(westward) contours are dashed.

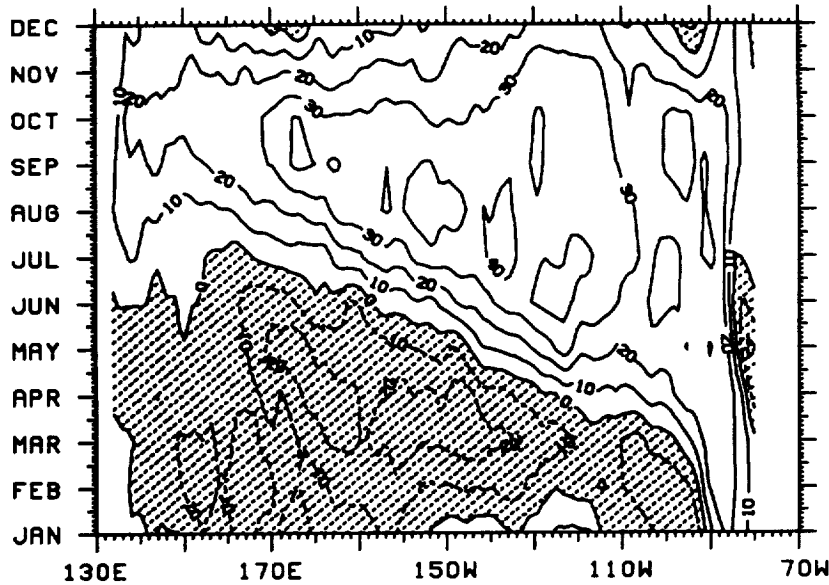


Figure 3.10 Hovmöller diagram of the zonal current component at 5 m and 7°N. The contour interval is 10 cm s^{-1} and negative (westward) currents are shaded.

annual cycle of the NECC continues to propagate westward during August and September. By October, the NECC extends from coast to coast.

b. Vertical structure of the zonal component

The subsurface structure was investigated by analyzing cross-sections along the selected longitudes spanning the current. At 160°W the annual mean latitudinal range of the NECC is from 5.1°N to 9.2°N and the vertical extent ranges from 13 m to 187 m (see Table 3.3). In addition the NECC is observed to disappear from the uppermost 15 m from February through June. During this period the subsurface current becomes less defined as velocities drop below 10 cm s^{-1} . In July the NECC strengthens and is again present in the surface layer. By September it reaches velocities of more than 40 cm s^{-1} and after September it starts to weaken again.

Table 3.3. Monthly mean NECC boundaries. The missing values appear because the NECC is not defined according to the criteria stated in the text at certain longitudes and times of the year.
 * Subjectively determined as discussed in the text.

		JAN	FEB	MAR	APR	MAY	JUN	JUL	AUG	SEP	OCT	NOV	DEC	AVR.	S. D.
150°E	North	9.3	9.3	10.0	9.7	9.0	-	-	5.0	8.3	9.0	9.0	9.0	8.8	1.4
South	6.3	6.7	7.3	7.3	7.7	-	-	-	2.0*	4.3	4.7	5.3	5.3	2.2	
Top	11.0	12.0	9.0	5.0	5.0	-	-	-	5.0	5.0	8.0	10.0	8.0	2.7	
Bottom	137.0	141.0	138.0	132.0	83.0	-	-	-	207.0	155.0	156.0	177.0	168.0	149.0	32.6
180°	North	9.7	9.7	9.3	-	4.3	7.3	7.7	9.0	9.7	10.0	10.0	9.7	8.7	1.7
South	5.3	6.0	6.3	-	3.0	3.3	3.7	4.3	5.0	5.0	5.0	5.0	5.0	4.7	1.1
Top	14.0	15.0	25.0	-	5.0	8.0	7.0	9.0	5.0	5.0	7.0	10.0	10.0	6.0	
Bottom	164.0	144.0	114.0	-	233.0	155.0	150.0	167.0	296.0	302.0	165.0	166.0	187.0	62.2	
160°W	North	9.0	9.0	8.7	8.3	7.3	8.0	9.3	9.7	10.0	10.3	10.3	10.0	9.2	1.0
South	5.0	5.7	6.3	7.7	4.7	3.3	4.7	5.0	5.0	4.7	4.7	5.0	5.1	1.1	
Top	11.0	25.0	25.0	25.0	14.0	9.0	6.0	6.0	9.0	5.0	5.0	10.0	13.0	8.0	
Bottom	142.0	115.0	93.0	75.0	109.0	148.0	276.0	310.0	337.0	275.0	199.0	161.0	187.0	90.6	
140°W	North	9.3	9.0	7.7	7.0	8.0	9.0	9.7	10.3	10.7	10.3	10.3	10.0	9.3	1.1
South	4.7	5.0	5.0	3.7	3.7	4.0	4.7	4.7	5.0	4.7	4.7	4.7	4.7	4.5	0.5
Top	9.0	17.0	25.0	22.0	7.0	5.0	5.0	5.0	5.0	5.0	5.0	6.0	8.0	10.0	6.9
Bottom	146.0	109.0	122.0	219.0	223.0	202.0	93.0	156.0	136.0	138.0	164.0	152.0	155.0	41.3	
125°W	North	8.7	8.0	6.3	7.0	8.0	8.7	9.3	10.0	10.3	10.3	10.3	10.0	8.9	1.4
South	4.7	3.7	4.0	4.3	4.3	4.0	4.7	4.7	5.0	5.3	4.7	4.3	4.5	0.5	
Top	6.0	17.0	5.0	5.0	5.0	5.0	5.0	5.0	5.0	5.0	5.0	5.0	6.0	3.5	
Bottom	148.0	178.0	196.0	161.0	168.0	117.0	136.0	120.0	108.0	128.0	122.0	103.0	140.0	29.7	
110°W	North	6.7	5.0	5.0	6.7	7.0	7.7	8.3	8.7	9.0	7.0	7.3	7.3	7.1	1.3
South	3.7	3.0	3.3	3.3	3.3	4.0	4.7	5.3	5.3	3.0	2.7	3.0	3.7	0.9	
Top	13.0	45.0	25.0	13.0	5.0	5.0	5.0	5.0	5.0	1.6.0	16.0	16.0	14.0	11.7	
Bottom	128.0	164.0	150.0	163.0	162.0	151.0	127.0	70.0	55.0	106.0	143.0	144.0	130.0	36.0	

Figure 3.11 shows meridional sections of the annually averaged u component. The current structure is seen to vary greatly in longitude. The section along 150°E , representing the western Pacific, is characterized by eastward flow from 2°N to 8°N in the surface layers and by two connected sub-surface maxima, one near 3°N and the other centered between $7^{\circ}\text{-}8^{\circ}\text{N}$. At this longitude, it is thus difficult to distinguish the NECC from the EUC. In the other five sections from 180° to 110°W , the NECC is separated from the EUC by the westward flow of the northern branch of the SEC. Except at 110°W , maximum flow occurs sub-surface near 50 m. Maximum flow is near 25 cm s^{-1} in the 160° , 140° , 125° and 110°W sections, 20 cm s^{-1} and 10 cm s^{-1} at 180° and 150°E , respectively.

The annual average NECC (defined by $u > 5 \text{ cm s}^{-1}$) is generally confined to the upper 200 m. The thickness of the NECC is subject to significant variation, however. The current boundaries are discussed further in section 3.3. The zonal velocity variance is shown in Fig. 3.12. The strength of the sub-surface flow is not subject to as much seasonal variation as the surface flow. In the NECC latitude band from roughly $5^{\circ}\text{-}10^{\circ}\text{N}$, standard deviations of $15\text{-}20 \text{ cm s}^{-1}$ are common in the upper 50 m whereas values of 4 to 8 cm s^{-1} are typical of the flow between 100 - 200 m.

c. Vertical structure of the meridional component

The westward blowing trade winds cause a poleward Ekman transport in the surface layers. An equatorward geostrophic flow below the thermocline corresponds to the sea level sloping downward towards the east (Wyrtki and Kilonsky 1984). The annual cycle of the meridional circulation is illustrated in the monthly plots of the v -component in the $y\text{-}z$ plane for the 6 longitude sections in Appendix C.2. Figure 3.13 shows the annual mean. Similar to the picture of the transverse circulation suggested by

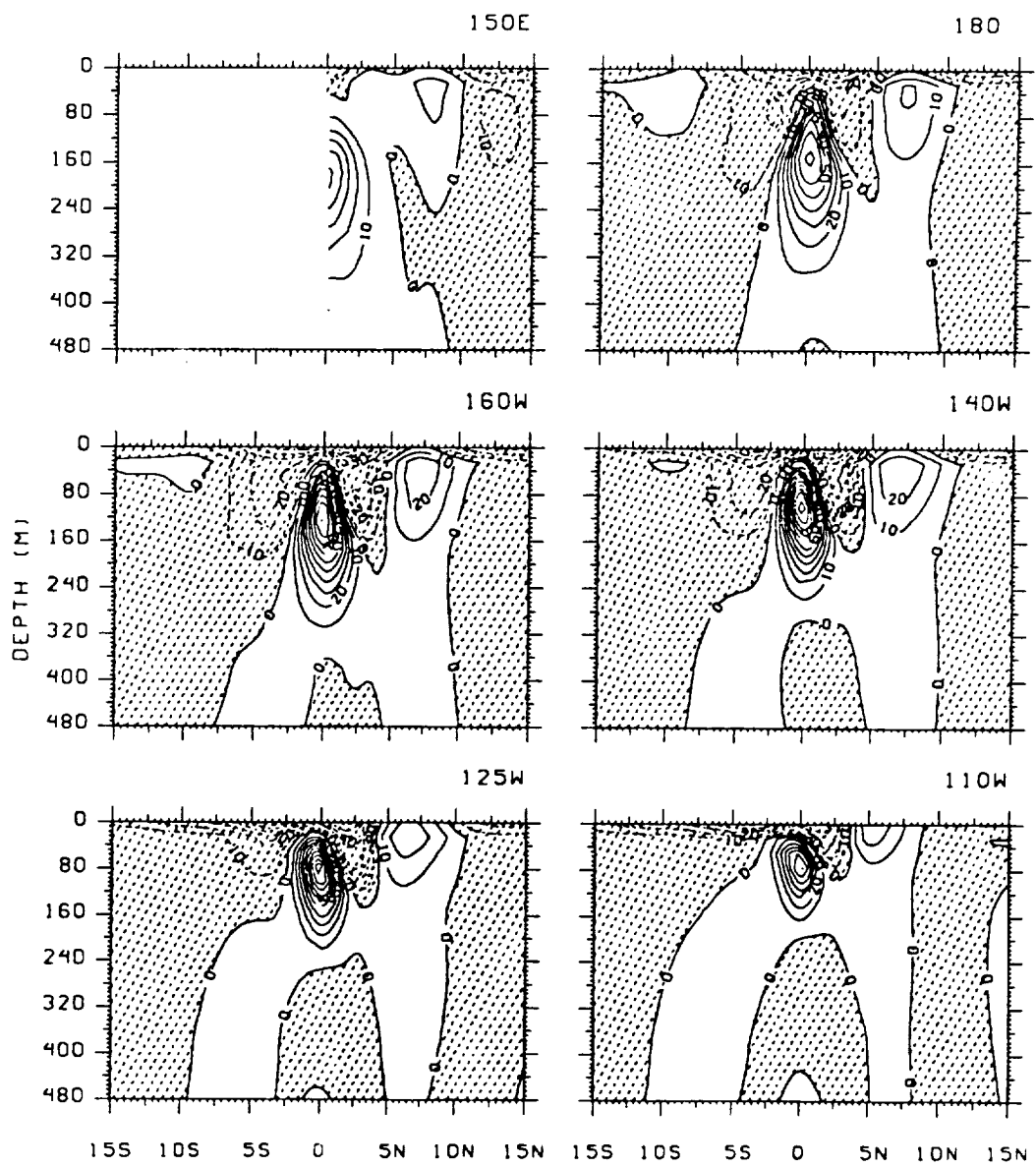


Figure 3.11 Latitude-depth diagram of the annual mean zonal current component. The contour interval is 10 cm s^{-1} and negative (westward) currents are shaded.

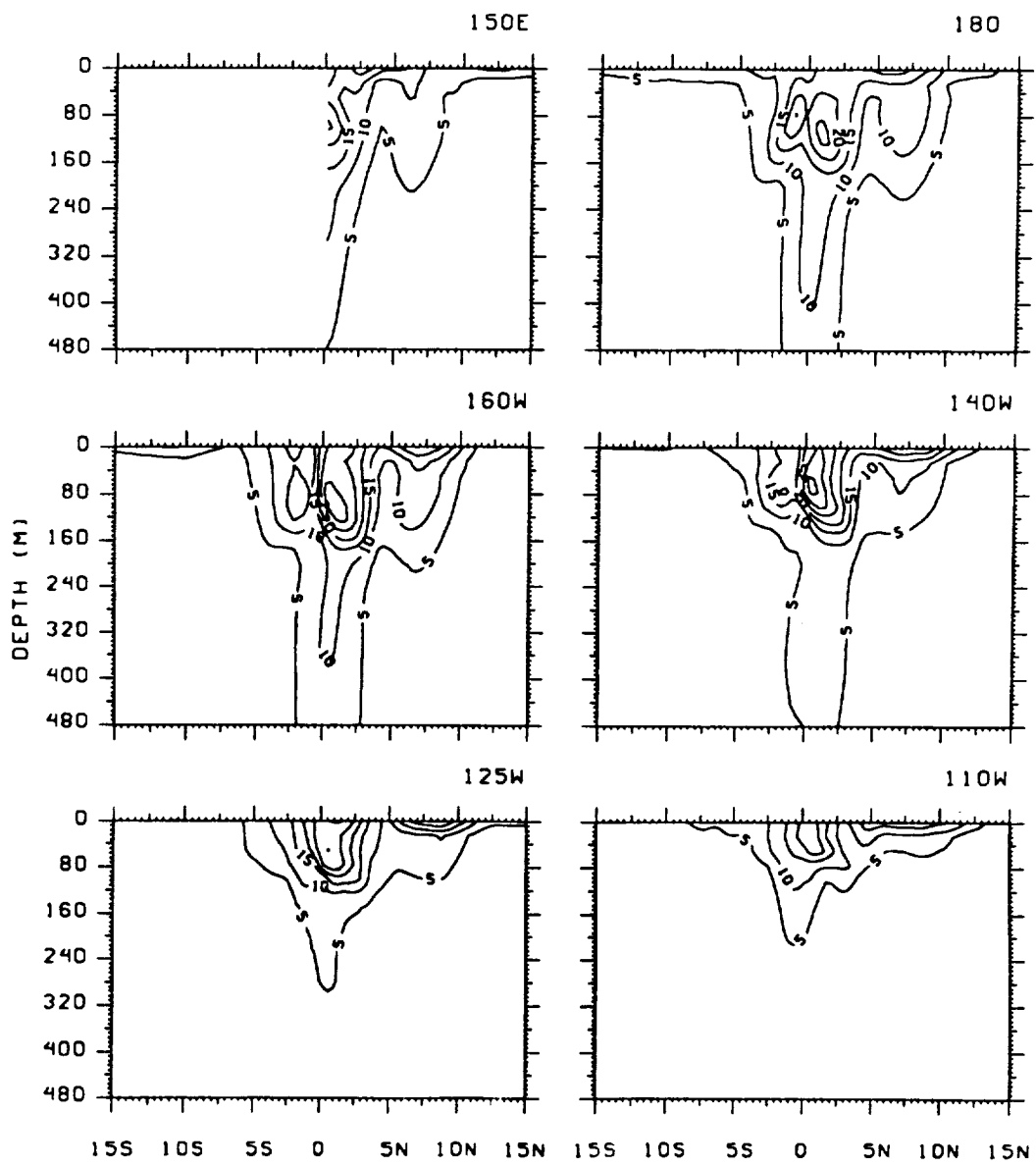


Figure 3.12 Latitude-depth diagram of the zonal current component standard deviation. The contour interval is 5 cm s^{-1} .

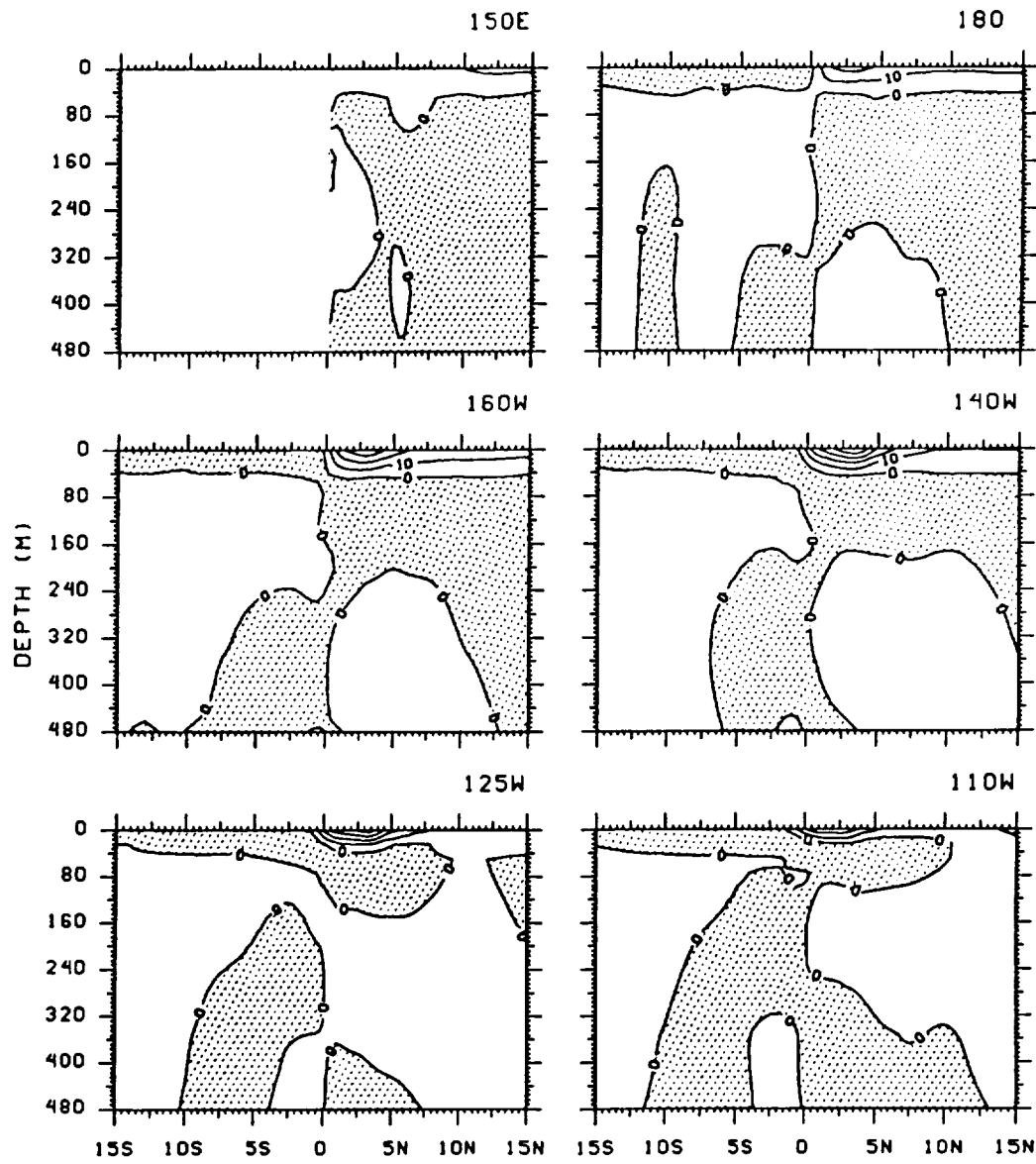


Figure 3.13 Latitude-depth diagram of the annual mean meridional current component. The contour interval is 10 cm s^{-1} and negative (westward) currents are shaded.

Wyrki and Kilonsky (1984), the model-simulated mean circulation at 150°E, 180°, 160°W and 140°W is characterized by poleward flow in the upper 50 m and equatorward flow below 50 m. This transverse circulation is not clearly defined everywhere in the NECC region throughout the year. At 160°W, for example, the equatorward flow is absent below 50 m from June to August between 4°N and 7°N. The flow in the upper 50 m across the NECC region is always poleward in the 180°, 160°, 140° and 125°W sections but the flow below 50 m is not always equatorward. In the sections near the western and eastern boundaries, 150°E and 110°W, the transverse circulation is more complicated. At 150°E there is some equatorward flow from June through September. At 110°W the poleward current is confined to a shallow layer 20-25 m thick and it is only sustained throughout the year in a narrow latitude band to 7°N. Below 50 m there are often alternating bands of north-south flow.

From approximately August to March when the northeast trades are strong and the Intertropical Convergence Zone (ITCZ) is located near the core of the NECC, the northward transport is convergent near the southern boundary of the NECC resulting in downwelling and a depressed thermocline and divergence near the northern boundary resulting in upwelling and a shallow thermocline. The simulated northward drift in the upper 10 m is very strong, often attaining speeds of 40 cm s^{-1} near 3°-4°N in the central Pacific (see Appendix C.2). Across the NECC speeds average 10 cm s^{-1} in the upper 50 m. Seasonally, the northward near-surface current is strongest from October to February. The variance of the v-component across the NECC seems to be concentrated at 160°, 140° and 125°W (Fig. 3.14) in the upper 150 m. In the 160° and 140°W sections, the standard deviations decrease from 10 cm s^{-1} near the southern boundary to 2 cm s^{-1} near the northern boundary. In the eastern sections 125° and 110°W, and the

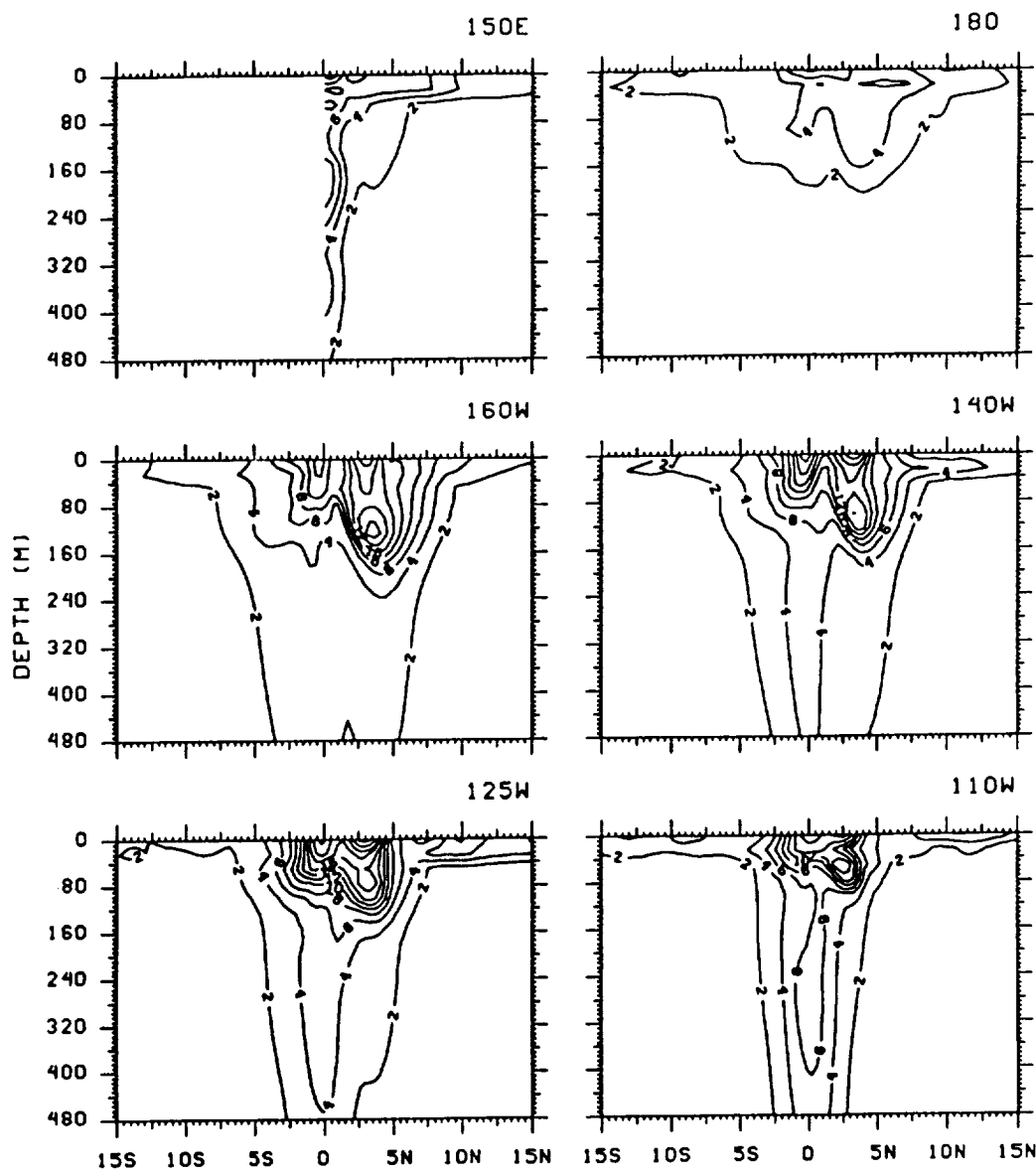


Figure 3.14 Latitude-depth diagram of the meridional current component standard deviation. Contour interval is 2 cm s^{-1} .

western sections, 150° and 180° , standard deviations are between 2 to 6 cm s^{-1} in the upper 80 m.

c. Vertical structure of the vertical component

The vertical velocity in the model is a diagnostic variable estimated from continuity. The monthly averages for January, April, July and October along 160°W are shown in Fig. 3.15. Aside from the familiar pattern of equatorial upwelling within 2° of the equator, distinct regions of downwelling are located between $3^\circ - 5^\circ$ north and south. The downwelling is strongest in the northern hemisphere in October.

The vertical motion near 10°N , the northern boundary of the NECC, is much smaller in magnitude. At 160°W w changes sign during the year at this latitude. The vertical velocity is downward in April from 10-310 m and in October in the upper 20 m. In January and July w is upward throughout the column. The model-simulated vertical velocity will be further discussed and compared with the Ekman pumping in chapter 5.

3.3.3 Transport

a. Method

Monthly eastward volume transports of the NECC were calculated using the trapezoidal method. The transports are calculated by integrating over the thickness and width of the current:

$$T^{\text{NECC}} = \int_{y_1}^{y_2} \int_{z_1}^{z_2} u(z) dz dy \quad [\text{m}^3 \text{ s}^{-1}]. \quad (3.1)$$

Equation (3.1) may be approximated by the following two second-order accurate finite difference equations:

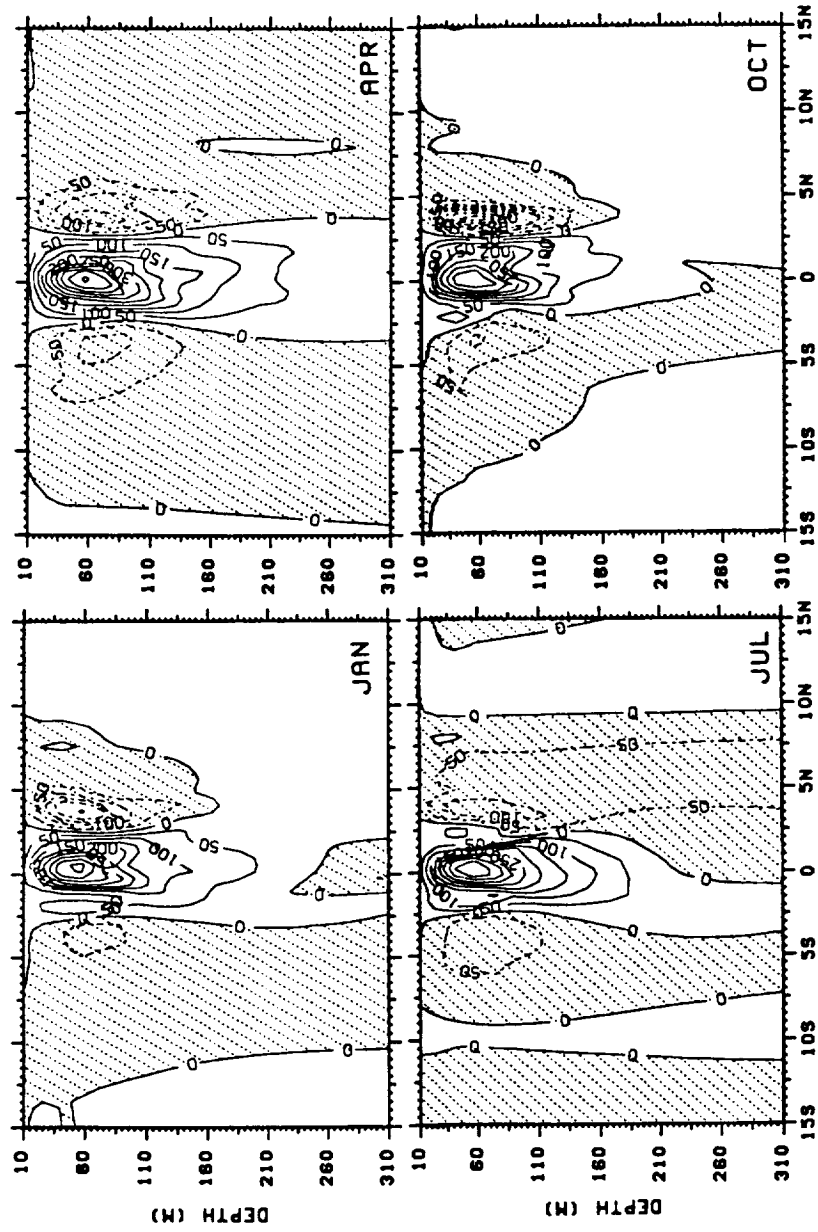


Figure 3.15 Latitude-depth diagram of the monthly mean vertical velocity along 160°W for January, April, July, and October. The contour interval is 50 cm day⁻¹ and shaded values indicate downwelling.

$$\int_{z_1}^{z_2} u(z) dz = \frac{\Delta z_k}{2} \left(u_{k-1} + u_n + 2 \sum_{k=2}^{n-1} u_k \right) + O(\Delta z)^2 \\ = Q_x, \quad (3.2)$$

where Q_x is the zonal component of the volume transport vector, \mathbf{Q} , as a function of latitude. Integrating Q_x over the region of the NECC yields the total volume transport of the NECC across a longitude section, T^{NECC} :

$$\int_{y_1}^{y_2} Q_x(y) dy = \frac{\Delta y_j}{2} \left(Q_{j-1} + Q_n + 2 \sum_{j=2}^{n-1} Q_j \right) + O(\Delta y)^2 \\ = T^{\text{NECC}}. \quad (3.3)$$

One of the difficulties associated with calculating the transport by a specific current is determining the current's boundaries. It is therefore necessary to define certain criteria such that the limits of integration are determined objectively. In this study the following criteria were used to identify a particular point as belonging to the NECC: 1) velocity is eastward and equal to or greater than 5 cm s^{-1} and 2) values of 5 cm s^{-1} or greater are found in the two adjacent layers, both below and above. It is often the case that the EUC and the NECC are indistinguishable west of the date line based on the selected criteria. In those instances the vertical structure of the flow was taken into consideration in defining the southern boundary. Since the NECC rarely disappears below 25 m (see the monthly meridional profiles of u in Appendix C.1) at any of the six longitudes, the region of the NECC occurs where the flow penetrates to the top layers immediately north of the EUC even though the two currents appear connected below 100 m.

b. Boundaries

Table 3.3 summarizes the boundaries of the NECC resulting from the above criteria. A graphical presentation of the information in Table 3.3 is presented in Figs. 3.16.a and b. The latitudinal width of the NECC has a pronounced annual cycle. At all longitudes, the current is narrow or undefined from about February to May after which it gradually widens during the northern hemisphere summer and fall. The annual mean width varies from 4.8 degrees at 140°W to 3.4 degrees at both 150°E and 110°W . As intensification and widening occurs in the summer and fall, the current is also observed to shift northward. The shift is about 1 degree at 180° , 160°W , 140°W and 125°W and almost 2 degrees at 110°W .

The 150°E section is associated with the largest variability. The standard deviation of the southern boundary is twice that of the other two western sections and more than three times greater than the eastern Pacific sections. This may be associated with the formation of seasonal synoptic scale eddies near the origin of the NECC in the West Pacific as observed by Lukas *et al.* (1991). It is, however, unclear to what extent these observed features are simulated by the present version of the OGCM which lacks a realistic western boundary and Indo-Pacific throughflow. Similarly, in the eastern Pacific where NECC waters enter the cyclonic circulation around the Costa Rica Dome in the summer and fall, there is significant annual variation of the boundaries. The Costa Rica Dome has been simulated successfully with a version of the model used in the present study (Umatani and Yamagata 1991). In their simulations, the dome is centered at 10°N and 90°W (it is also evident in the results described here, see Appendix B.3). The 110°W section is therefore influenced by the seasonal presence of the Costa Rica Dome.

The thickness of the NECC also exhibits great annual variation (Fig. 3.16.b). During September, the month of maximum transport at 160°W , the NECC extends to

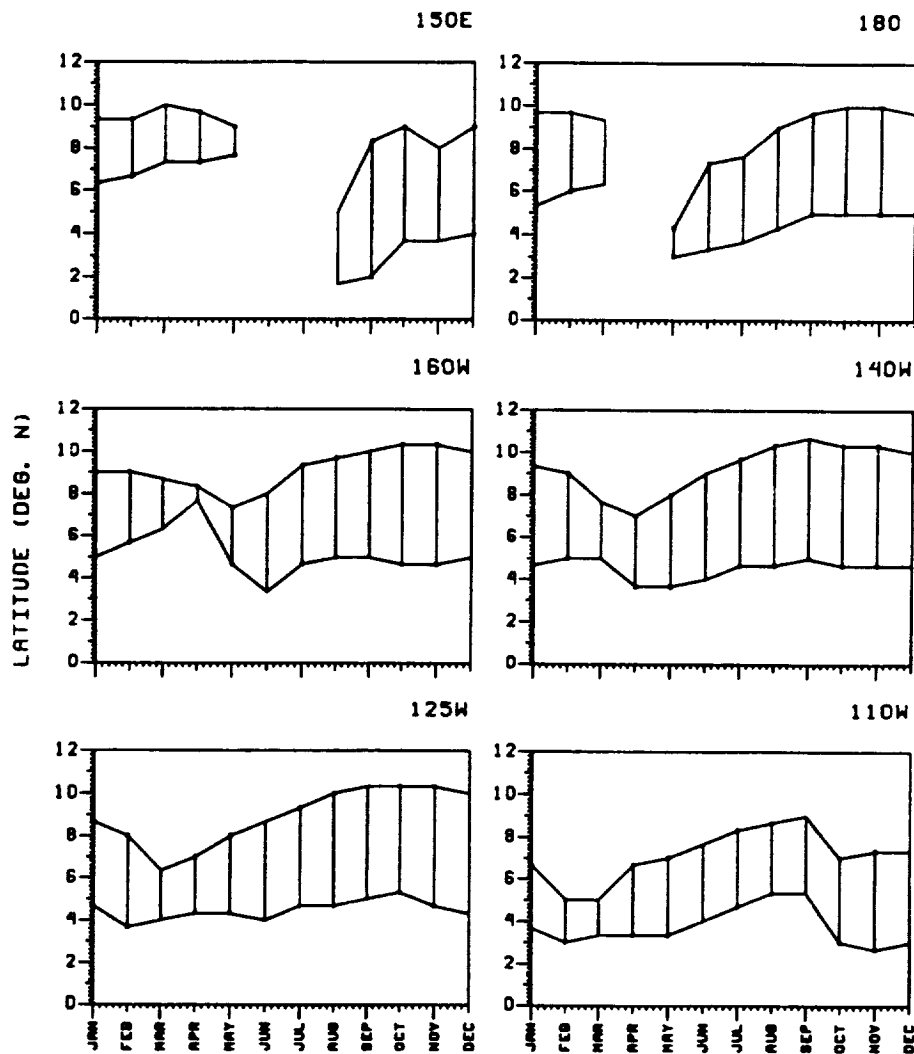


Figure 3.16.a Annual cycle of the latitudinal width of the NECC in degrees.

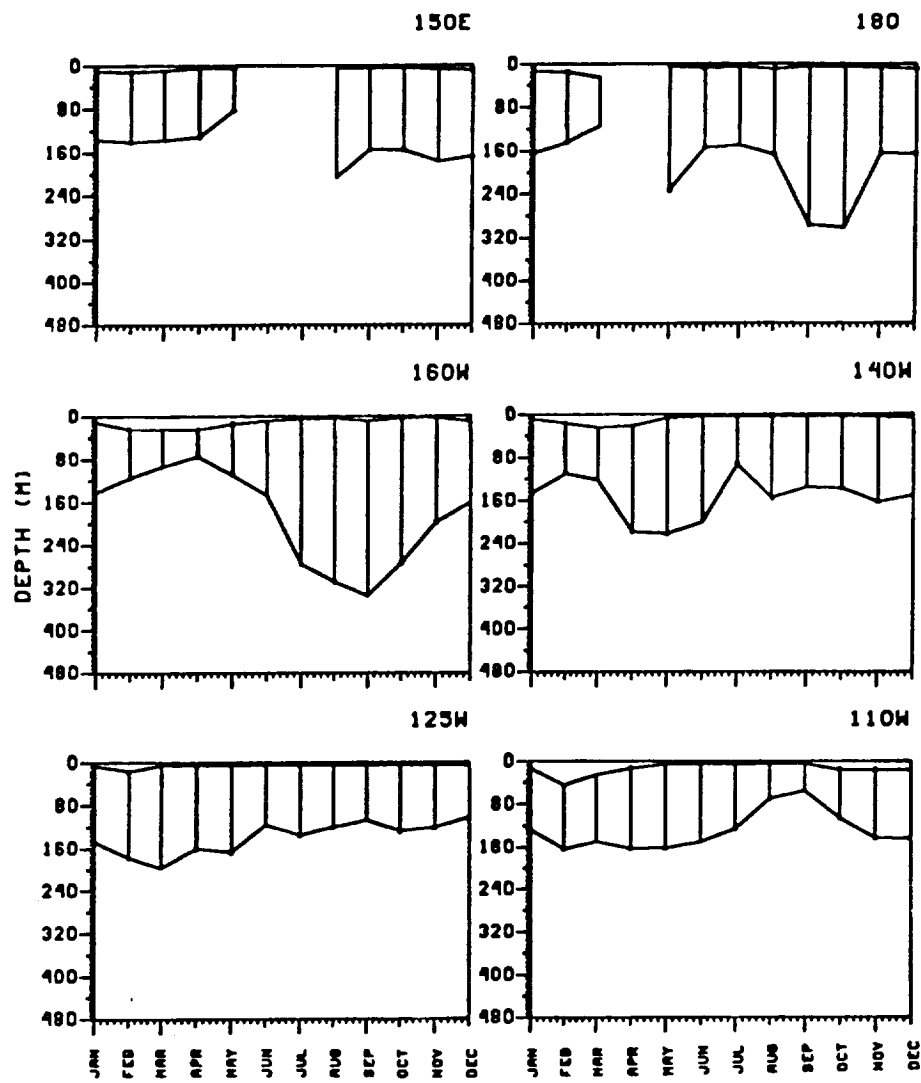


Figure 3.16.b Annual cycle of the thickness of the NECC in meters.

300 m in the 160°W section. In the eastern Pacific, the eastward flow is confined to a shallow layer in the upper 150 m and is subject to much less annual variation. The annual average bottom is deepest at 160°W and 180° at 187 m, though the mean bottom depth is fairly uniform across the Pacific.

3.3.3.c Results

The results of the transport calculation are shown in Fig. 3.17. The greatest annual mean transport (19.9 Sv) and the greatest standard deviation (2.5 Sv) occur at 160°W. The annual mean transport increases from the western Pacific (14.4 Sv at 150°E) toward the central Pacific (19.9 Sv at 160°W) and it decreases gradually from the central Pacific toward the eastern Pacific (6.2 Sv at 110°W). Extreme values are 1.9 Sv in March (110°W) and 34.0 Sv in September (160°W).

The annual variation of the transports is different at the different longitudes. For example, along 180°, 160°W and 140°W the fluctuations consists of one maximum and one minimum whereas along 150°E, 125°W and 110°W there are secondary minima and maxima (see Fig. 3.17). Along all six longitudes, minimum transport occurs in the boreal spring: in February at 150°E, 180° and 160°W; in March at 140°W and 110°W and in April at 125°W. There is substantial variation in the occurrence of the maximum. Along 180° and 160°W it occurs in September but at 150°E, 140°W and 110°W it occurs in June, July and May, respectively.

3.4 Comparison with observations

There are differences in the thickness and the depth of the thermocline observed by Wyrtki and Kilonsky (1984) and the simulated thermocline. The depth range of the model thermocline, 110-200 m at 5°N and 60-180 m at 10°N, is large compared with the

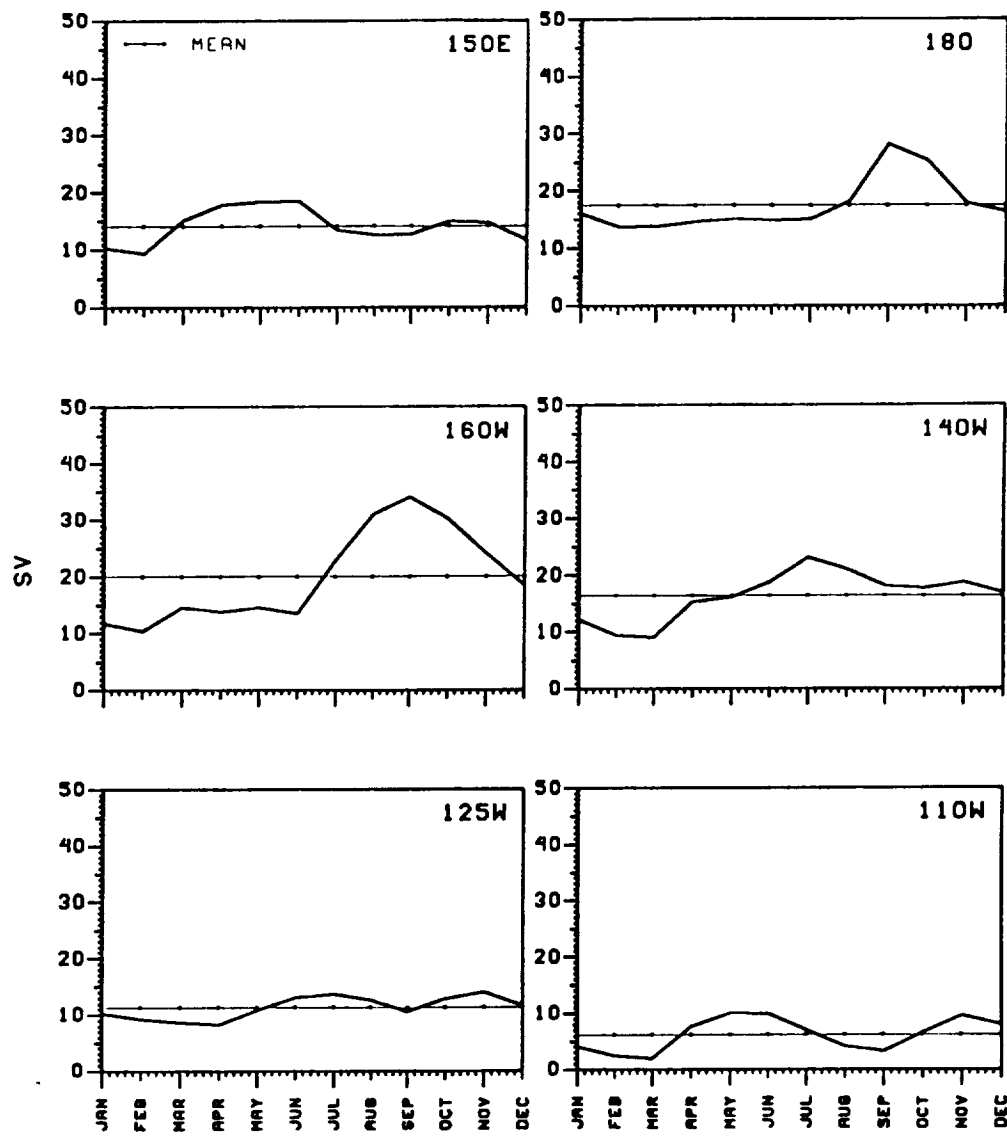


Figure 3.17 Annual cycle of the eastward transport of the NECC in Sv ($1 \text{ Sv} = 10^6 \text{ m}^3 \text{ s}^{-1}$). The thin dotted line is the annual mean.

observed range of 105-170 m and 40-110 m. The model thermocline is also more diffused as the thickness is larger (compare the simulated 90 m and 120 m at 5° and 10°N in Fig. 3.5 with the respective observed values of 65 m and 70 m in Fig. 2.1).

The simulated climatological mean u-component is somewhat weaker than the annual profile obtained during the Hawaii-to-Tahiti Shuttle Experiment (Wyrtki and Kilonsky 1984). The HTSE annual mean (Fig. 2.1) is the average over the period from April 1979 to March 1980 which was a normal year when the Southern Oscillation Index was near zero. The model annual average NECC at 160°W has an approximate core speed of 25 cm s^{-1} compared to near 40 cm s^{-1} in the HTSE. Differences between the climatological model-simulated flow and one year's observed flow are not unexpected since the NECC is known to exhibit interannual variability (Chao 1990; Meyers and Donguy 1984). The simulated subsurface core is located at a depth of 50 m which is similar to the observations. The model and observed latitudinal boundaries are 4.5°N - 10°N and 5.1°N - 9.2°N, respectively.

The annual average transport at 160°W is 19.9 Sv, which is remarkably close to the 19.8 Sv observed by Wyrtki and Kilonsky (1984). Thus, reasonable correspondence exists between the observed and the simulated annual cycles of the NECC near 160°W. There is therefore good reason to believe that the annual cycle of the NECC along the other five longitudes is realistically simulated by the model. The detailed descriptions of the model-simulated NECC in the eastern and western Pacific presented in this chapter are so far the only descriptions of the longitudinal variation of the NECC.

3.5 Discussion

Calculations of volume transport along 150°E, 180° and 160°W, 140°W, 125°W and 110°W reveal an annual mean transport maximum at 160°W. It is interesting to note that, at this point, it appears that the maximum transport at 160°W is associated with the occurrence of the largest vertical extent of the current at this longitude. For example, at 160°W the sharp annual peak in transport in September coincides with the greatest vertical extent of 337 m at any time or longitude. The fact that the NECC is wider at 140°W does not seem to affect the transports. The depth of the current, though, is not a consistent predictor of the annual cycle. For example, at 140°W the NECC reaches the deepest levels in April and May but a maximum in transport does not occur until July.

Chapter 4

Degree of Geostrophy

Knowledge of the degree of geostrophy is important in assessing the applicability of the geostrophic method for calculation of currents in the NECC. Widespread direct current measurements are not feasible due to high cost and technological requirements but widespread observations of temperature and salinity, which are much cheaper to obtain, are taken routinely. Geostrophic currents are, therefore, often used to represent the flow with only limited opportunities to verify their applicability. In this chapter the geostrophic current is calculated at the six longitude sections used previously in order to investigate the spatial variation of the geostrophic balance.

The zonal geostrophic current component can be derived from the meridional momentum balance which is given by

$$\begin{aligned} \frac{\partial v}{\partial t} + u \frac{\partial v}{\partial x} + v \frac{\partial v}{\partial y} + w \frac{\partial v}{\partial z} = -\frac{1}{\rho} \frac{\partial p}{\partial y} - fv + A_v \frac{\partial^2 v}{\partial z^2} \\ + A_h \left(\frac{\partial^2 v}{\partial x^2} + \frac{\partial^2 v}{\partial y^2} \right) \end{aligned} \quad (4.1)$$

where f is the Coriolis parameter and A_V and A_H are the coefficients of vertical and horizontal eddy viscosity, respectively. If inertial acceleration, advection and frictional effects are considered negligible compared to the Coriolis acceleration, the flow is in geostrophic balance:

$$u_g = -\frac{1}{\rho f} \frac{\partial p}{\partial y} \quad (4.2)$$

Here u_g is the geostrophic current component on an isobaric surface. Equation 4.2 is easily applied in meteorology to calculate the geostrophic wind at the surface because the surface pressure is usually known. In practice it is more convenient to use the geostrophic equation in geopotential coordinates:

$$f u_g = -\frac{\partial \Phi}{\partial y} \quad (4.3)$$

where Φ is the geopotential height defined as $\Phi \approx gz$ and u_g is now the geostrophic velocity on a constant-pressure surface relative to a geopotential surface. The difference between the latitudinal gradients on the constant-level surface and the constant-pressure surface is so small that it is usually considered unimportant in practical applications (Gill 1982, p. 217). In observational oceanography the error associated with interchanging the two coordinate systems is considered negligible.

A few studies have focused on comparing direct current observations with currents inferred from the geostrophic method. Using data obtained during the Hawaii-to-Tahiti Shuttle Experiment, Johnson *et al.* (1988) compared geostrophic currents computed from CTD data and DAL (Doppler acoustic log) current observations. The study of Johnson *et al.* (1988) was limited to the upper 117 m from 4°S to 10°N during August 1979 to June 1980. Since the difference between the time mean DAL velocities and the zonal geostrophic velocities was found not to be statistically significant at 95% confidence, Johnson *et al.* (1988) concluded that the mean zonal velocity was in

approximate geostrophic balance. Although correlations between the time-varying DAL velocities and the zonal geostrophic velocities were statistically significant in the NECC region, no more than 50% of the observed variance of the time-dependent flow could be predicted using geostrophic currents. Johnson *et al.* (1988) thus suggested that the time-dependent flow of the NECC cannot be characterized as predominantly geostrophic. They further suggested that deviations from geostrophy in the NECC are due primarily to the meridional inertial acceleration, $\partial v / \partial t$, associated with near-inertial internal waves.

4.1 Method

The calculation of the zonal geostrophic currents was performed using the vertical profiles of the model temperature and salinity fields. As mentioned above, the approach in this study is one of using the model fields as a proxy for real data. Thus the method used for the calculation of the geostrophic current is derived from methods in observational oceanography. A commonly used practical version of Eq. 4.3 in terms of the dynamic height anomaly between two isobars, ΔD (Pond and Pickard 1987, p. 73) is given by

$$u_{g_k} - u_{g_{k+1}} = \frac{10}{\Delta y f} (\Delta D_{j+1} - \Delta D_j) \quad (4.6)$$

Here the discrete vertical levels are subscripted with k (increasing downward) and the meridional grid points with j (increasing northward), ΔD is the anomaly of geopotential thickness between two isobars, k and k+1, in units of dynamic meters ($10 \text{ dyn m}^{-1} \text{ m}^2 \text{s}^{-2}$, Sverdrup *et al.* 1942) and Δy is the north-south distance between two grid points. The finite difference scheme was chosen independently of the finite difference schemes used in the model. The Coriolis parameter, f , is computed at the midpoint

latitude of Δy . The calculated velocity is thus the relative velocity between two horizontal levels averaged between two meridional points. If the reference isobaric surface represents a geopotential surface it is called the "level of no motion." When the "level of no motion" can be estimated, the absolute surface geostrophic current can be obtained. A reference level of 483.5 m (or 483.5×10^4 Pa) was used to represent the "level of no motion" since the meridional gradient (between 4°N and 10°N) of ΔD between this level and 1000×10^4 Pa, i.e. the $483.5/1000 \times 10^4$ Pa dynamic height anomaly, was less than 1 dyn cm.

The first step is to calculate ΔD such that Eq. 4.3 can be used. ΔD at a grid point is defined as

$$\Delta D = \int_{p_2}^{p_1} \delta dp \quad (4.7)$$

where $\delta = \alpha(s, t, p) - \alpha(35, 0, p)$ is the specific volume anomaly given by the difference between the total specific volume, $\alpha(s, t, p)$, and the specific volume of a standard ocean of 0°C and 35 PSU (Practical Salinity Unit). The specific volume, $\alpha(s, t, p)$, is calculated from the vertical profiles of T, S and p as

$$\alpha(s, t, p) = \alpha(s, t, 0) / [1 - p / K(s, t, p)] \quad (4.8)$$

where K is the secant bulk modulus used to correct for high pressure (Millero *et al.* 1980). The specific volume anomaly as a function of T and S at one standard atmosphere pressure, $\alpha(s, t, 0)$, was calculated using the one-atmosphere International Equation of State of Sea Water, 1980 (IES 80). Both $\alpha(s, t, 0)$ and K are given in Millero and Poisson (1981) or Pond and Pickard (1987). The pressure at each constant-level surface is estimated using the depth of a level in meters such that $p \approx 10^4 z_k$ Pa, where z_k is level k in meters. An example of a vertical profile and the corresponding

dynamic height anomalies are shown in Table 4.1. The 5 m geostrophic current, u_g , relative to 484×10^4 Pa will be referred to as the 5/484 u_g .

4.2 Results

The geostrophic currents were calculated from 2.67° N to 15.27° N using the 3-day-averages of temperature and salinity. Figure 4.1 shows the annual average geostrophic currents. Note the surface maximum which is in contrast to the *subsurface* maximum of the total model velocity, u_m (Fig. 3.8). The surface maximum occurs at all longitude sections. However, in the case of the monthly-mean sections, the surface maximum did not occur at 125° and 110° W in April (see Appendix C). Another feature is that $u_m > u_g$ throughout the year at all sections. The magnitude of the difference, however, depends on the strength of the flow. For example, at 160° W and 140° W the core u_m is greater than the core u_g by about 10 cm s^{-1} in September but in March when the NECC is weak, $u_m \approx u_g$ (compare Figs. 4.2 and 4.3). In the boreal late summer, fall and winter when the NECC u_m extends to the surface, the latitudinal boundaries of the u_m and the u_g eastward flow are fairly similar except for the location of the northern boundary during September and October. In October the NECC u_g extends further north by $1.5 - 2.0$ degrees (see Appendix C).

Table 4.2 summarizes the values of monthly mean total zonal current at 5 m, 5-m u_m , and 5/484 u_g averaged over the NECC region. The 5/484 u_g is at no time westward in the NECC latitudinal core region as is the case with the 5-m u_m from January to March in the 150° E, 180° , 160° W, 140° W and 125° W sections. The fact that the 5/484 u_g is always eastward means that the north-south slope of the 5/484 ΔD always has the same sign; that is, the characteristic pattern of a trough near 10° N and a ridge near 5° N

Table 4.1. Example of a vertical integration of the dynamic height anomaly, ΔD . The profile is from January at a location of 150°W, 5°N. T is temperature (°C) and S is salinity in Practical Salinity Unit (S).

Depth (m)	T (°C)	S (S)	σ_t^*	δ^{**}	ΔD^{***} (dyn m)	Sum (dyn m)
5.00	26.84	35.07	22.84	502.932	0.050	1.241
15.00	26.85	35.07	22.84	503.641	0.050	1.190
25.00	26.85	35.07	22.84	504.041	0.050	1.140
35.00	26.87	35.07	22.83	505.054	0.051	1.089
45.00	26.87	35.07	22.83	505.447	0.051	1.039
55.00	26.90	35.07	22.82	506.782	0.051	0.988
65.00	26.90	35.07	22.82	507.176	0.051	0.938
75.00	26.91	35.07	22.82	507.855	0.051	0.887
85.00	26.91	35.07	22.82	508.255	0.051	0.836
95.00	26.79	35.03	22.83	507.909	0.057	0.785
106.25	26.23	34.94	22.94	497.889	0.067	0.729
120.00	25.21	34.90	23.22	471.085	0.072	0.662
136.25	23.31	34.87	23.77	419.623	0.072	0.590
155.00	20.32	34.80	24.55	345.653	0.067	0.518
177.50	16.08	34.74	25.55	250.012	0.059	0.451
205.00	12.55	34.73	26.29	179.249	0.059	0.392
240.00	11.29	34.73	26.53	156.927	0.073	0.333
288.50	10.48	34.73	26.68	143.862	0.104	0.260
362.50	9.79	34.70	26.77	136.006	0.157	0.157
483.50	8.50	34.63	26.93	122.726		0.000

* σ_t is a convenient expression of sea water density at standard atmospheric pressure: $\sigma_t = (\rho(s,t,0) - 1000.00)$. Units are [kg m⁻³] but they are usually omitted.

** δ is defined as $\delta = \alpha(s,t,p) - \alpha(35.0,p)$. Units are [m³ kg⁻¹]. (Specific volume (α) is given by $\alpha=1/\rho$).

*** ΔD is obtained by averaging δ between the two layers and multiplying by the difference in pressure.

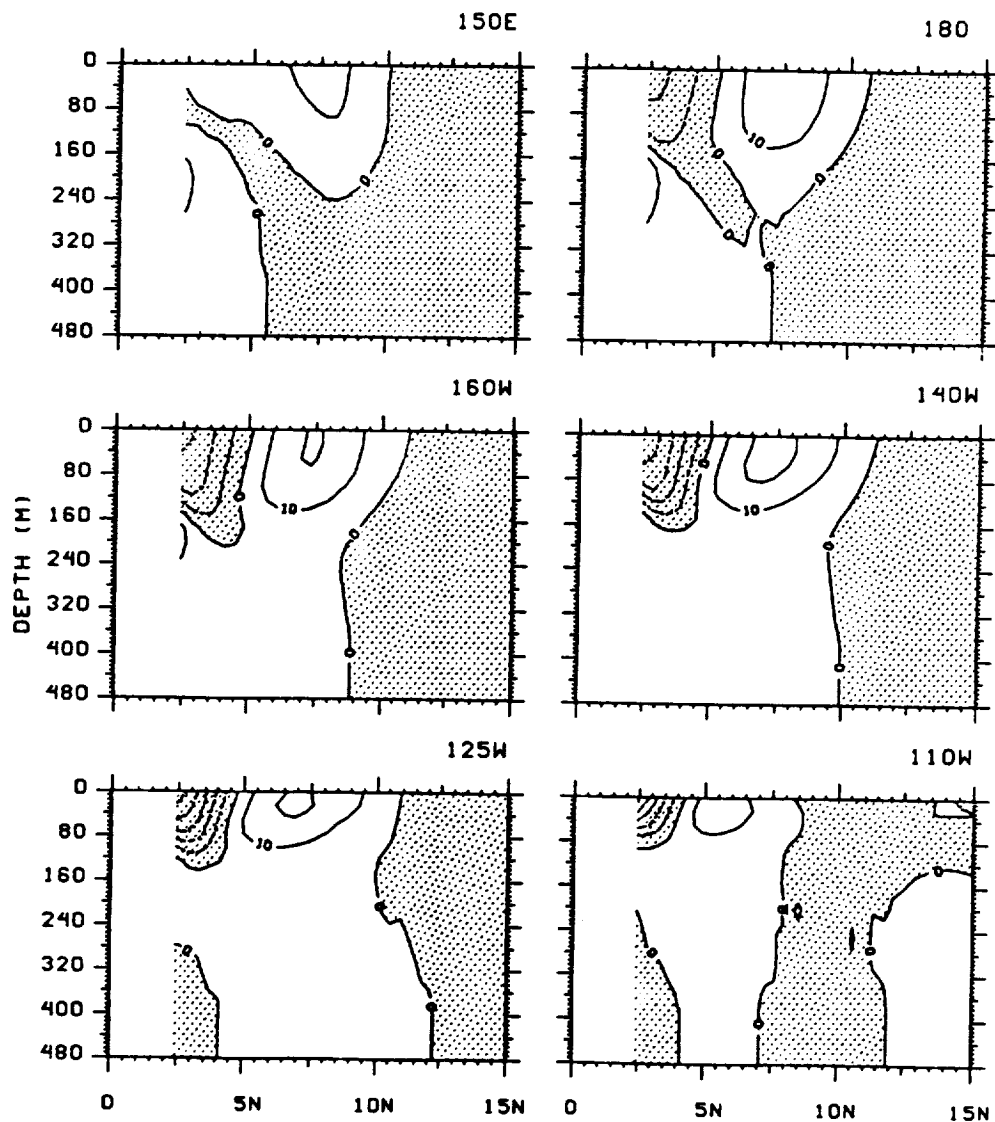


Figure 4.1 Latitude-depth diagram of the annual mean zonal geostrophic current component from 2.7°N to 15°N. The contour interval is 10 cm s⁻¹ and negative (westward) currents are shaded.

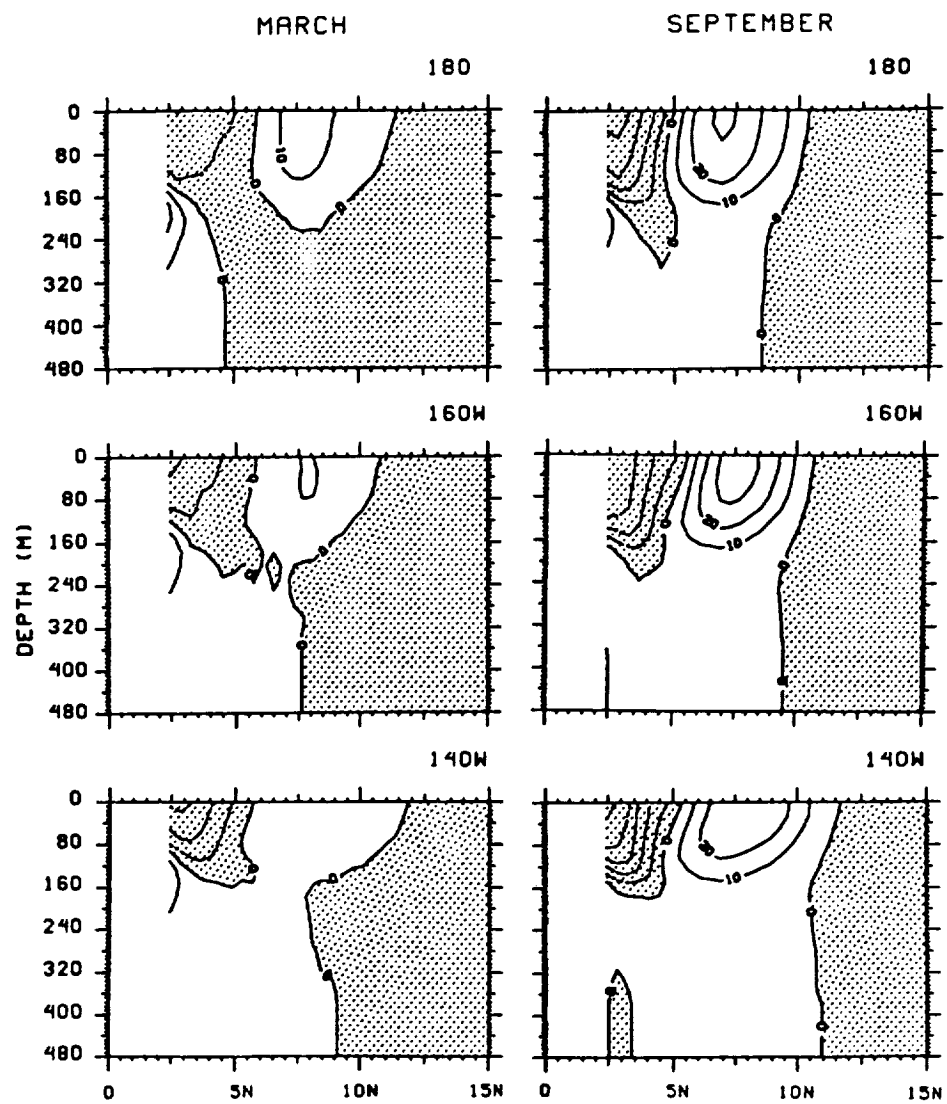


Figure 4.2 Latitude-depth diagram of the zonal geostrophic current component from 2.7°N to 15°N for March and September. The contour interval is 10 cm s⁻¹ and negative (westward) currents are shaded.

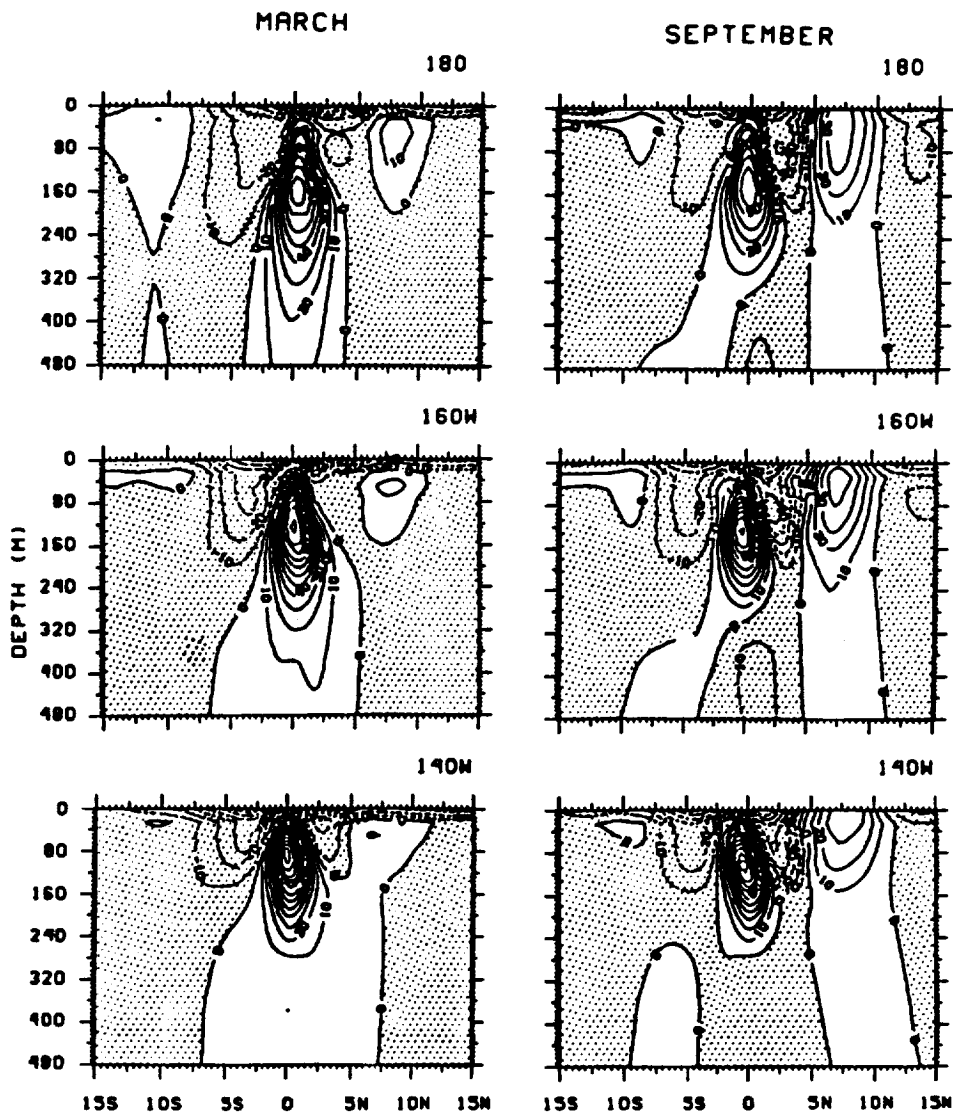


Figure 4.3 Latitude-depth diagram of the zonal current component from 15°S to 15°N for March and September. The contour interval is 10 cm s⁻¹ and negative (westward) currents are shaded.

Table 4.2. Monthly mean zonal geostrophic velocity at 5 m relative to 484×10^4 Pa (u_g) and 5 m total velocity (u_m) averaged over the NECC region using the monthly mean boundaries in Table 3.3.

	JAN	FEB	MAR	APR	MAY	JUN	JUL	AUG	SEP	OCT	NOV	DEC
150°E												
u_g	13.3	12.1	12.5	12.0	8.5	-	-	13.9	10.5	14.6	16.1	15.3
u_m	-7.8	-8.8	-1.9	0.8	0.7	-	-	22.6	16.1	17.4	10.7	1.5
180°												
u_g	16.5	15.2	10.4	-	2.2	6.1	8.8	14.7	20.0	18.7	16.4	16.2
u_m	-9.0	-10.3	-14.8	-	-3.0	-0.2	4.5	18.1	25.3	18.2	5.1	-4.7
160°W												
u_g	14.2	10.2	8.5	6.7	6.0	9.2	14.8	19.6	18.8	17.4	17.5	17.0
u_m	-10.7	-17.2	-23.7	-21.5	-8.2	2.4	13.1	23.3	21.8	16.4	8.6	-2.6
140°W												
u_g	15.2	10.5	2.7	2.6	8.8	13.9	19.4	17.8	18.0	18.2	19.1	17.5
u_m	-3.4	-14.2	-21.7	-9.3	8.7	19.4	29.7	28.2	25.3	21.6	12.5	4.8
125°W												
u_g	17.2	5.6	7.6	15.0	13.4	15.3	16.5	13.7	14.5	18.3	17.9	16.6
u_m	7.2	-5.1	-3.6	15.2	24.6	31.1	31.3	29.4	26.9	28.4	21.8	11.5
110°W												
u_g	8.4	-5.6	-2.8	6.2	11.6	11.6	8.8	7.8	5.9	-2.2	1.0	6.6
u_m	7.5	-6.5	1.8	22.6	35.7	35.8	31.2	29.3	25.0	21.1	17.0	14.8

is maintained year-round. The monthly average 5/484 ΔD profiles along 160°W for February, April, June, August, October and December are shown in Fig. 4.4.

Figure 4.5 shows a comparison between the 5-m u_m and the 5/484 u_g for February, May, August and November at 160°W; monthly profiles at each longitude are shown in Appendix C.3.2. Although the profiles of total current and the geostrophic current have similar shapes, their differences across the NECC vary depending on the season (Table 4.2). From January to May, the 5/484 u_g is greater than the 5-m u_m by more than 20 cm s⁻¹ between 5°N and 10°N at 160°W. From July to October, however, the two almost coincide across the NECC region (see Table 4.2). Similarly, at 180° and 150°E, 5/484 u_g is greater than 5-m u_m : the difference being large (15-20 cm s⁻¹), from January to March, and small (5 cm s⁻¹) from May to October. This pattern is reversed in the eastern Pacific. Here the 5/484 u_g is still greater than the 5-m u_m but the large differences of 10-15 cm s⁻¹ occur later in the year: from May to October at 125°W and from April to November at 110°W. Deviations from geostrophy are smallest in April, November and December at 125°W and January, February and March at 110°W.

Another method to compare the two velocities is to calculate the correlation coefficient, R, for the two time series consisting of 3-day-averages (N=120). High positive correlations indicate that the seasonal variation of u_m and u_g are in-phase; high negative correlations mean out-of-phase. Maps of R^2 are shown in Fig. 4.6. They represent the percent variance of u_m that can be predicted using the variance of u_g . Values of R^2 greater than 0.02 are different from zero at 95% confidence. In general, values of R^2 greater than 0.50 (shaded contours) are found between 8°-10°N in the upper 150 m. In the southern half of the NECC region, R^2 is typically less than 0.1.

The largest correlations in the NECC region occur in the 160°W section. Here 50-60% of the variance in the northern half of the NECC from 7.5°-10°N, 5-200 m can be

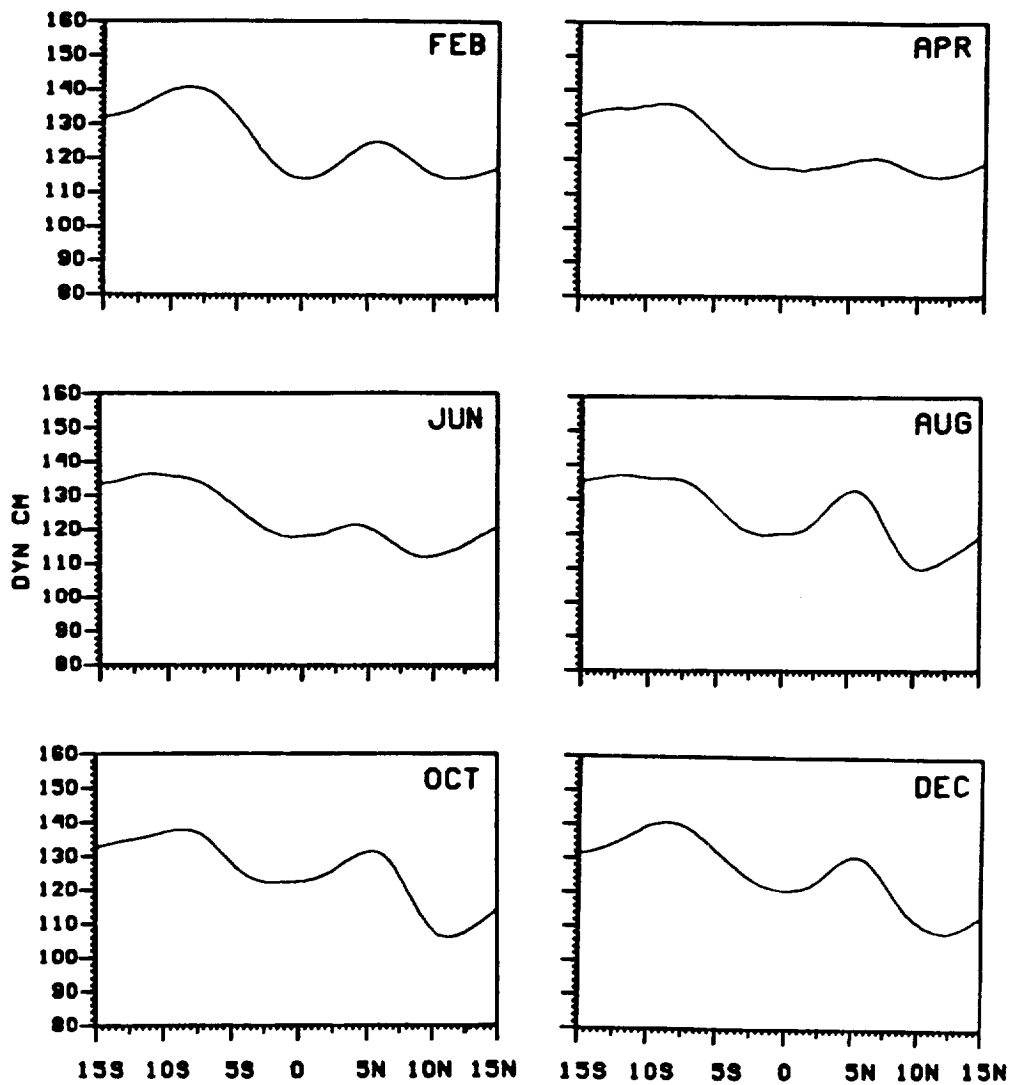


Figure 4.4 Profile of monthly mean surface dynamic height anomaly (in dyn cm) relative to 484 Pa along 160°W for February, April, June, August, October, and December.

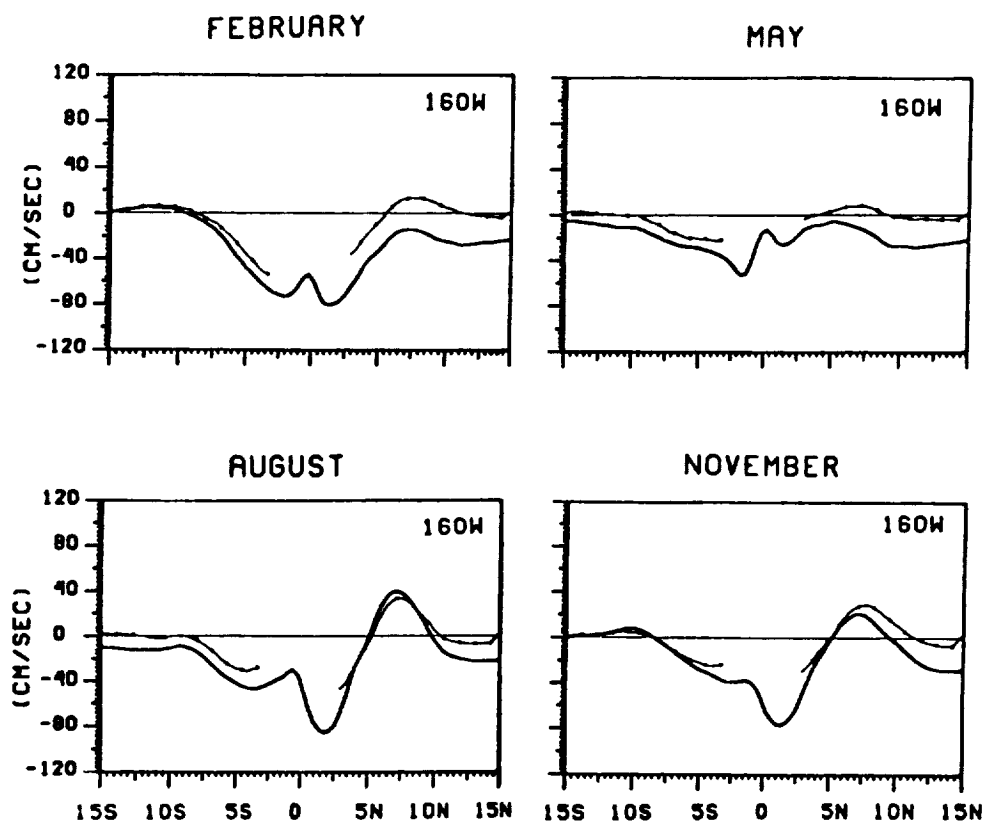


Figure 4.5 Comparison between the $5/484 \times 10^4$ Pa geostrophic current, u_g , (thin dotted curve) and the 5 m model total zonal current, u_m , (thick curve) along 160°W for February, May, August, and November.

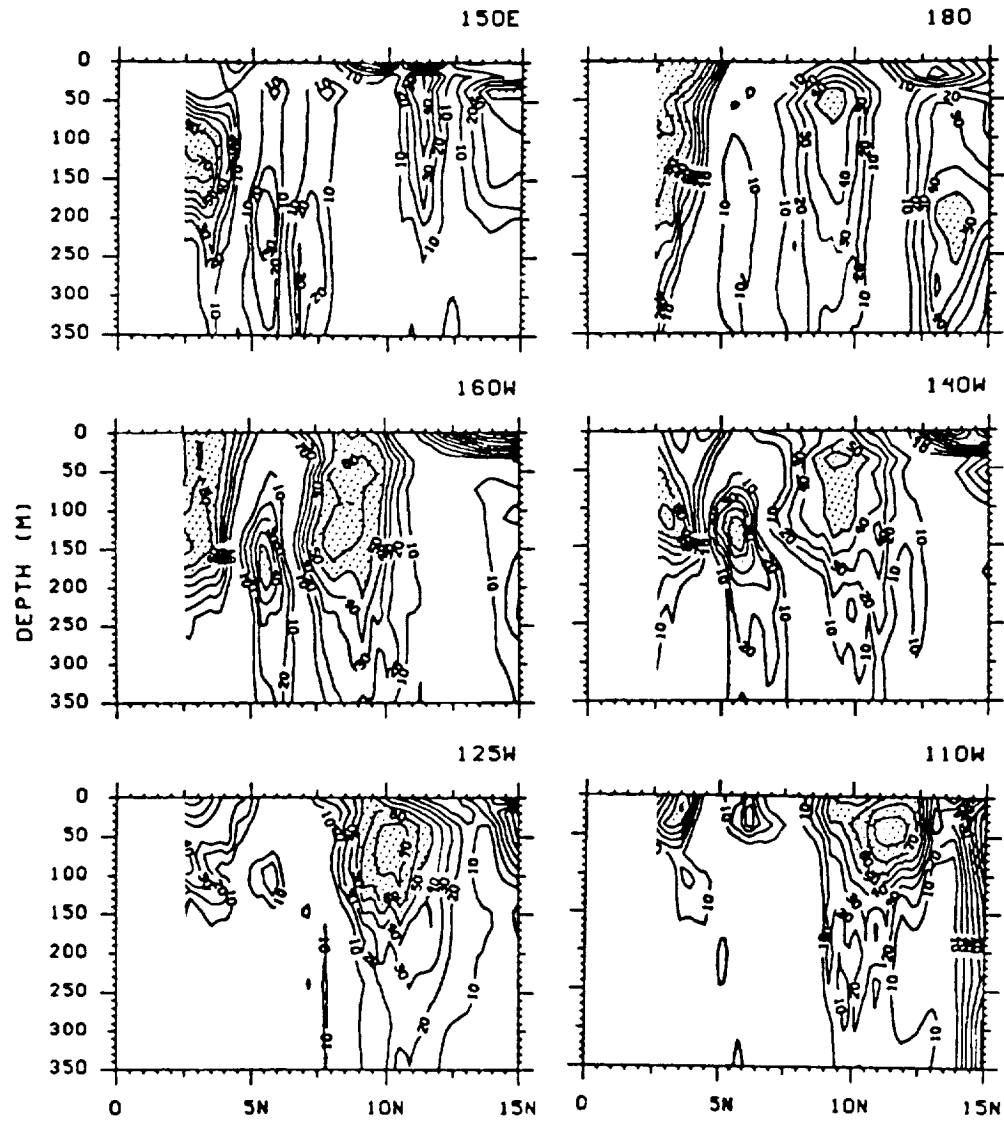


Figure 4.6 Latitude-depth maps of per cent explained variance (R^2) of u_m by u_g from 2.3°N to 15°N .

explained by u_g . In the western Pacific along 150°E, maximum values of 0.3 to 0.4 are found only in the top layer between 9-10°N. In the date line section, highest values (≈ 0.4) occur between 8°-10°N throughout the column and a small area of 0.5 is located near 50 m between 9°-10°N. In the eastern sections the greatest values are also located near the northern boundary of the NECC. The annual mean boundaries of the NECC at 110°W are 3.7°-7.1°N and 14-130 m. Within this region, R^2 of 0.2 to 0.4 are found only in a small region between 5.5°-6.5°N and 10-40 m. The highest values of explained variance (70%) within the annual range of the NECC boundaries, 2°N-10.7°N, are found in the 125°W section between 9.5°-11°N, 50-100 m. At this longitude, however, the NECC extends this far north only from August to December (see Table 3.3).

4.3 Discussion

There are several characteristics of the total zonal velocity field, u_m , which do not have counterparts in the zonal geostrophic velocity field, u_g . First, the appearance of a westward u_m at the surface from about January to April in the central Pacific does not correspond to a westward surface geostrophic flow, u_g . It is not clear from this analysis what causes the total surface current to be westward. It is possible, though, that significant westward Ekman currents appear in the upper 15 m from January to April. The northeast trade winds are seasonally strong (greater than 1×10^{-1} N m $^{-2}$) and have a southward component across the NECC region during this time (see Fig. 3.1). For example along 160°W in March, the southward component of the wind stress is $\approx -5 \times 10^{-2}$ N m $^{-2}$ averaged between 5°N and 10°N. The corresponding zonal Ekman current at 5 m calculated using Eq. 2.3.a and Eq. 2.5 with $A_z = 3 \times 10^{-3}$ m 2 s $^{-1}$ is westward at -13.6 cm s $^{-1}$; about 57% of the latitudinally averaged total zonal velocity at 5 m (Table

4.2). A value of $3 \times 10^{-3} \text{ m}^2 \text{ s}^{-1}$ for A_z yields values of D_E of 68 m at 5°N and 48 m at 10°N .

Secondly, as evidenced by the low correlation coefficients, u_m and u_g have very different variances near the southern boundary of the NECC, particularly in the eastern Pacific. Johnson *et al.* (1988) found significant deviations from geostrophy in the NECC which they attributed to the meridional inertial acceleration, $\partial v / \partial t$, associated with near-inertial internal waves. In a model run similar to the one described here, Philander *et al.* (1986) found waves with a period near 30 days in all three velocity components east of 140°W . The low correlations reported here near the surface between 4°N and 7°N in the 180° , 160°W , 140°W and 125°W sections may thus be partially explained by the meridional inertial acceleration term becoming important due to the presence of waves.

The annual mean meridional inertial acceleration at 5 m, $\partial v_{5m} / \partial t$, is smaller than $f(u_{5m})$ and $f(u_g 5/484)$ (Fig. 4.7). The climatological meridional inertial acceleration therefore appears to have little effect on the meridional momentum balance on the annual time scale. The meridional inertial acceleration does, however, seem to contribute seasonally. Figure 4.8 compares the variances of the Coriolis acceleration terms due to the total zonal velocity at 5 m and the zonal geostrophic velocity, $f(u_{5m})$ and $f(u_g 5/484)$, respectively and $\partial v_{5m} / \partial t$. The variance of $\partial v_{5m} / \partial t$ is relatively small north of 7°N and not large enough to balance the excess total velocity variance. Between 5°N and 7°N , $\partial v_{5m} / \partial t$ constitutes no more than 10% of the total velocity variance. Between 3°N and 5°N , $\partial v_{5m} / \partial t$ contributes significantly along 160°W , 140°W and 125°W ; it represents approximately 25% of the $f(u_{5m})$ variance. Thus, $\partial v_{5m} / \partial t$ is large enough to account for the difference between the $f(u_{5m})$ and $f(u_g 5/484)$ in the 160°W and 140°W between 3°N and 5°N but not large enough anywhere between 5°N and 7°N .

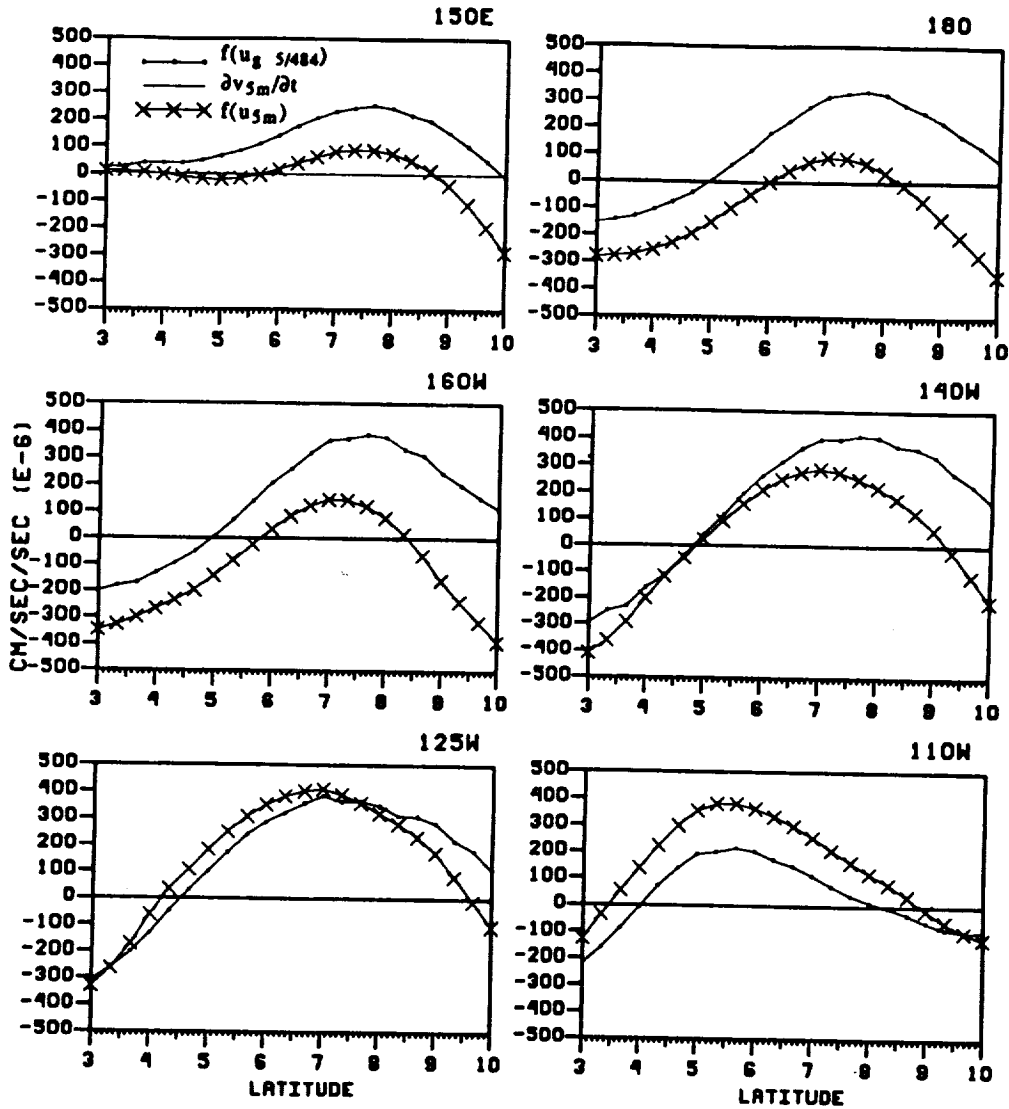


Figure 4.7 Annual mean of the zonal Coriolis acceleration terms, $f(u_g, 5/484)$ (thin dotted curve) and $f(u_{5m})$ (crosses), and the meridional acceleration, $\partial v_{5m}/\partial t$, in $10^{-6} \text{ cm sec}^{-2}$ from 3°N to 10°N . The curve of $\partial v_{5m}/\partial t$ overlies the zero line as the magnitude of $\partial v_{5m}/\partial t$ is small relative to the other two terms.

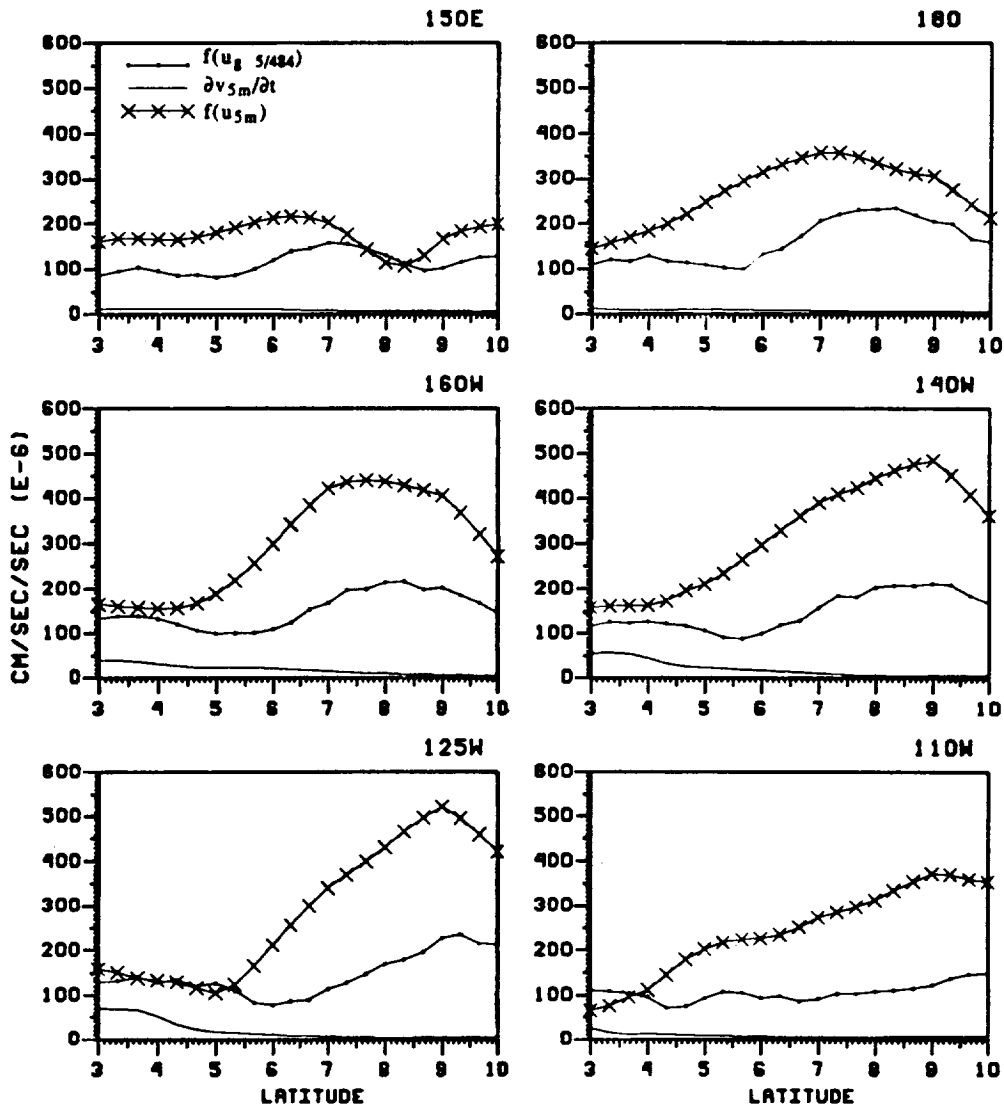


Figure 4.8 Standard deviations of the zonal Coriolis acceleration terms, $f u_g$ 5/484 (thin dotted curve) and $f u_{5m}$ (crosses), and the meridional acceleration, $\partial v_{5m}/\partial t$, in 10^{-6} cm sec⁻² from 3°N to 10°N.

The seasonal and latitudinal variation of the relative contribution to the meridional momentum balance of $\partial v_{5m}/\partial t$, $f(u_{5m})$ and $f(u_g)_{5/484}$ are evident in Fig. 4.9. Only at $4.5^\circ N$ is the magnitude of $\partial v_{5m}/\partial t$ comparable to the Coriolis acceleration terms. The size of the residual, which is defined as

$$\frac{\partial v_{5m}}{\partial t} + f(u_{5m} - u_{g5/484}) = \text{residual} \quad (4.4)$$

is, however, similar to the size of $f(u_{5m})$. Since the annual mean residual at $4.5^\circ N$ is very small ($11 \times 10^{-6} \text{ cm s}^{-2}$), the annual mean meridional momentum balance of the NECC at $4.5^\circ N$, $140^\circ W$ appears to consist of a balance between the Coriolis acceleration due to the zonal velocity and the north-south pressure gradient. At $7^\circ N$ and $9^\circ N$ the residuals are large from December to April. In contrast to $4.5^\circ N$, the annual mean residuals at $7^\circ N$ and $9^\circ N$, $112 \times 10^{-6} \text{ cm s}^{-2}$ and $279 \times 10^{-6} \text{ cm s}^{-2}$, respectively, are large indicating that the remaining terms of the annual mean meridional momentum balance of the NECC are important. Further study is required to identify those terms.

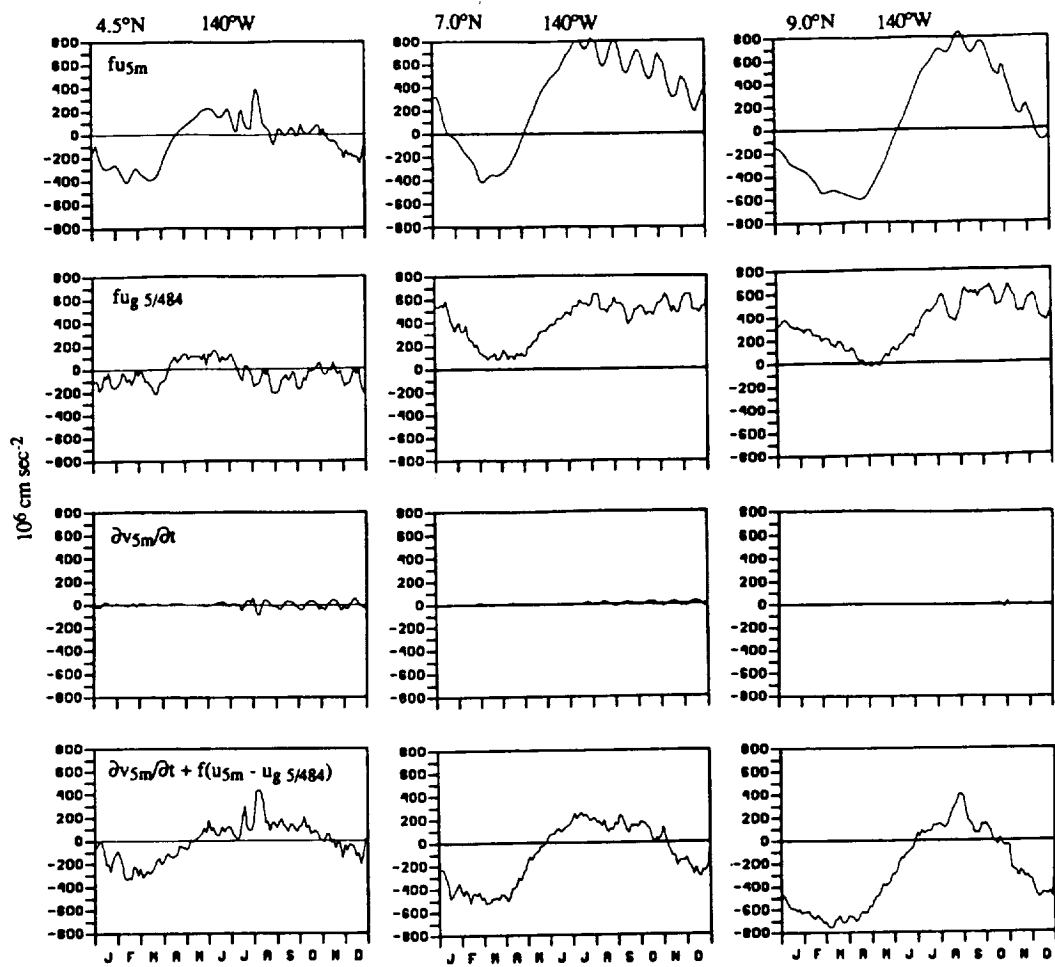


Figure 4.9 Time series of the zonal Coriolis acceleration terms, $f u_g 5/484$ (thin dotted curve) and $f u_{5m}$ (crosses) and the meridional acceleration, $\partial v_{5m} / \partial t$, in $10^{-6} \text{ cm sec}^{-2}$ at 4.5°N , 7°N and 9°N . The bottom row of figures represent the residual, defined as $\partial v_{5m} / \partial t + f(u_{5m} - u_g 5/484)$.

Chapter 5

Relationship between Wind Stress Curl and Thermocline Displacement

In this chapter the Ekman pumping is computed using the wind stress curl calculated from the H&R monthly mean wind stress. In the past, Ekman pumping has been estimated by the movement of an isotherm in the thermocline (e.g., Yoshida 1955; Meyers 1975; Harrison *et al.* 1989). Here, the 20°C isotherm is chosen to represent the center of the thermocline. The questions of interest are: 1) is the vertical movement of the thermocline related to Ekman pumping? and 2) how does Ekman pumping and vertical movement of the thermocline compare with the model simulated total vertical velocity?

5.1 Motivation

In chapter 2 an equation relating the wind stress curl to vertical velocity at the bottom of the Ekman layer was derived. It is common practice in observational oceanography to assume that the local time variation in the depth of the thermocline is similar to the theoretical vertical velocity computed from the wind stress as in Eq. 2.15.

The depth of the 20°C isotherm was used by Meyers (1975) and Harrison *et al.* (1989) to indicate thermocline displacement because the isotherm is located in the approximate center of the thermocline (Fig. 2.1; Fig. 3.4). Denoting the local time rate of change of the vertical displacement of the 20°C isotherm by $\partial h_{20}/\partial t$ (z-axis is positive upward) an alternative version of Eq. 2.15 is given by

$$\frac{\partial h_{20}}{\partial t} = \frac{1}{\rho f} (\text{curl}_z \tau - M_y^E \beta). \quad (5.1)$$

It is the purpose of this chapter to test the validity of Eq. 5.1 in the region of the NECC. In addition, the application of model fields in this problem provides a rare opportunity to compare the theoretical Ekman pumping velocity, w_E , given by the r.h.s of Eq. 5.1, the vertical velocity of the thermocline, given by the l.h.s of Eq. 5.1, with the total vertical velocity, w , predicted by the model. Differences between the Ekman pumping velocity and the total vertical velocity are expected because the latter includes effects due to the full nonlinear equations of motion and the former merely reflects the effect of the surface forcing due the wind stress.

In Eq. 5.1 the total time change in the depth of an isotherm, h , is assumed to be equal to the local time derivative. That is the equation for the total change in h , which is given by $dh / dt = \partial h / \partial t + u \partial h / \partial x + v \partial h / \partial y$, is linearized with the result that $dh / dt \approx \partial h / \partial t$. In some circumstances $dh / dt \approx \partial h / \partial t$ is a poor assumption. For example, if the depth of the isotherm varies spatially the advective terms cannot be ignored. As illustrated in chapter 3 the isotherm slopes upwards to the north across the region of the NECC (see Fig. 3.5). Equation 5.1 may therefore not be a good approximation in the region of the NECC.

5.2 Method

To compute $\partial h_{20}/\partial t$ the vertical distribution of the 3-day averaged temperature, T , was interpolated to 1-m intervals. The depth, h , at which the difference between the temperature at h , T_h , and 20°C is minimum is stored as the depth of the 20°C isotherm, h_{20} , for every 3-day averaged temperature profile. The change in h_{20} between two 3-day averages, $(h_{20,t} - h_{20,t+1}) / 3$ days, yields the vertical velocity of the 20°C isotherm, $\partial h_{20}/\partial t$. Since the time series of h_{20} (Fig. 3.8) show significant oscillations due to the unstable waves described by Philander *et al.* (1986), the values of $\partial h_{20}/\partial t$ were monthly averaged prior to computation of the correlation coefficients.

The density, ρ , was assigned a constant value of $1.022 \times 10^3 \text{ kg m}^{-3}$. The Coriolis parameter, $f = 2\Omega\sin\theta$, and its meridional gradient, $\beta = 2\Omega\cos\theta/R$, where $\Omega = 7.29 \times 10^{-5} \text{ rad s}^{-1}$ and R is the radius of the earth, were calculated for latitudes $\theta = 4.5^\circ\text{N}$ and 9.2°N . The method for computing $\text{curl}_z \tau$ at the grid point (i,j) was outlined in section 3.2. The meridional Ekman transport, $M_y^E = -\tau_x / f$, at (i,j) were computed using the monthly averaged value of the x -component of the H&R wind stress, τ_x , at (i,j) . The applied version of Eq. 5.1 is thus given by:

$$\frac{[(h_{20})_i - (h_{20})_{i+1}]}{3 \text{ days}} = \frac{1}{\rho f_j} [(\text{curl}_z \tau)_{i,j} - (M_y^E)_{i,j} \beta_j] \quad [\text{cm day}^{-1}]. \quad (5.2)$$

The relationship between Ekman pumping, r.h.s of Eq. 5.2, vertical velocity of the 20°C isotherm, l.h.s of Eq. 5.2, and the model vertical velocity is investigated for 3 cases. Correlation coefficients are calculated for Case I: $\partial h_{20}/\partial t$ and w_E , Case II: w and w_E and Case III: $\partial h_{20}/\partial t$ and w . The model-simulated, monthly-averaged vertical velocity at 60 m is used to represent w at the point (i,j) because that is the approximate depth of the Ekman layer across the NECC as given by the H&R wind stress.

Qualitatively, the sign of $\partial h_{20}/\partial t$ is determined by the relative magnitude of the two terms on the r.h.s of Eq. 5.1. The Coriolis parameter is always positive in the NECC

region, but $\text{curl}_z \boldsymbol{\tau}$ changes sign during the year in this region (see Fig. 3.2) such that $\text{curl}_z \boldsymbol{\tau}/\rho f$ can be negative or positive. The sign of the second term on the r.h.s, $M_y^E \beta/\rho f$ is given by the sign of M_y^E , the meridional Ekman mass transport, since f and β are positive north of the equator. Positive (negative) curl implies upward (downward) vertical velocity if $\text{curl}_z \boldsymbol{\tau} > M_y^E \beta$. Since the NECC is strongly forced by the relatively small-scale north-south thermocline slope, the degree to which Ekman pumping physics apply will indicate the sensitivity of the current to the structure of the wind stress curl.

5.3 Results

Table 5.1 contains a summary of the annual mean and standard deviations of the three quantities for 150°E, 180°, 160°W, 140°W, 125°W and 110°W and 4.5°N and 9.2°N. The two latitudes are the typical annual mean southern and northern boundaries of the NECC. The annual mean w_E , denoted by $\langle w_E \rangle$, at 4.5°N is downward at approximately -50 to -60 cm day⁻¹ from 180° to 125°W. At 4.5°N the standard deviation of w_E is largest at 125°W (45.5 cm day⁻¹) and smallest at 160°W (10.6 cm day⁻¹) and the standard deviations are smaller than the annual mean except at 150°E. Compared to w_E at 4.5°N, w_E at 9.2°N has less variance; at most longitudes it is near 10 cm day⁻¹.

At all longitudes, the magnitude of $\langle \partial h_{20} / \partial t \rangle$ is smaller than $\langle w_E \rangle$. The standard deviations of $\partial h_{20} / \partial t$ at both 4.5°N and 9.2°N range from 13.9 to 6.3 cm day⁻¹. The standard deviations of $\partial h_{20} / \partial t$ are more than 10 times greater than the annual mean at 160°W, 140°W, 125°W and 110°W. The vertical velocity of the 20°C isotherm is greater at 9.2°N than at 4.5°N along 180, 160°W, 140°W and 125°W and vice versa at 150°E and 110°W. In contrast, $\langle w_E \rangle$ is always larger at 4.5°N.

Table 5.1. Annual mean and standard deviation (rms) of the movement of the 20°C isotherm ($\partial h_{20}/\partial t$), Ekman pumping (w_E) and the model-simulated vertical velocity (w) at 4.5°N (near the southern boundary of the NECC) and 9.2°N (near the northern boundary of the NECC) in cm day^{-1} . The correlation coefficient (R) is computed for $\partial h_{20}/\partial t$ and w_E in Case I, w_E and w in Case II, and $\partial h_{20}/\partial t$ and w in Case III. R values greater than 0.57 (or less than -0.57) are significantly different from zero at 95% confidence.

	$\partial h_{20}/\partial t$		w_E		w		Case I	Case II	R Case III
	Mean	rms	Mean	rms	Mean	rms			
150°E									
4.5°N	-4.0	12.9	2.8	18.6	-0.1	22.4	-0.68	0.74	-0.19
9.2°N	3.0	-1.4	-1.4	8.1	-1.1	14.2	0.66	0.73	0.67
180°									
4.5°N	2.4	6.3	-36.9	11.5	-25.8	28.9	-0.23	0.19	0.07
9.2°N	4.6	13.8	-8.6	9.9	-10.3	22.7	-0.15	0.27	0.10
160°W									
4.5°N	2.4	7.7	-57.6	10.6	-71.8	51.2	0.05	0.22	0.35
9.2°N	-0.3	11.1	-4.5	10.3	-7.0	17.6	-0.03	0.43	-0.35
140°W									
4.5°N	1.1	9.8	-64.6	18.3	-223.5	176.3	0.12	0.78	0.08
9.2°N	-0.8	11.5	-8.7	9.6	1.1	14.5	-0.09	0.82	-0.38
125°W									
4.5°N	-1.9	7.9	-53.6	42.5	151.5	156.4	0.39	0.45	0.24
9.2°N	0.5	13.9	-1.5	18.3	12.0	13.1	0.21	0.09	-0.10
110°W									
4.5°N	0.0	11.6	51.7	27.5	-14.7	31.2	0.30	0.56	0.12
9.2°N	1.6	10.9	-3.4	8.7	4.4	10.8	0.06	0.10	-0.14

Of the three variables the annual mean model vertical velocity, $\langle w \rangle$, has the largest longitudinal and latitudinal variation. At 140°W and 160°W, for example, $\langle w \rangle$ is -223.5 and -151.5 cm day^{-1} , respectively, at 4.5°N but only 1.1 and 12.0 cm day^{-1} at 9.2°N. The small values of $\langle w \rangle$ at 4.5°N, 150°E (-0.1 cm day^{-1}) and 110°W (-14.7 cm day^{-1}) are associated with large standard deviations of 31.2 and 22.4 cm day^{-1} , respectively.

a. Case I

The correlation between $\partial h_{20}/\partial t$ and w_E is computed in Case I. The correlation coefficients (R) are shown in Table 5.1. Values of R greater than 0.57 (or less than -0.57) are significantly different from zero at 95% confidence. Only at 150°E is the linear relationship between $\partial h_{20}/\partial t$ and w_E statistically significant. Note that R is negative at 4.5°N, 150°E suggesting a significant out-of-phase correlation as it is the inverse of the relationship between vertical motion and thermocline displacement suggested in Eq. 5.1. Although not statistically significant, large R values are also found at 160°W, 4.5°N (0.50), 125°W, 4.5°N and 9.2°N (0.39 and 0.21) and 110°W, 4.5°N (0.30). There does not seem to be any linear relationship between $\partial h_{20}/\partial t$ and w_E at 9.2°N along 180°, 160°W, 140°W and 110°W.

The annual cycles of $\partial h_{20}/\partial t$ and w_E are illustrated in Fig. 5.1 (note that the y-axis scale is different at 4.5°N and 9.2°N). Whereas $\partial h_{20}/\partial t$ alternates between upward and downward movements at 4.5°N, w_E remains negative throughout the year, except at 150°E and 125°W. The only case in which $\partial h_{20}/\partial t$ and w_E are both upward at 4.5°N is in March at 125°W.

At 9.2°N, 160°W from November to April, Ekman pumping does not seem related to the upward movement of the thermocline (Fig. 5.1.b). From May to June the two terms are both positive and are both negative from July to October. Similarly, at 9.2°N, 140°W the model-simulated results do not substantiate Eq. 5.1 from January to April but are very consistent with the dynamics expressed by Eq. 5.1 from May to December. At 125°W the direction of thermocline movement and Ekman pumping match from January to April and from June to August; and at 110°W they match during the period from

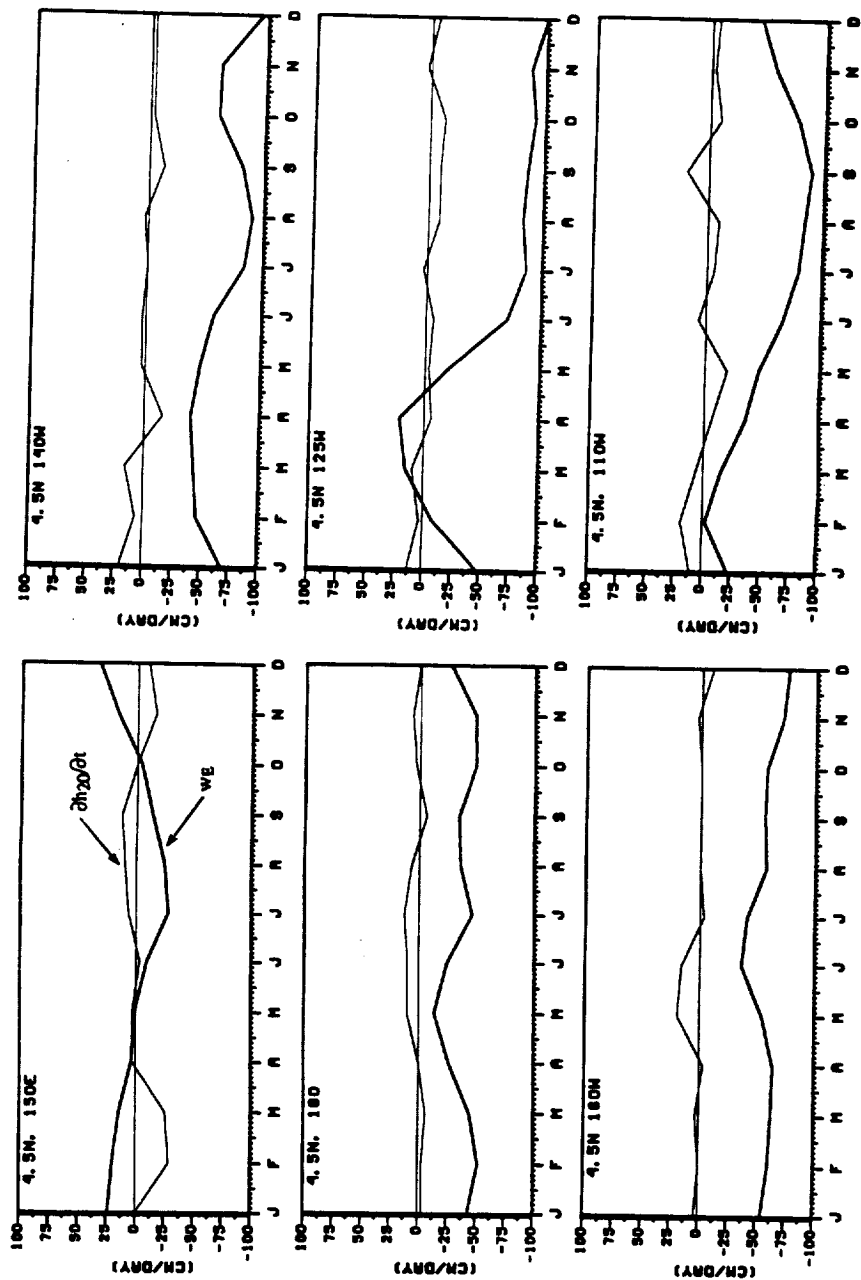


Figure 5.1.a Comparison of monthly averaged Ekman pumping, w_E (thick curve) and vertical velocity of the 20°C isotherm, $\partial\theta_{20}/\partial t$ (thin curve) in cm day^{-1} at 4.5°N .

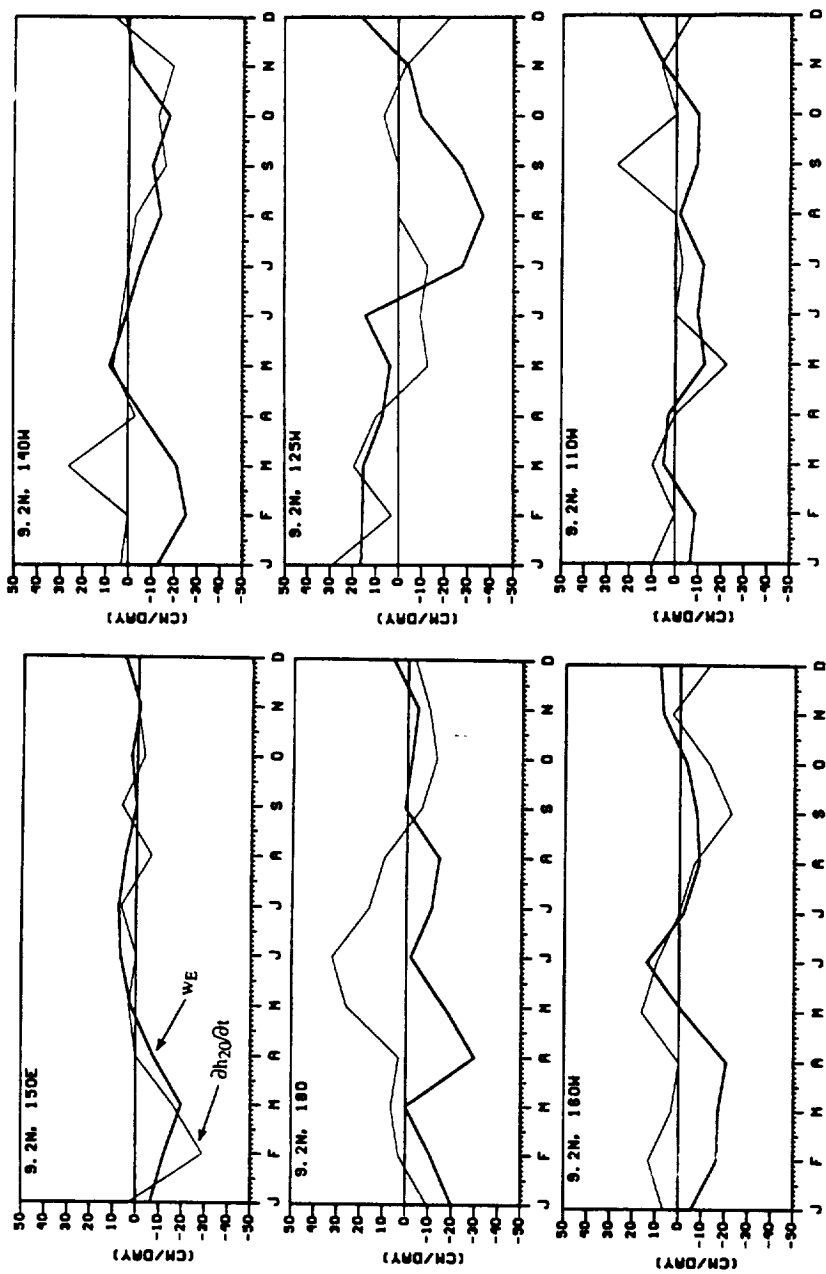


Figure 5.1.b Comparison of monthly averaged Ekman pumping, WE (thick curve) and vertical velocity of the 20°C isotherm, $\partial h_{20}/\partial t$ (thin curve) in cm day^{-1} at 9.2°N .

March to August. The only place where Eq. 5.1 appears to be a rough model of the annual cycle is at 9.2°N, 150°E.

b. Case II

Case II explores the relationship between w_E and w at 60 m. The correlation of w_E with w is generally greater than that of w_E with $\partial h_{20}/\partial t$ (see Table 5.1). The linear relationship is significant in the 150°E and 140°W sections at both 4.5°N and 9.2°N. High correlations were also found at 4.5°N, 110°W and 4.5°N, 125°W. As indicated by the fact that all the R values for Case II are positive, w_E and w are in-phase. The lowest correlations of 0.09 and 0.10 occur at 9.2°N in the 125°W and 110°W sections.

Figure 5.2 contrasts the annual cycles of w_E and w (note the variable scale on the y-axis). It is difficult to discern a relationship between w_E and w at 4.5°N along 140°W and 125°W because the annual fluctuations in w are very large; standard deviations of w are 176.3 and 156.4 cm day⁻¹ at 140°W and 125°W, respectively, compared to those of w_E of 18.3 and 42.5 cm day⁻¹. However, the correlation coefficient at 4.5°N, 140°W (0.78) is significant at 95% confidence. At 4.5°N, 150°E there is close correspondence between w_E and w ($R=0.74$). Their magnitudes are also comparable from March to August. At 4.5°N along 180°, the curves of w_E and w have similar patterns only from May to September. Along 160°W there is significant disagreement throughout the year.

Along 9.2°N in the western and central Pacific (i.e. 150°E, 180°, 160°W and 140°W), the period of upward w lasts roughly from June to November. In the far eastern Pacific, w is predominantly upward. At 9.2°N, 150°E, the correlation coefficient is 0.73 indicating a strong relationship between w and w_E . In contrast at 9.2°N, 125°W and 110°W, w and w_E are uncorrelated as evidenced by the low values of R of 0.09 and 0.10.

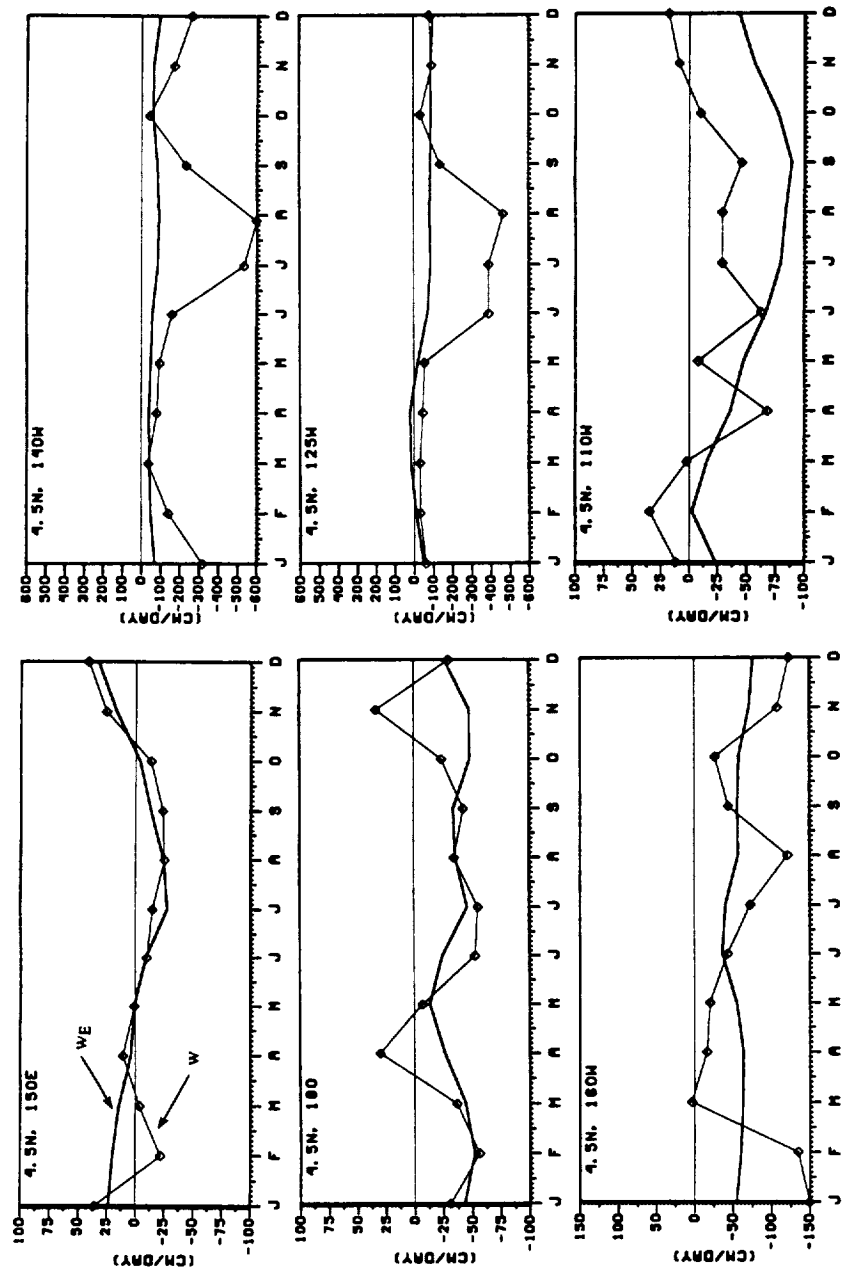


Figure 5.2.a. Comparison of monthly averaged Ekman pumping, w_E (thick curve) and the model-simulated vertical velocity, w (diamonds) in cm day^{-1} at 4.5°N .

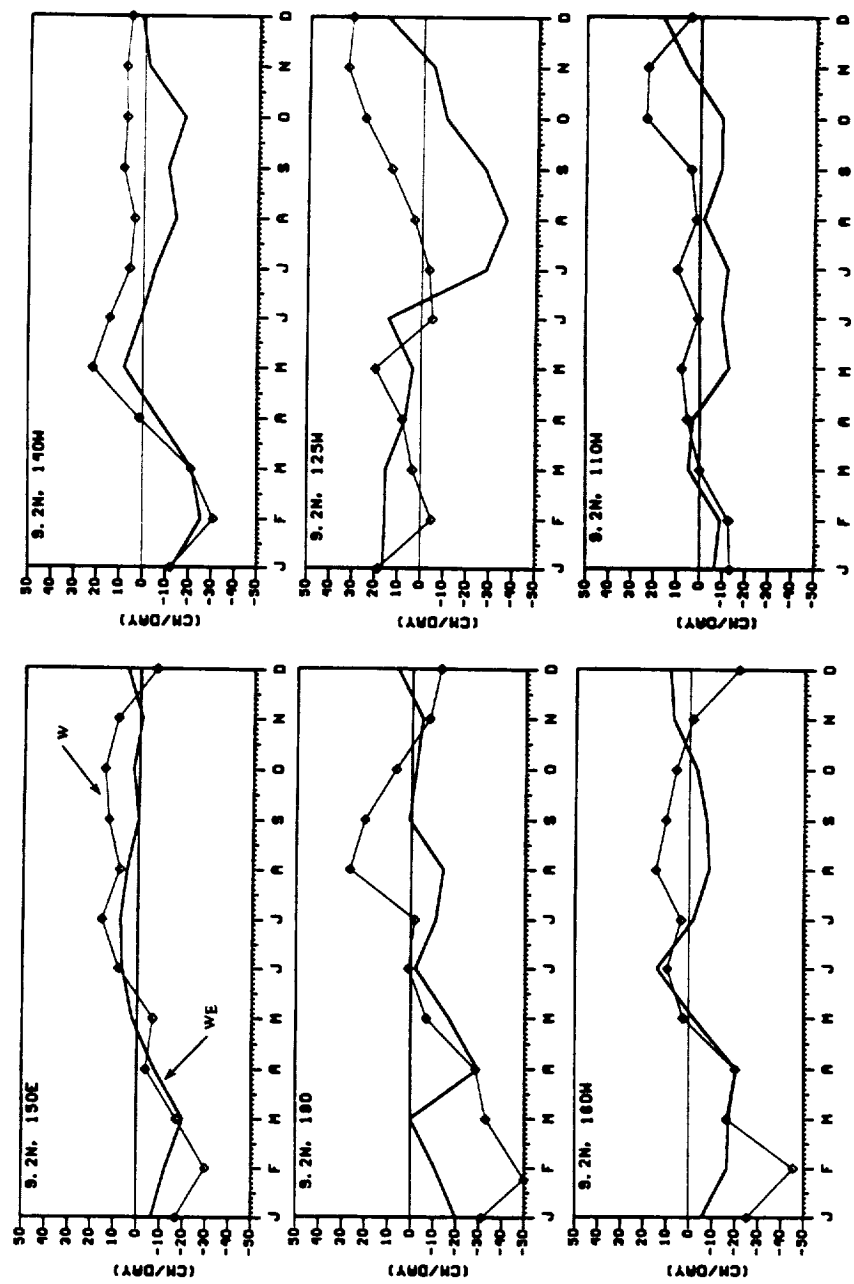


Figure 5.2.b Comparison of monthly averaged Ekman pumping, w_E (thick curve) and the model-simulated vertical velocity (diamonds) in cm day^{-1} at 9.2°N.

c. Case III

Case III describes the relationship between w and $\partial h_{20}/\partial t$. This relationship appears to be the weakest of the three cases. At $4.5^\circ N$, especially along $160^\circ W$, $140^\circ W$ and $125^\circ W$, there is a large disparity in the magnitude of the annual fluctuation in w and $\partial h_{20}/\partial t$ (Fig. 5.3.a). There is no statistical significance between w and $\partial h_{20}/\partial t$ at each of the six longitudes at $4.5^\circ N$ and there does not appear to be any coherent period where w and $\partial h_{20}/\partial t$ are in the same direction (Fig. 5.3.a).

The only statistically significant R value (0.67) in Case III is found at $150^\circ E$, $9.2^\circ N$. At $9.2^\circ N$, $140^\circ W$ and $160^\circ W$, the negative correlation coefficients of -0.35 and -0.38 indicate that w and $\partial h_{20}/\partial t$ are out-of-phase (Fig. 5.3.b). At $9.2^\circ N$, the relationship is weakest at $110^\circ W$, $125^\circ W$ and 180° where R values are less than 0.14.

5.4 Discussion

The question of whether the vertical movement of the thermocline is related to Ekman pumping, as expressed in Eq. 5.1, was addressed in Case I. The results indicate that only at $150^\circ E$ is the relationship between w_E and $\partial h_{20}/\partial t$ statistically significant. From the annual cycles of w_E and $\partial h_{20}/\partial t$, it was revealed that, at most of the other location, Eq. 5.1 fails to model the annual cycle. Comparing the correlation coefficients for w_E and $\partial h_{20}/\partial t$ at $4.5^\circ N$ and $9.2^\circ N$, the correlation coefficients are higher at $4.5^\circ N$ at all six longitudes. However, the annual means of w_E and $\partial h_{20}/\partial t$ at $4.5^\circ N$ are very different.

At $4.5^\circ N$ the Ekman pumping was found to be large and negative, far exceeding the movement of the $20^\circ C$ isotherm. The Ekman pumping is negative throughout the year at all longitudes, except $125^\circ W$, despite the fact that $\text{curl}_z \tau$ is positive during parts

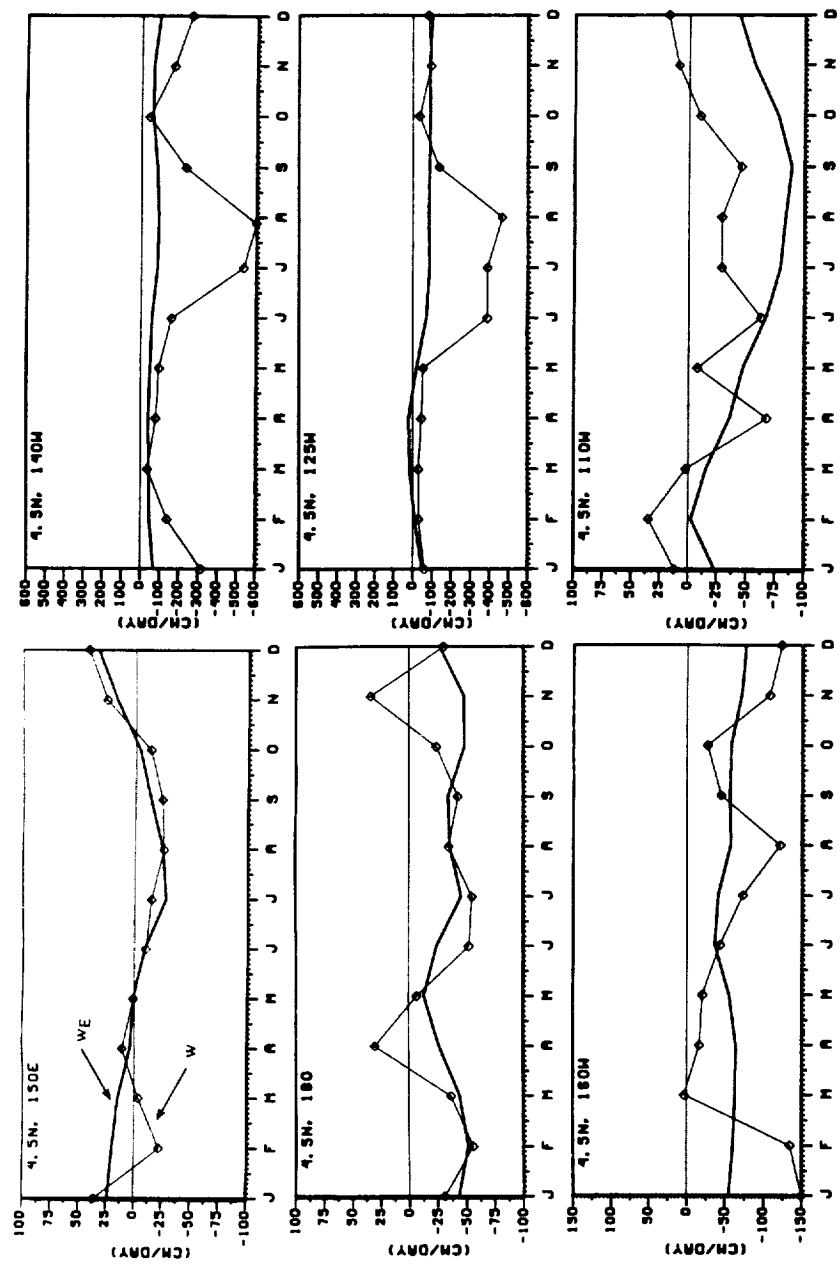


Figure 5.3.a Comparison of monthly mean vertical velocity of the 20°C isotherm, $\partial h_{20}/\partial t$ (thick curve) and model-simulated vertical velocity, w (diamonds), in cm day $^{-1}$ at 4.5°N.

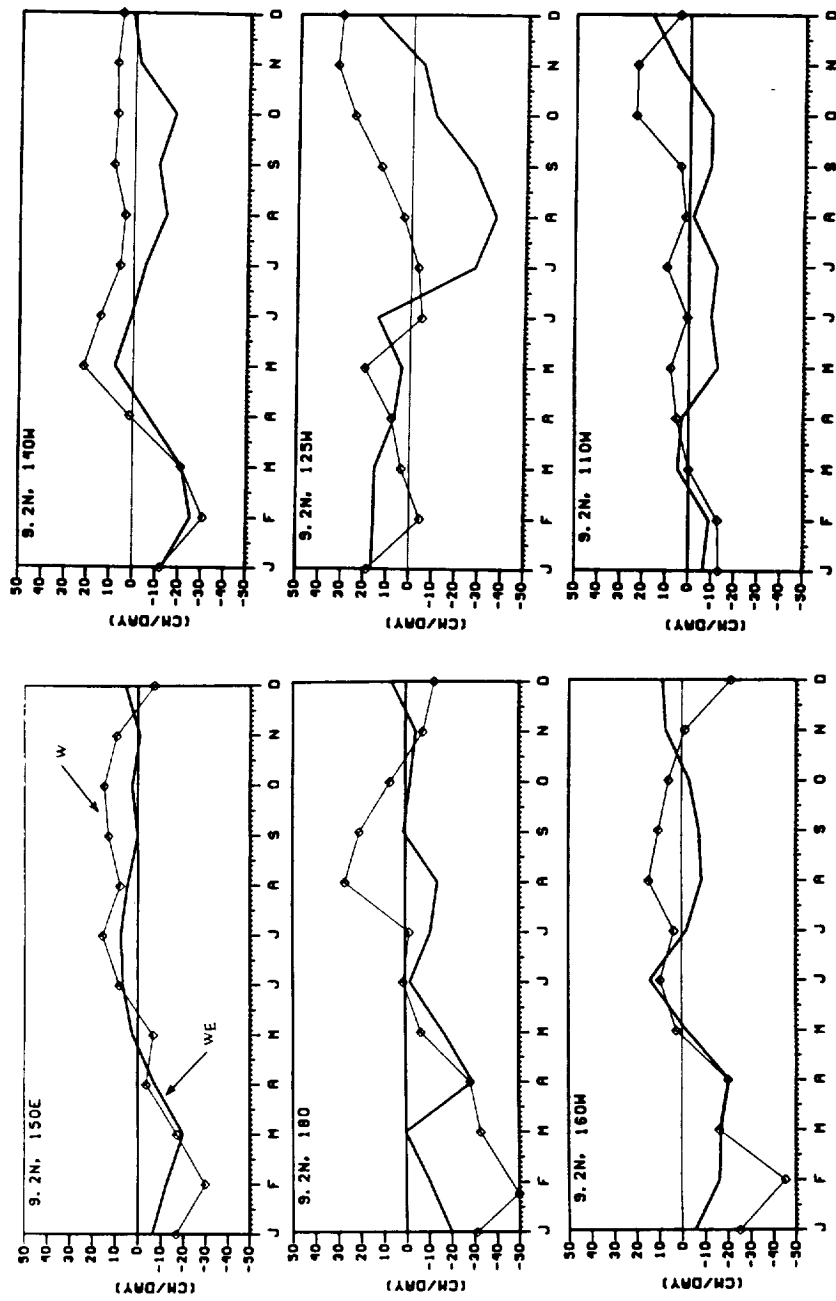


Figure 5.3.b Comparison of monthly mean vertical velocity of the 20°C isotherm, $\partial h_2 / \partial t$ (thick curve) and model-simulated vertical velocity w (diamonds), in cm day⁻¹ at 9.2°N.

of the year. This indicates that the magnitude of $M_y^E \beta$, on the r.h.s of Eq. 5.1, is comparable to the magnitude of $\text{curl}_z \tau$. Table 5.2 compares the values of $\text{curl}_z \tau$ and $M_y^E \beta$ at 4.5°N along 160°W and 125°W. The Ekman pumping at 4.5°N, 160°W is negative throughout the year (Fig. 5.1.a) evidently because the value of $M_y^E \beta$ exceeds that of $\text{curl}_z \tau$. The only occurrence of positive Ekman pumping at 4.5°N east of 180° is at 125°W from March to May. As shown in Table 5.2, this is the only time and location at which the value of $\text{curl}_z \tau$ exceeds the value of $M_y^E \beta$. Since the values of $\text{curl}_z \tau$ and $M_y^E \beta$ at 9.2°N also are of similar magnitude, both terms should be included in estimates of Ekman pumping in the region of the NECC.

At 9.2°N the magnitudes of the w_E and $\partial h_{20} / \partial t$ are more comparable than those at 4.5°N but the signs do not always agree. There are many instances of movement of the 20°C isotherm in opposite direction of the Ekman pumping. There are two striking examples in Figs. 5.1.b and 5.3.b. The first feature is the relatively fast ($\approx 30 \text{ cm day}^{-1}$) upward movement of the 20°C isotherm in May, June and July along 180°. This is difficult to explain since there is no apparent forcing from either the Ekman pumping or the total vertical velocity. The second feature is the peak in downward Ekman pumping in August along 125°W.

Table 5.2 Comparison of the values of the two terms determining the sign of the Ekman pumping velocity, w_E at 4.5°N. If $\text{curl}_z \tau > M_y^E \beta$, $w_E > 0$, or if $\text{curl}_z \tau < M_y^E \beta$, $w_E < 0$.

	160°W		125°W	
	$\text{curl}_z \tau$	$M_y^E \beta$	$\text{curl}_z \tau$	$M_y^E \beta$
	(10^{-8} N m^{-3})		(10^{-8} N m^{-3})	
JAN	14.0	20.2	7.5	9.2
APR	12.9	17.0	18.0	8.2
JUL	6.0	11.0	-10.3	10.8
OCT	-2.7	9.8	-10.1	6.4

This peak in negative w_E is associated with a longer period of downward pumping from July to November. There is, however, no response in the isotherm during this time.

There are also several cases of large differences between w and w_E . The differences occur in the eastern Pacific, along 140° , 125° and 110°W at both 4.5°N and 9.2°N . At 4.5°N from June through August w reaches downward velocities between -400 to -600 cm day^{-1} but the Ekman pumping velocity remains near -100 cm day^{-1} . The discrepancy may be partially due to time-dependent motions associated with internal ocean dynamics which is reflected in w . Such effects are not included in the calculation of w_E , which is purely given by the wind stress. Unstable equatorial waves are associated with intense downwelling and upwelling events near 3°N in the eastern Pacific from June through February (Philander *et al.* 1986). The timing and location of the wave disturbances and the discrepancy between w and w_E are thus consistent. The difference between w and w_E at 9.2°N are not as likely to be due to time-dependent motions as the effects of these decrease with increasing distance from the equator.

The relation between NECC transports and the north-south thermocline slope across the NECC was established in chapter 3. In order to establish a relationship between the vertical velocities and the strength of the NECC, the north-south gradient of the vertical velocities should be compared to NECC transport across the six longitude sections. The largest magnitudes of the north-south gradient across the NECC of the annual mean w and w_E occur in the three central Pacific longitude sections from 140°W to 180° (Table 5.1). The annual mean NECC transport peaks at 160°W (19.9 Sv) and decreases smoothly eastward and westward. The longitudinal variations of w and w_E are thus largely consistent with the longitudinal variation of NECC transports. However, there are several inconsistencies. For example, the relatively large Ekman pumping at 125°W and 110°W of -53.6 and $-55.7 \text{ cm day}^{-1}$ (Table 5.1) is not reflected

transport which is the weakest at those two longitudes (Fig. 3.16). Also the large annual mean NECC transport at 180° (17.4 Sv) does not coincide with large vertical velocities relative to the other longitudes.

Chapter 6

Summary and Conclusions

An ocean general circulation model (OGCM) is used to study the longitudinal and seasonal variation of the Pacific North Equatorial Countercurrent (NECC). Observational data sets are limited in spatial and temporal extent. OGCMs provide high resolution, basin-wide fields that can be used to study the first-order dynamical balance of the current. In this case, the degree of geostrophy and the relationship between the wind stress curl, thermocline displacement and vertical motion are studied.

In chapter 3, latitude-depth sections of the zonal current along 150°E, 180°, 160°, 140°, 125° and 110°W were studied. The detailed description of the longitudinal variation of the NECC contained in chapter 3 is presently the only one of its kind. The simulated NECC has a subsurface maximum in all sections but at 110°W. The annual mean NECC is confined to the upper 187 m between 5.1°-9.2°N in the central Pacific. Near the boundaries of the basin, represented by the 150°E and the 110°W sections, the NECC shifts northward by 1 to 2 degrees and becomes narrower. The annual mean core speed is approximately 25 cm s⁻¹ at 160°W.

An algorithm is applied to the calculation of the transports such that monthly- and spatially-varying boundaries are determined objectively. Eastward NECC transport along 160°W, the strongest of the six longitudes, exhibits a maximum in September and a minimum in February. The NECC transport decreases eastward from 160°W and is lowest in the 110°W and 125°W sections. The seasonal changes in the transports can also be viewed in terms of the current's changing boundaries. In addition to the seasonal widening and northward shift, the thickness also changes. Especially large variations occur at 160°W where the depth varies from 75 m in April to 337 m in September. The 160°W transport maximum in September seems to be linked with the great vertical extent, the largest of any section and month.

In chapter 4 geostrophic currents were calculated using the model simulated temperature and salinity fields. Analysis of the geostrophic currents indicates that the degree of geostrophy varies with longitude and season. The major findings of this chapter are 1) the zonal geostrophic NECC has a surface maximum (in contrast to the subsurface maximum of the total zonal velocity field); 2) the zonal geostrophic surface current component, u_g , is smaller than the total zonal surface component, u_m , throughout the year; 3) the magnitude of $(u_g - u_m)$ is largest when the current is weak and smallest when it is strong; and 4) u_g explains the most variance ($\approx 50\%$) in u_m between 8°-9°N and 50-150 m.

In contrast to the surface maximum of the model-simulated zonal geostrophic NECC, studies using observational data (Wyrtki and Kilonsky 1984) have found a subsurface maximum in the strength of the geostrophic NECC. The reason why the eastward zonal surface current in the region of the NECC is not in geostrophic balance appears to be partially due to the presence of strong westward wind-driven currents. An example was given for 160°W where the southward wind stress in March, averaged

between 5°N and 10°N, cause a westward Ekman current at 5 m equal to 57% of the total zonal current at 5 m (Table 4.2). The magnitude of the meridional local acceleration was calculated and found to be insignificant in the annual mean meridional momentum balance. The meridional local acceleration does however play a role near the southern boundary of the NECC in the eastern Pacific (140°W) from July to January (Fig. 4.7).

The results of chapter 4 may have implications for observational methods. For example, certain aspects of the structure of the NECC such as the current width and thickness of the eastward flow can be inferred from the geostrophic method, but the near-surface structure cannot. It remains to be determined whether this is a physical characteristic or a consequence of the model design, particularly the application of the rigid-lid approximation. The rigid-lid approximation eliminates differences in sea surface elevation but it allows for pressure gradients to exist on the surface of the lid, which are not included in the calculation of the pressure gradient used in the geostrophic method outlined in chapter 4. In addition, the total zonal current component exhibits more variance than the zonal geostrophic current component, especially near the southern boundary of the NECC, such that typically less than 50% of the variance can be predicted using geostrophic currents.

In chapter 5, Ekman pumping, w_E , and vertical movement of the thermocline (approximated by the displacement of the 20°C isotherm), $\partial h_{20}/\partial t$, are calculated and compared to the model-simulated vertical velocity, w , at 60 m. The relationship between the three quantities is not simple and seems to have seasonal dependence. Calculations were made for 4.5°N and 9.2°N which are typical boundaries of the NECC. Correlation coefficients were computed for three cases 1) $\partial h_{20}/\partial t$ and w_E , 2) w and w_E and 3) $\partial h_{20}/\partial t$ and w . The results indicate that the relations in cases I and III are poor and the relation in Case II is also weak but stronger than cases I and III. Statistically

significant (95% confidence) relationships were found only in Case I at 150°E, 4.5°N and 9.2°N, Case II at 150°E and 160°W at both 4.5°N and 9.2°N and Case III only at 150°E, 9.2°N.

During the year, there appears to be a weak relationship between Ekman pumping and thermocline movement (Case I) at 4.5°N, but none is evident at 9.2°N. However, at 9.2°N there are periods of 4-6 months where $\partial h_{20}/\partial t$ and w_E seem correlated (Figure 5.1.b); these are 1) from May to October at 160°W, 2) from May to December at 140°W and 3) from January to May and July to August at 125°W. One distinct reason why the relationships in cases I and III are weak is the assumption that $dh / dt = \partial h / \partial t + u \partial h / \partial x + v \partial h / \partial y$ simplifies to $dh / dt \approx \partial h / \partial t$. This assumption is probably not appropriate in the region of the NECC because the depth of the 20°C isotherm changes significantly in the north-south direction. In Case II, the model-simulated vertical velocity may differ from the Ekman pumping velocity due to time-dependent motions such as the equatorial unstable waves described by Legeckis (1977), Cox (1980) and Philander *et al.* (1986).

The results of chapter 5 also have implications for both observational methods and methods of model diagnostical analyses. The results of Case III, which related $\partial h_{20}/\partial t$ and w suggest that the practice of using the temperature change at a fixed point in space to infer the vertical velocity is inappropriate since the two quantities are uncorrelated east of 180°. This is a method used both in observational studies (e.g. Meyers 1975) and in modelling studies (e.g. Harrison *et al.* 1989). Since the vertical velocity is a dynamical variable regularly stored in OGCMs, a more appropriate comparison would have involved comparing the wind stress curl-induced vertical velocity and the total model-simulated vertical velocity thus avoiding the assumptions inherent in using $\partial h / \partial t$.

All together the results show that the seasonal cycle has the largest amplitude in the central Pacific. Annual mean and standard deviation NECC transport, standard deviations of the u and v components and monthly displacements about the annual mean of the equatorial ridge near 4°N and the countercurrent trough near 10°N, are all largest at 160°W. The standard deviation of the surface dynamic height difference across the NECC, which gives the strength of the zonal geostrophic NECC, is greatest at 140°W. Whereas the annual mean thickness of the NECC is largest at 160°W (174 m), the annual mean width is largest at 140°W (4.8 degrees latitude). Future efforts to monitor the variability of the NECC should therefore be concentrated between 140°W and 160°W.

There are some remaining specific questions about the detailed dynamical balance of the climatological NECC which were not answered with the results presented herein:

- 1) What causes the 160°W maximum ?
- 2) What causes the maximum and minimum NECC transport to occur in widely different months along the six longitude sections? And why does the annual cycle of NECC transports along 180°, 160°W and 140° have *one* maximum and *one* minimum when that along 150°E, 125°W and 110°W has two?
- 3) What physical processes cause the variance of the total zonal surface velocity to exceed that of the zonal geostrophic surface velocity ?

4) What are the seasonal and longitudinal variations of the dynamical balance of the NECC ?

This study of the annual cycle of the NECC and its first-order dynamical balance was based on fields generated by an OGCM forced by monthly-averaged, climatological wind stress. There are thus some additional questions which should be addressed such as 1) How would the result be affected if the wind stress curl were allowed to vary on the sub-monthly scale? and 2) What are the inter-annual variations of the NECC annual cycle and dynamical balance? These are studies that could be carried out with an OGCM forced by one or more of the many wind stress products currently available.

Appendix A

A.1

Hellerman and Rosenstein (1983) climatological monthly mean wind stress. The zonal component is contoured with an interval of 0.1 N m^{-2} and negative (westward zonal wind stress) contours are dashed.

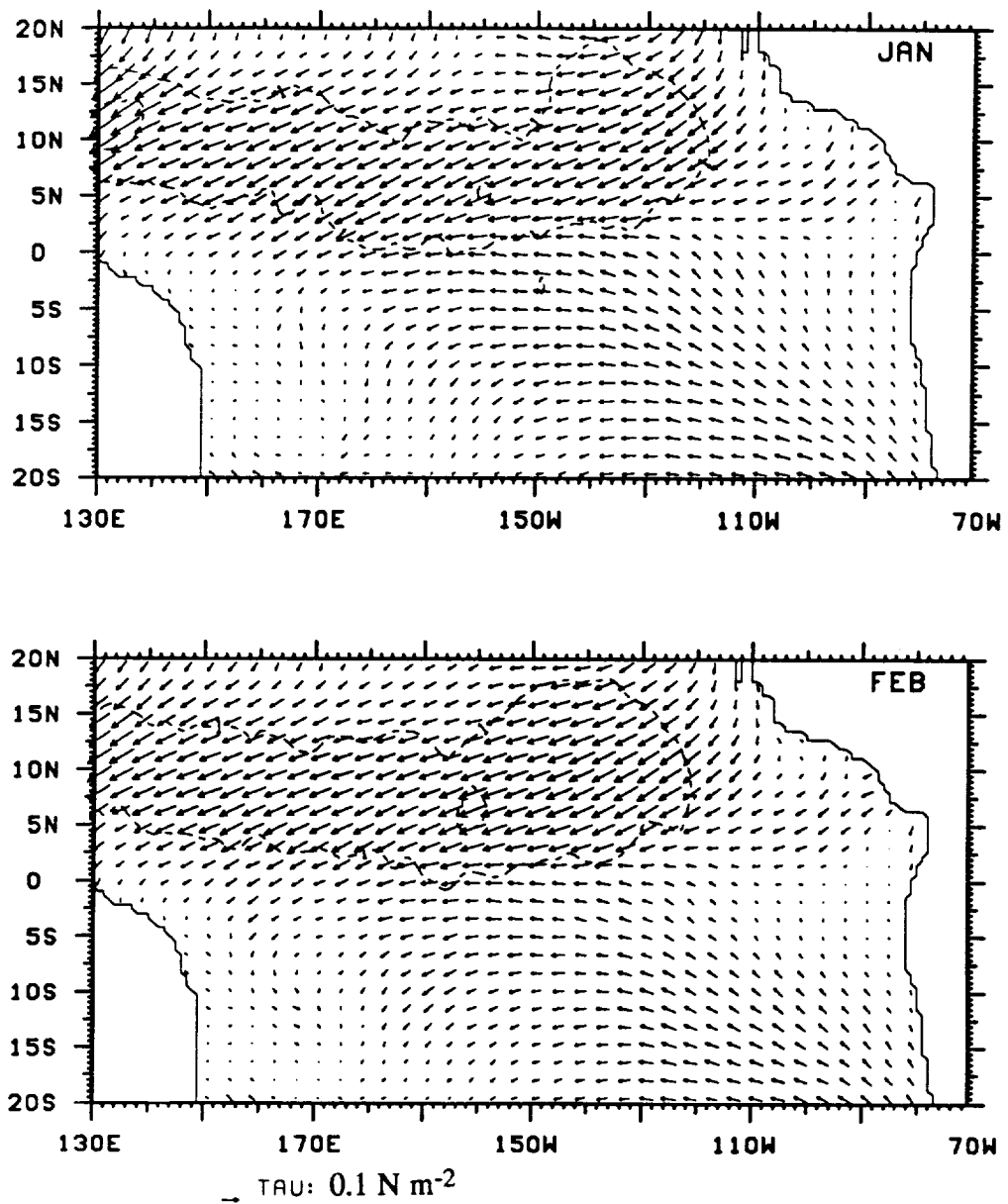


Figure A.1

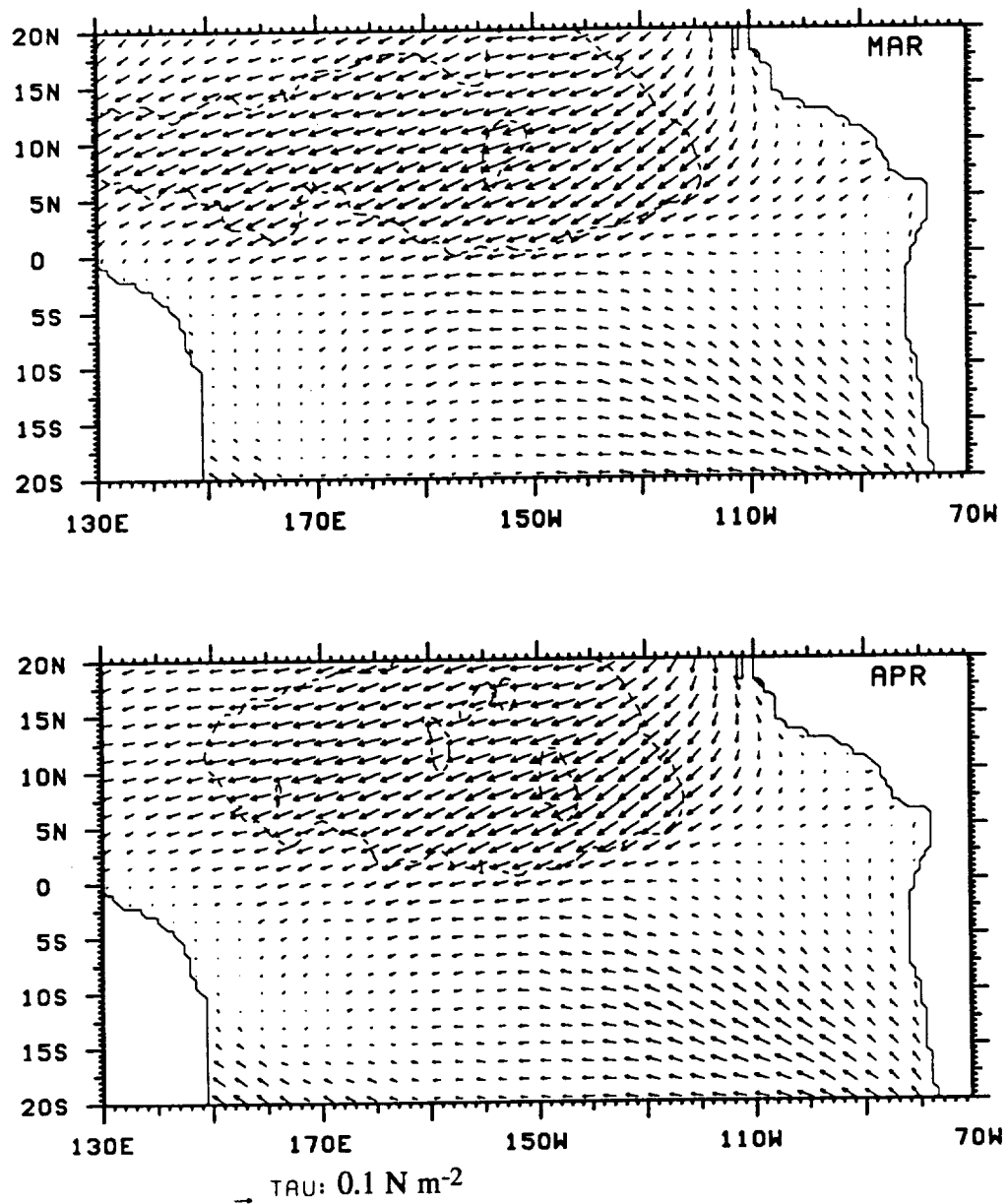


Figure A.1

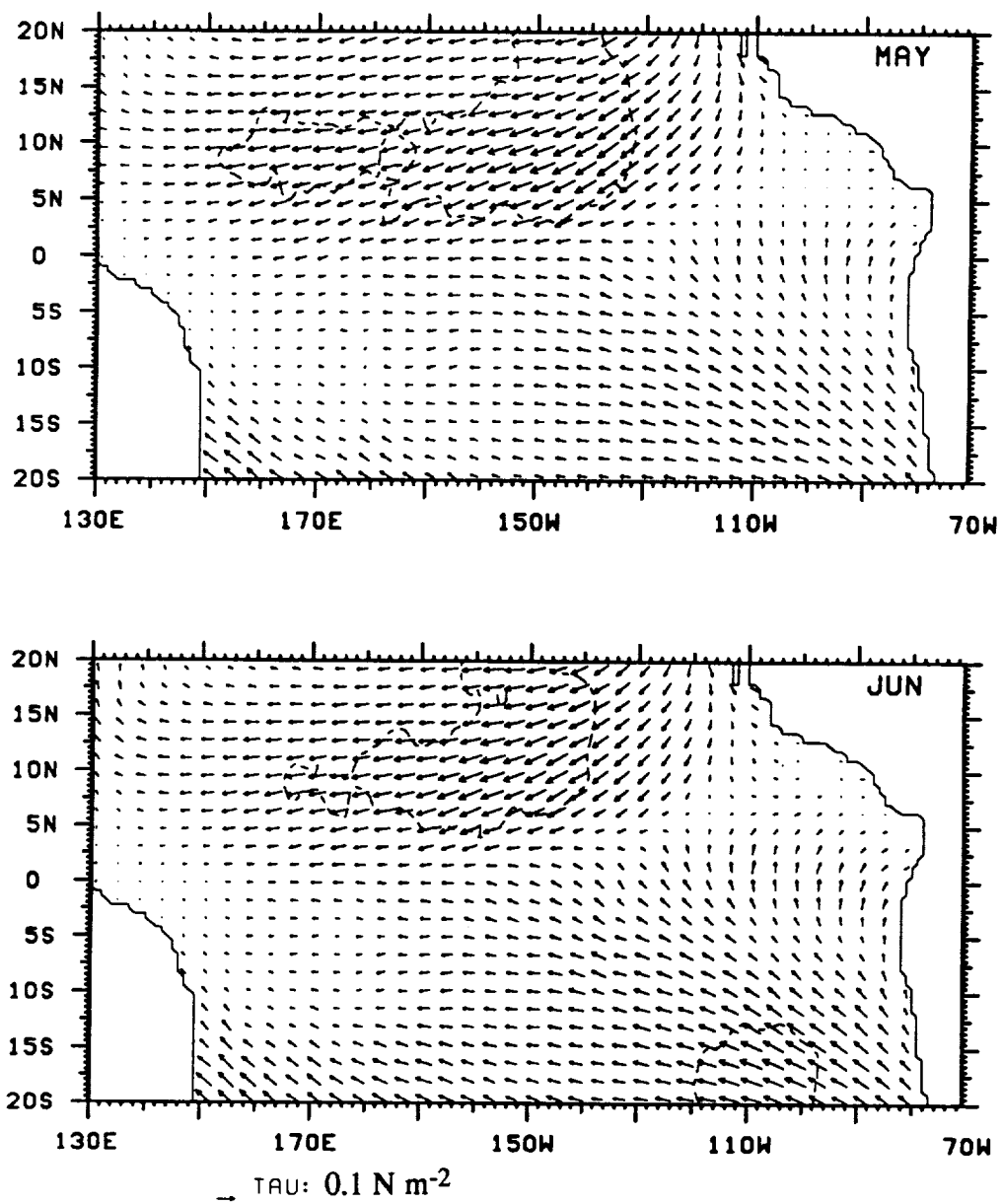


Figure A.1

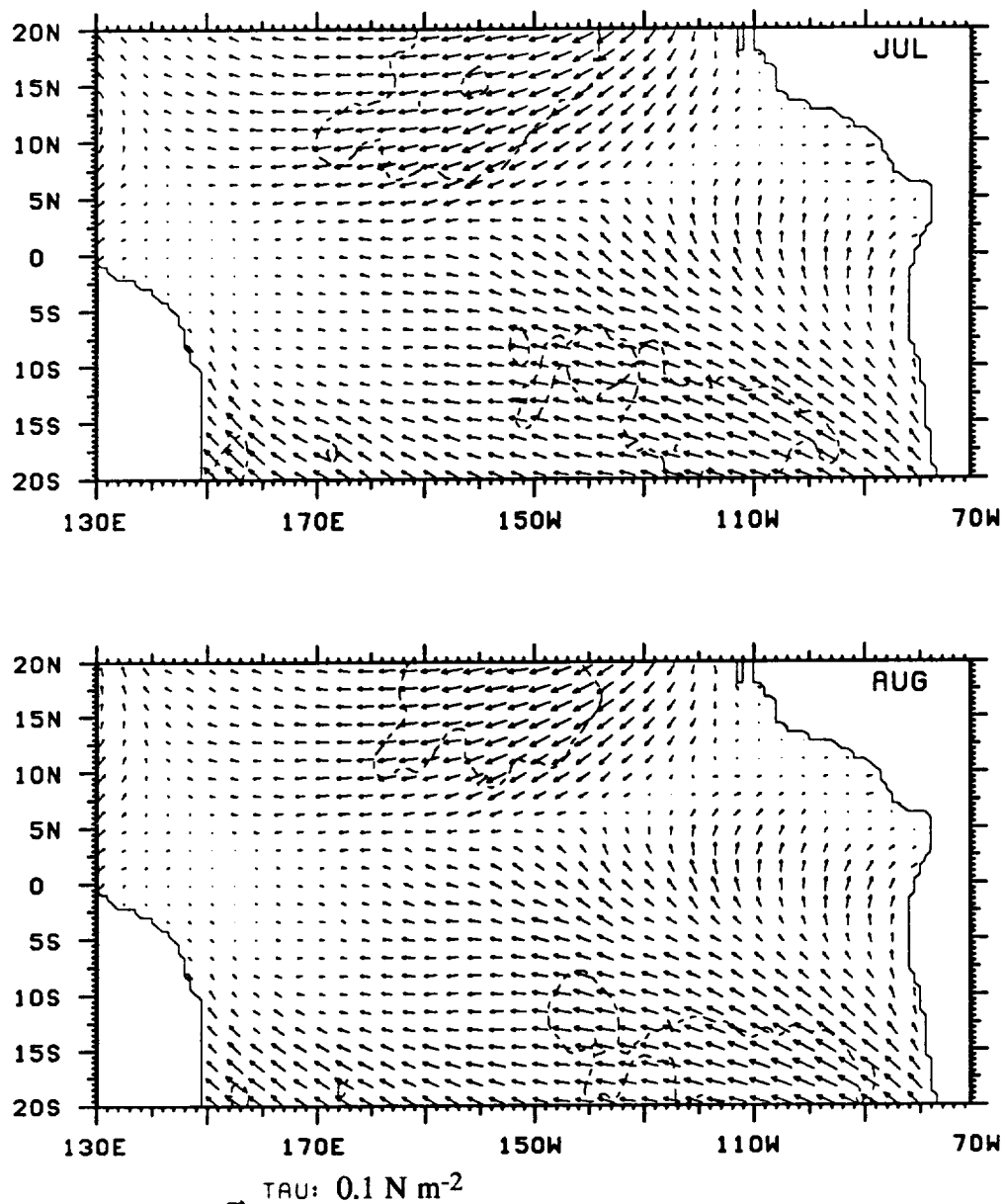


Figure A.1

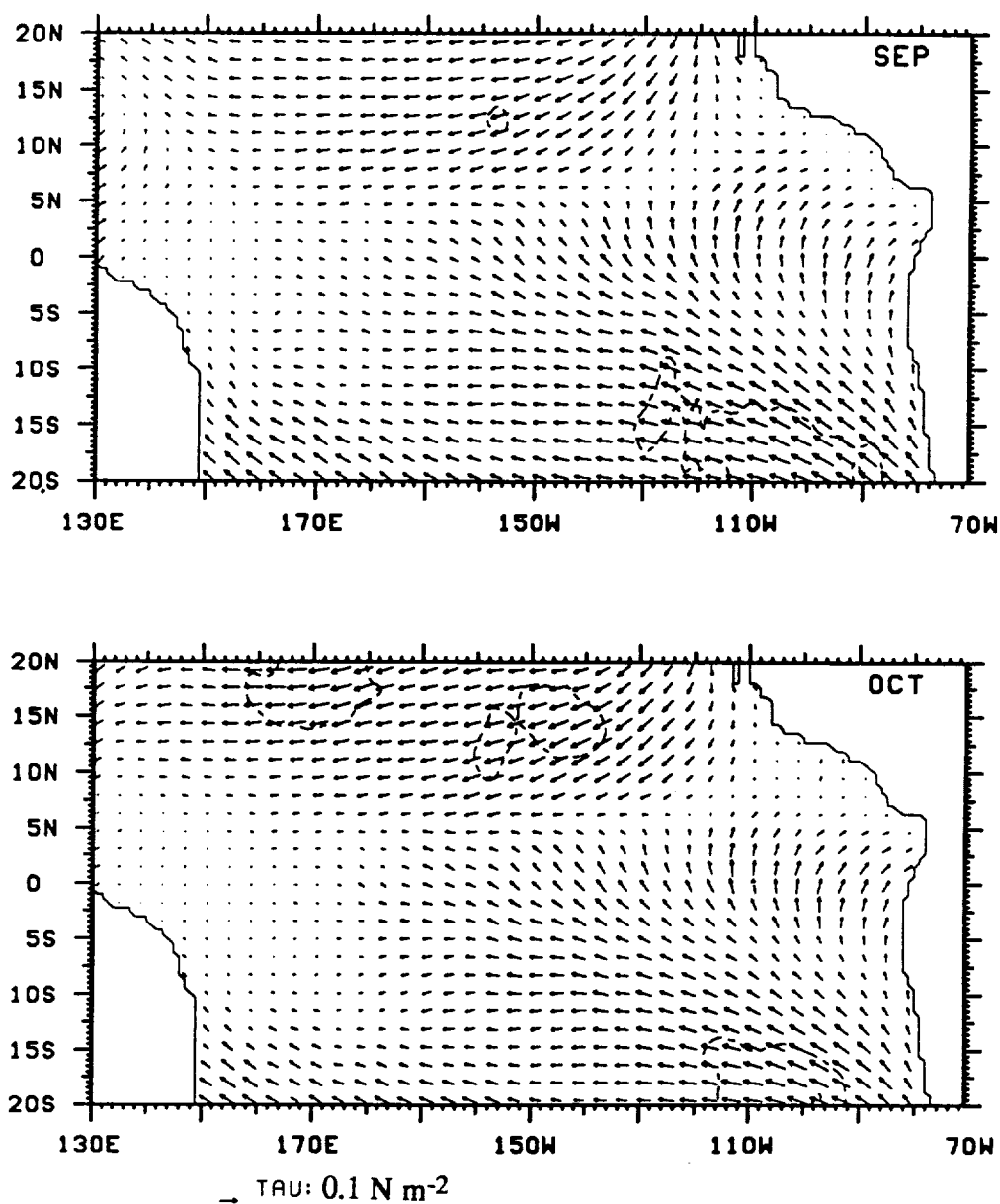


Figure A.1

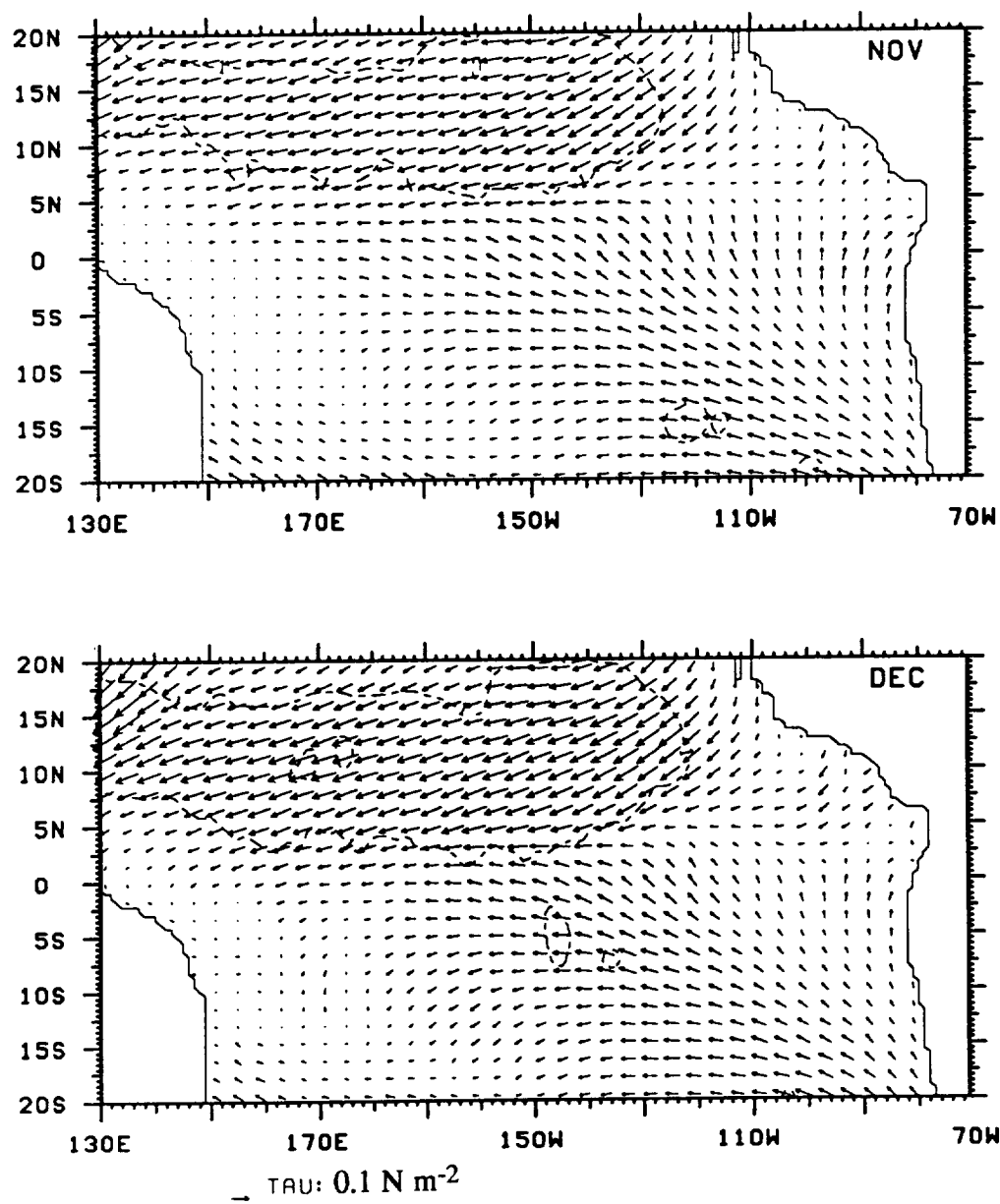


Figure A.1

A.2

Climatological monthly mean wind stress curl computed from Hellerman and Rosenstein (1983) wind stress. Contour interval is $5 \times 10^{-8} \text{ N m}^{-3}$ and negative contours are shaded.

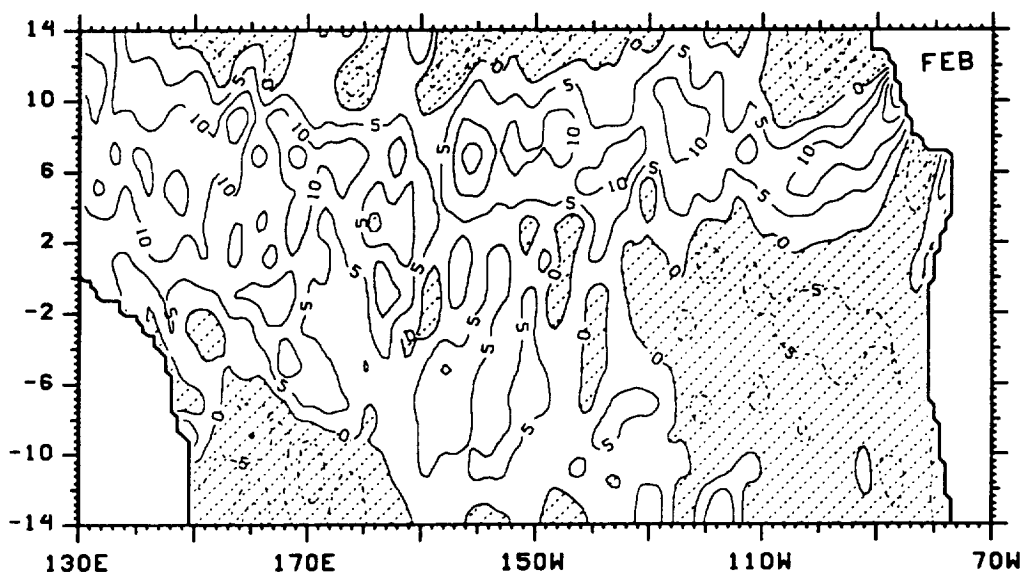
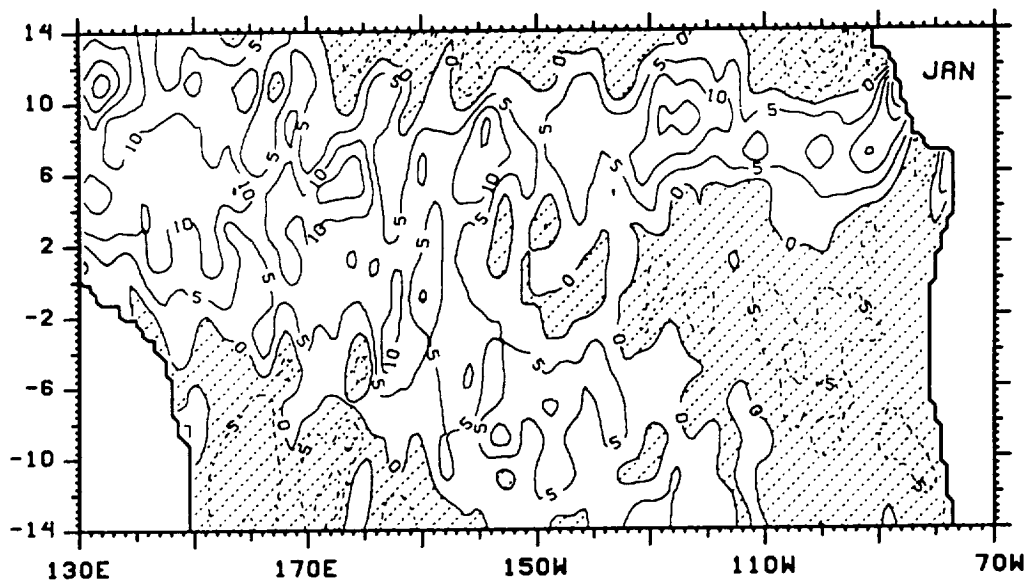


Figure A.2

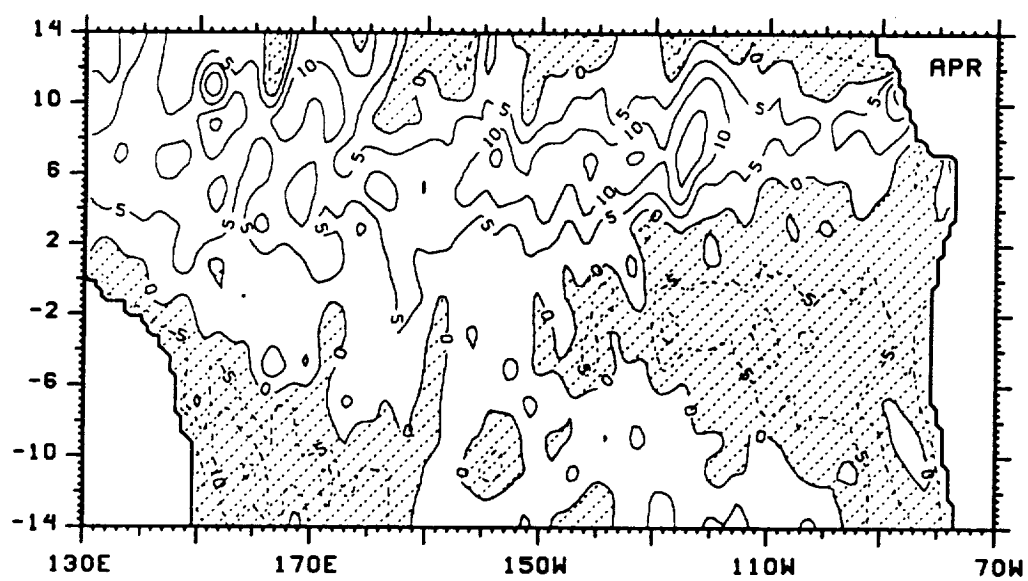
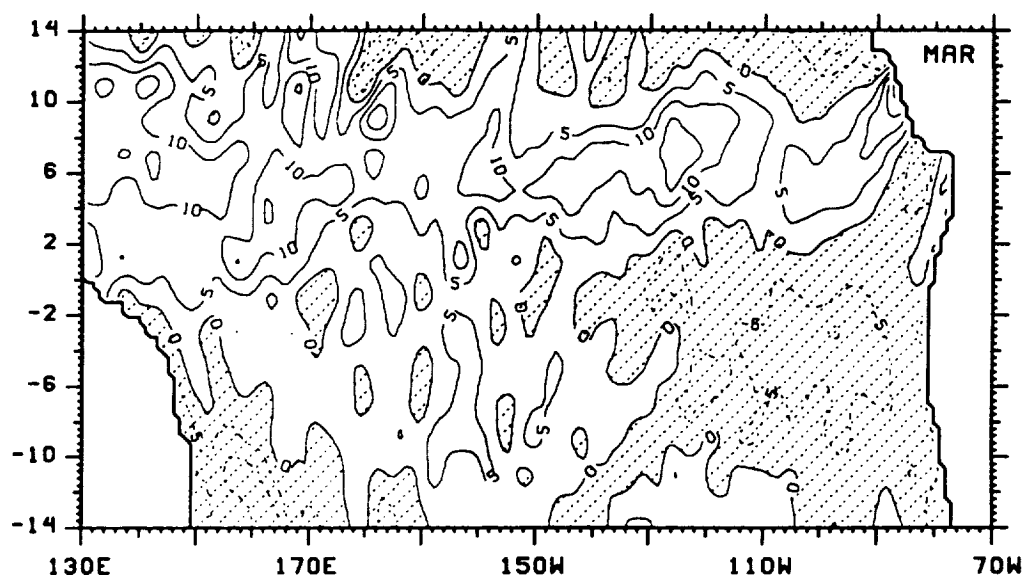


Figure A.2

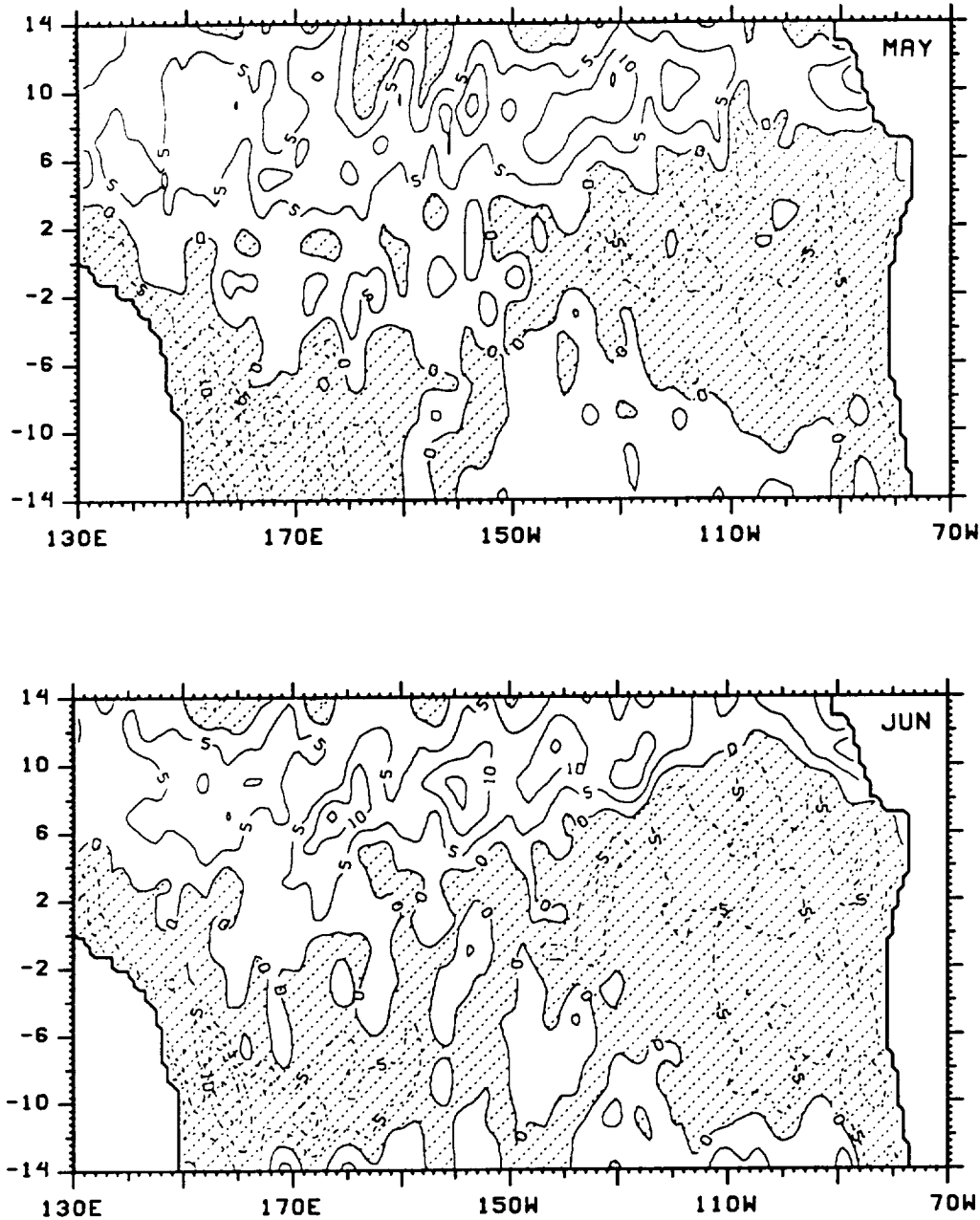


Figure A.2

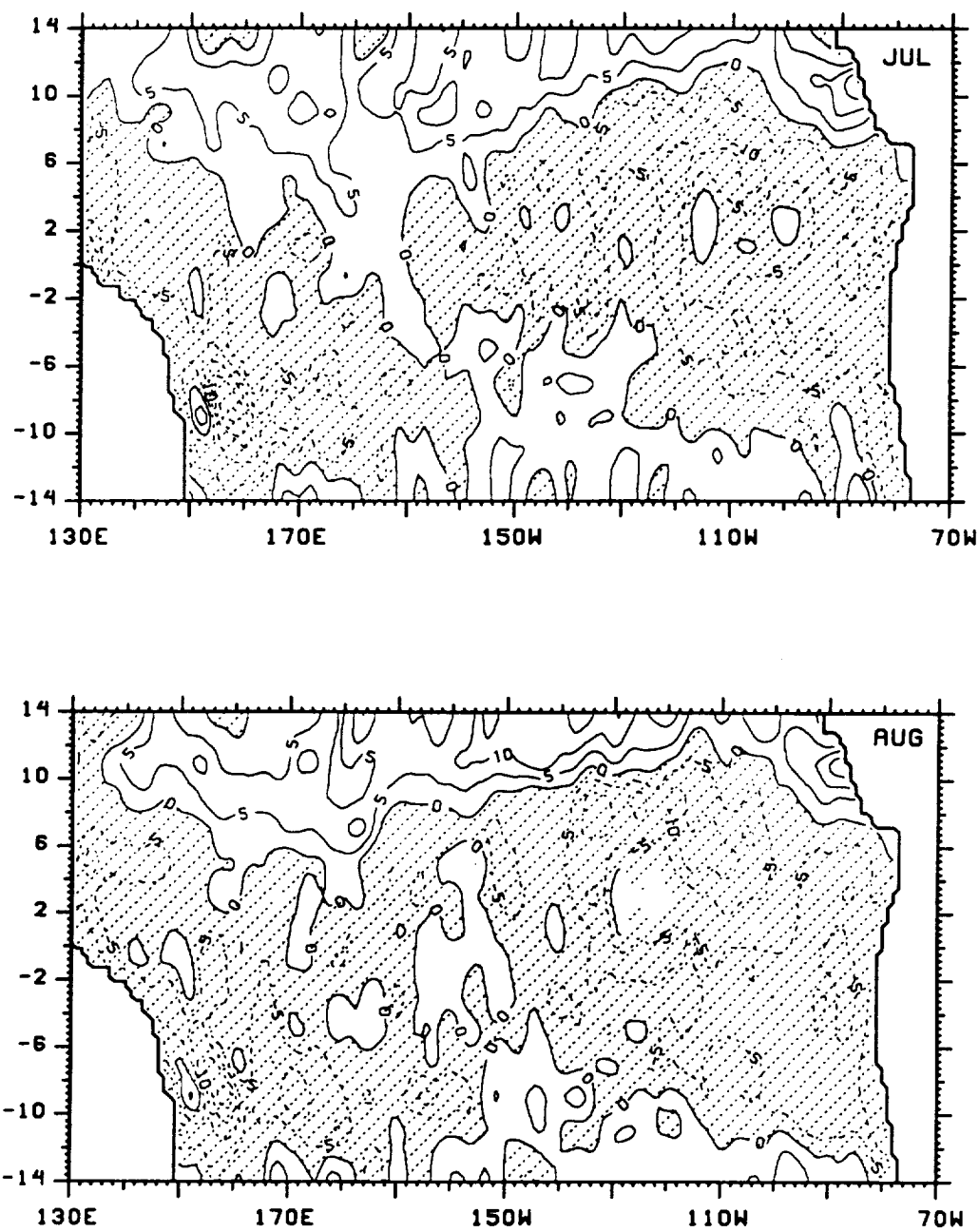


Figure A.2

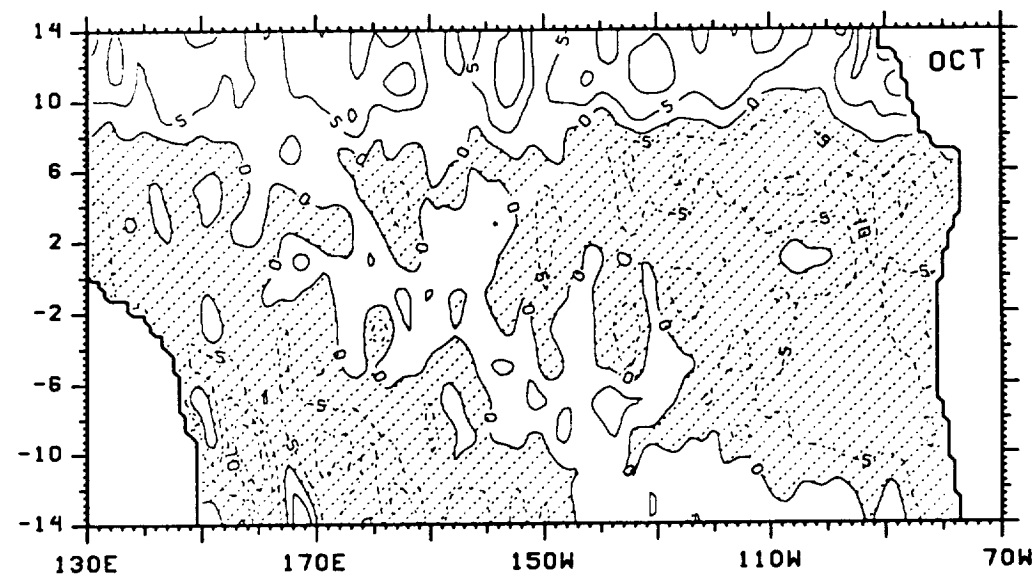
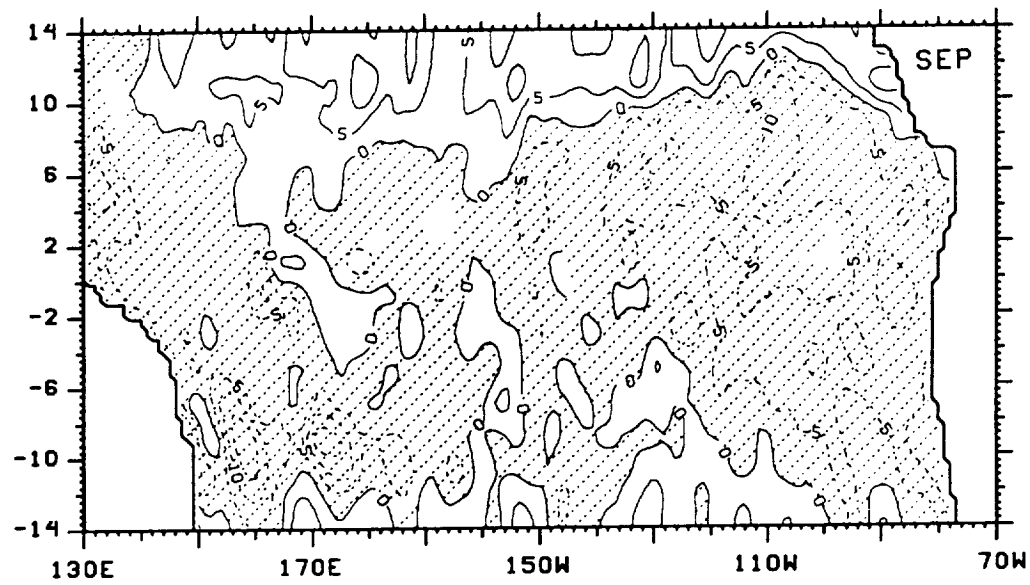


Figure A.2

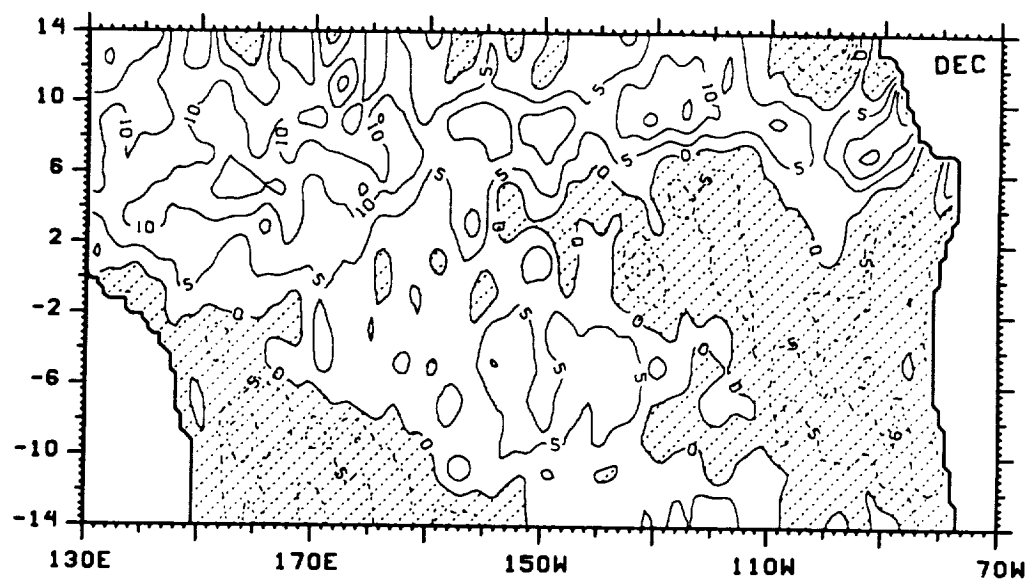
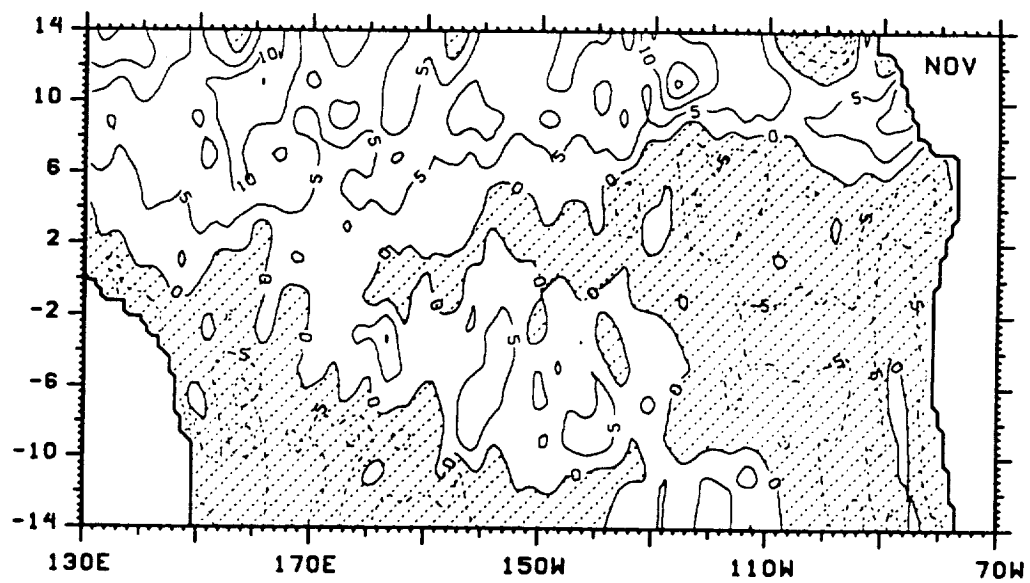


Figure A.2

Appendix B

B.1

Maps of monthly instantaneous sea surface temperature.

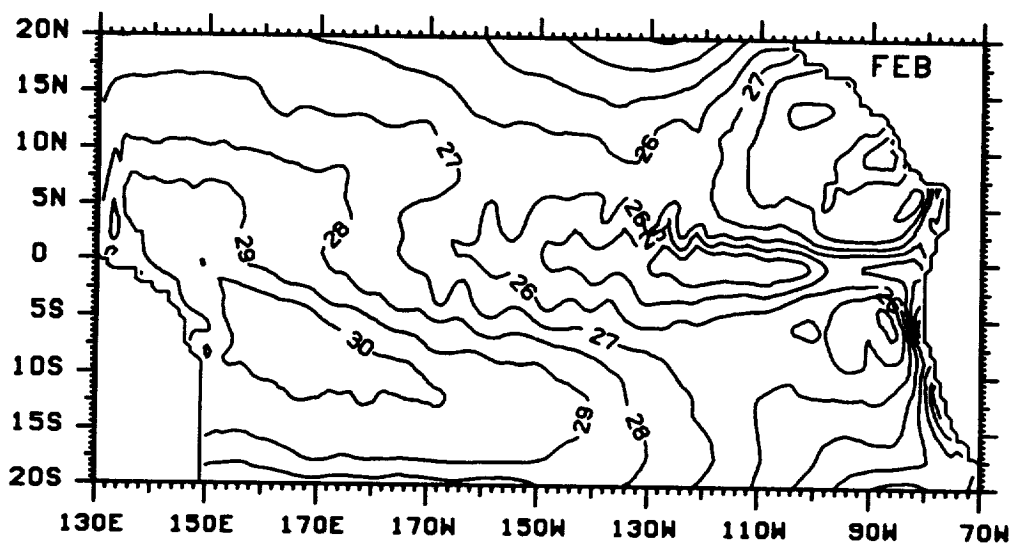
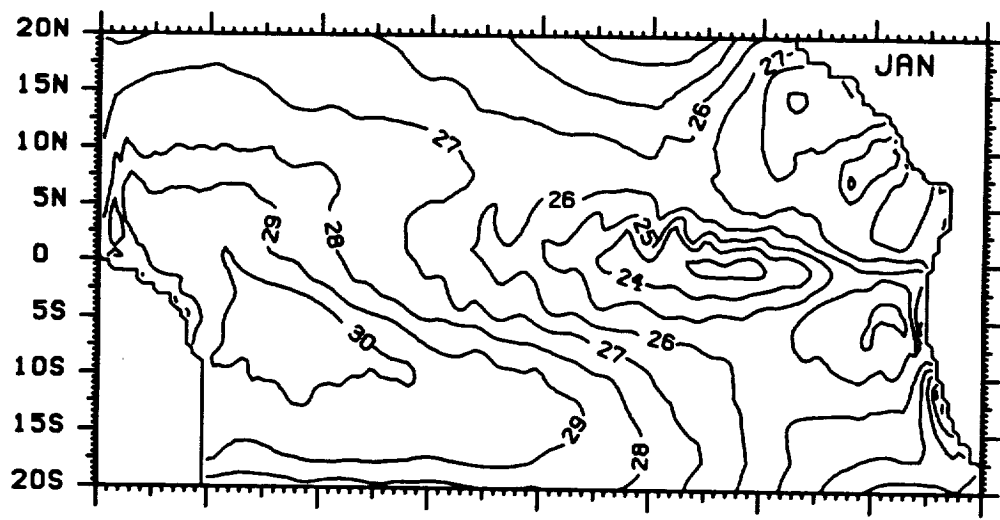


Figure B.1

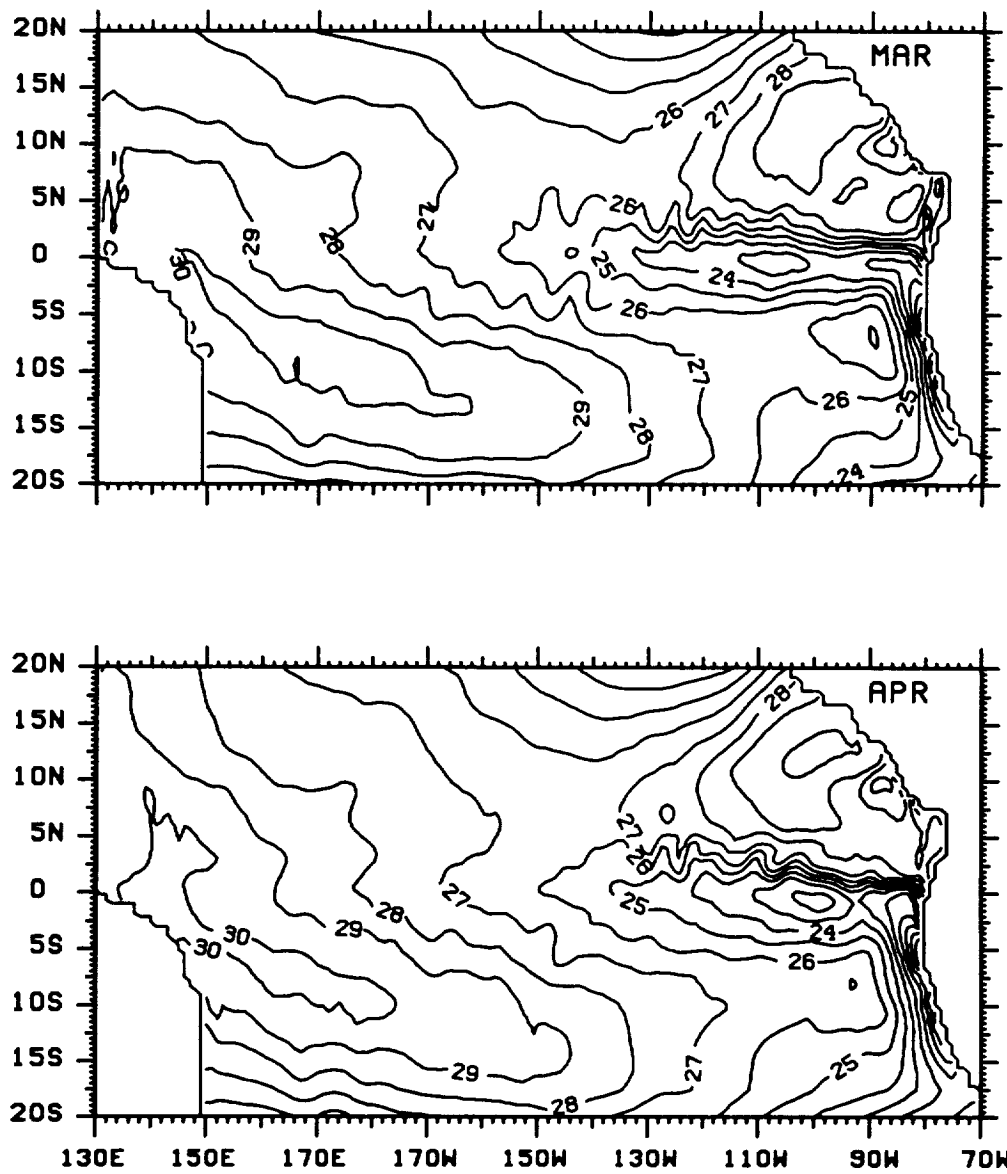


Figure B.1

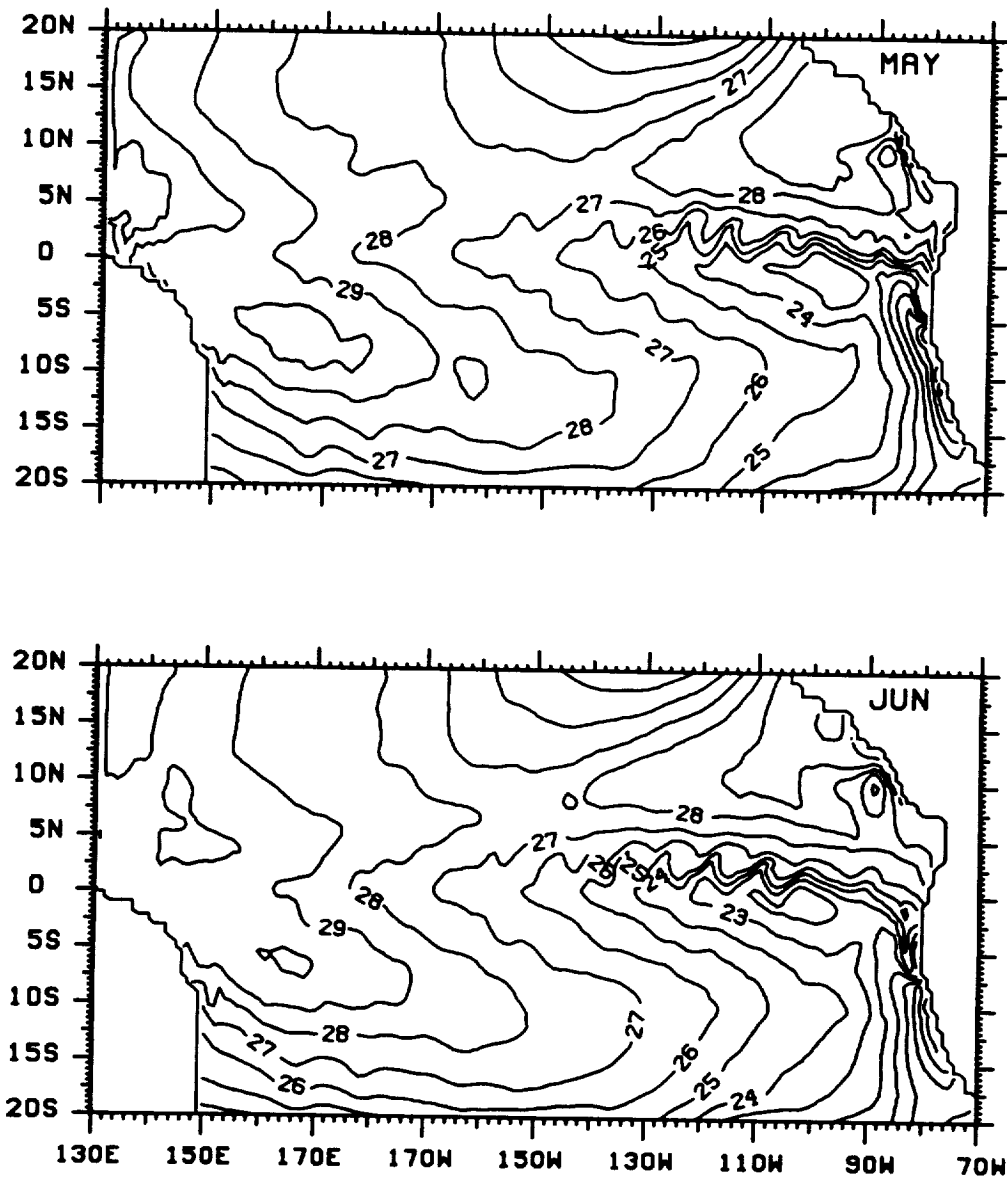


Figure B.1

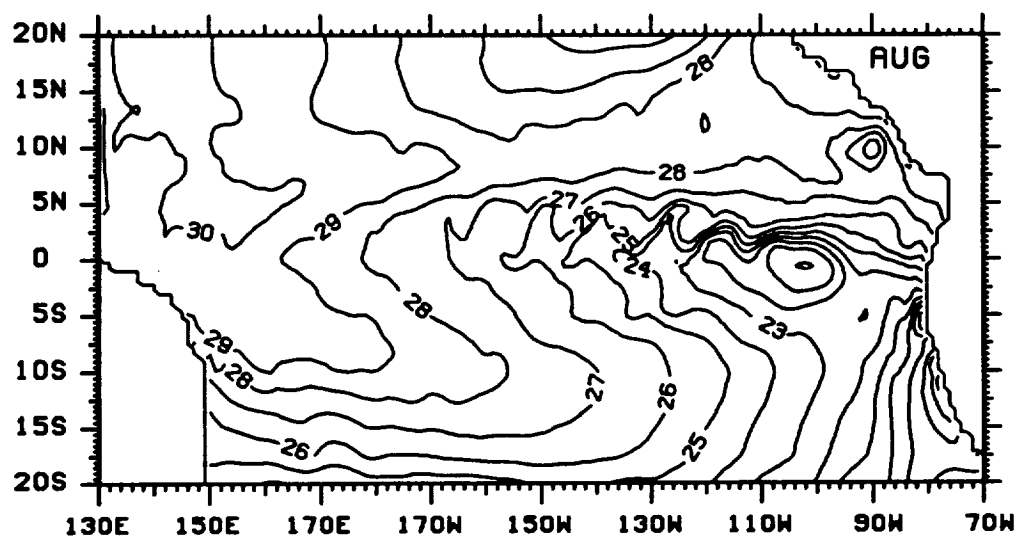
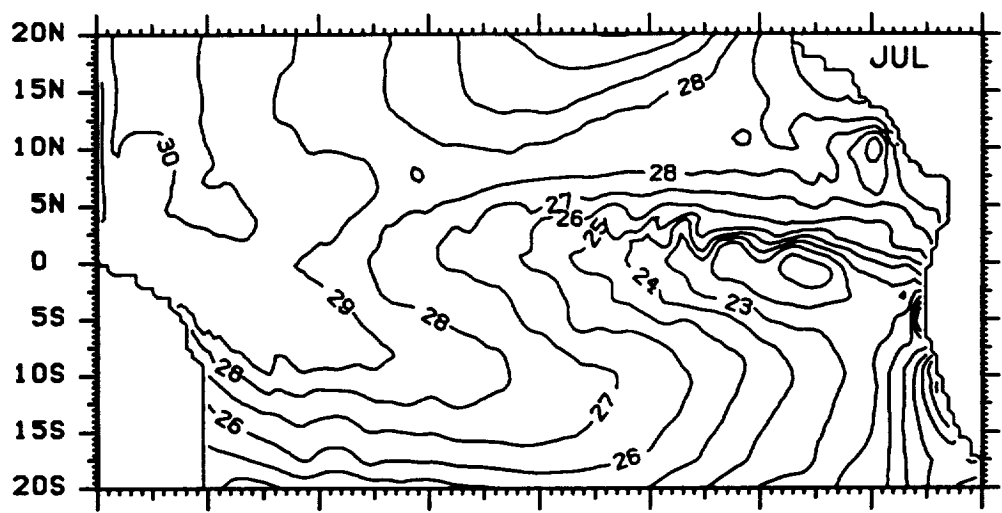


Figure B.1

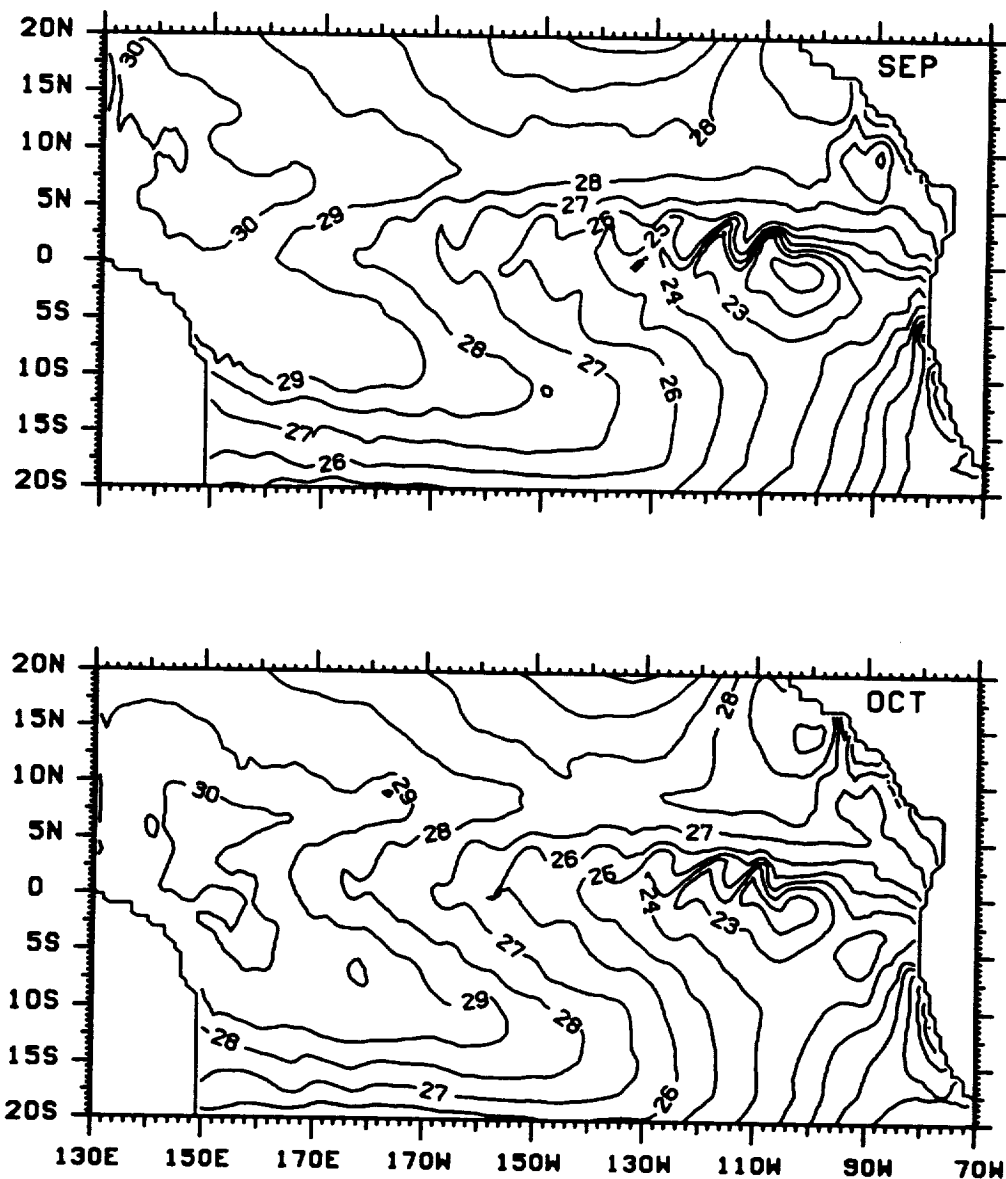


Figure B.1

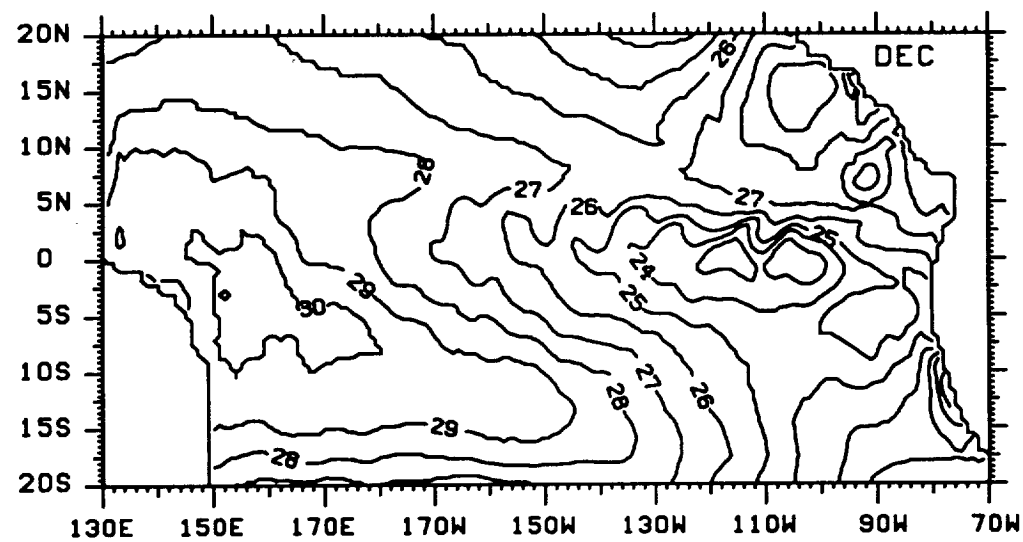
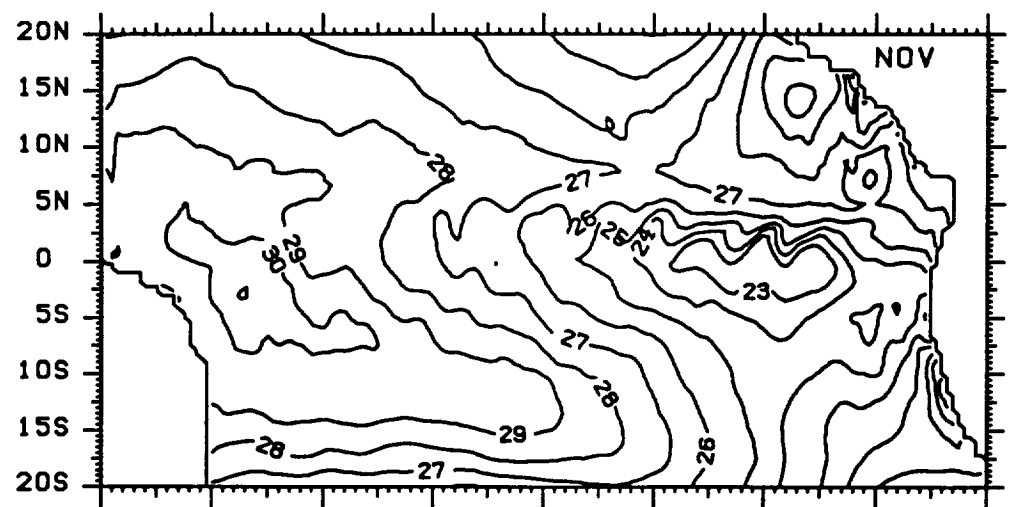


Figure B.1

B.2

Maps of monthly mean sea surface temperature.

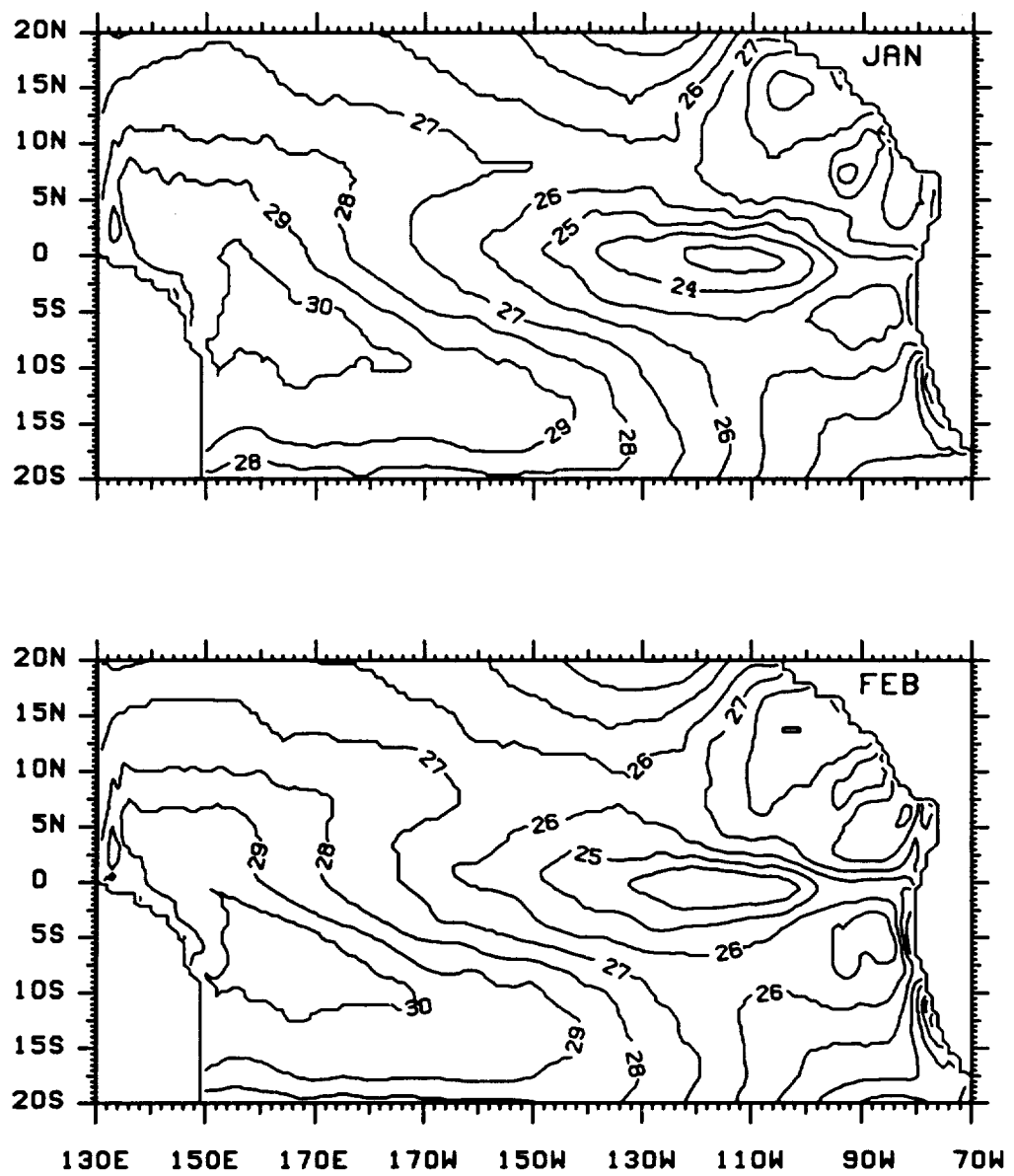


Figure B.2

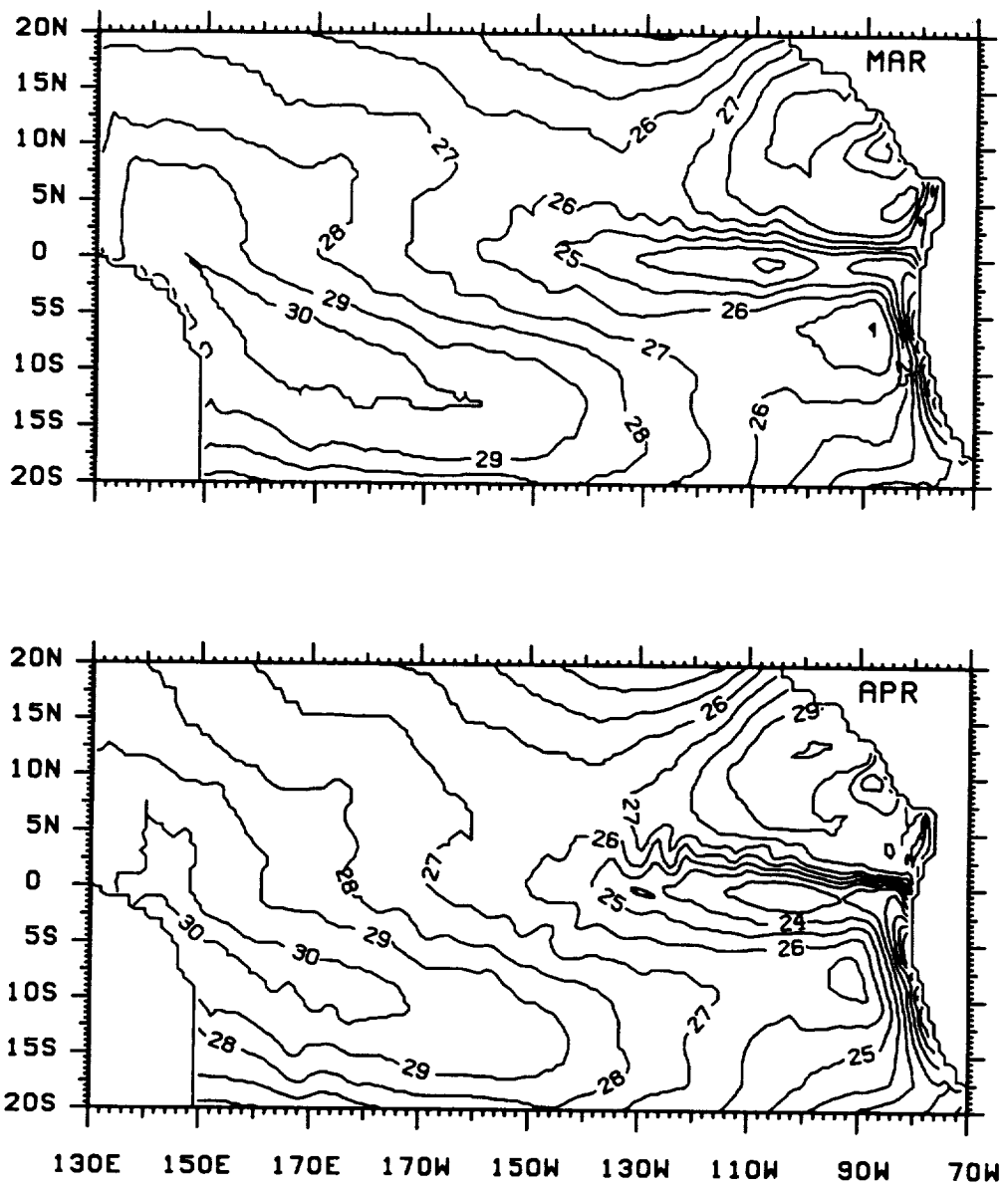


Figure B.2

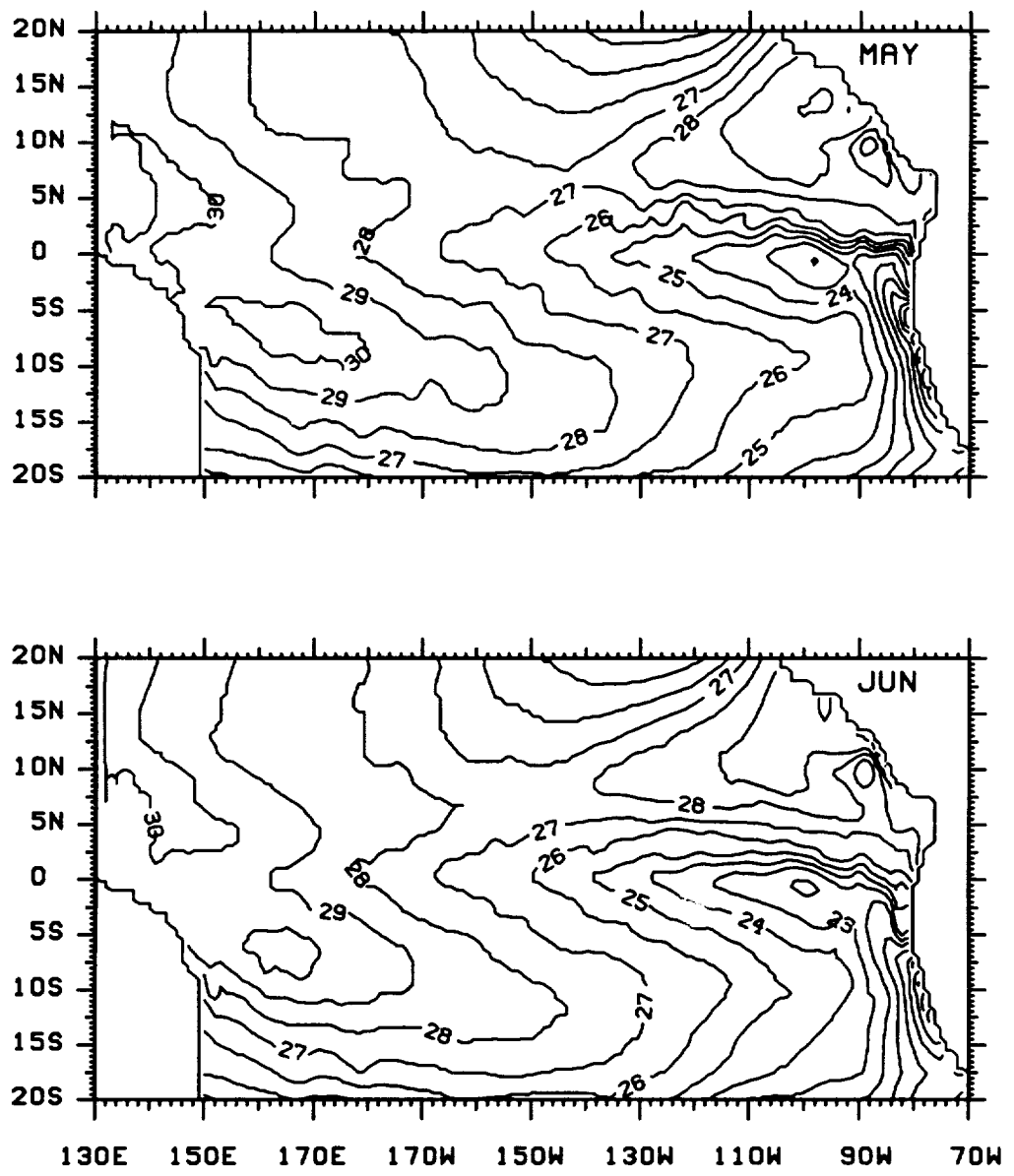


Figure B.2

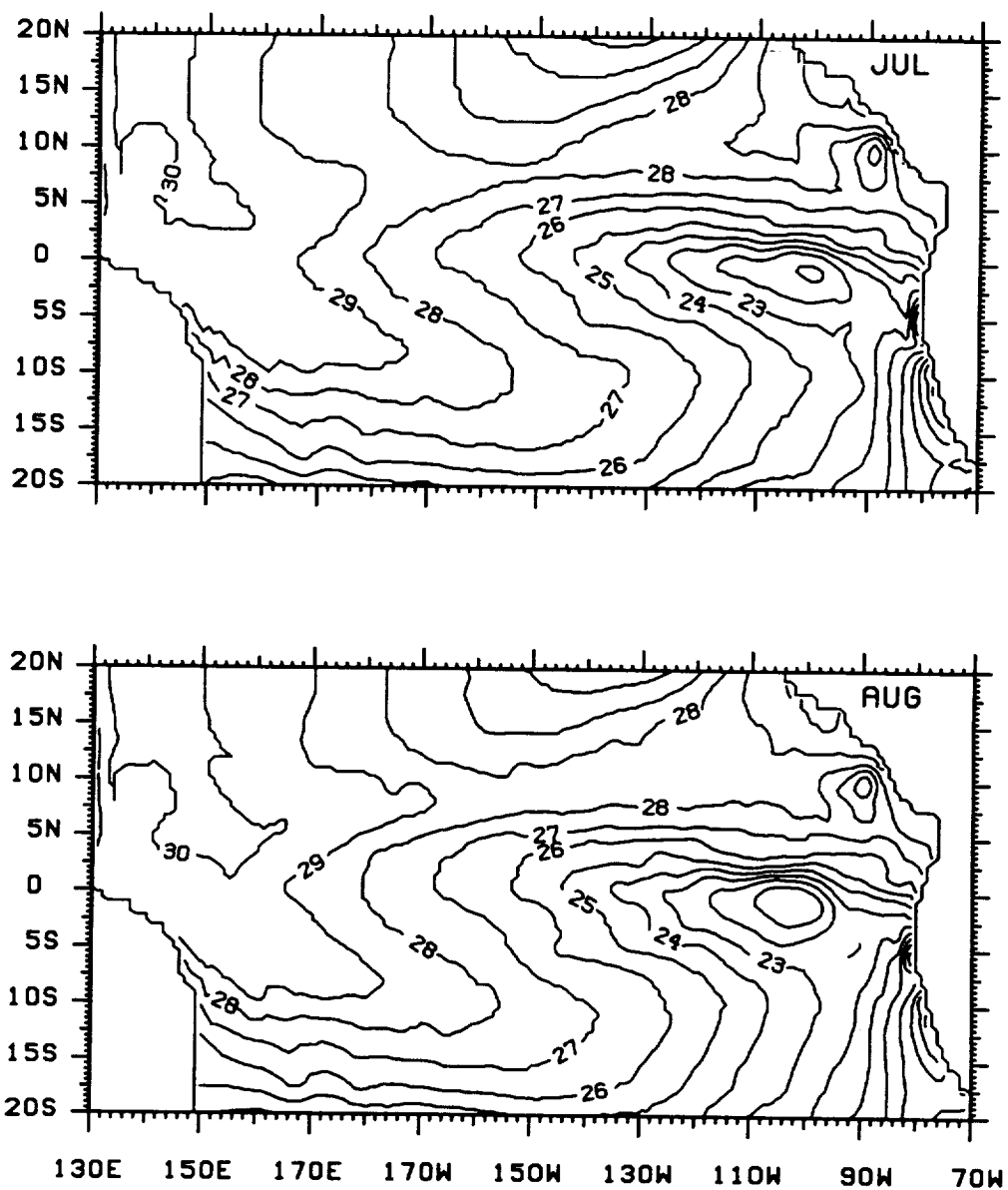


Figure B.2

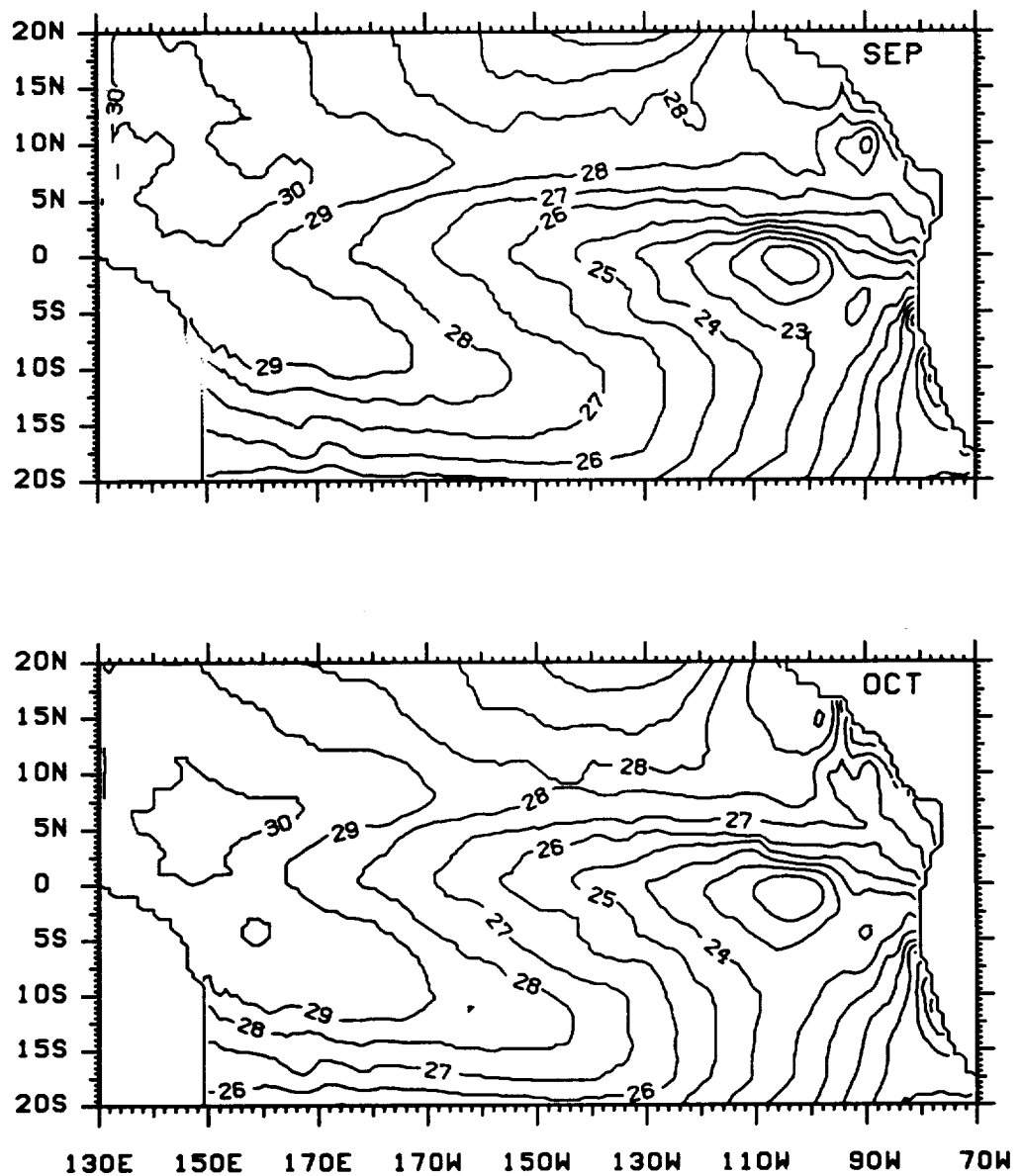


Figure B.2

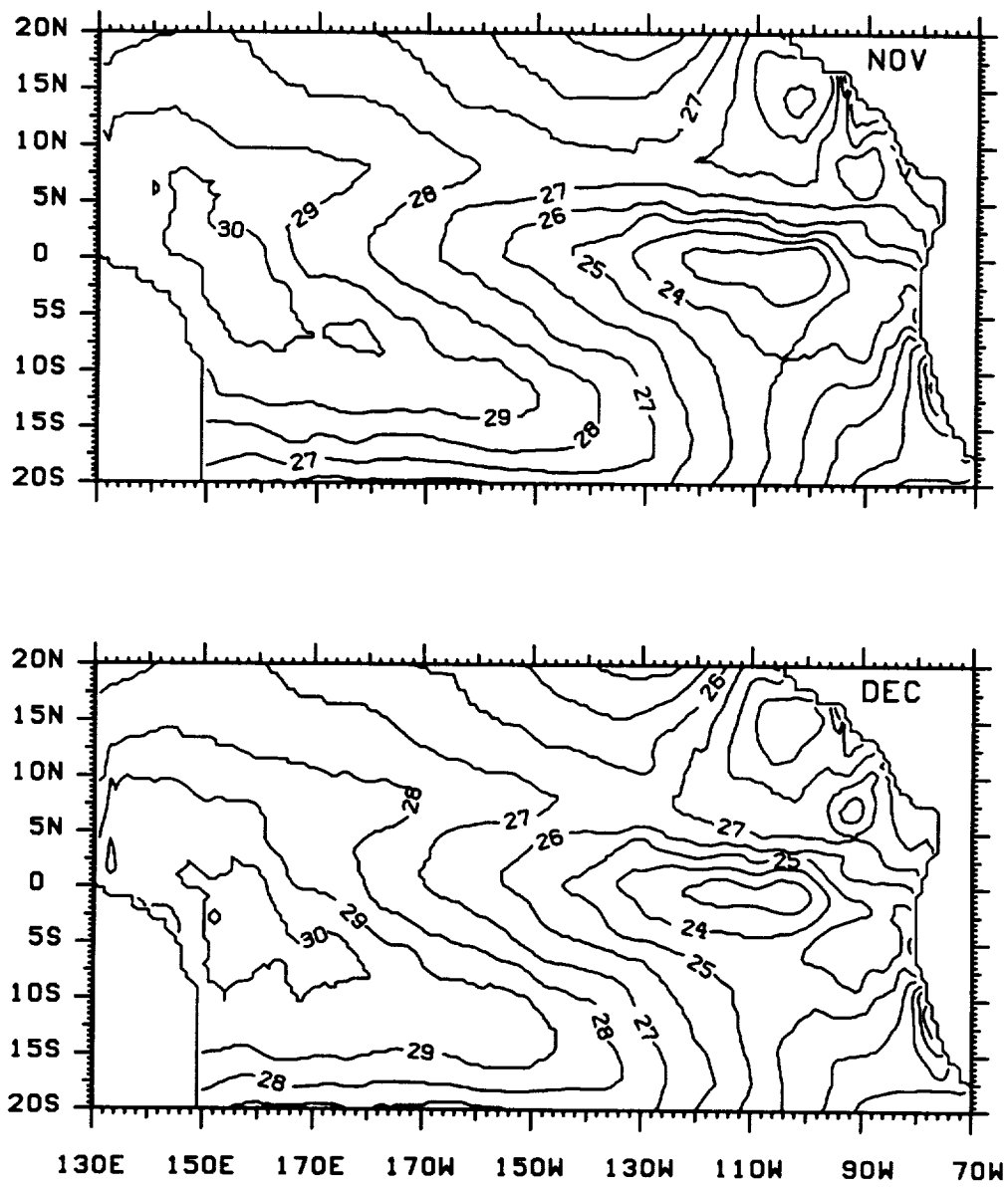


Figure B.2

B.3

Maps of monthly mean surface currents. The zonal component is contoured with an interval of 50 cm s^{-1} and negative (westward) contours are dashed.

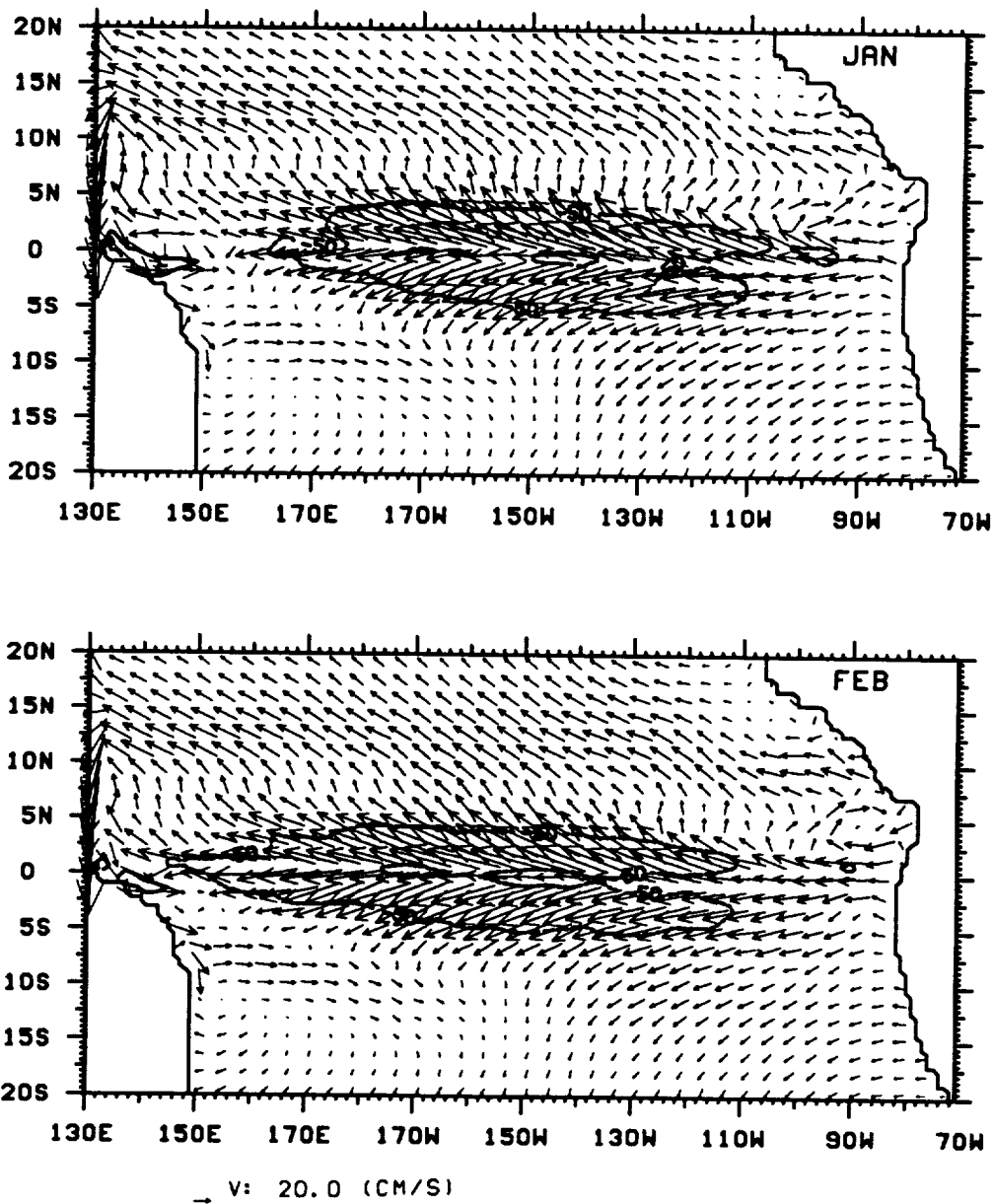


Figure B.3

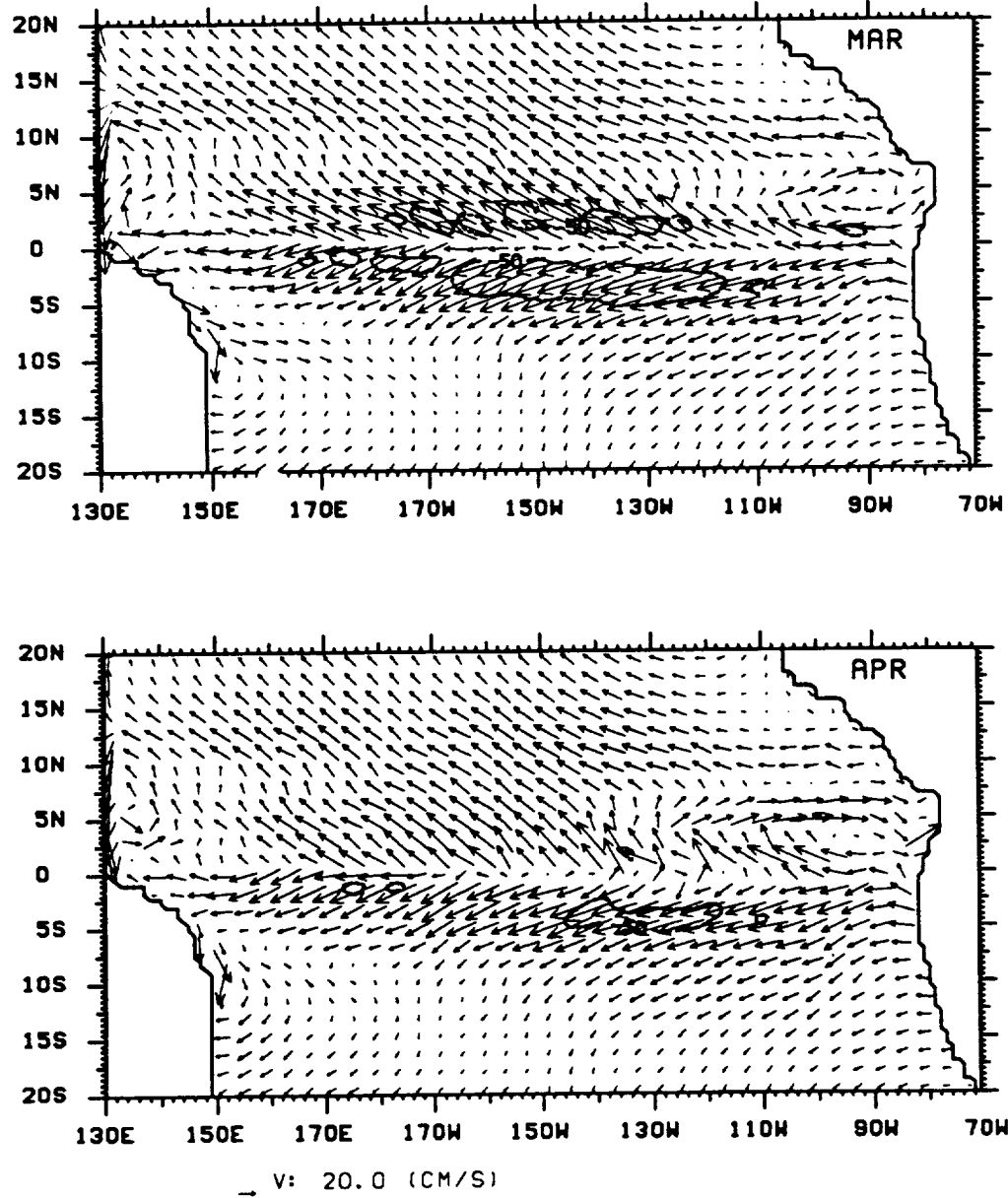


Figure B.3

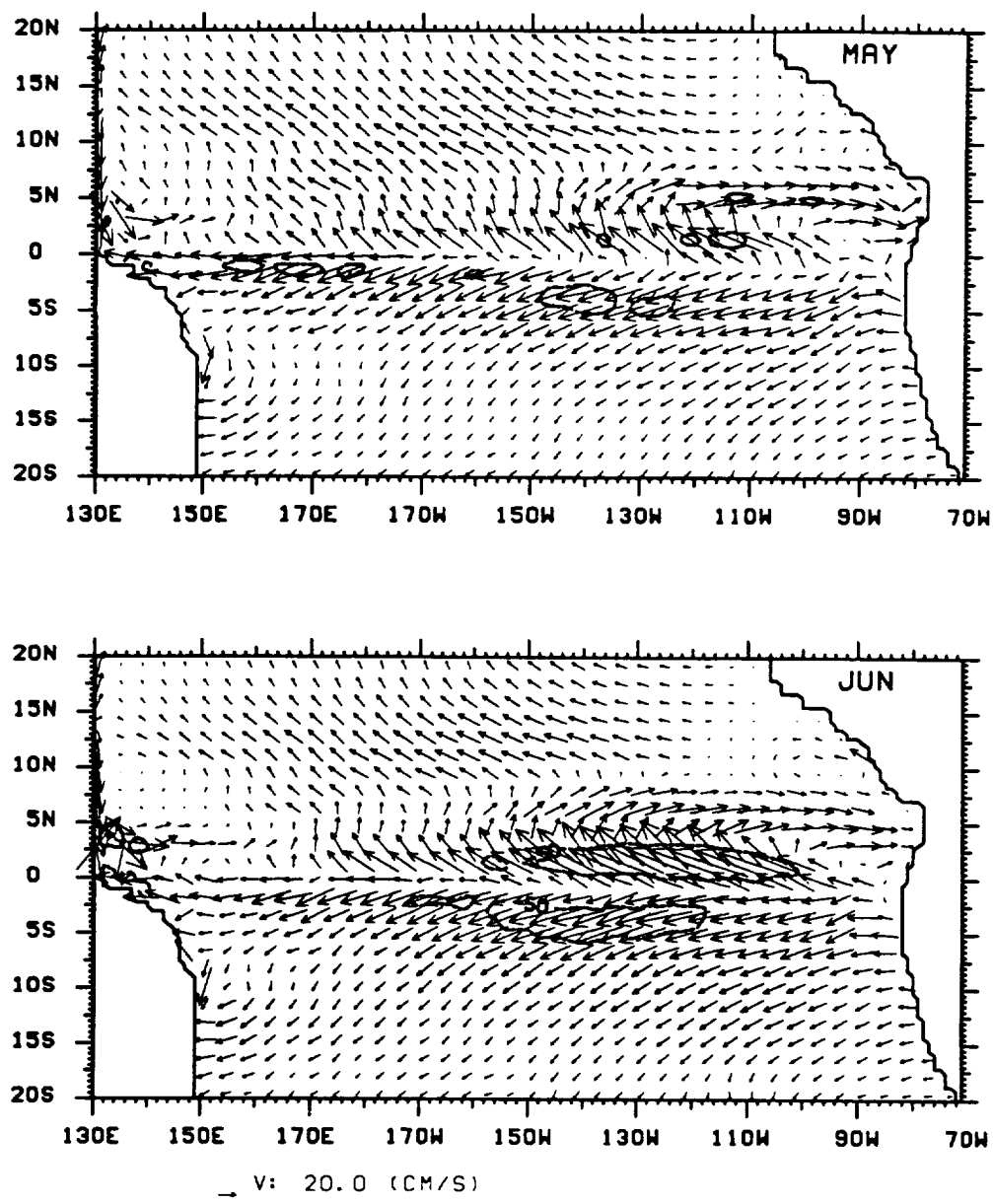


Figure B.3

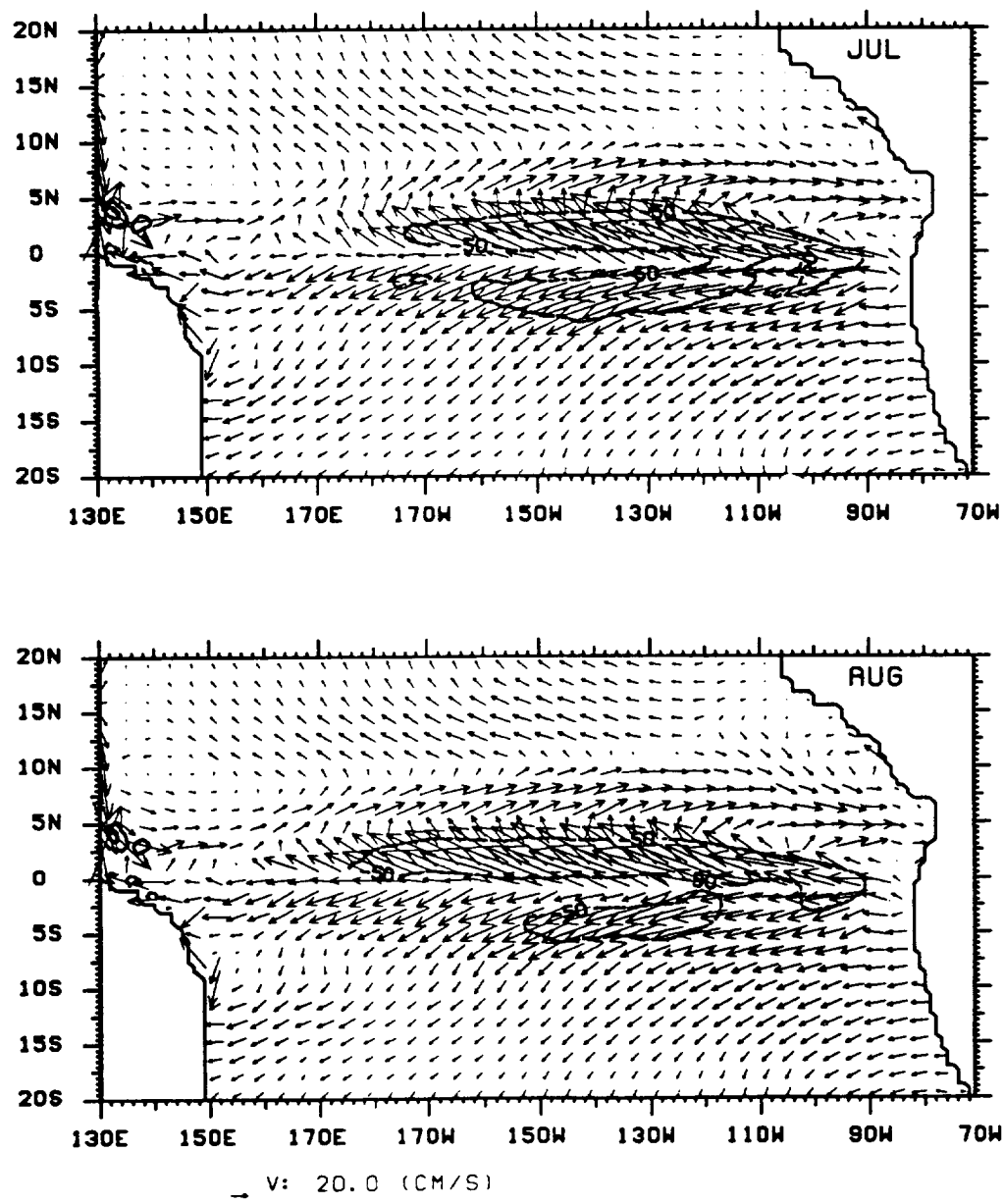


Figure B.3

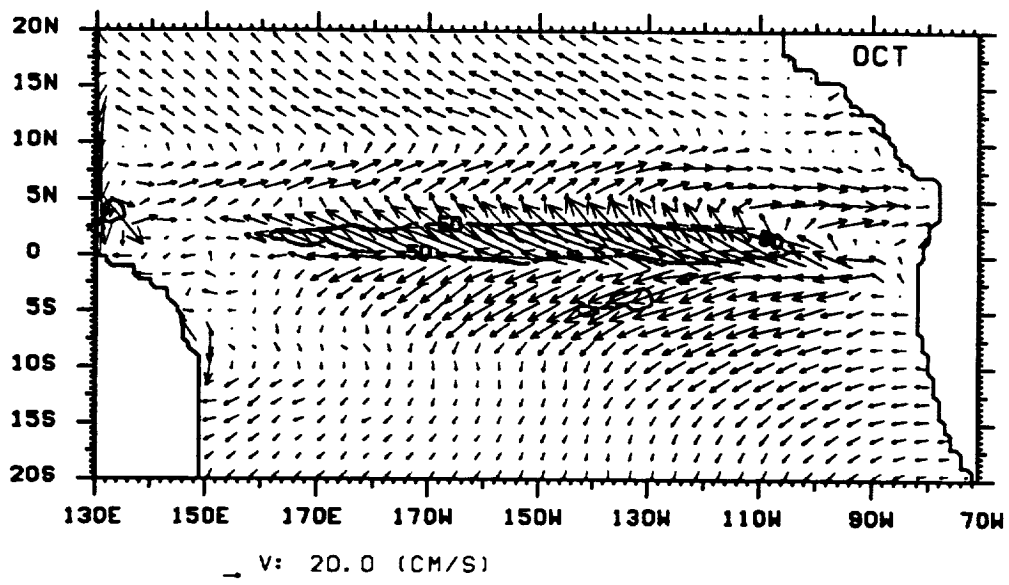
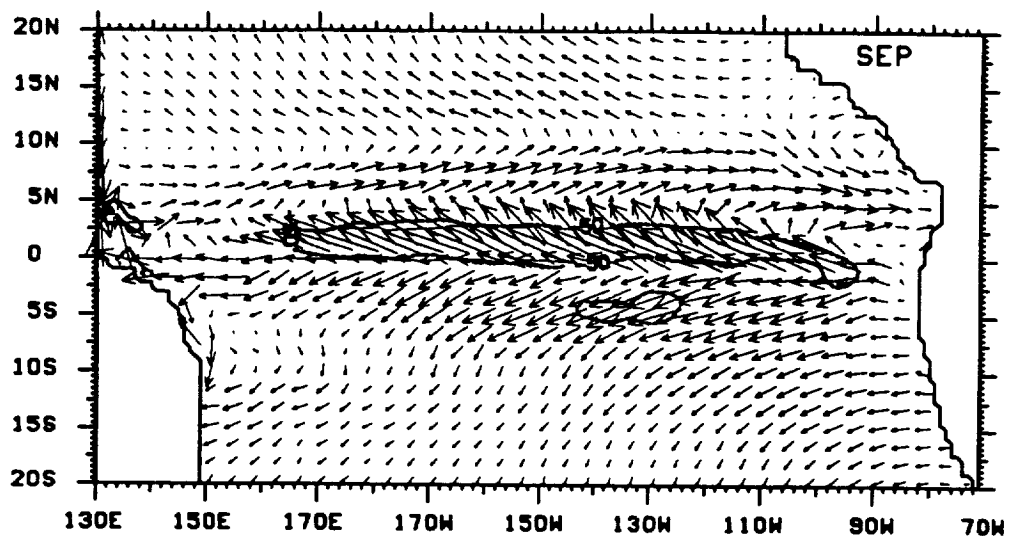


Figure B.3

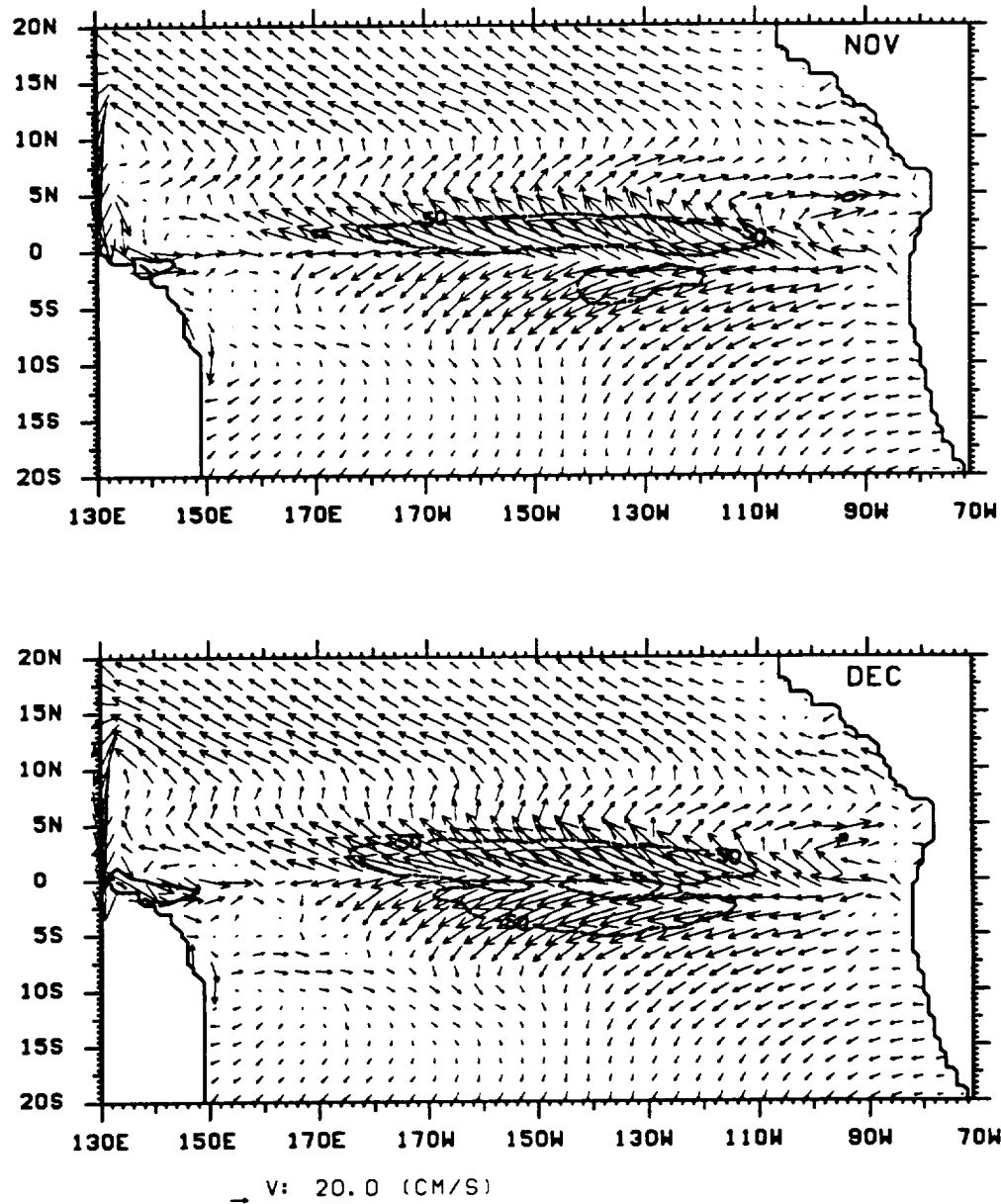


Figure B.3

Appendix C

**Latitude-depth sections of monthly mean model zonal and meridional currents,
zonal geostrophic current, temperature and dynamic height
along 150°E, 180°, 160°W, 140°W, 125°W and 110°W**

C.1

Zonal current

Contour interval is 10 cm s⁻¹ and negative currents are shaded

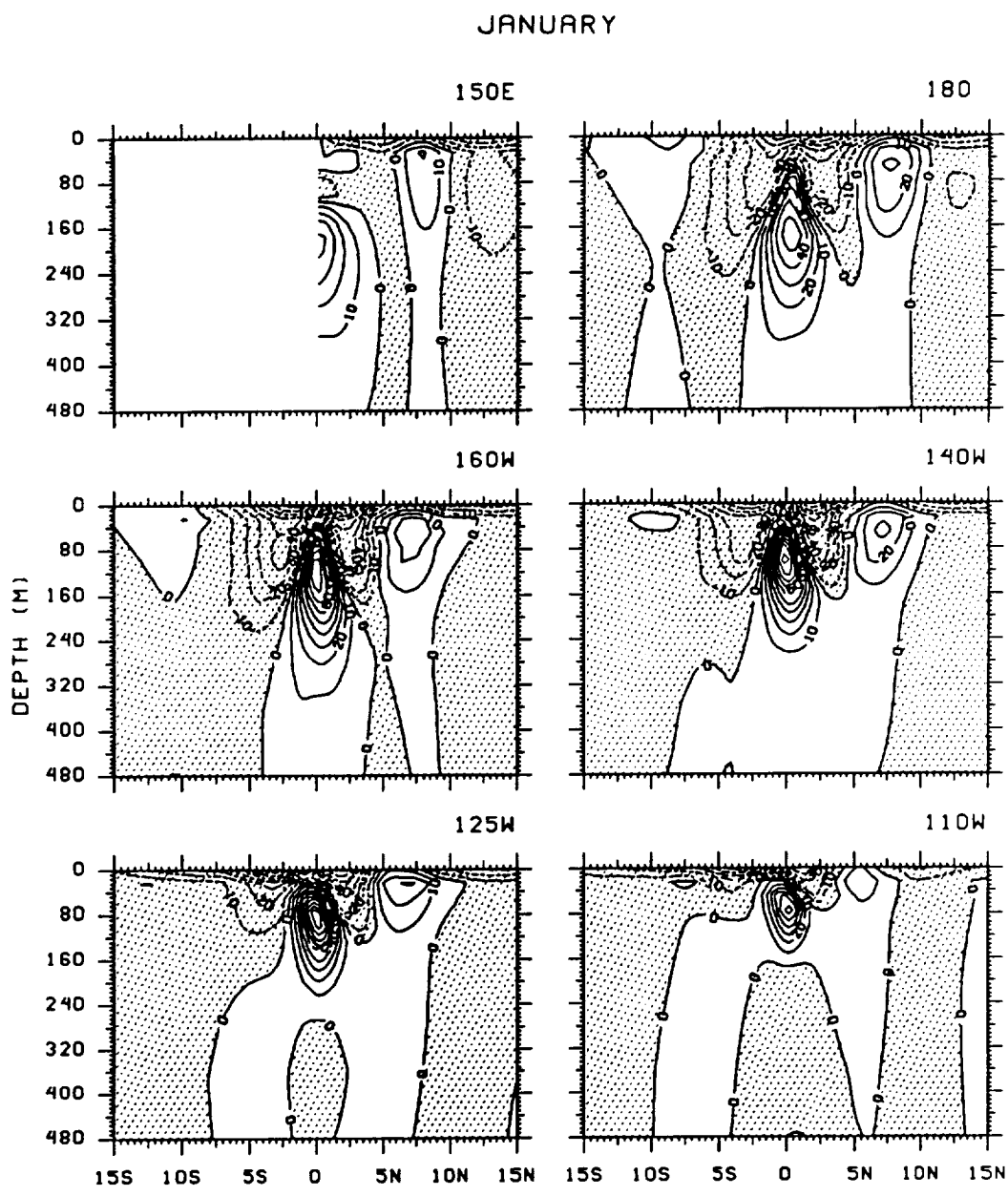


Figure C.1

FEBRUARY

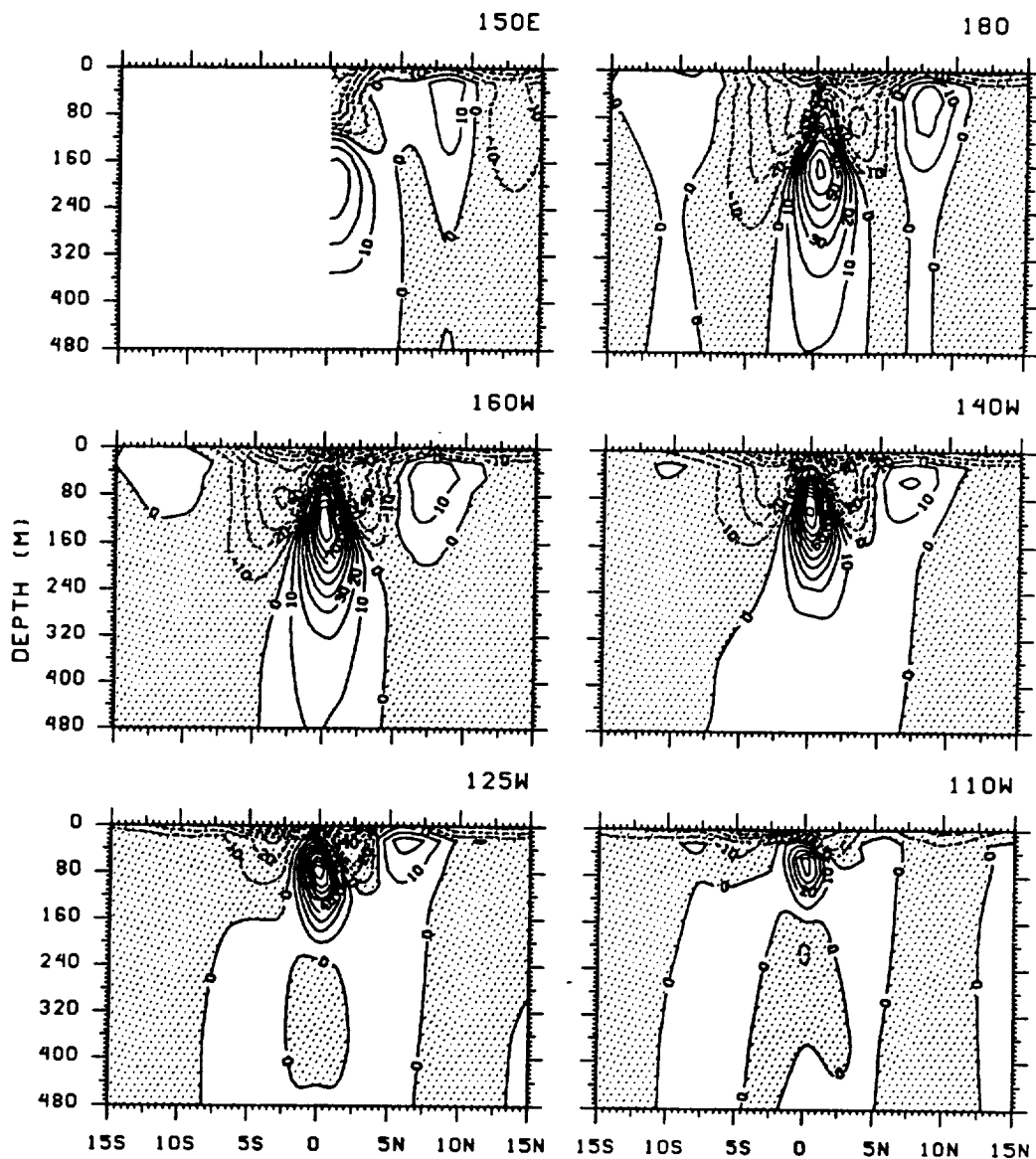


Figure C.1

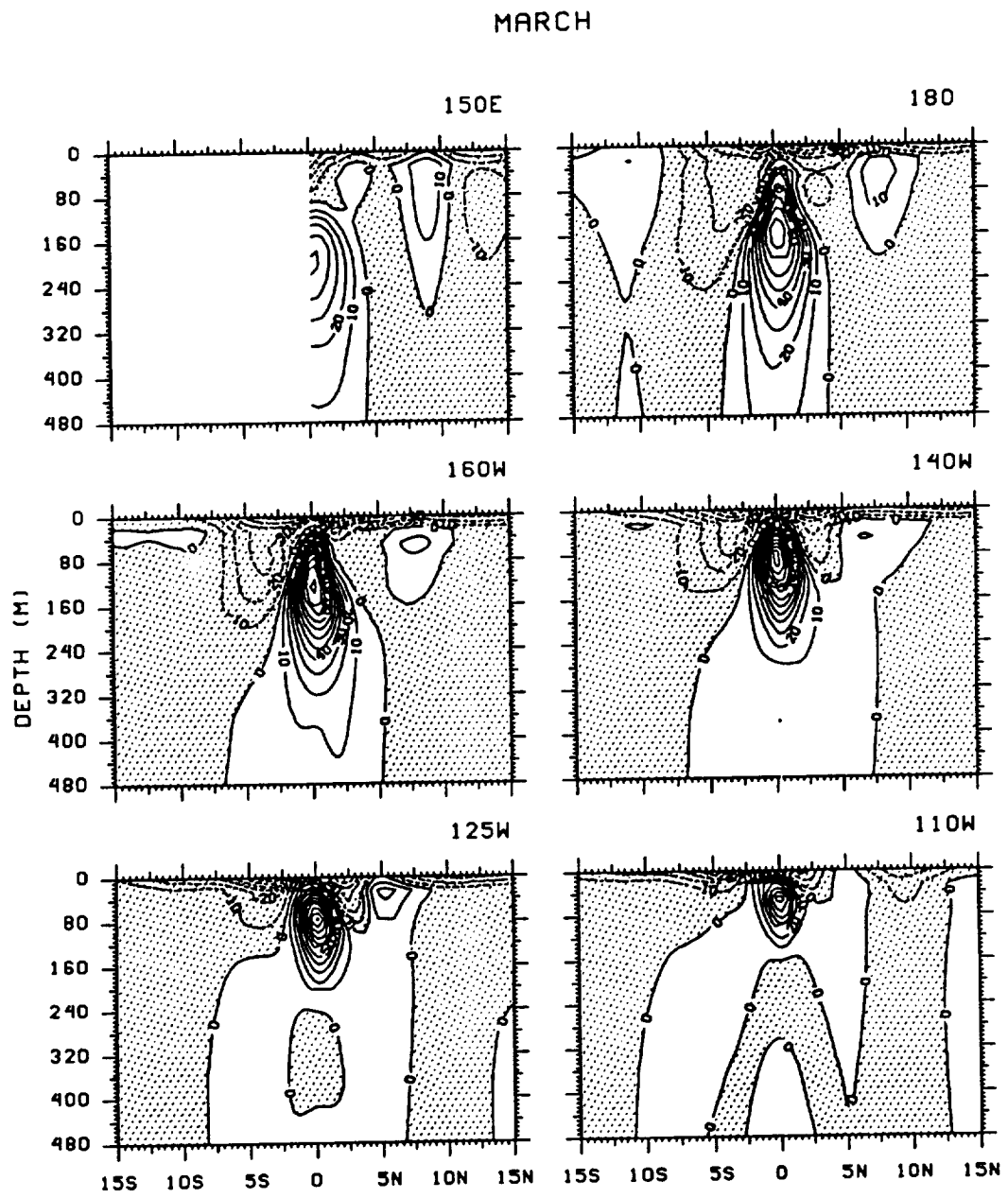


Figure C.1

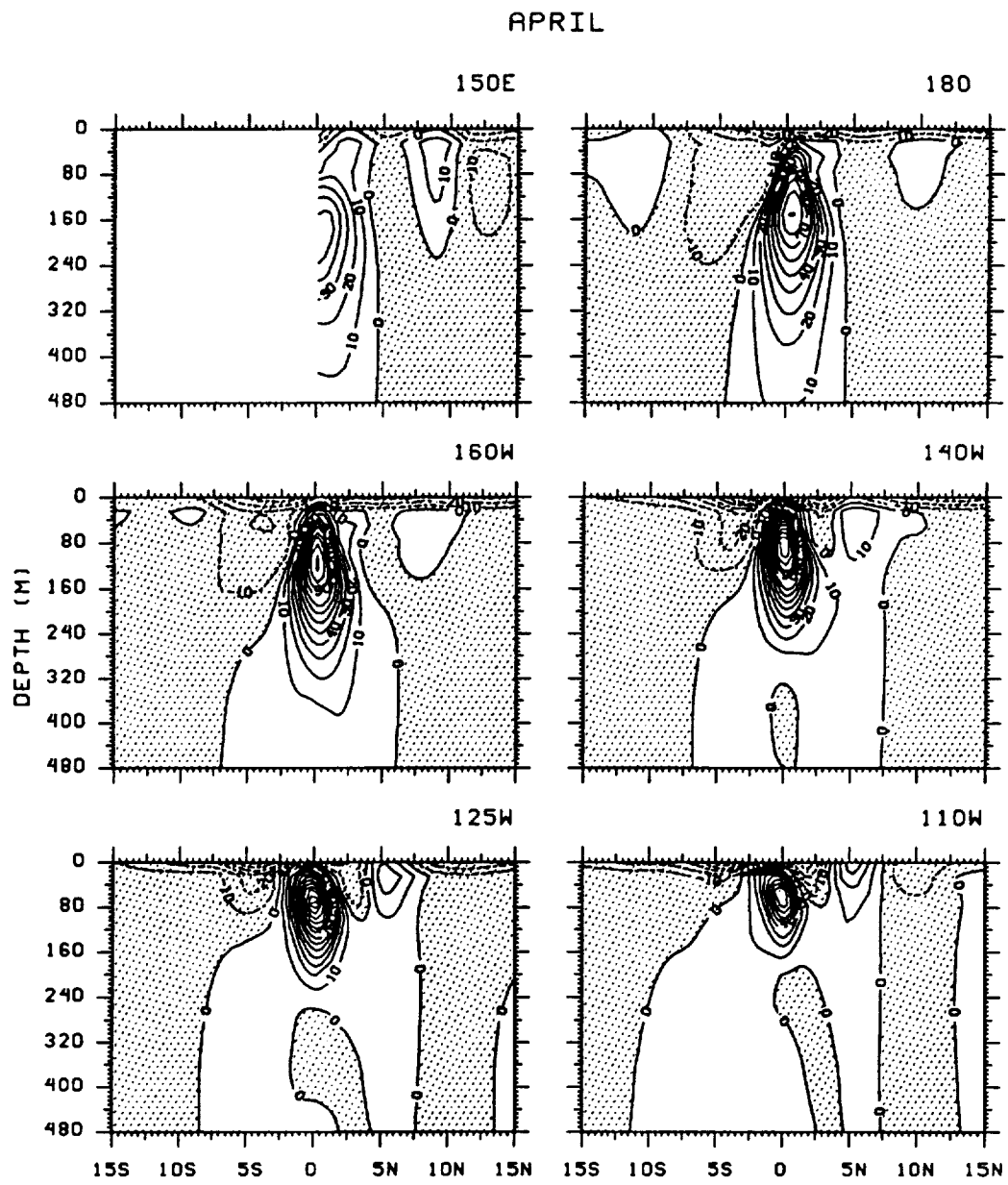


Figure C.1

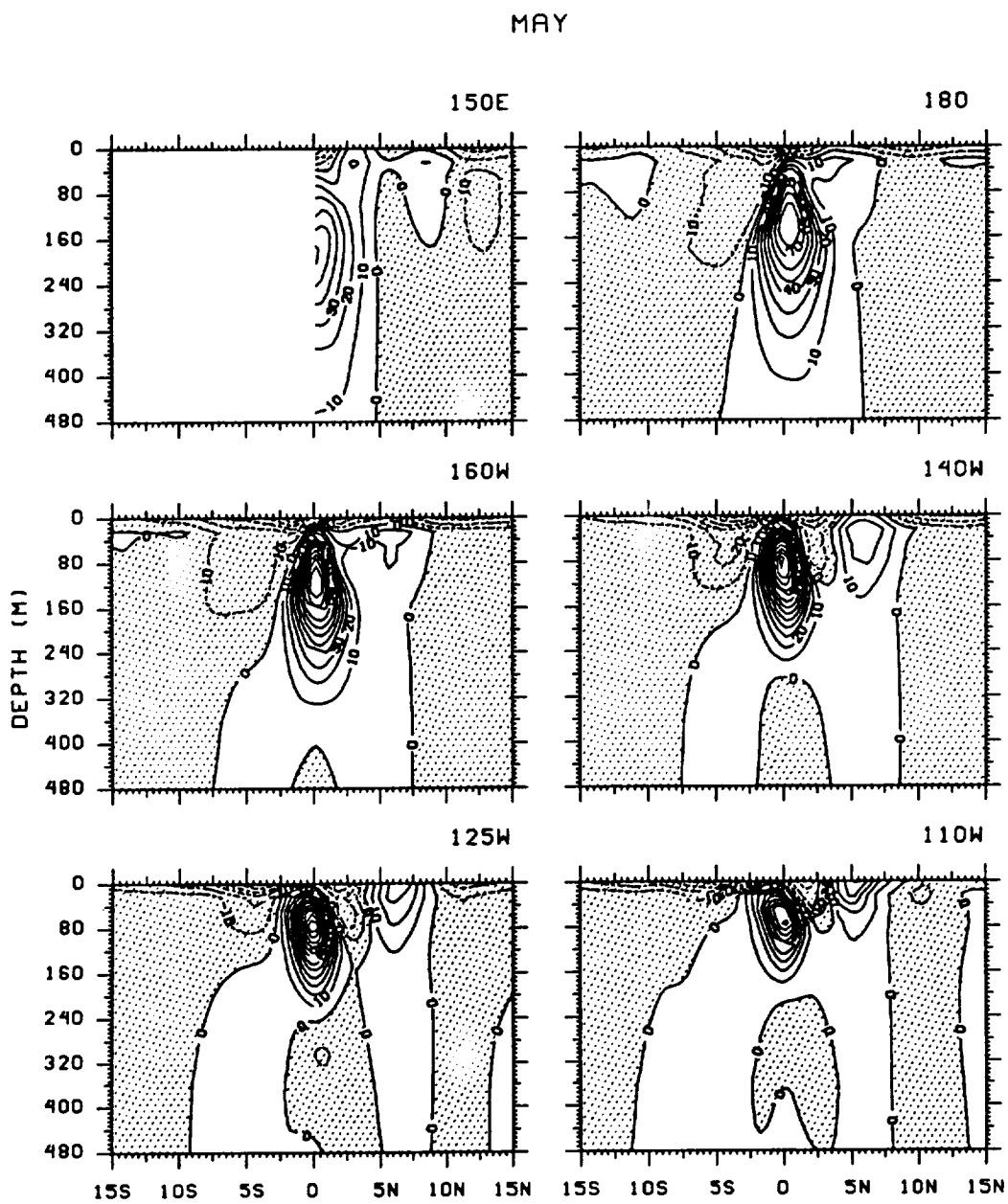


Figure C.1

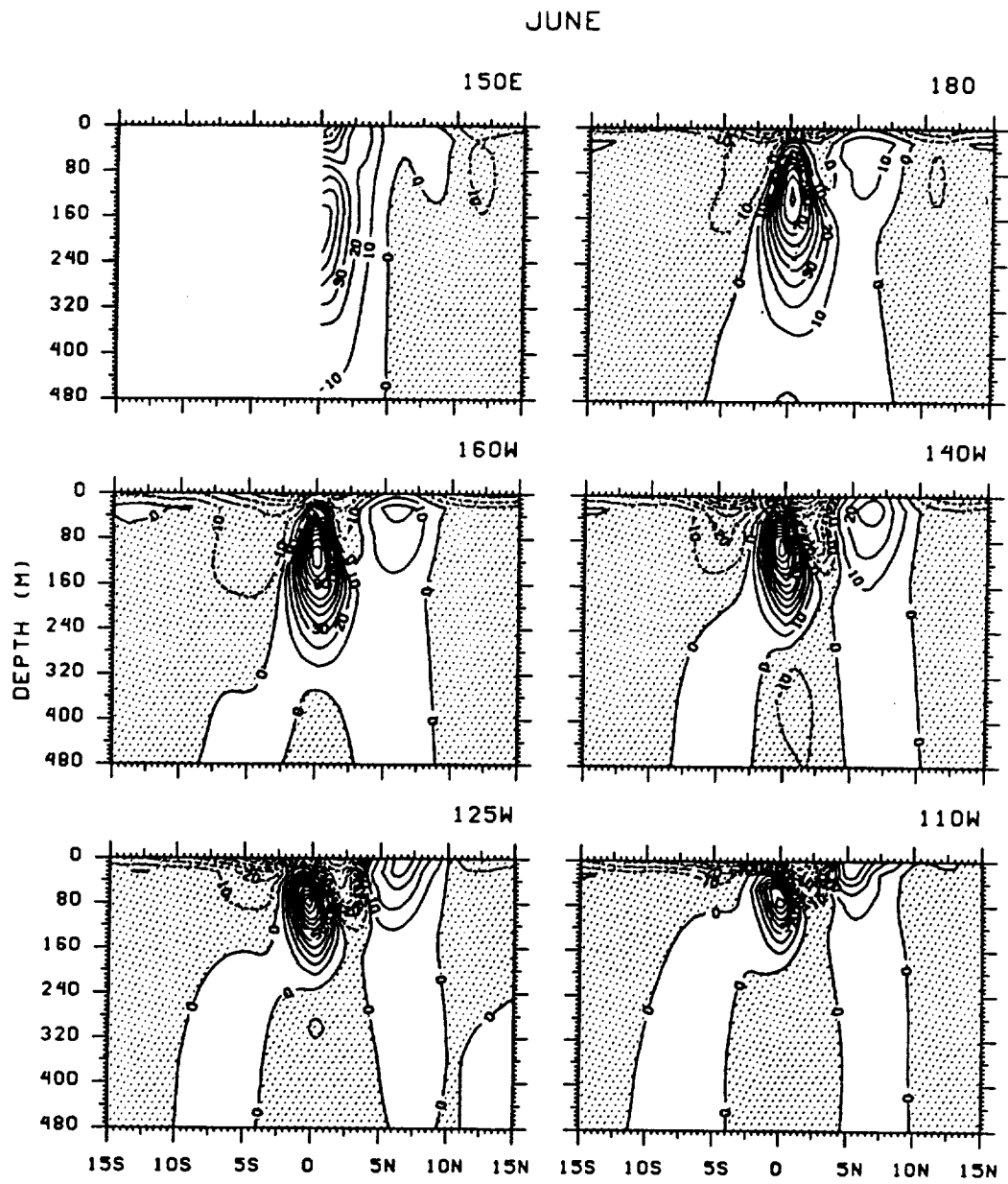


Figure C.1

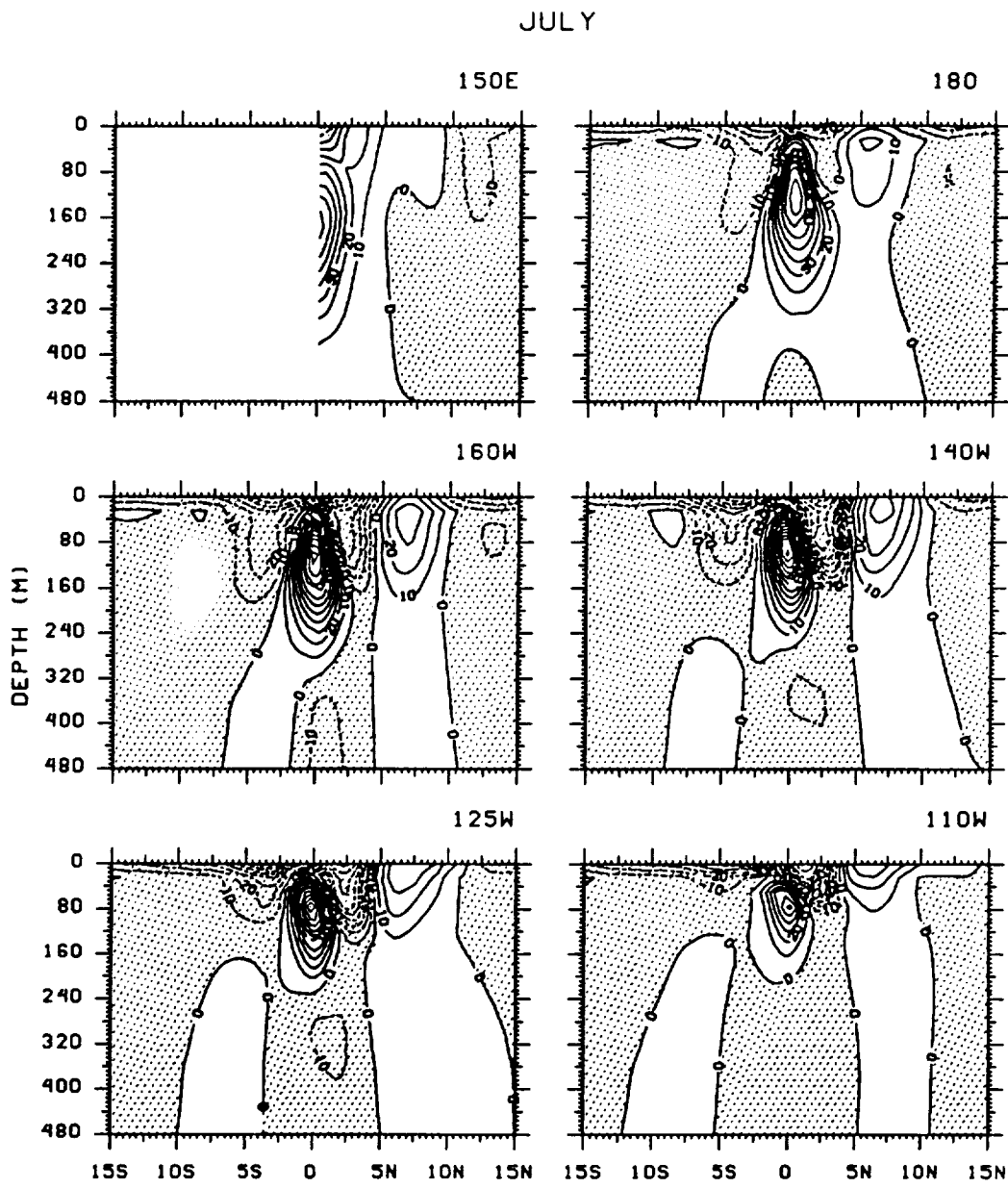


Figure C.1

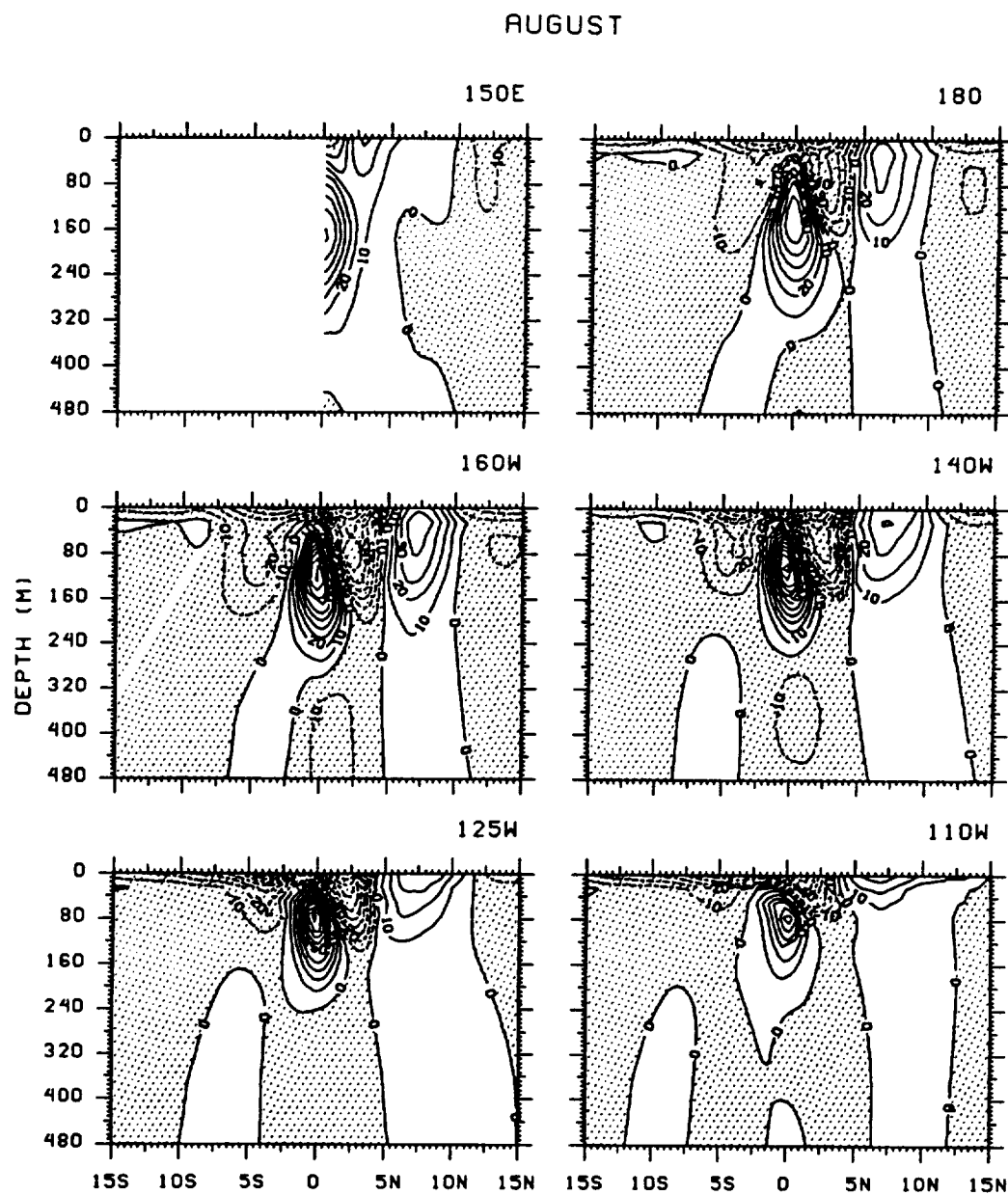


Figure C.1

SEPTEMBER

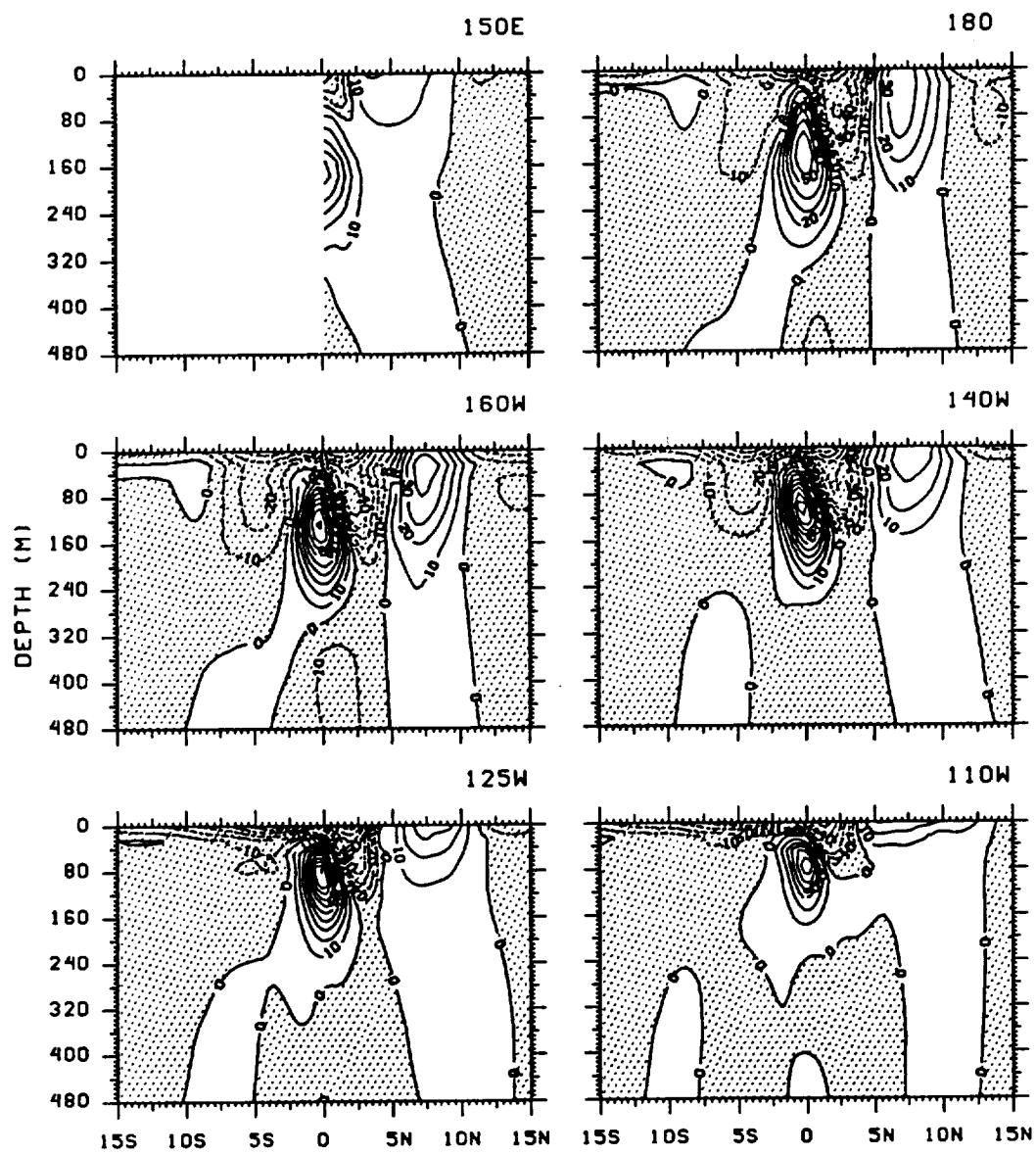


Figure C.1

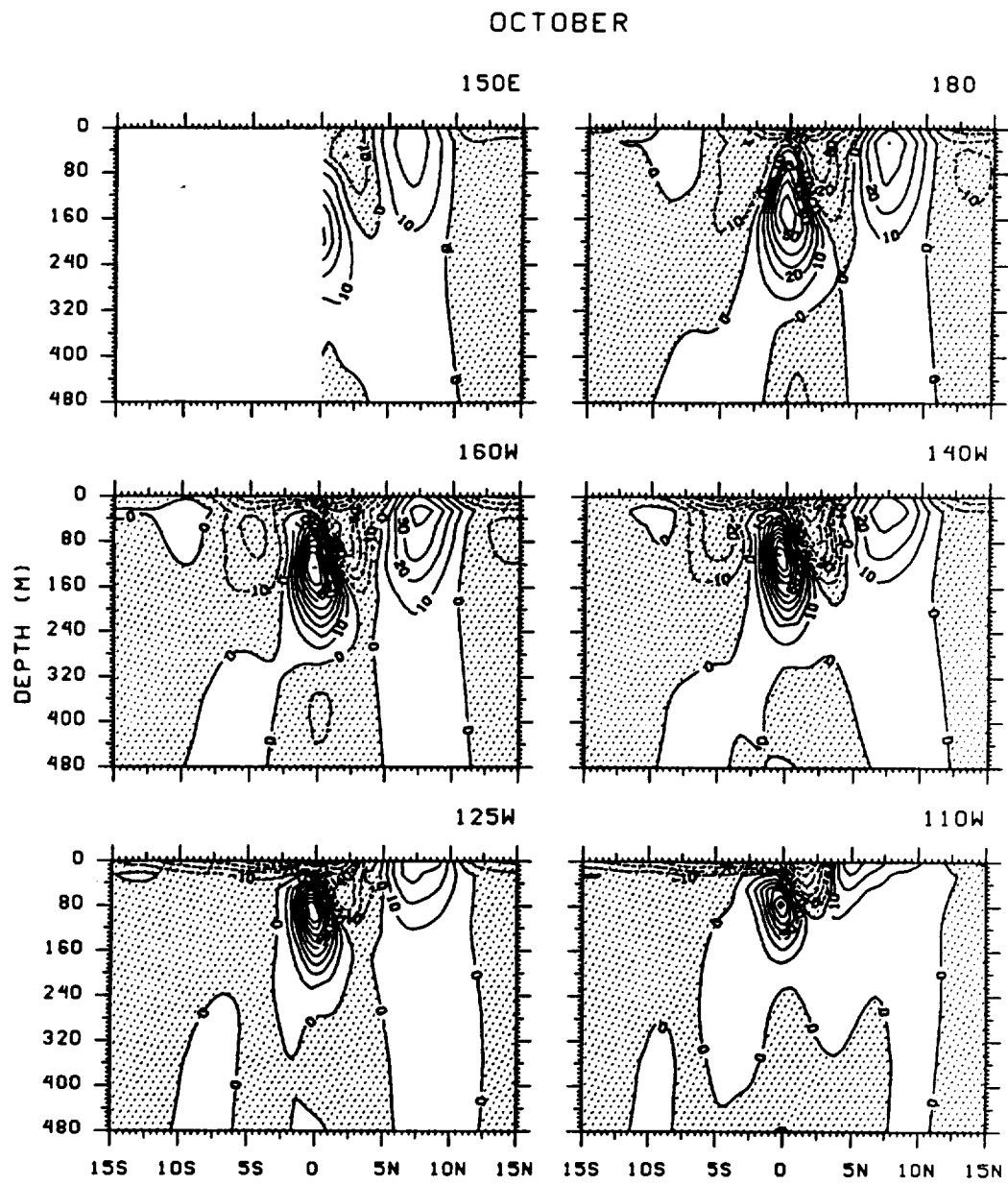


Figure C.1

NOVEMBER

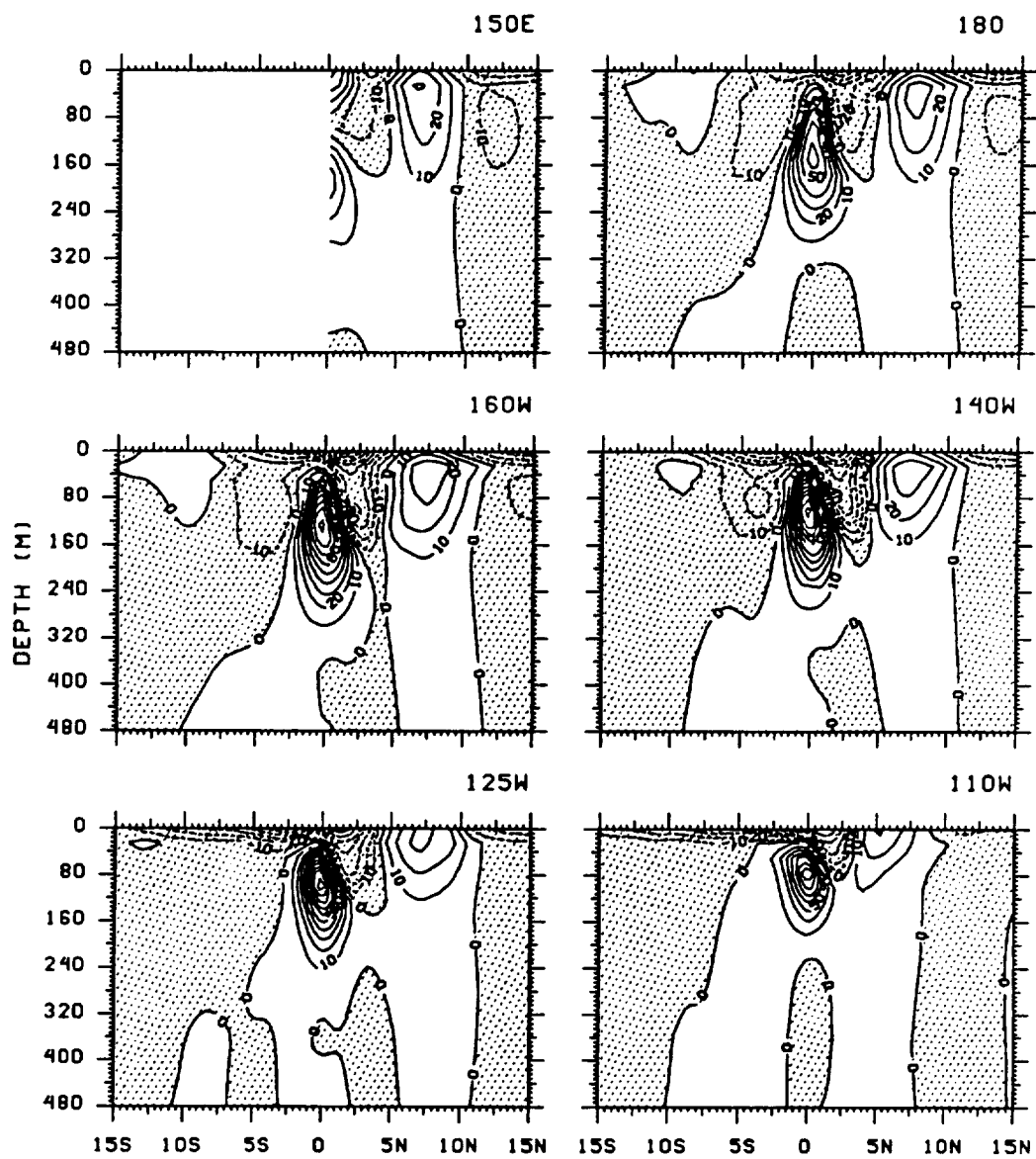


Figure C.1

DECEMBER

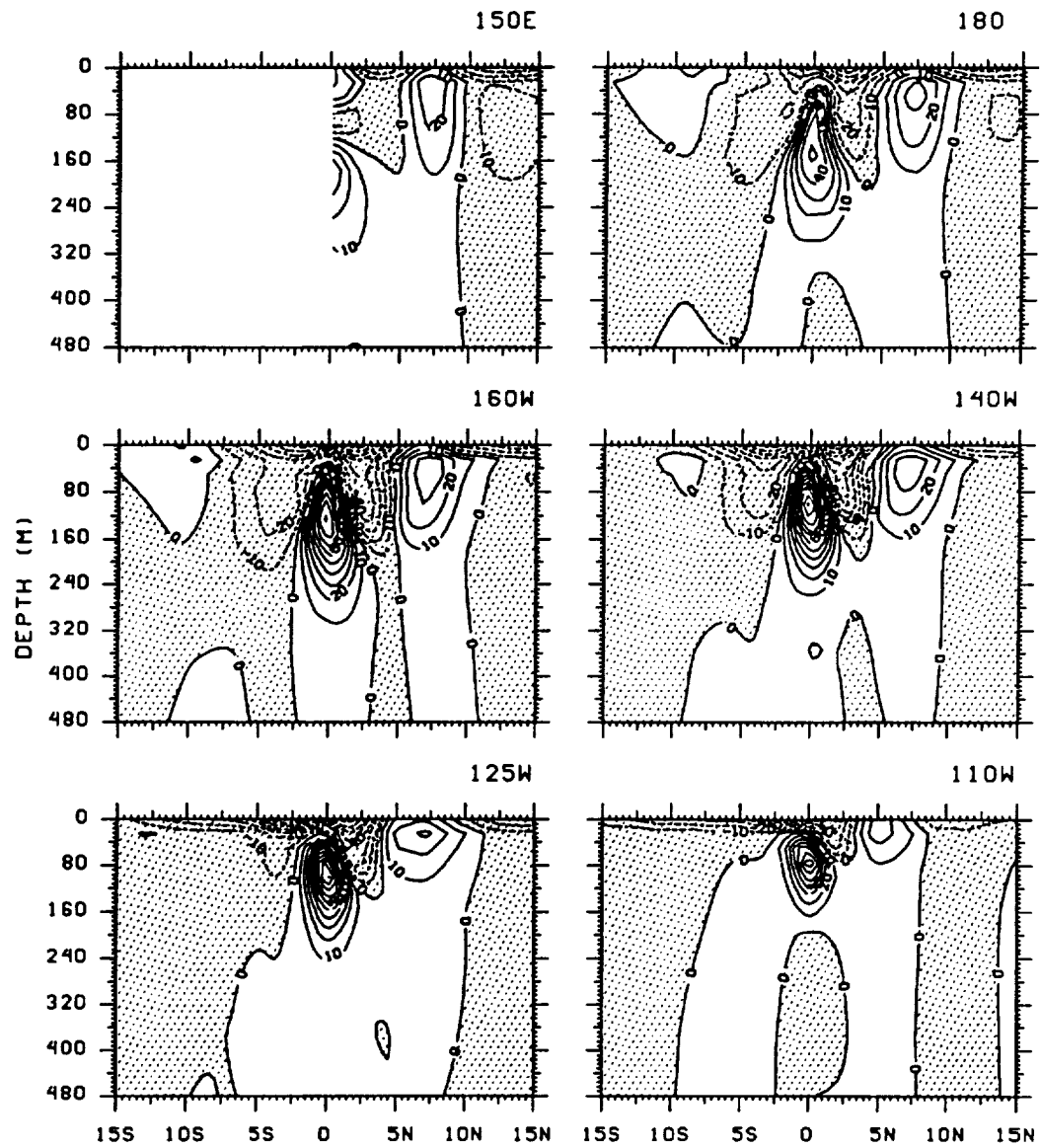


Figure C.1

C.2

Meridional Current

Contour interval is 10 cm s^{-1} and negative currents are shaded

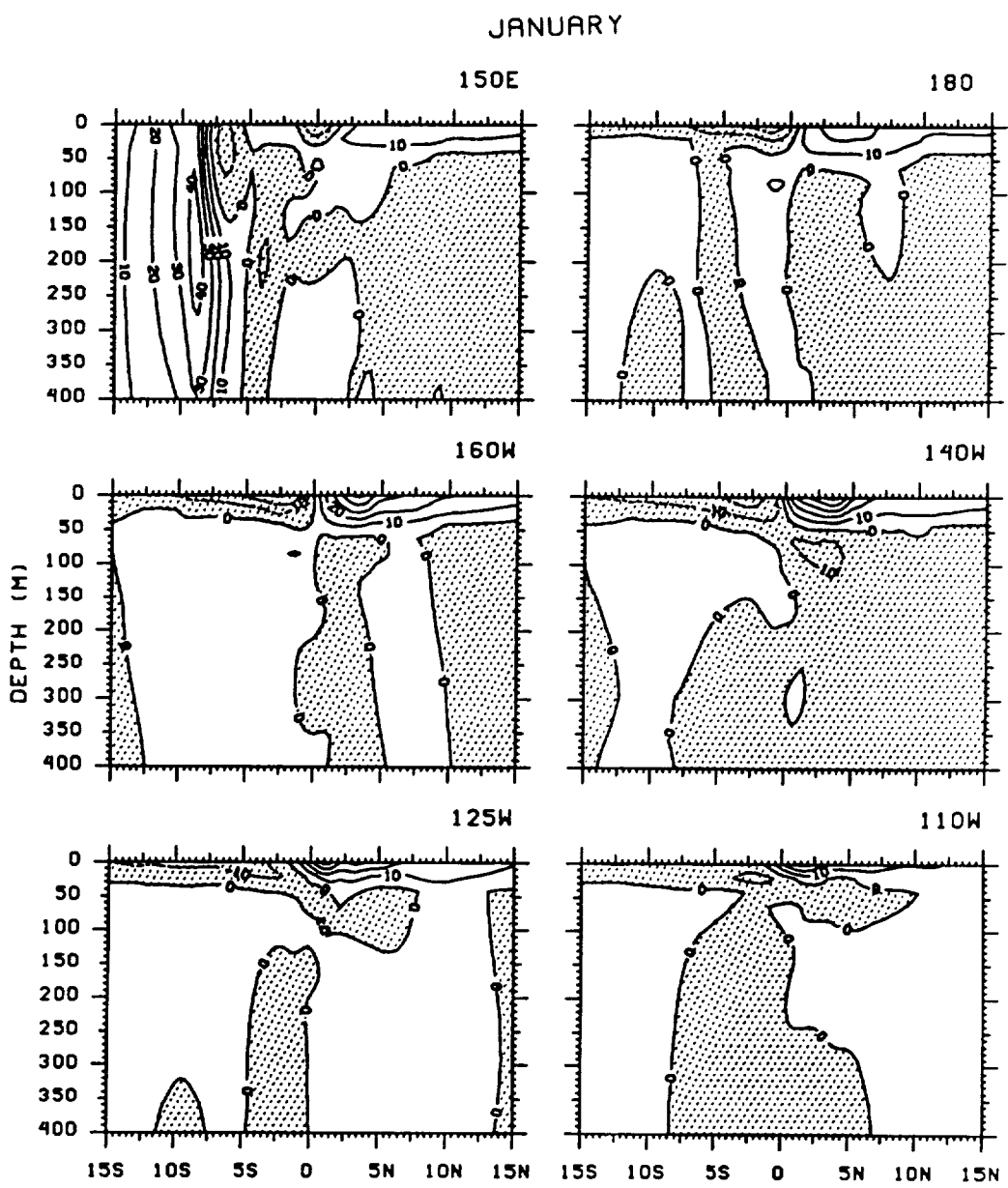


Figure C.2

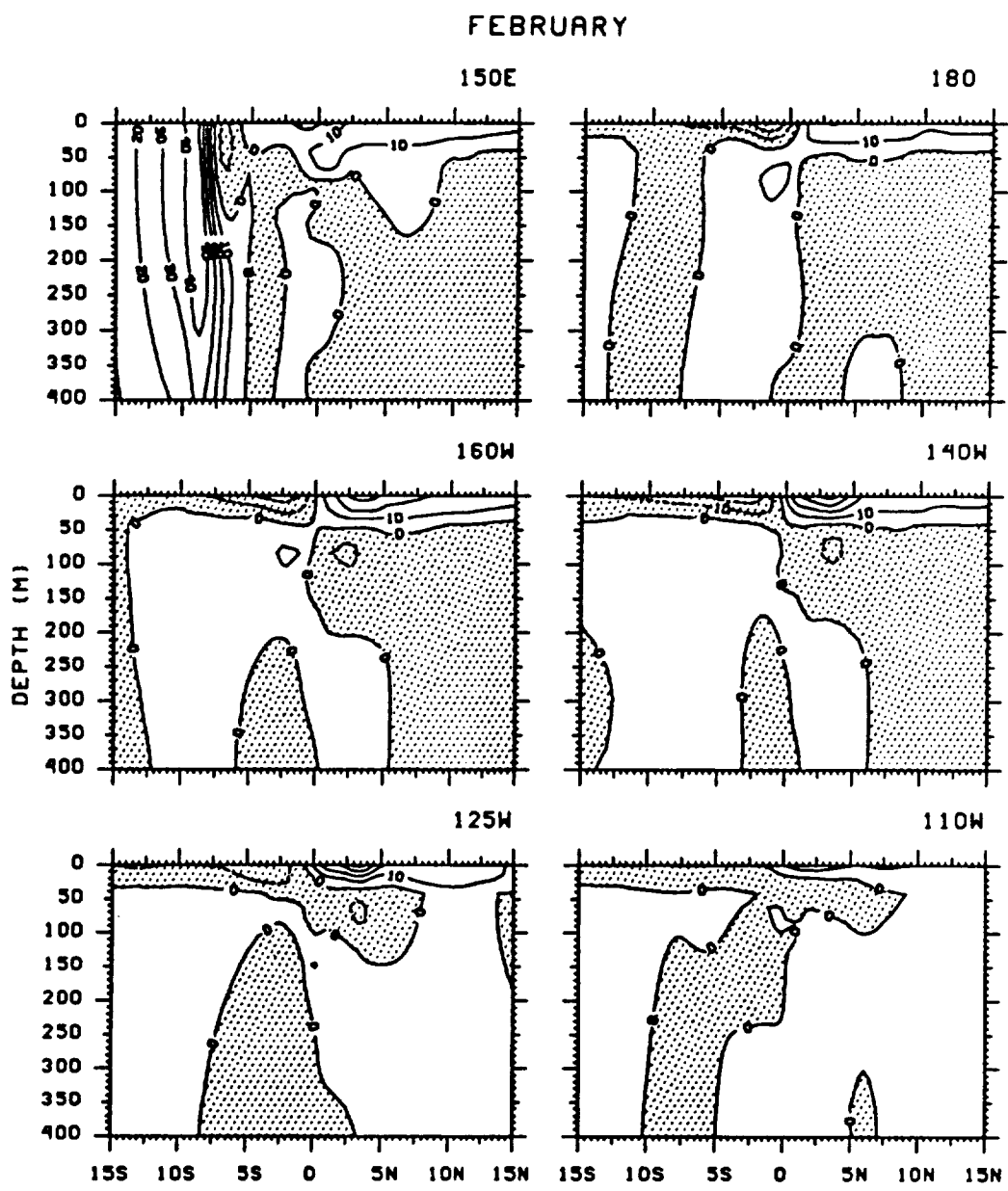


Figure C.2

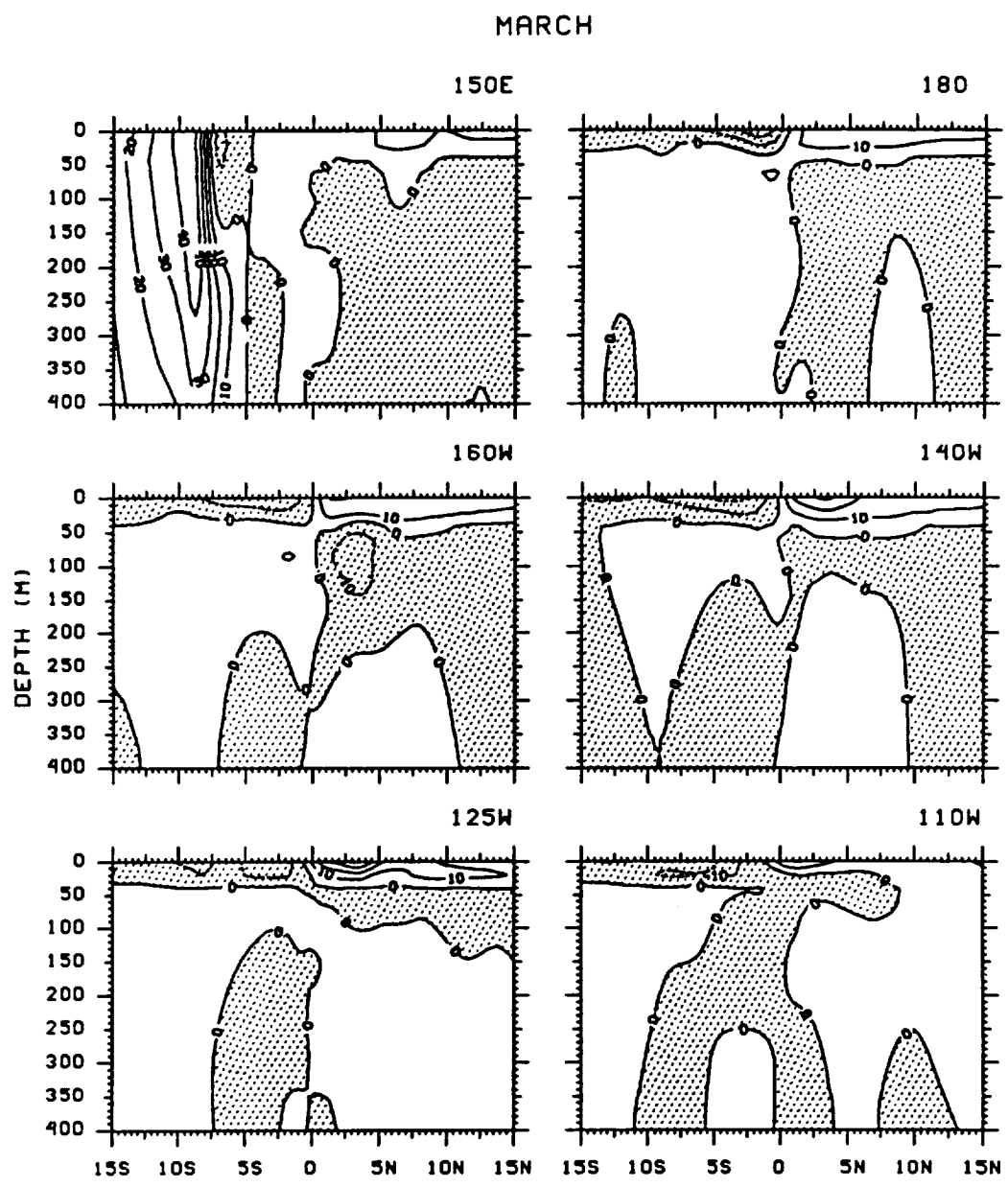


Figure C.2

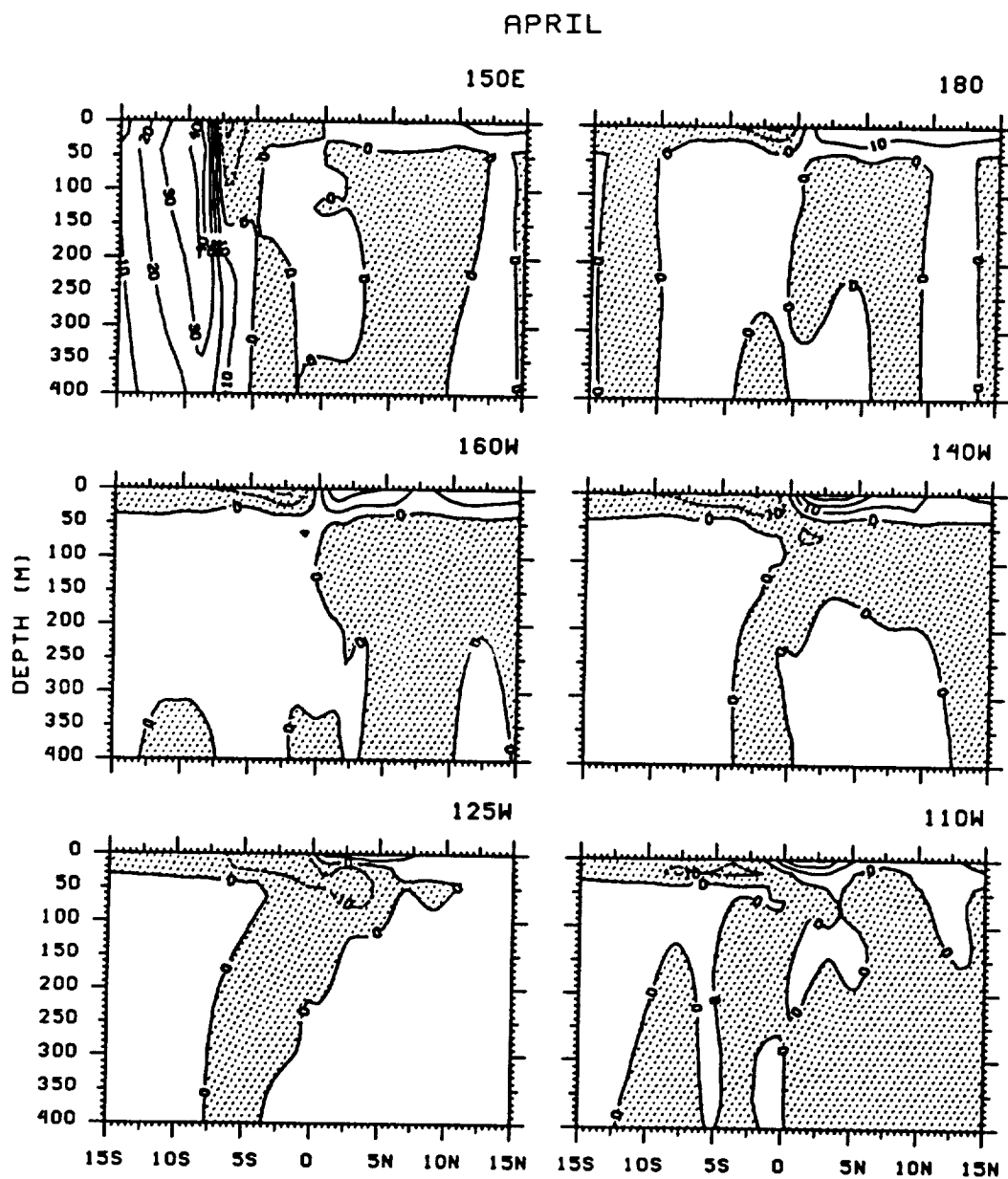


Figure C.2

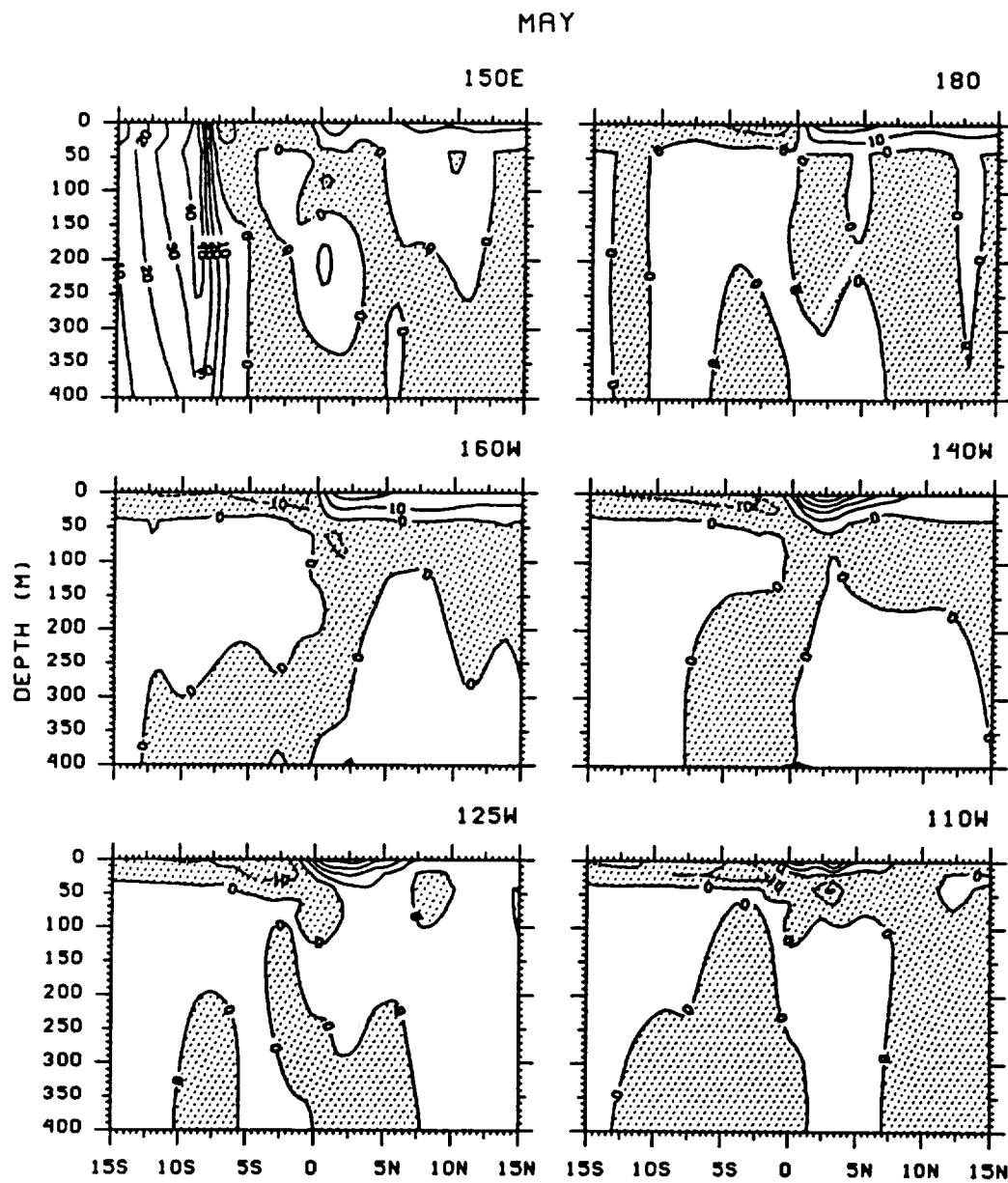


Figure C.2

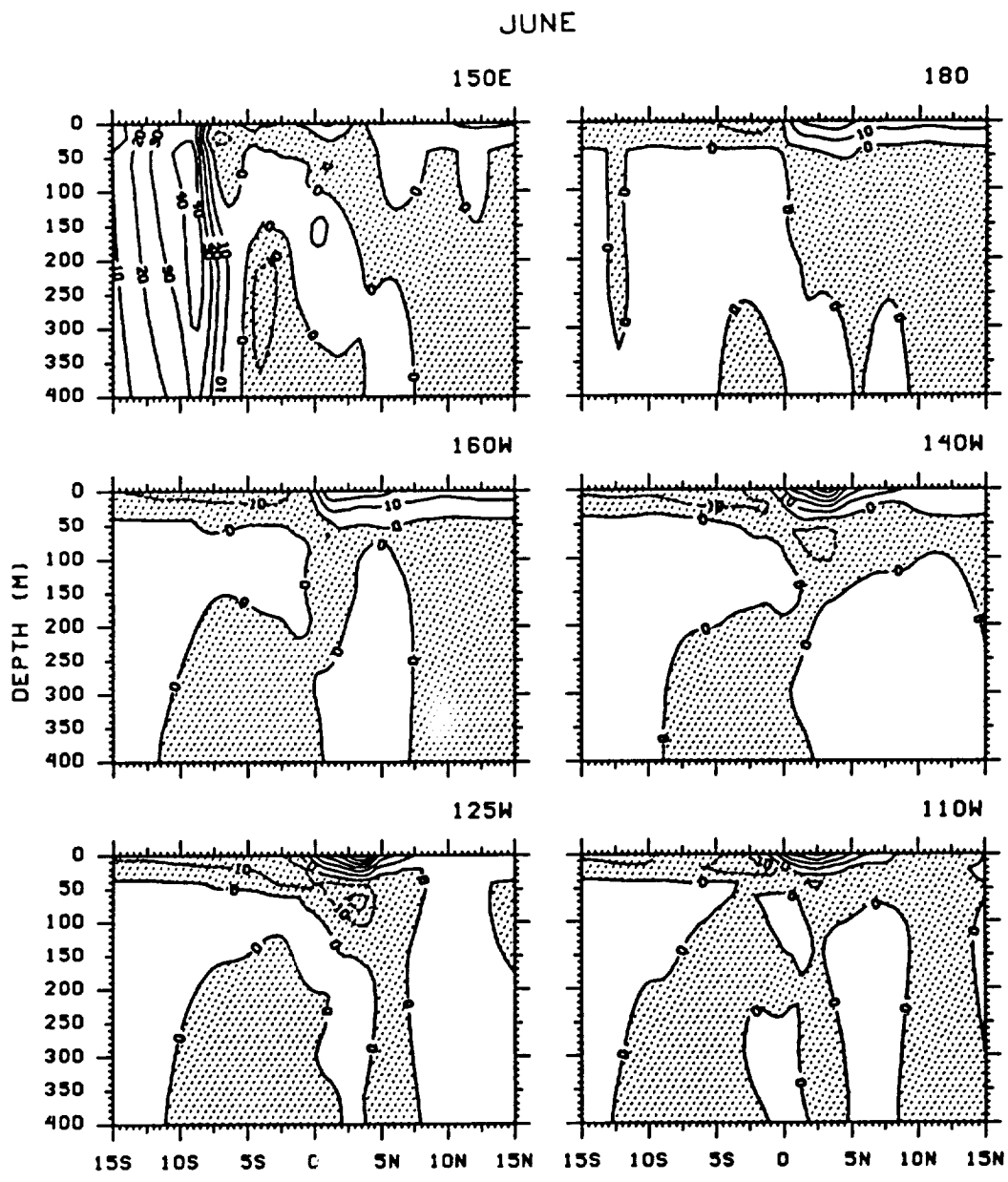


Figure C.2

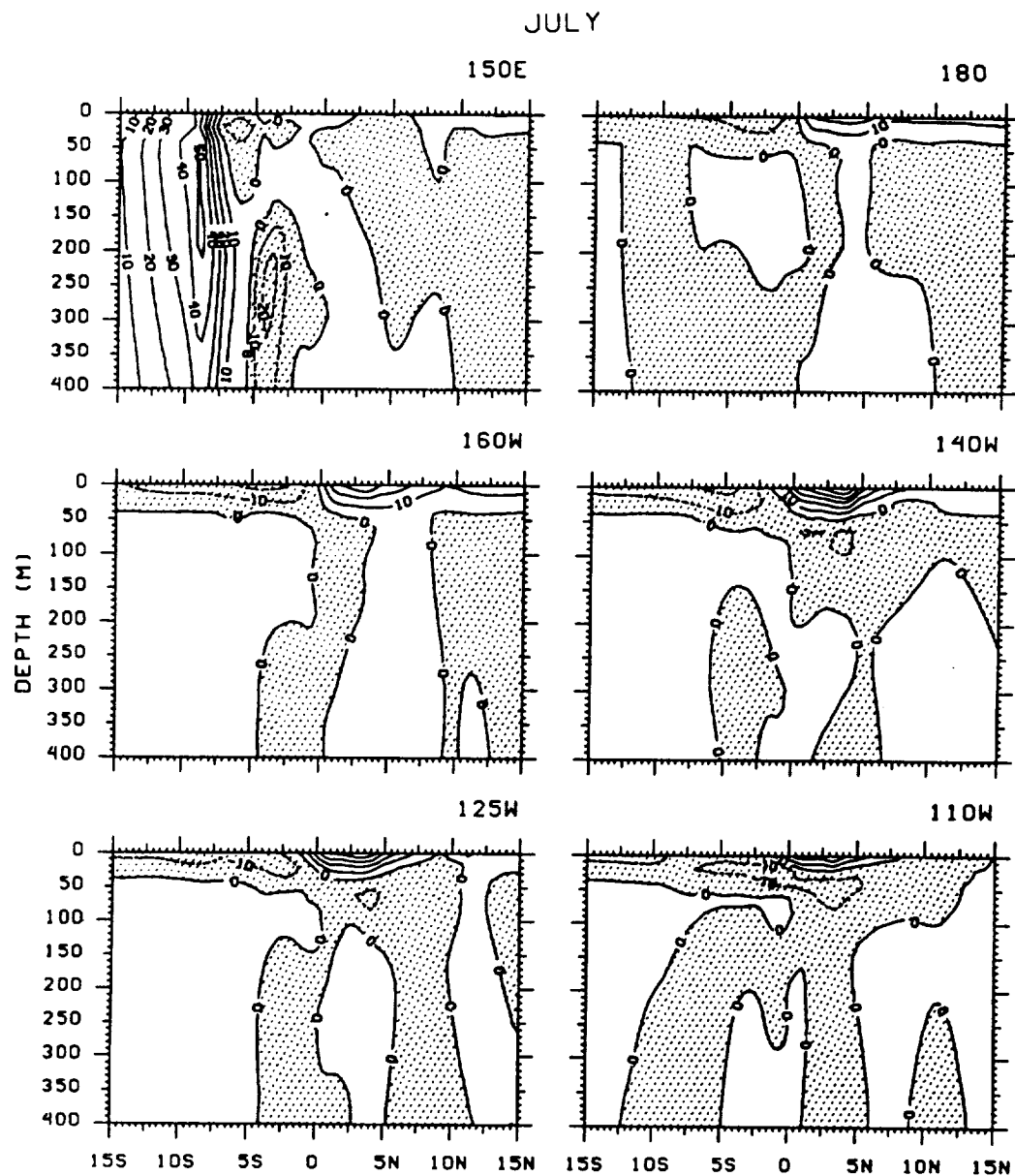


Figure C.2

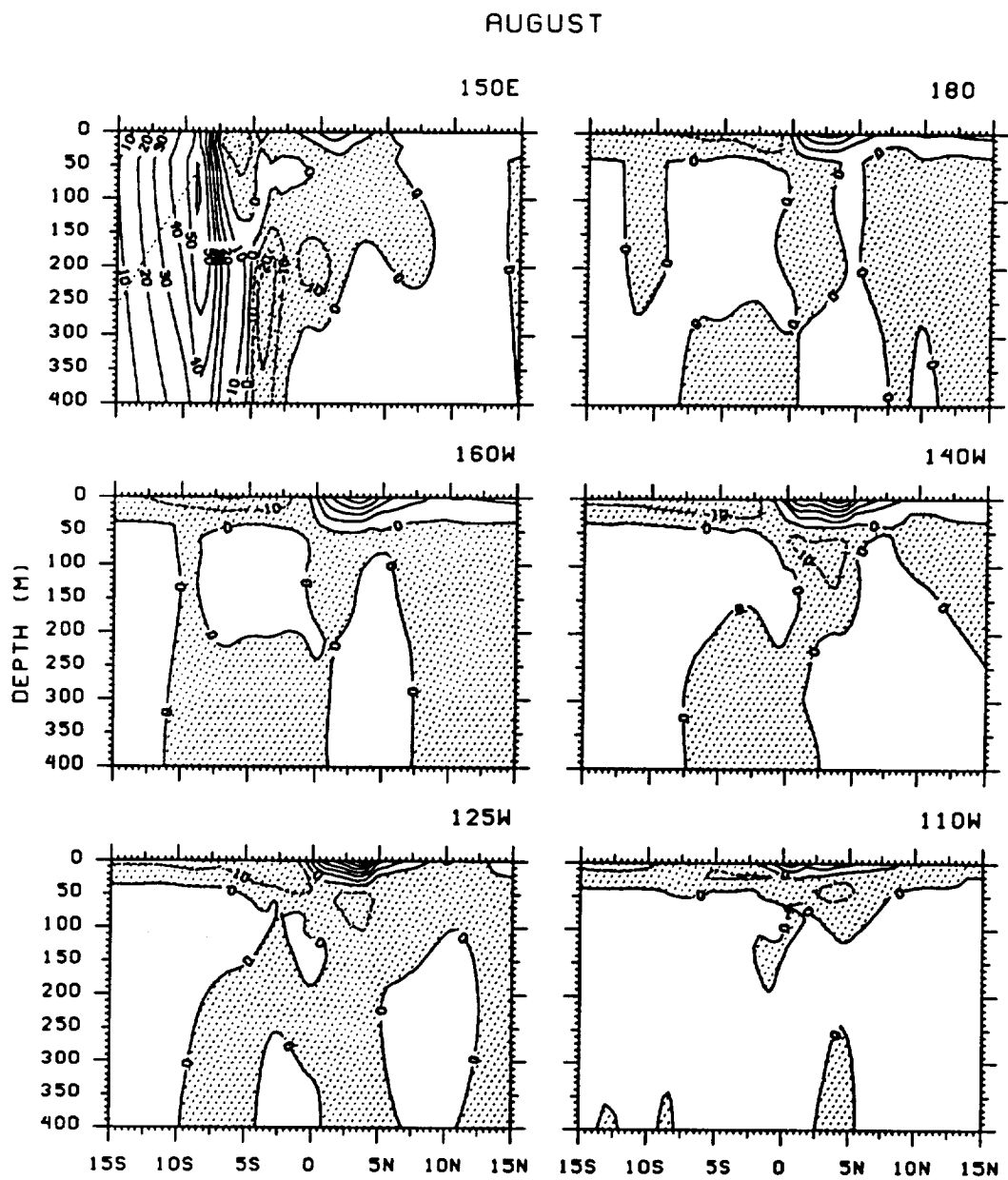


Figure C.2

SEPTEMBER

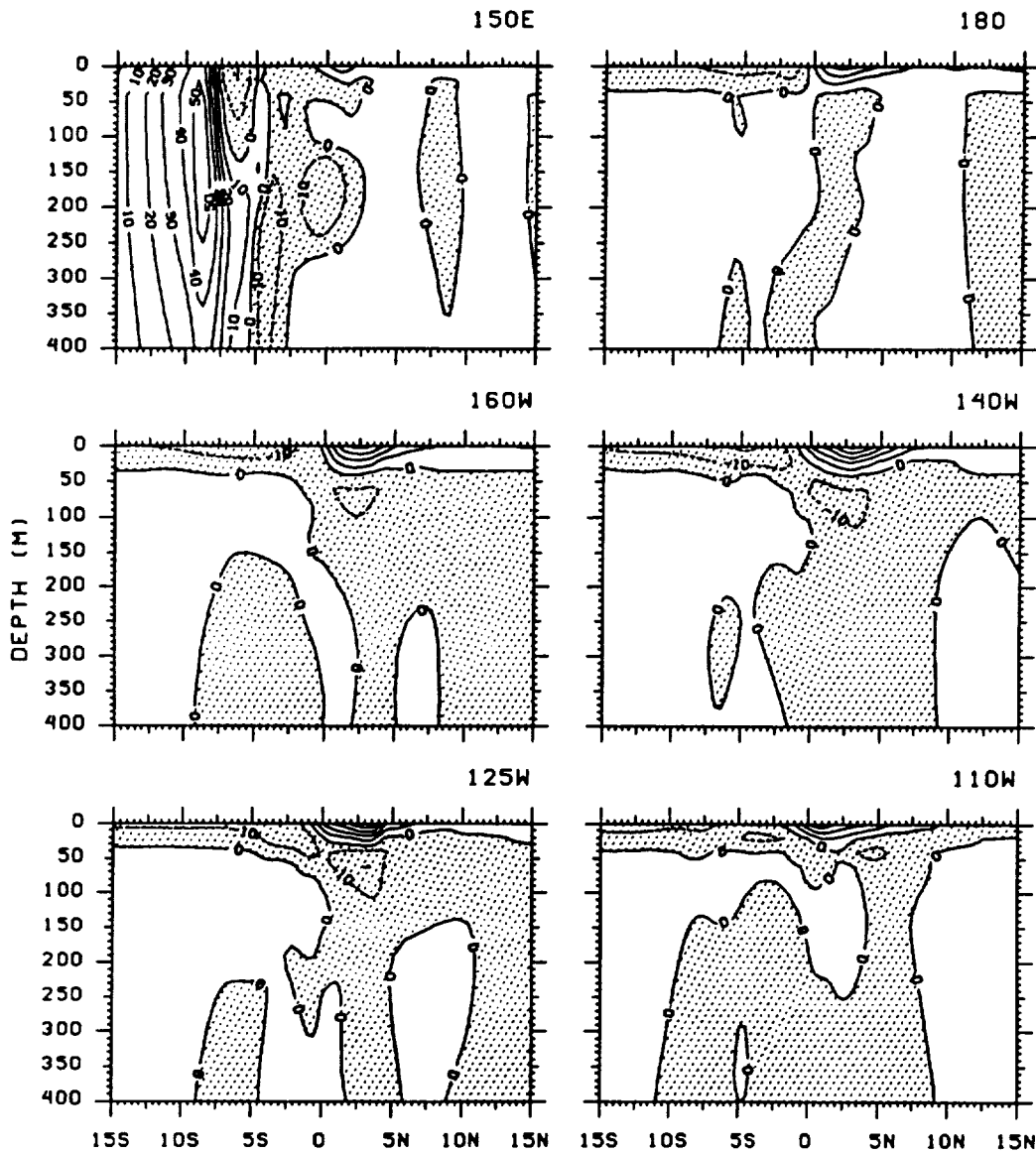


Figure C.2

OCTOBER

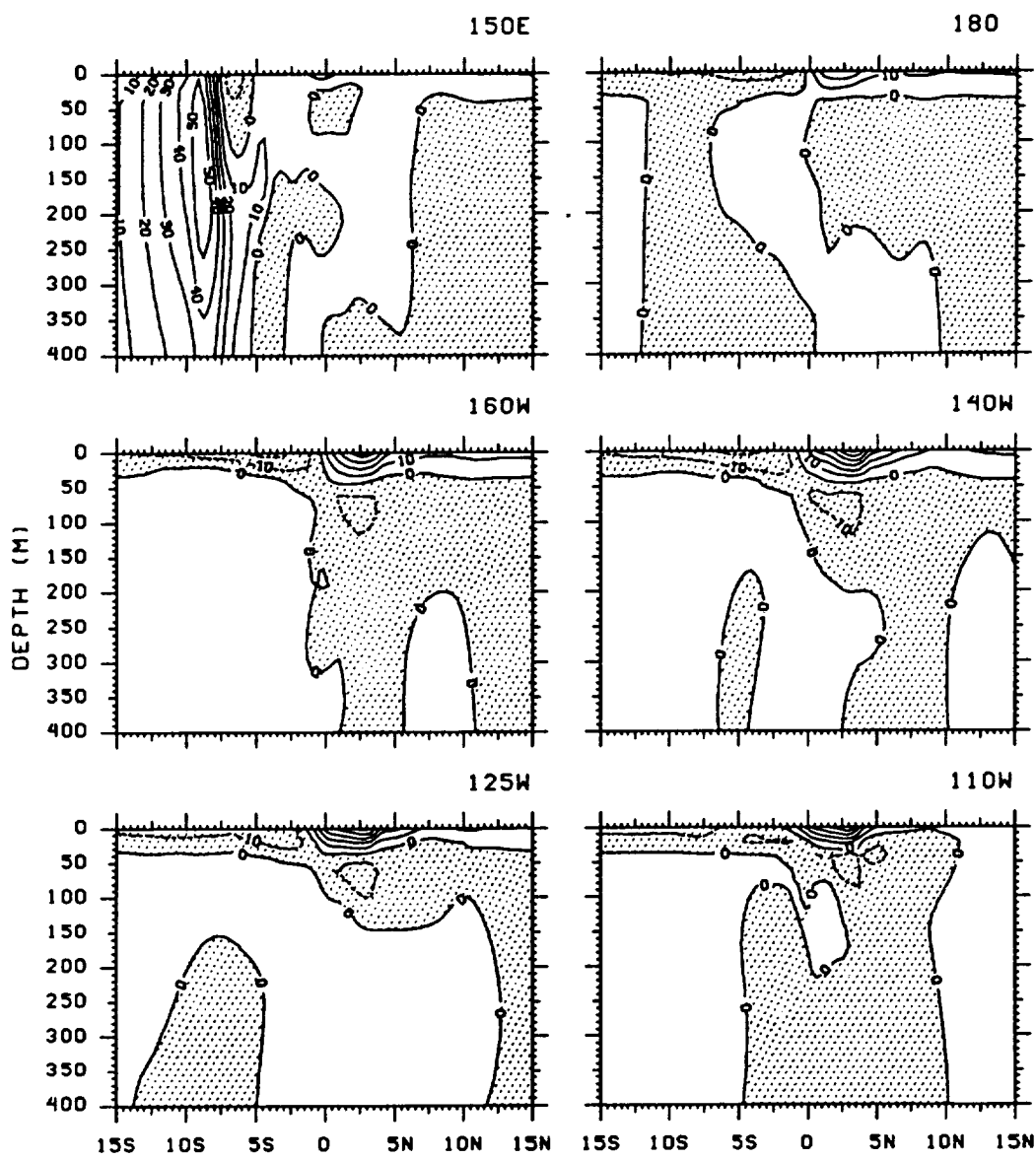


Figure C.2

NOVEMBER

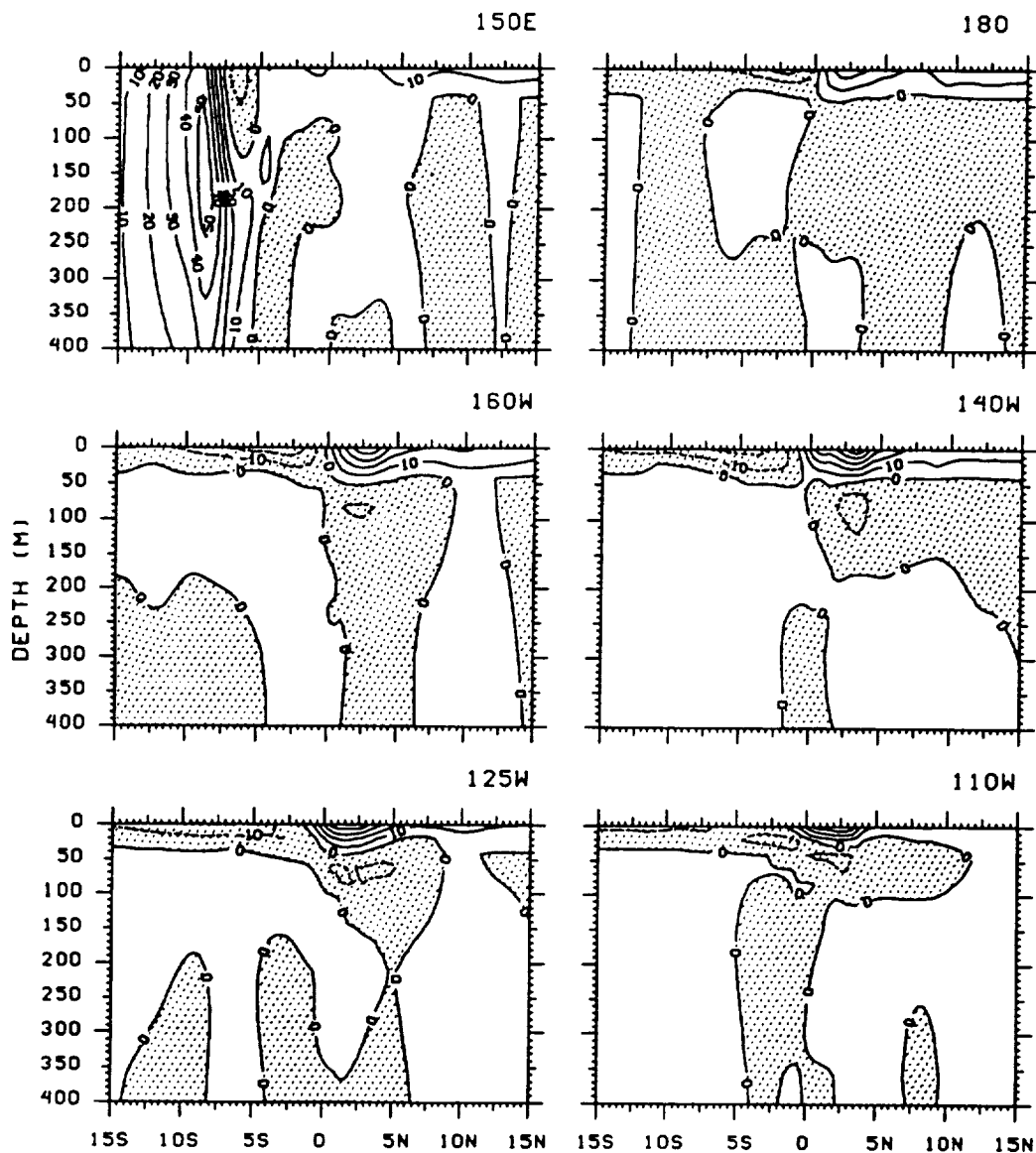


Figure C.2

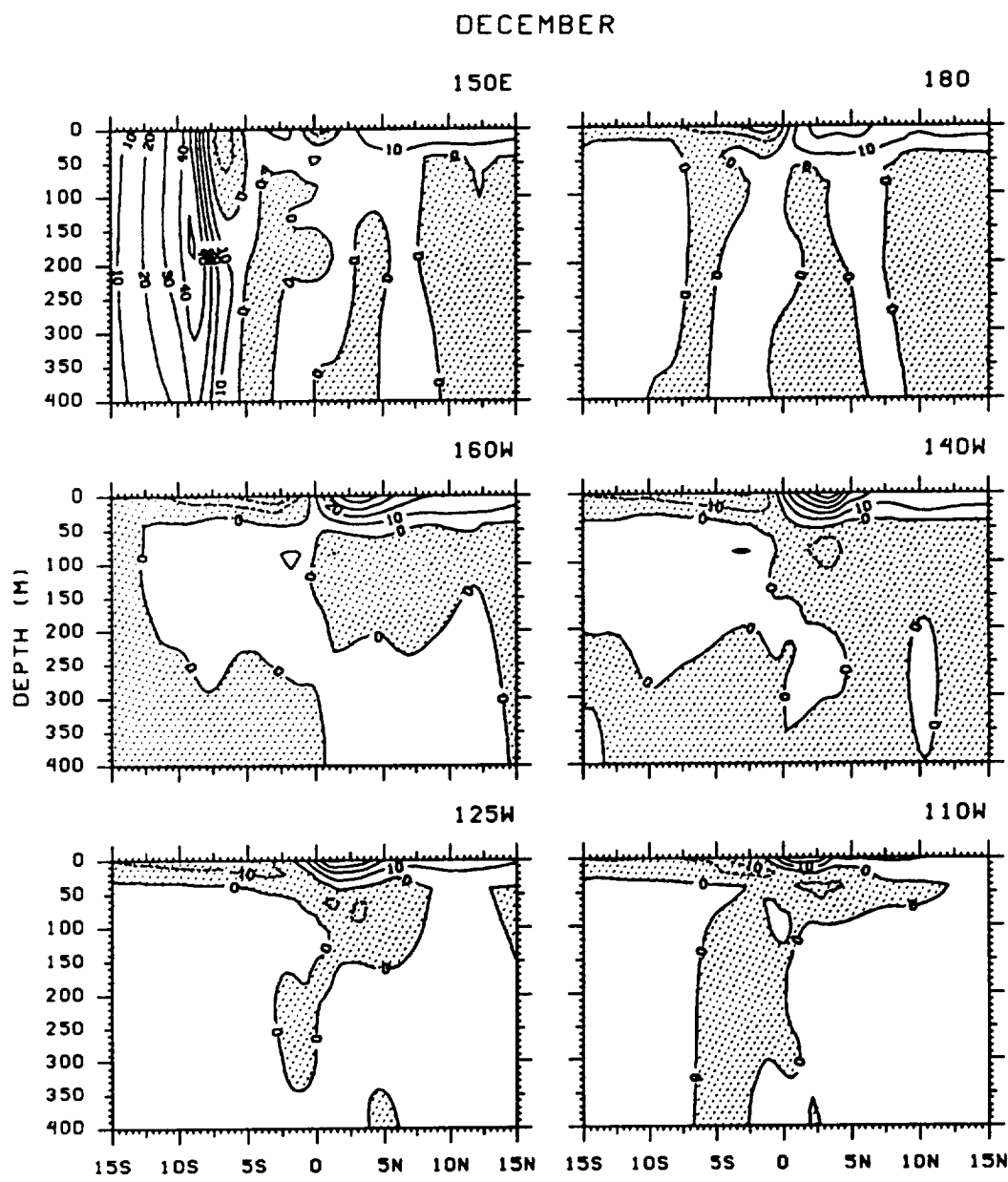


Figure C.2

C.3.1

Zonal geostrophic current from 2.3°N - 15°N

Contour interval is 10 cm s^{-1} and negative currents are shaded

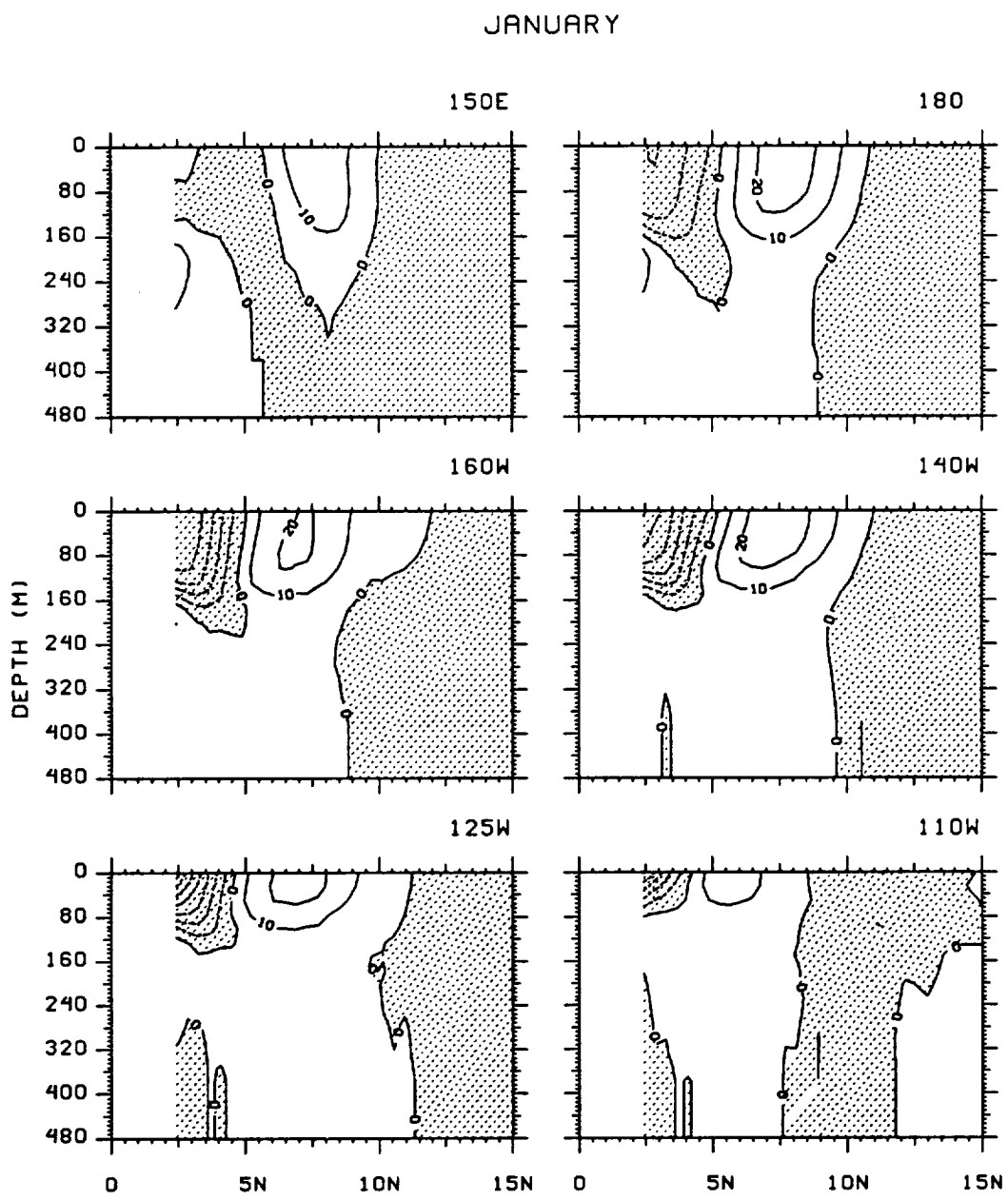


Figure C.3.1

FEBRUARY

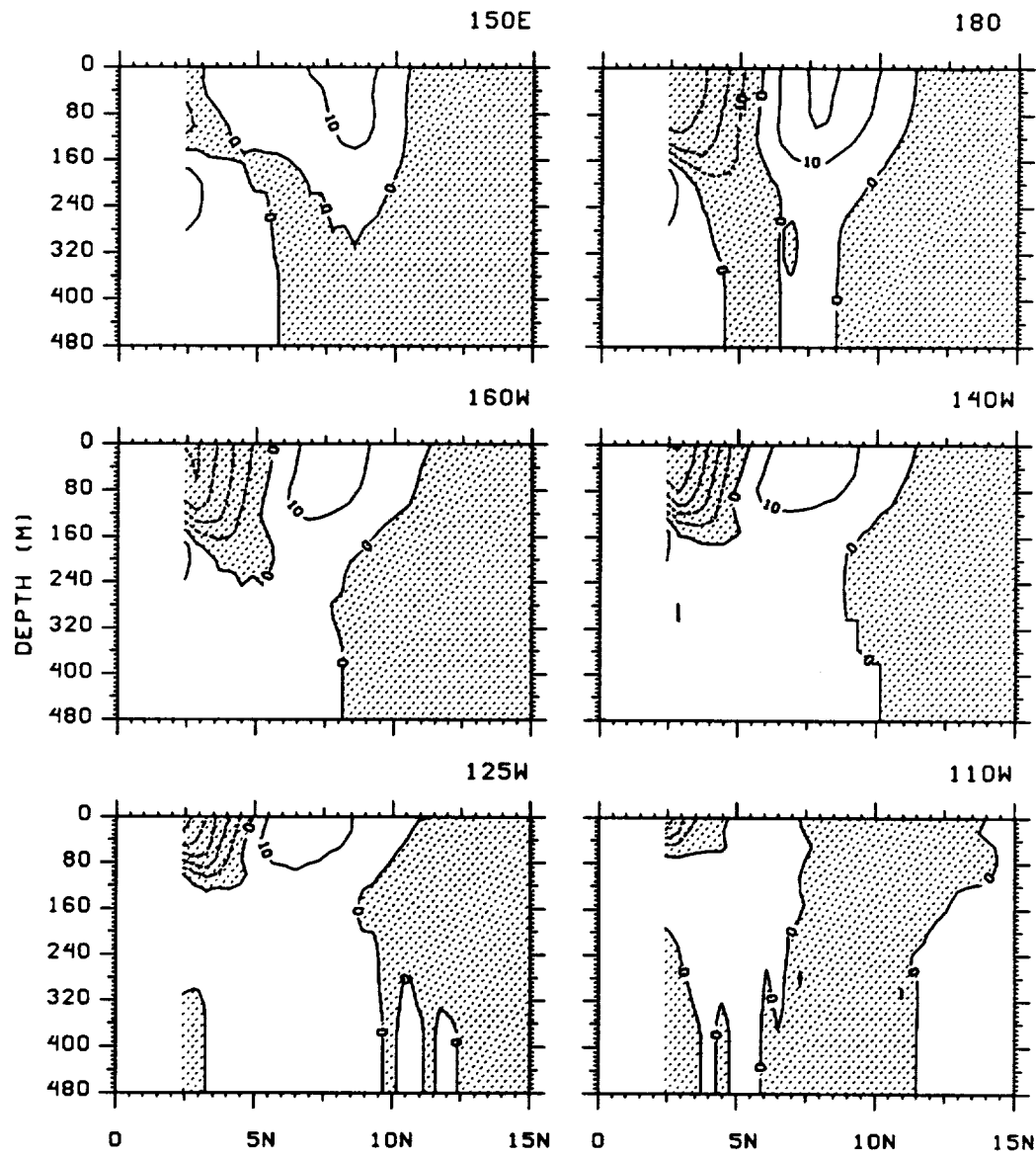


Figure C.3.1

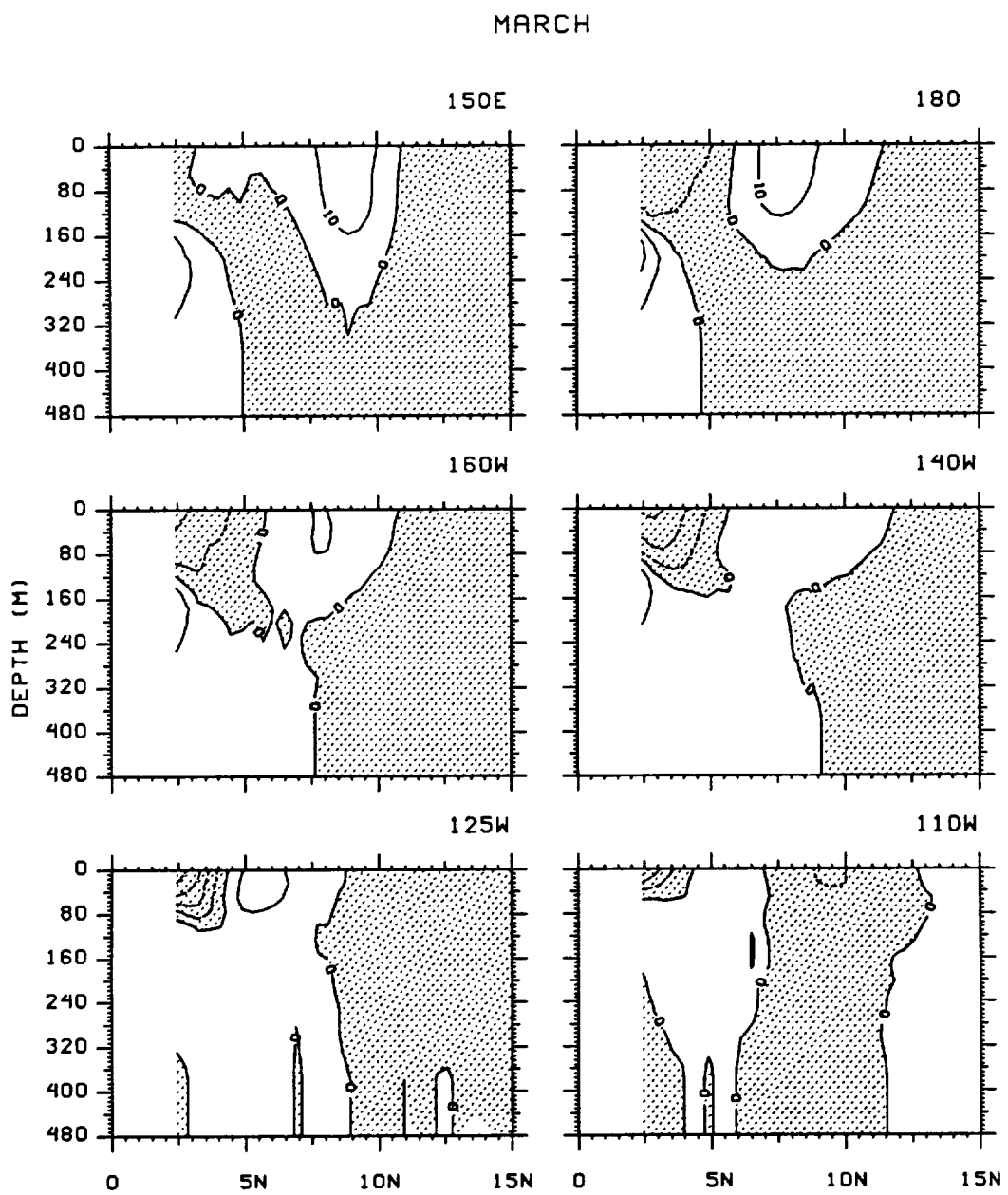


Figure C.3.1

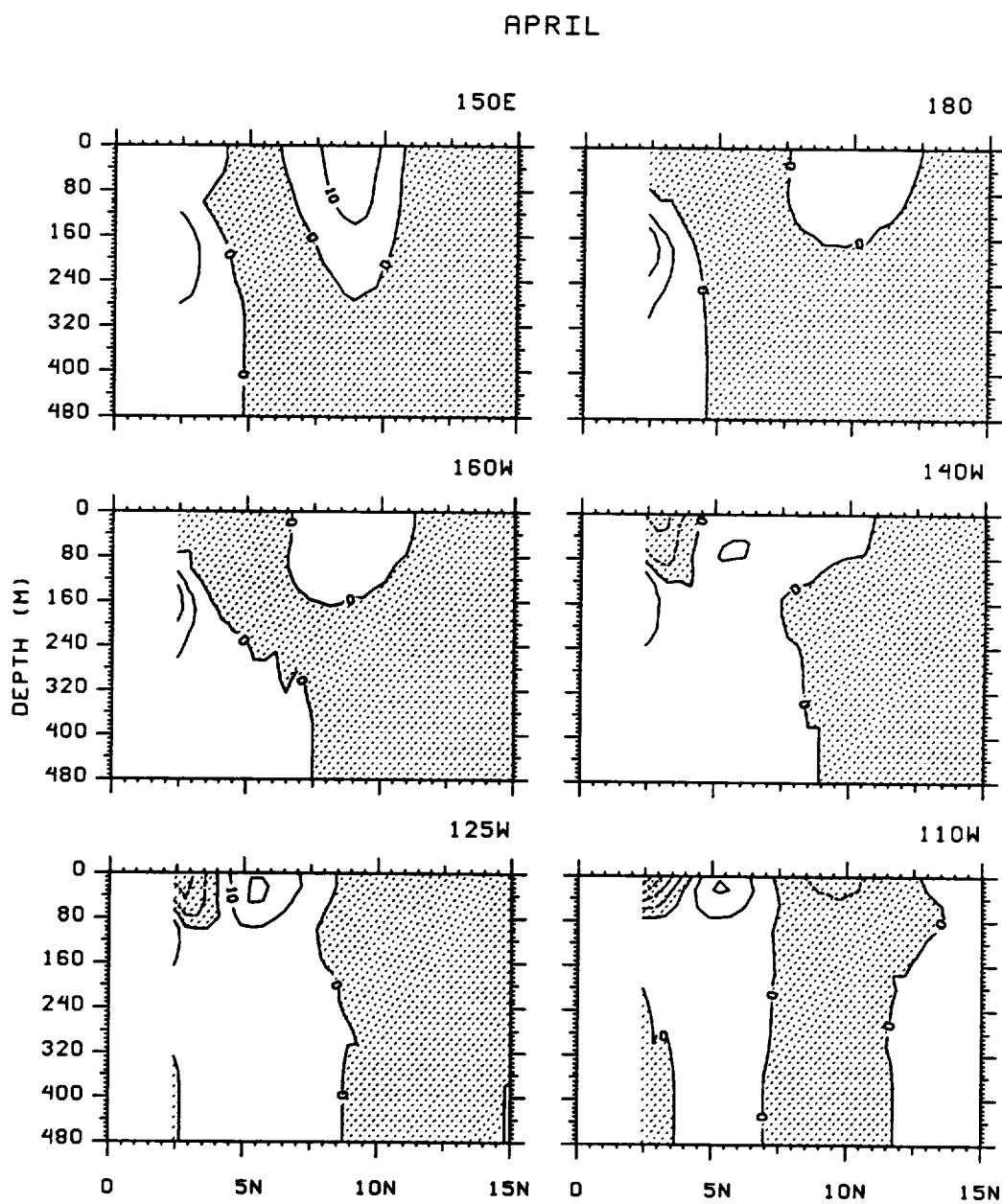


Figure C.3.1

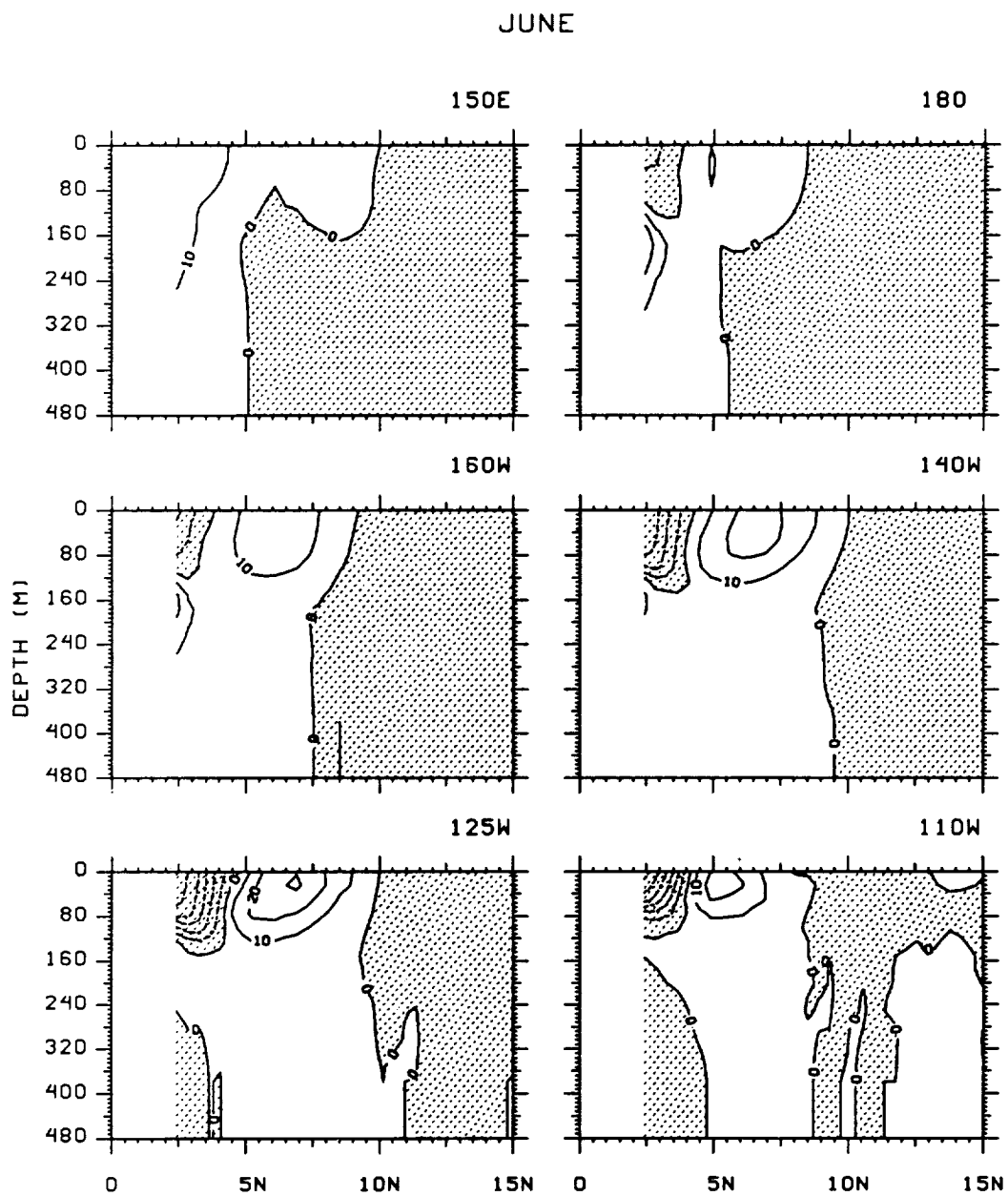


Figure C.3.1

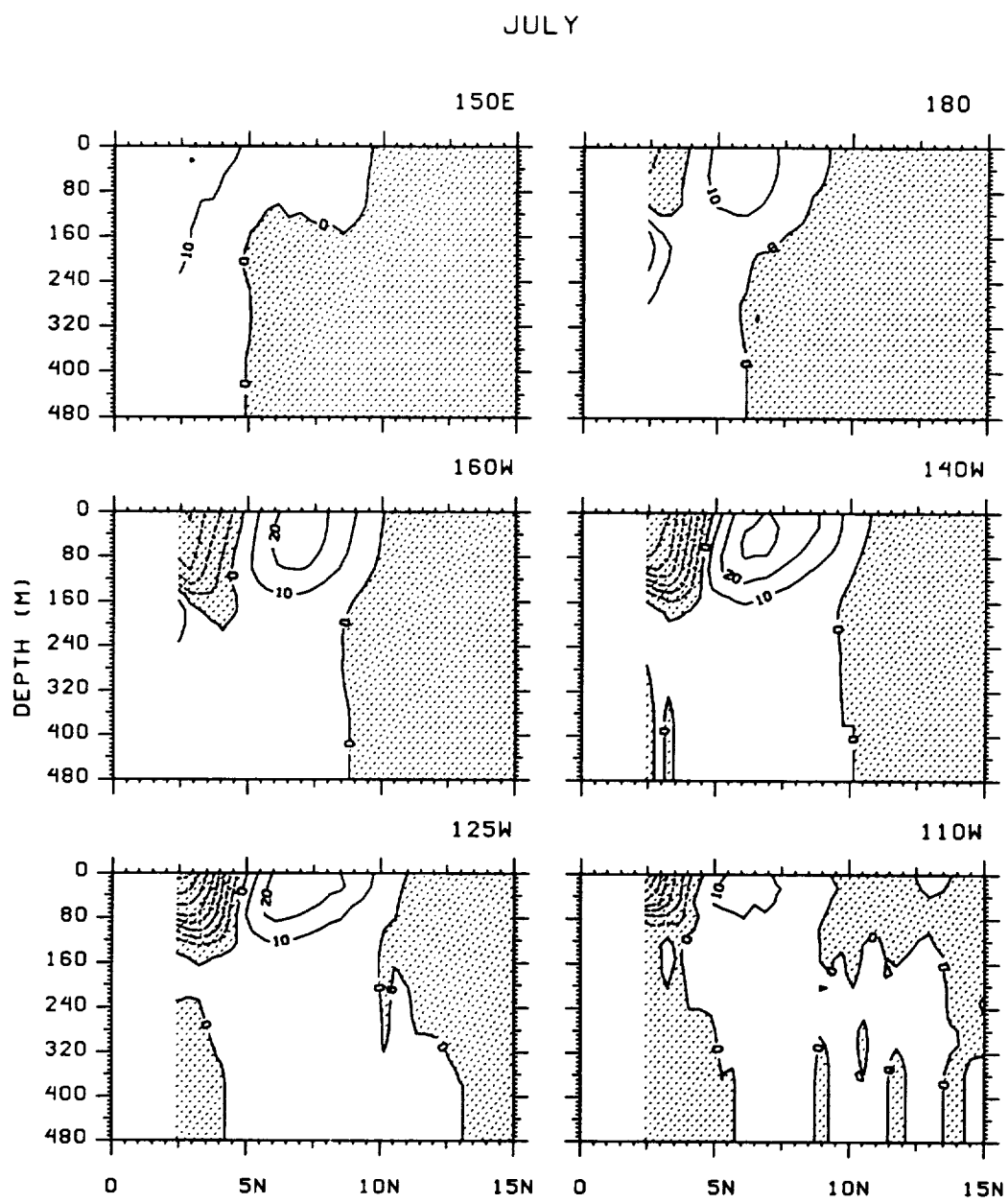


Figure C.3.1

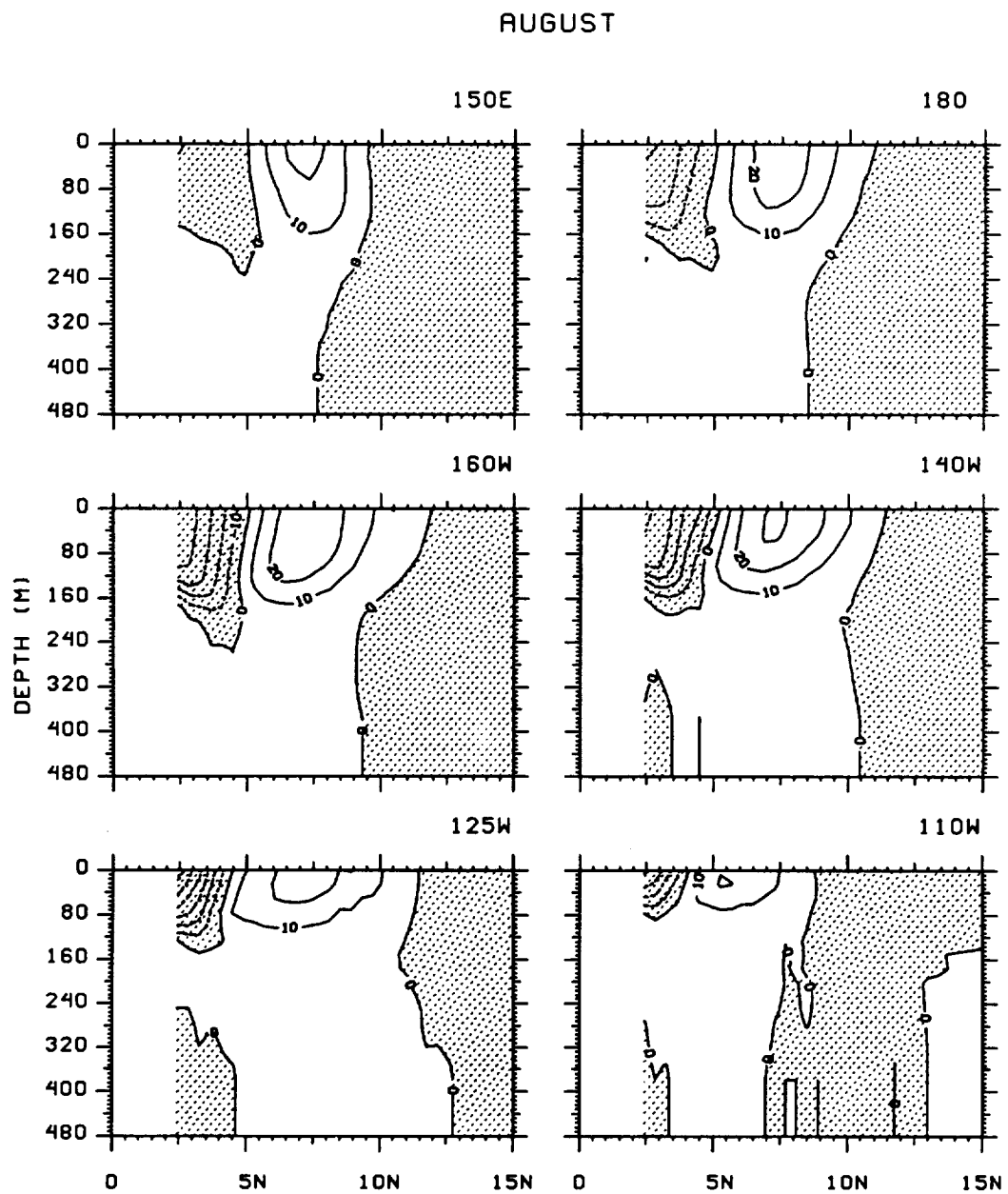


Figure C.3.1

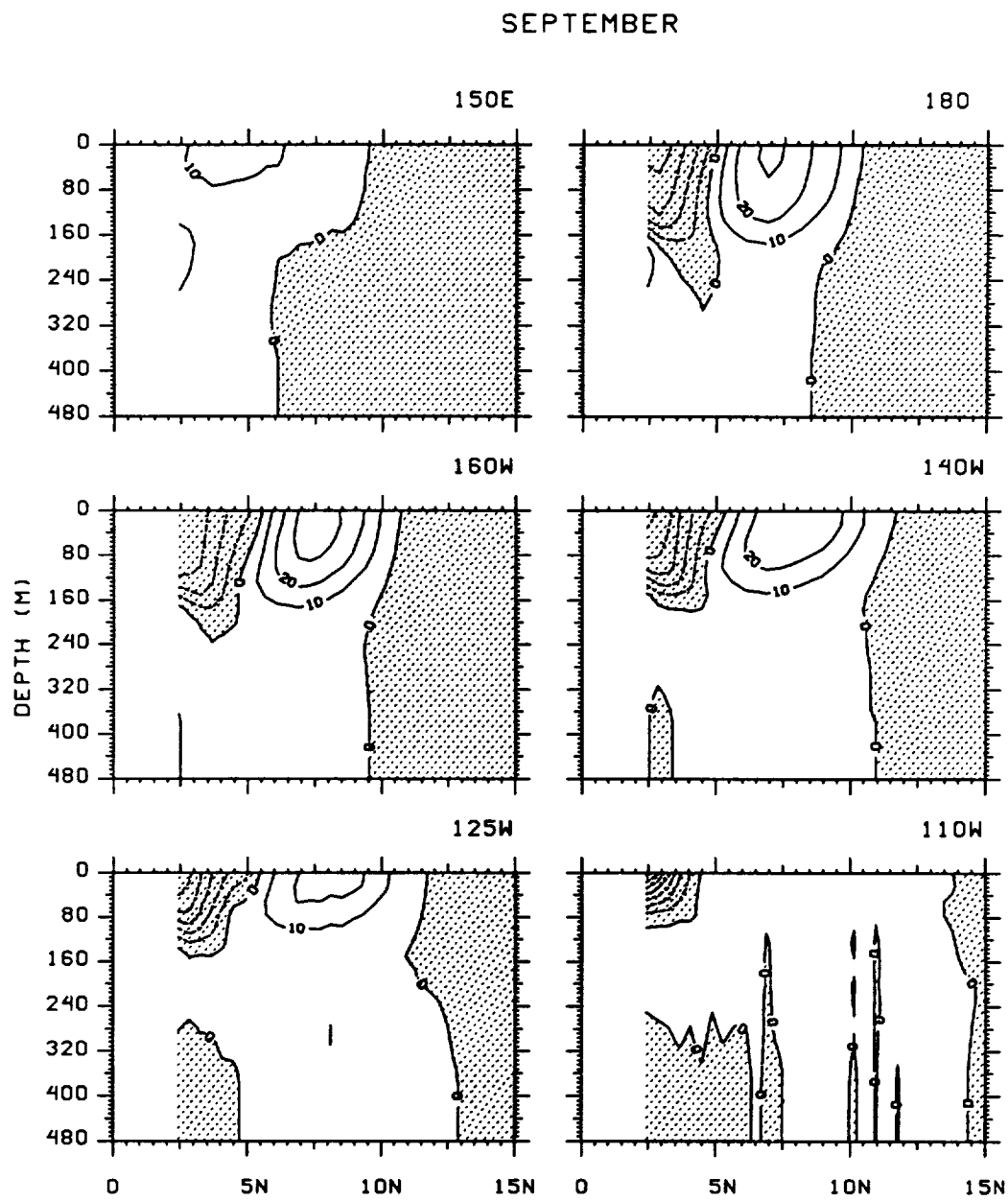


Figure C.3.1

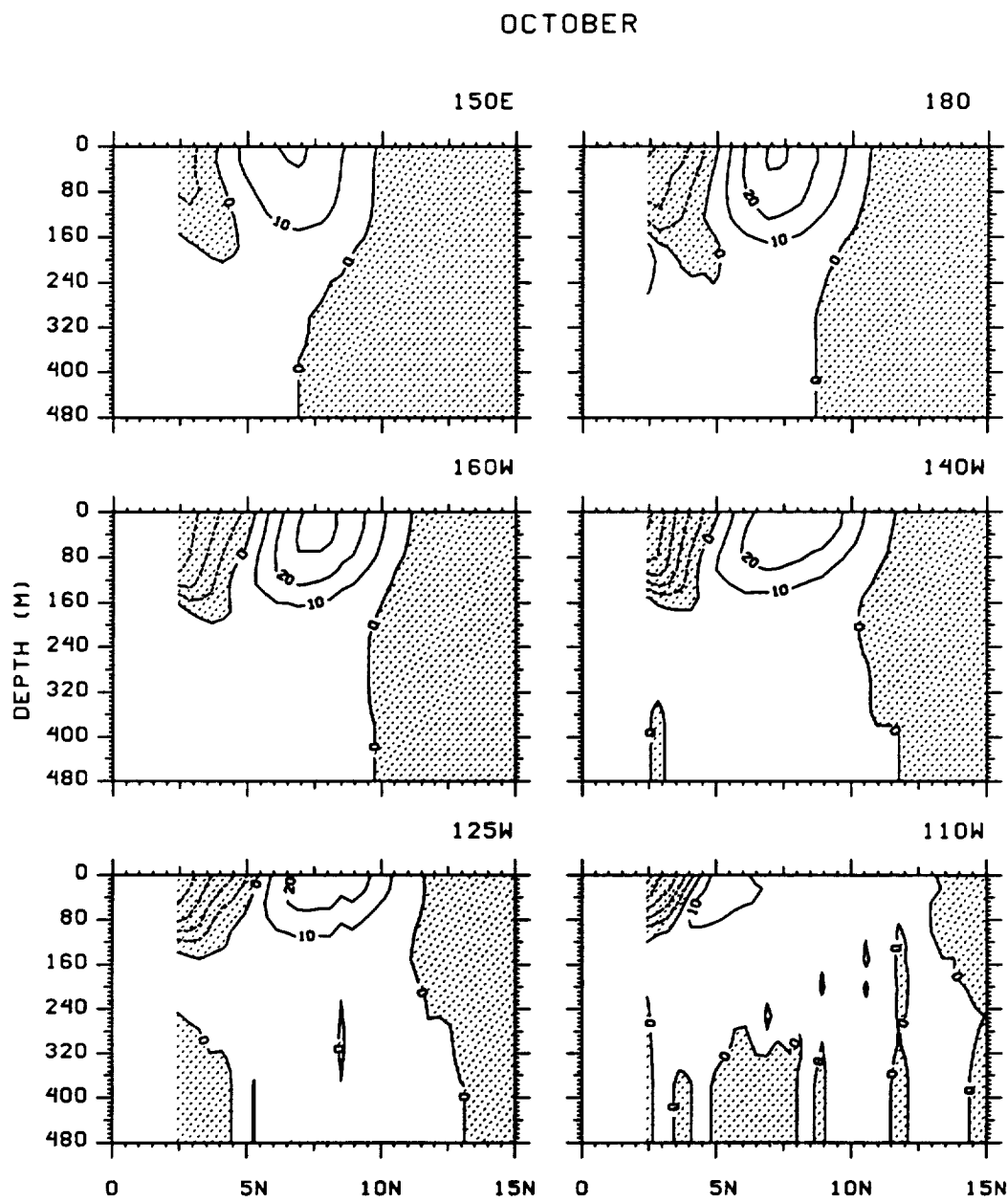


Figure C.3.1

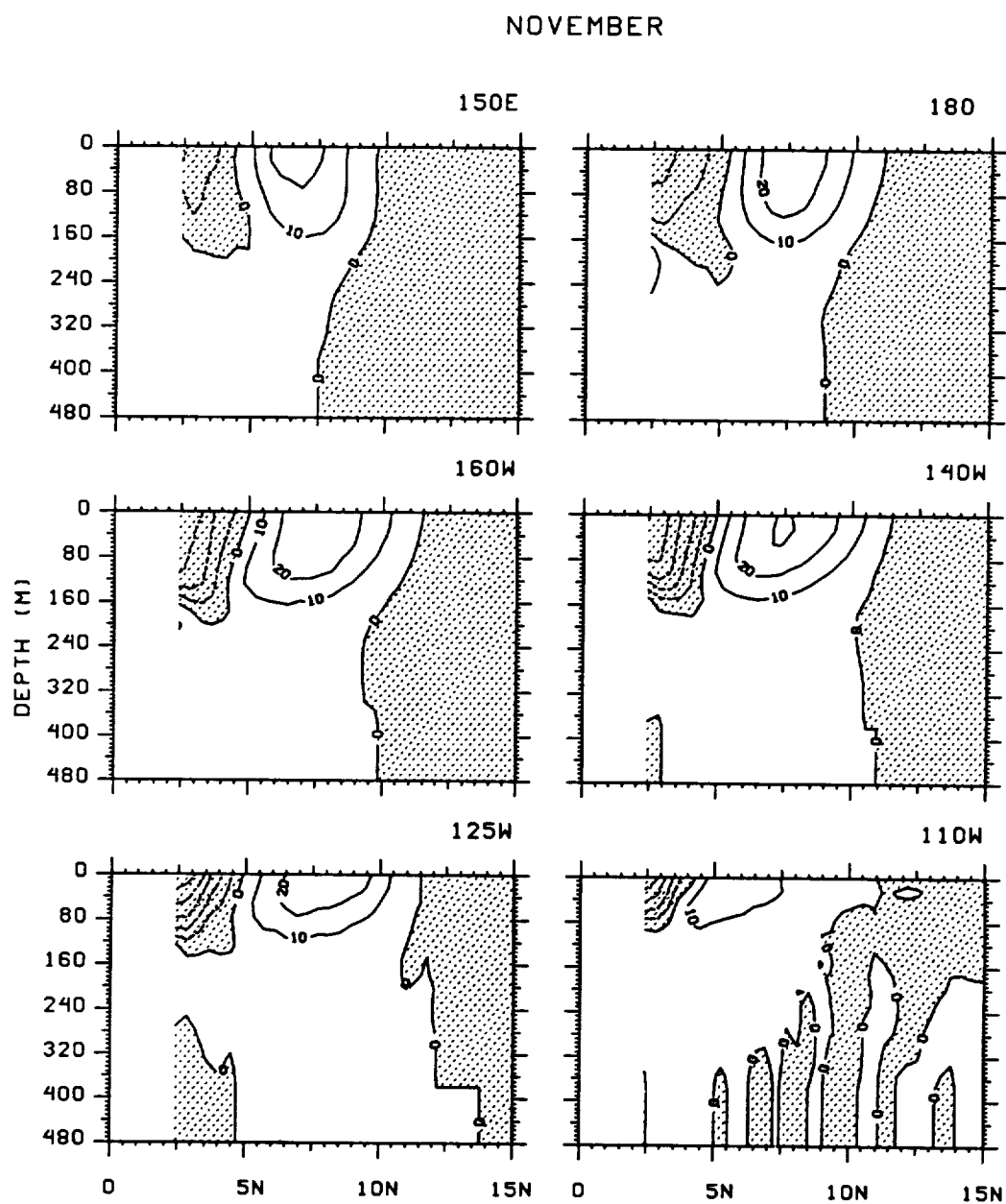


Figure C.3.1

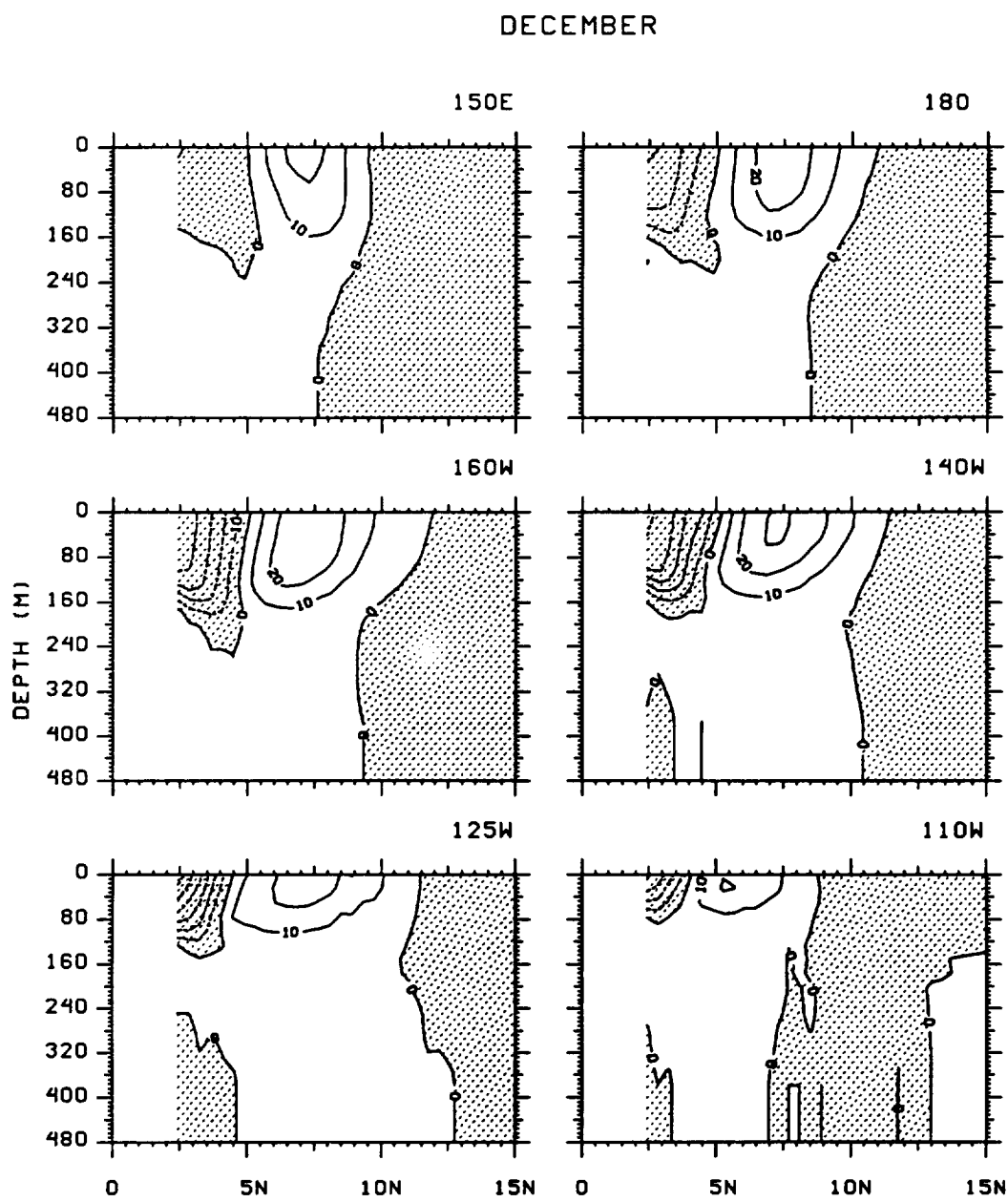


Figure C.3.1

C.3.2

Comparison between the zonal geostrophic current at 5 m relative to 484×10^4 Pa (thin dotted curve) and the 5 m model total zonal current (thick curve) in cm sec^{-1}

JANUARY

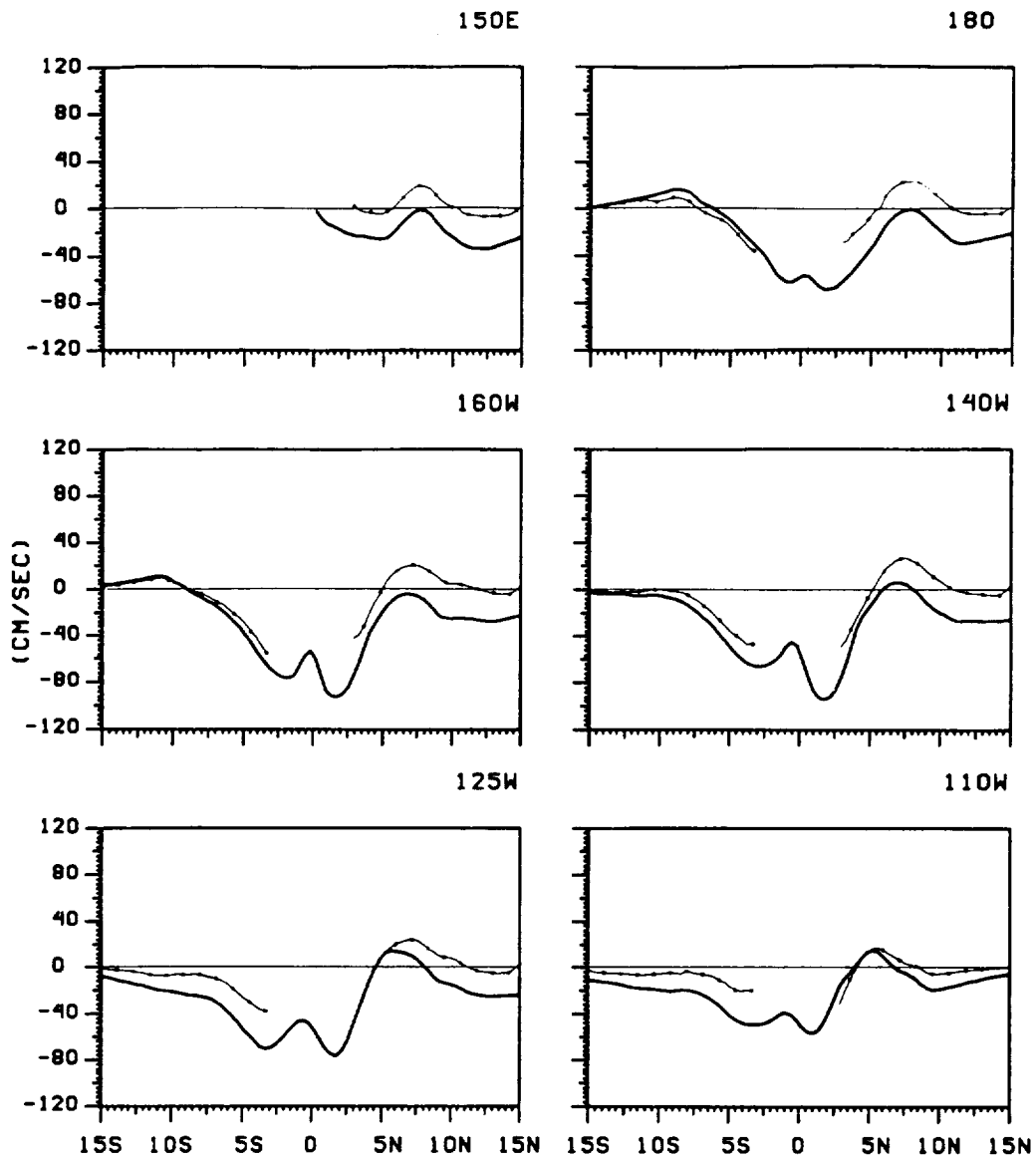


Figure C.3.2

FEBRUARY

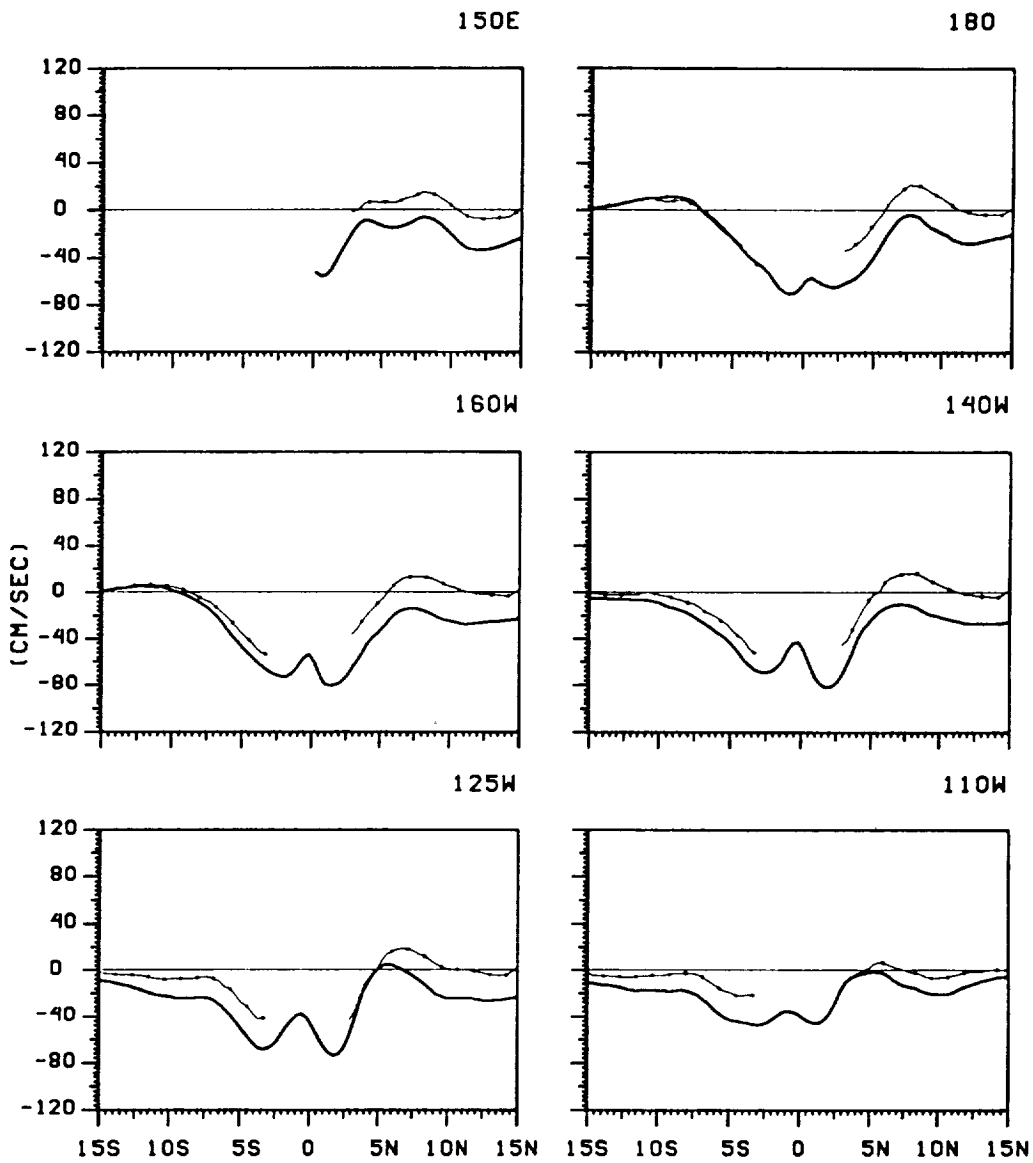


Figure C.3.2

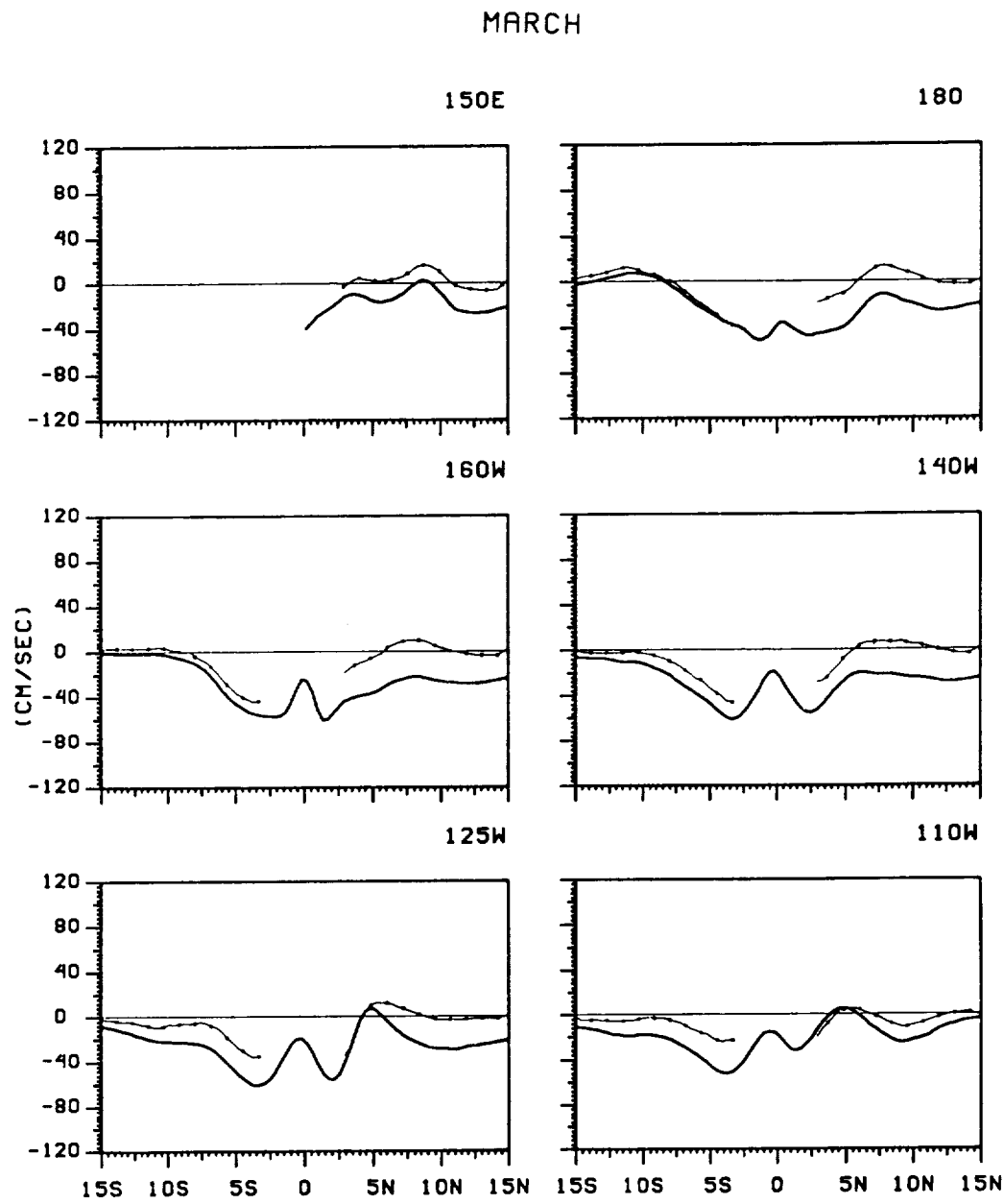


Figure C.3.2

APRIL

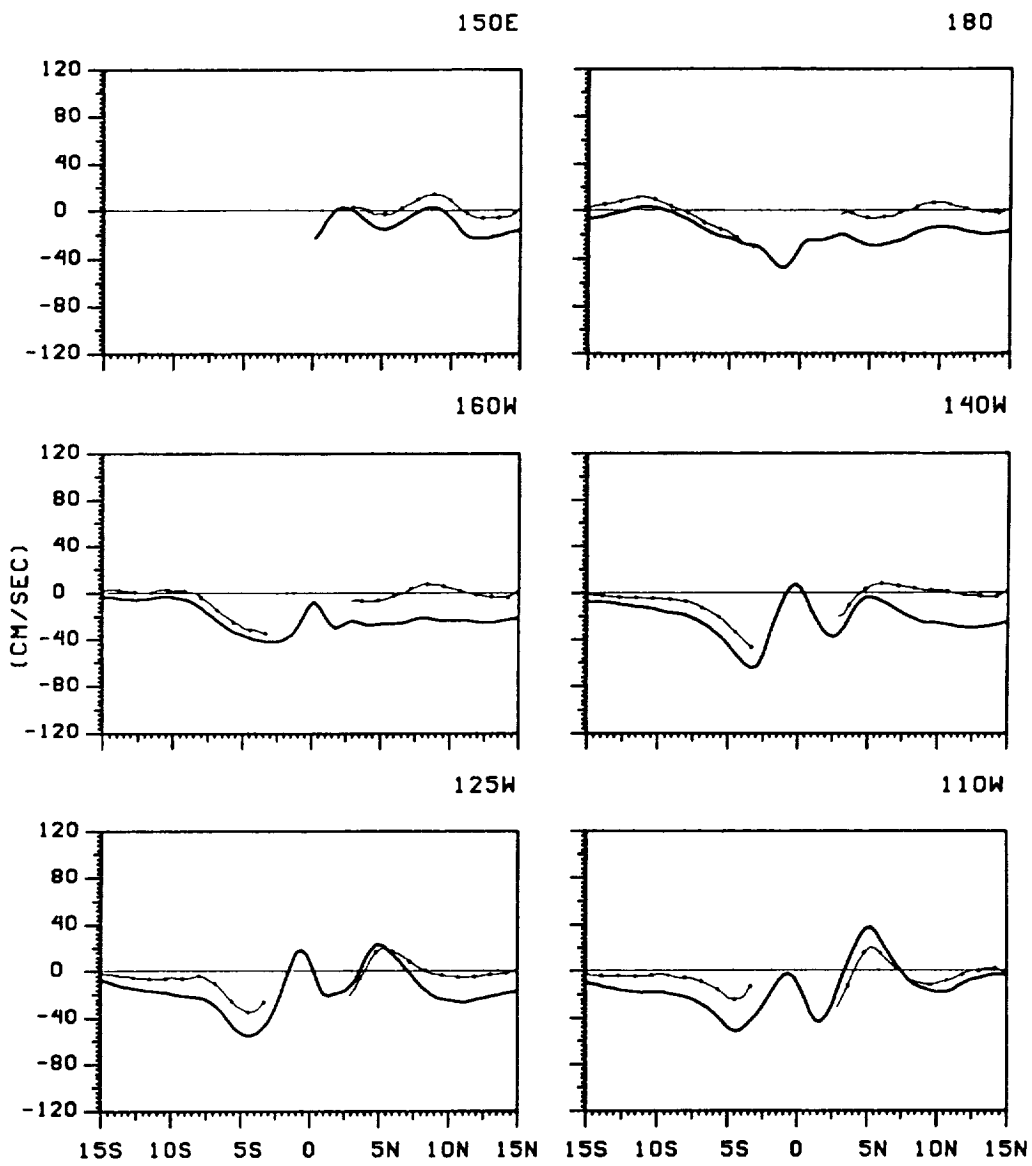


Figure C.3.2

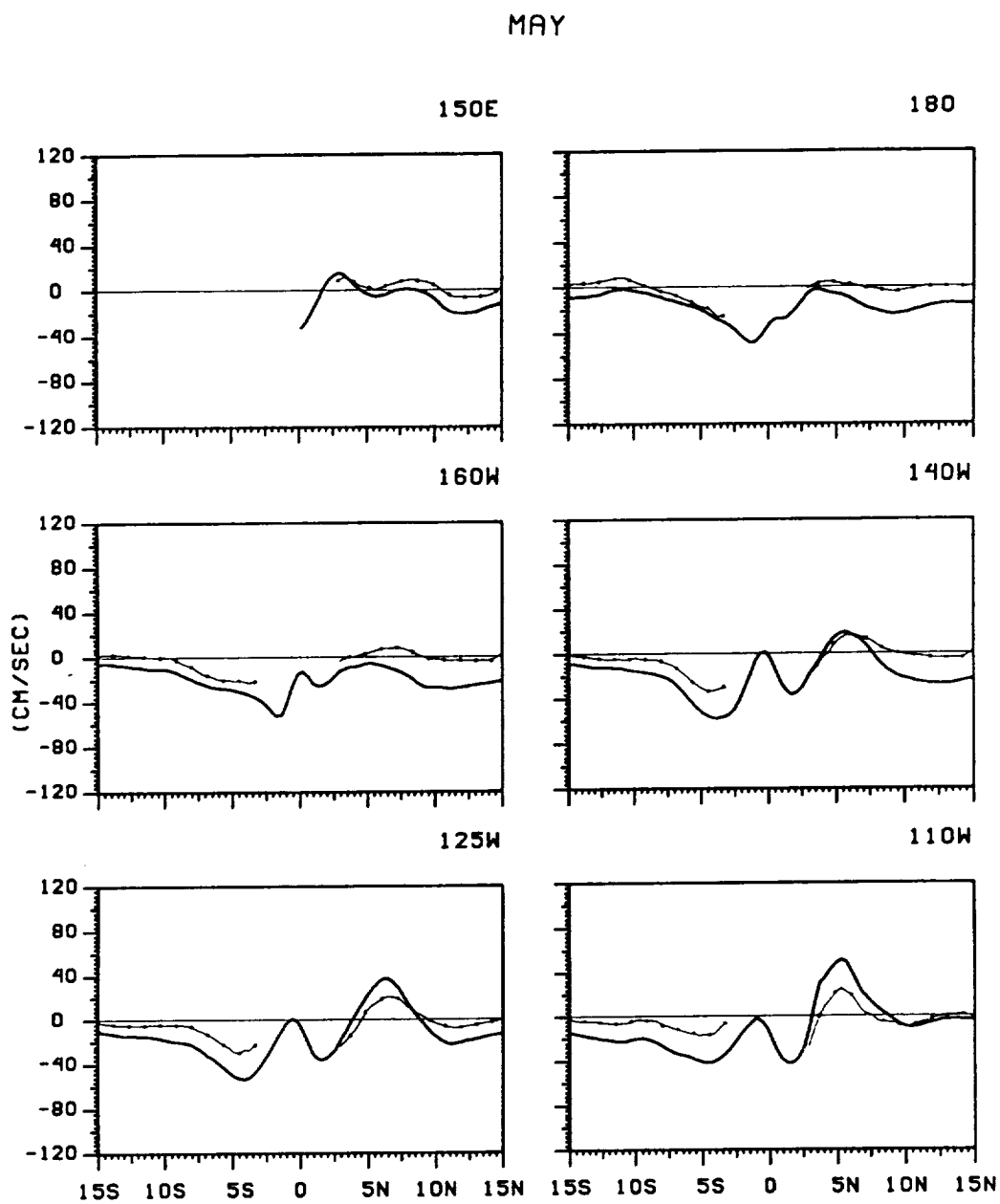


Figure C.3.2

JUNE

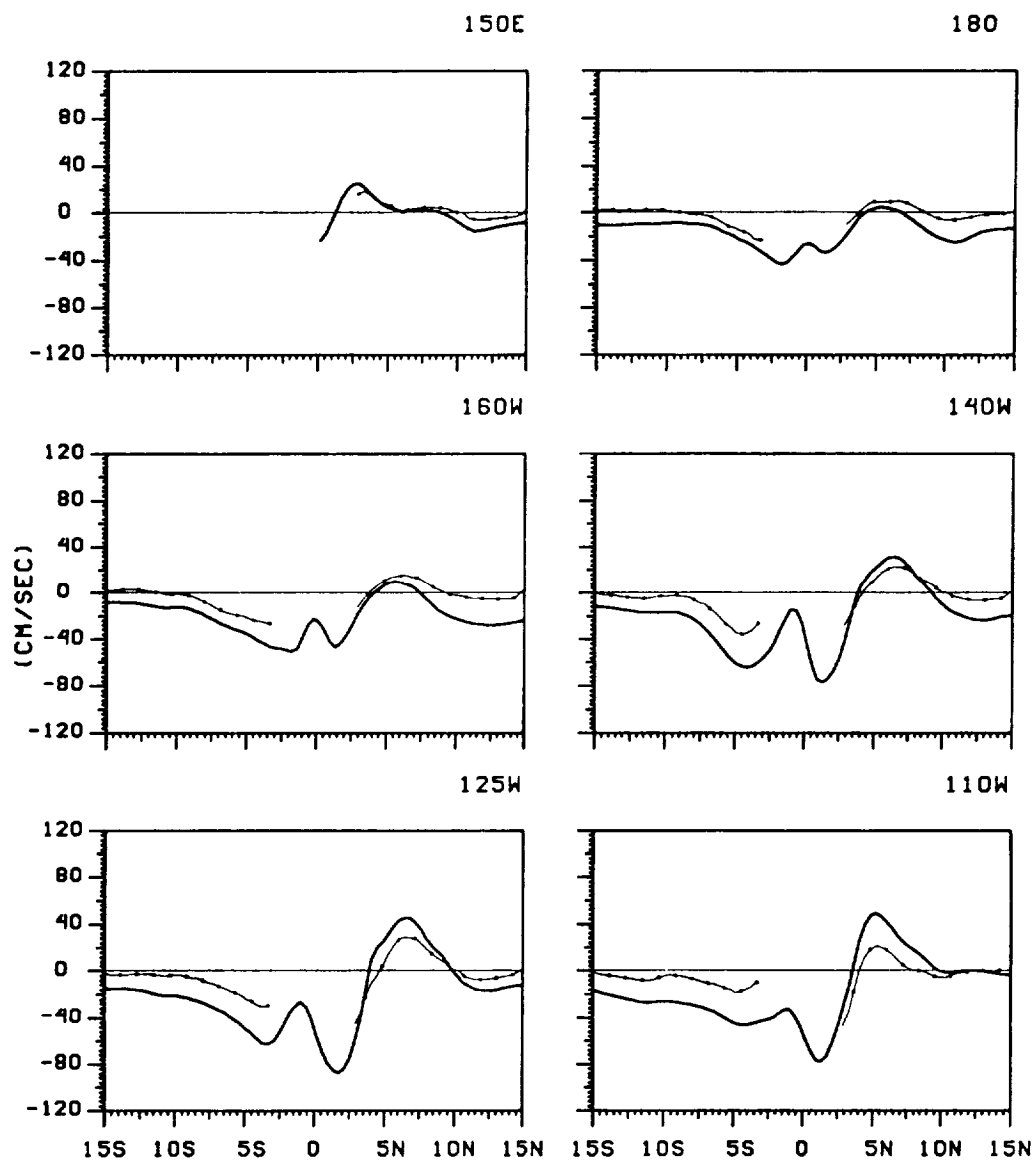


Figure C.3.2

JULY

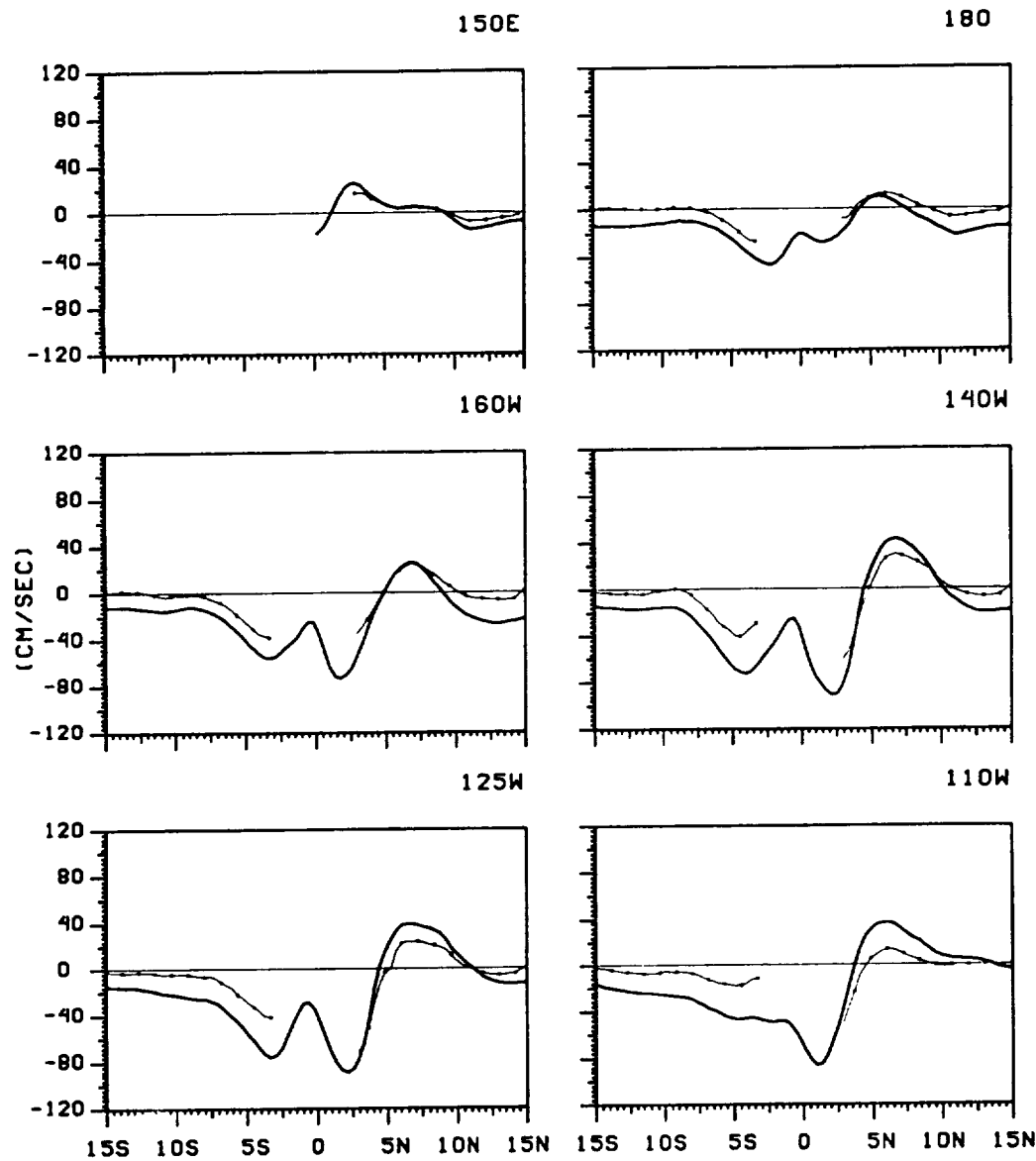


Figure C.3.2

AUGUST

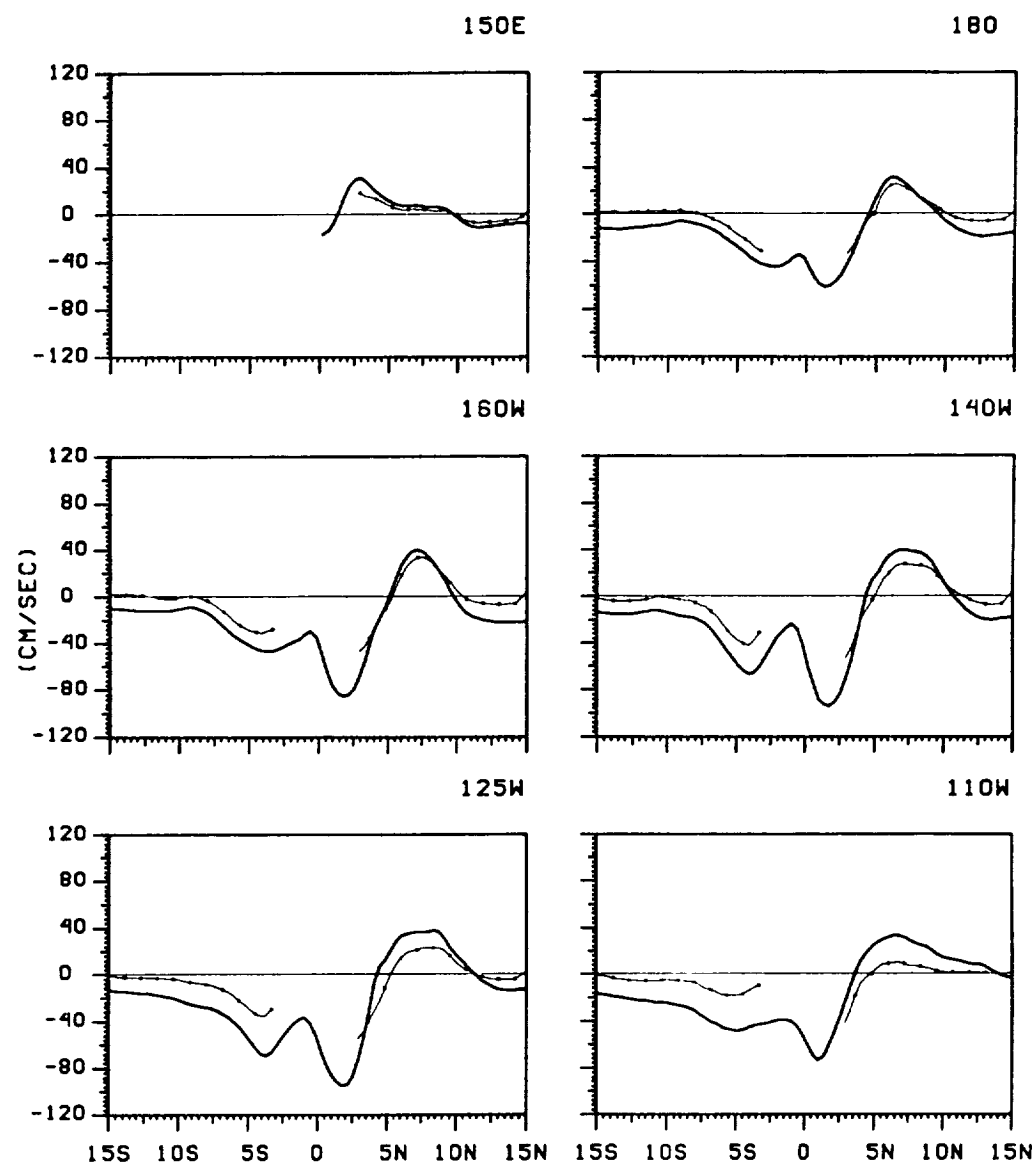


Figure C.3.2

SEPTEMBER

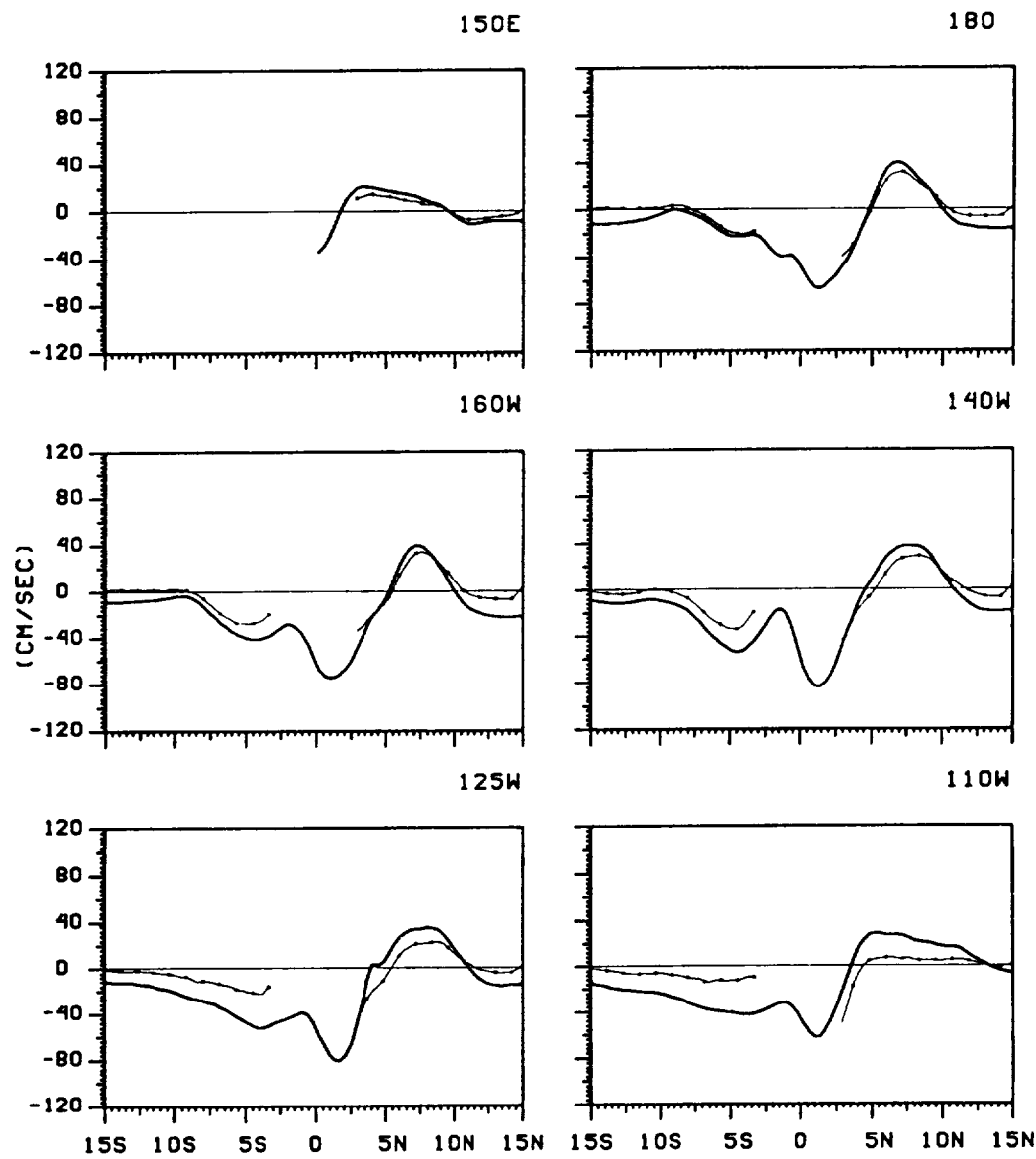


Figure C.3.2

OCTOBER

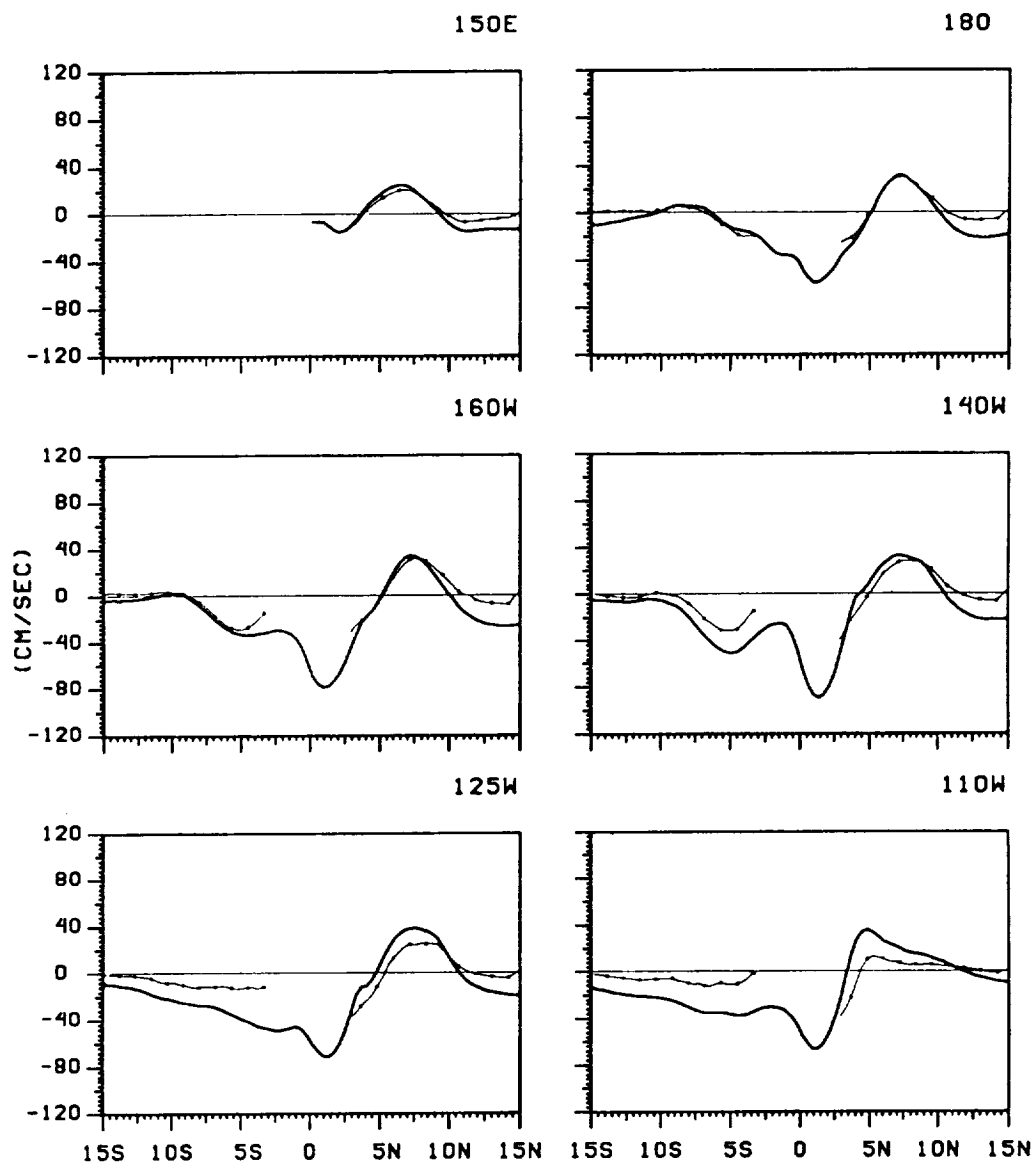


Figure C.3.2

NOVEMBER

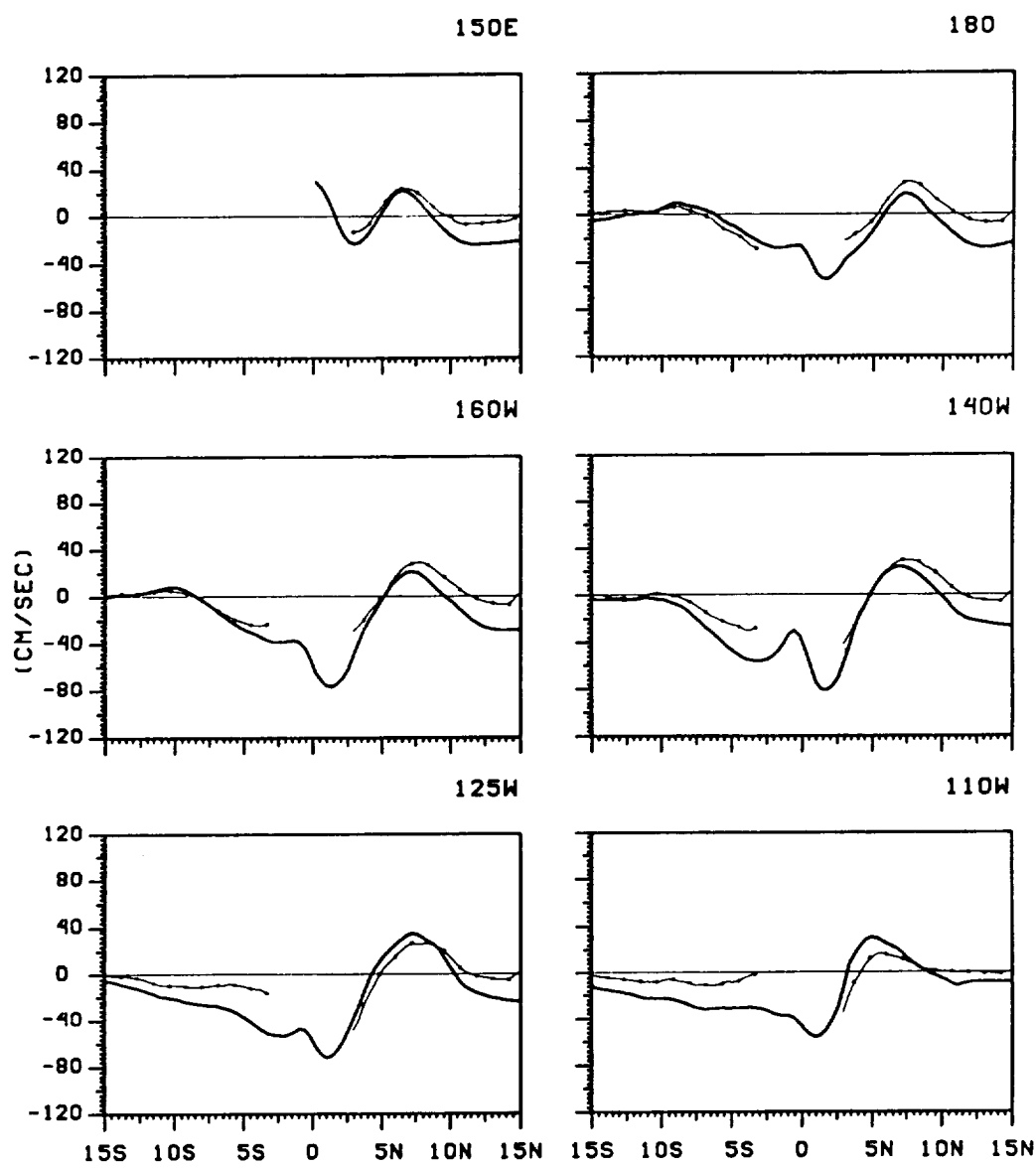


Figure C.3.2

DECEMBER

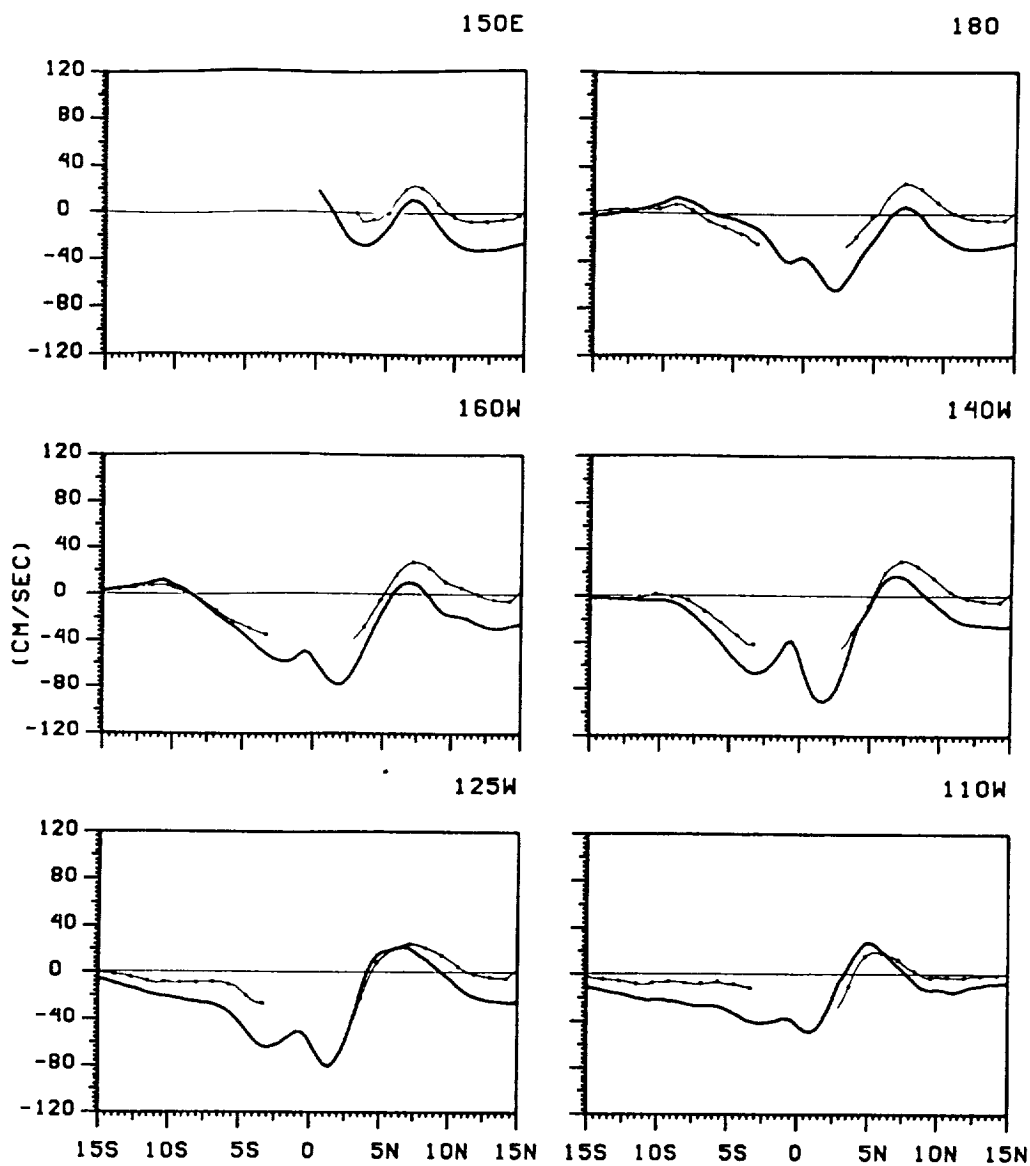


Figure C.3.2

C.4

Profiles of the dynamic height anomaly at 5 m relative to 484×10^4 Pa in dyn cm

JANUARY

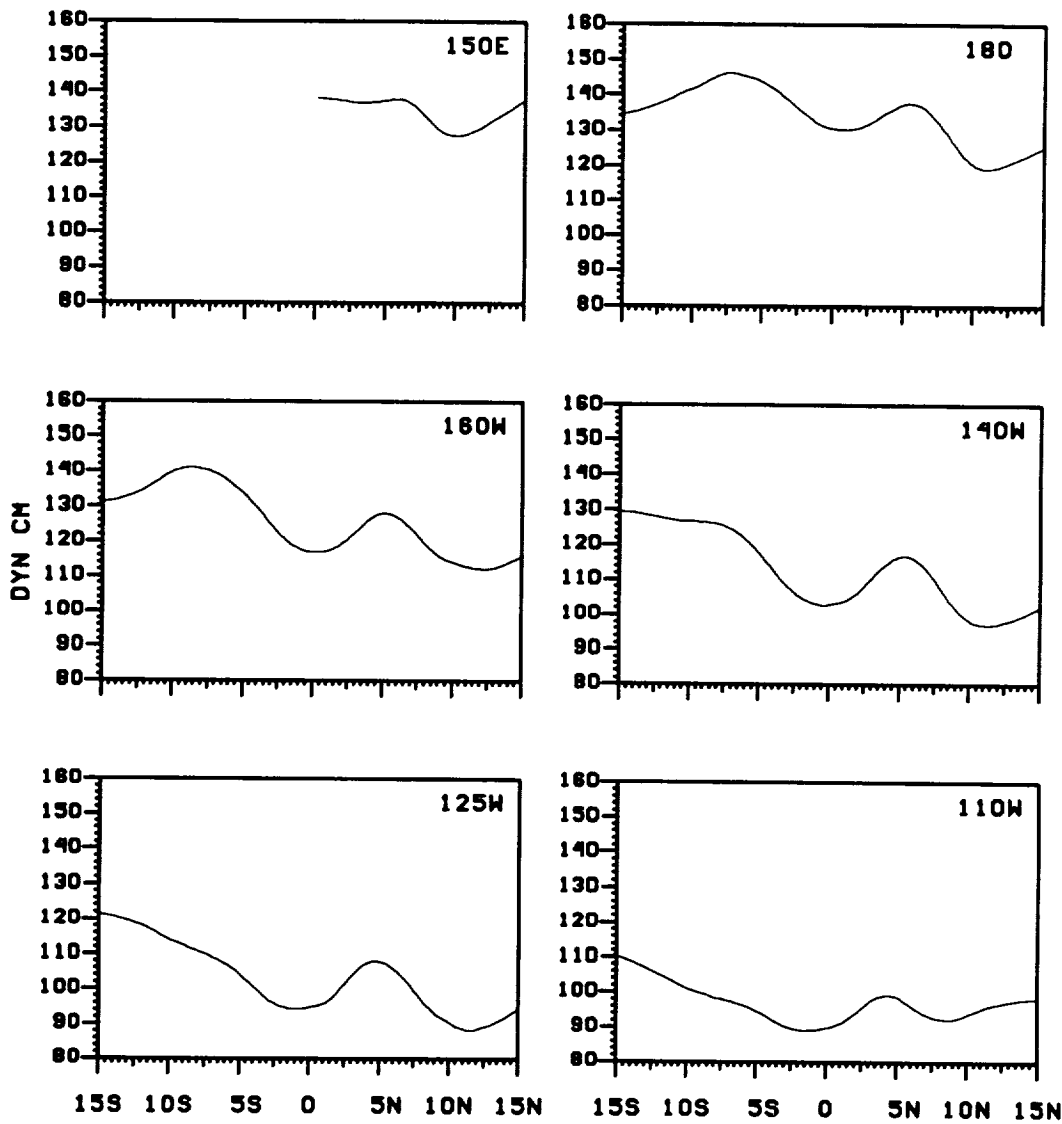


Figure C.4

FEBRUARY

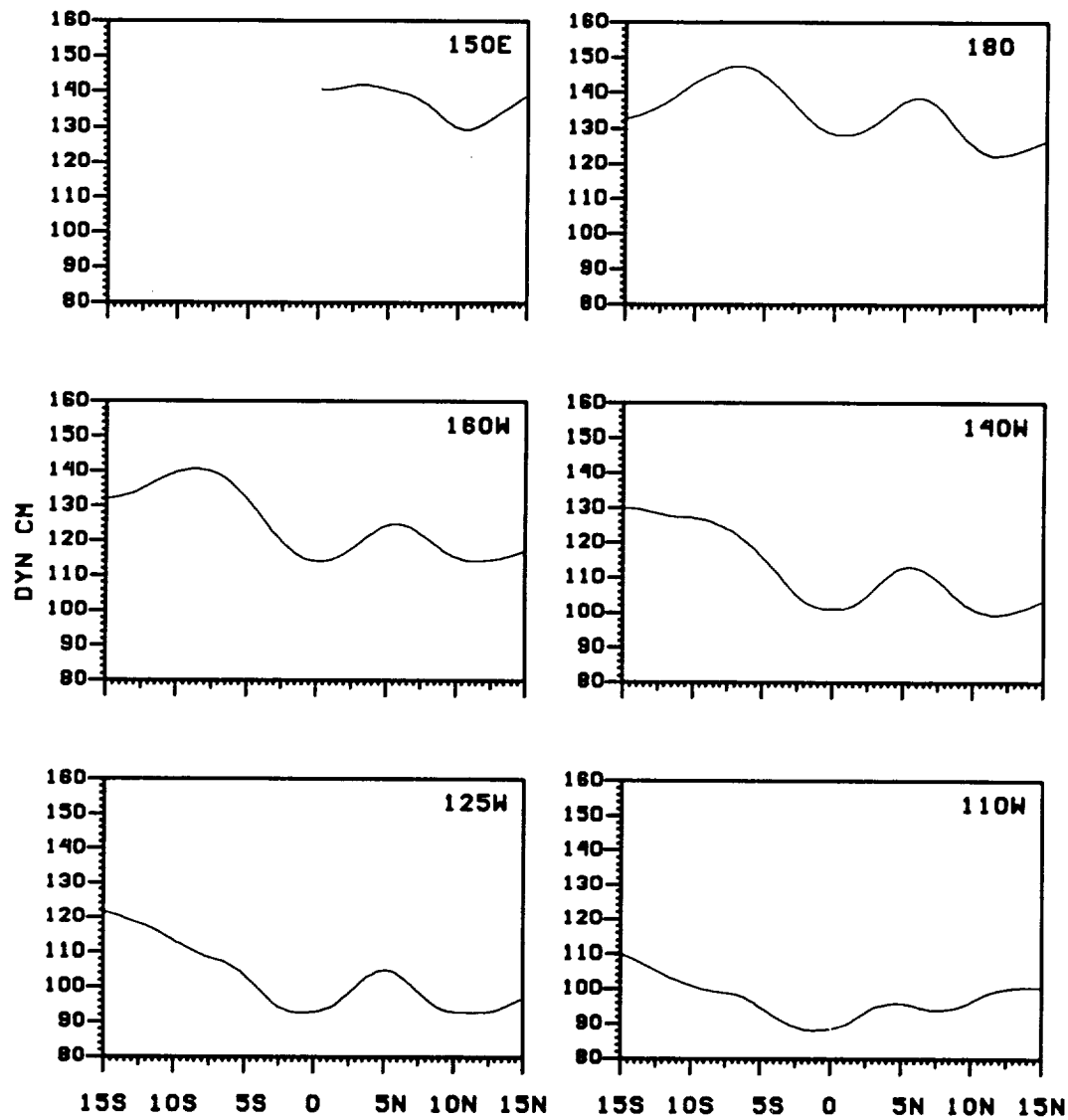


Figure C.4

MARCH

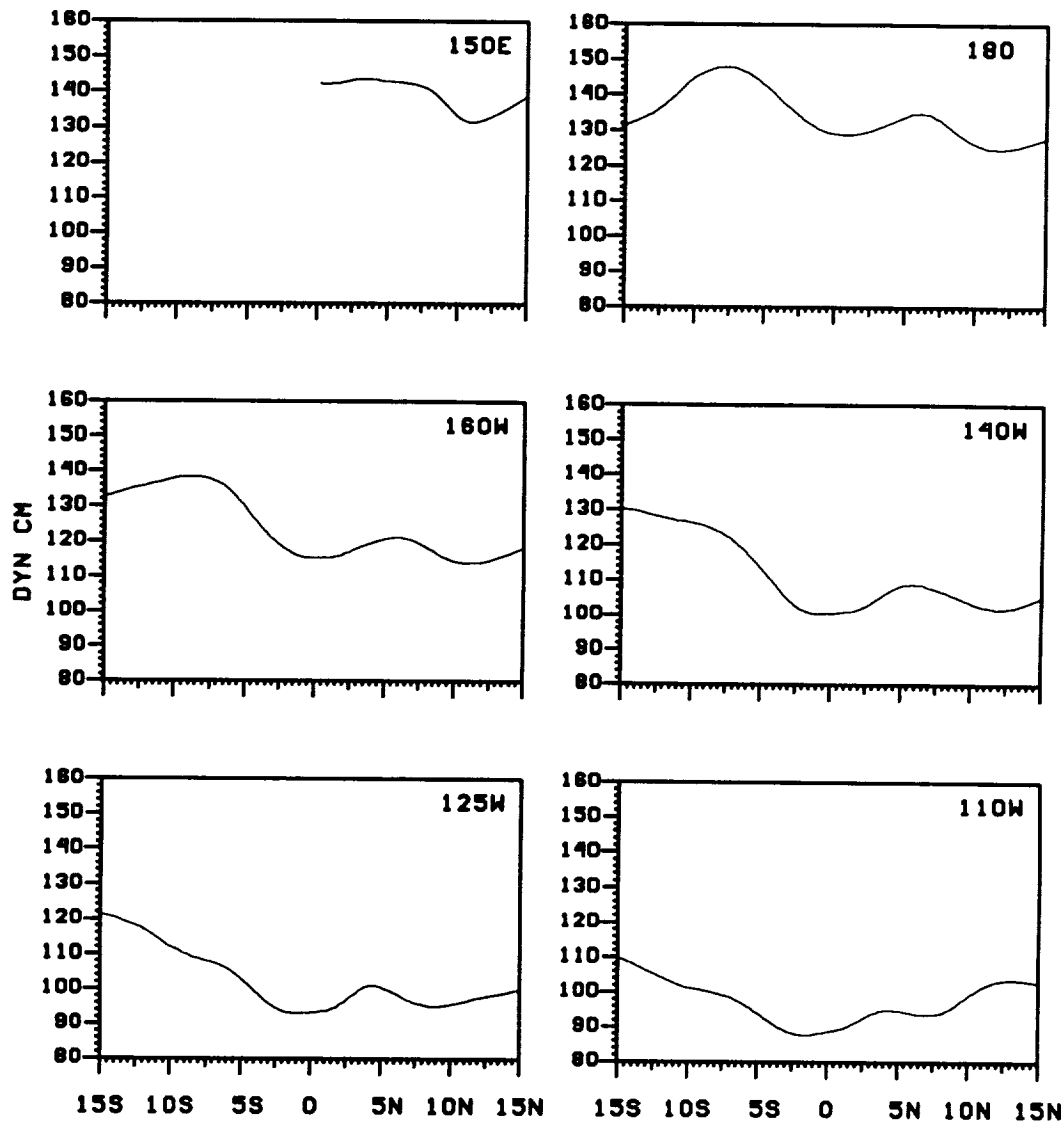


Figure C.4

APRIL

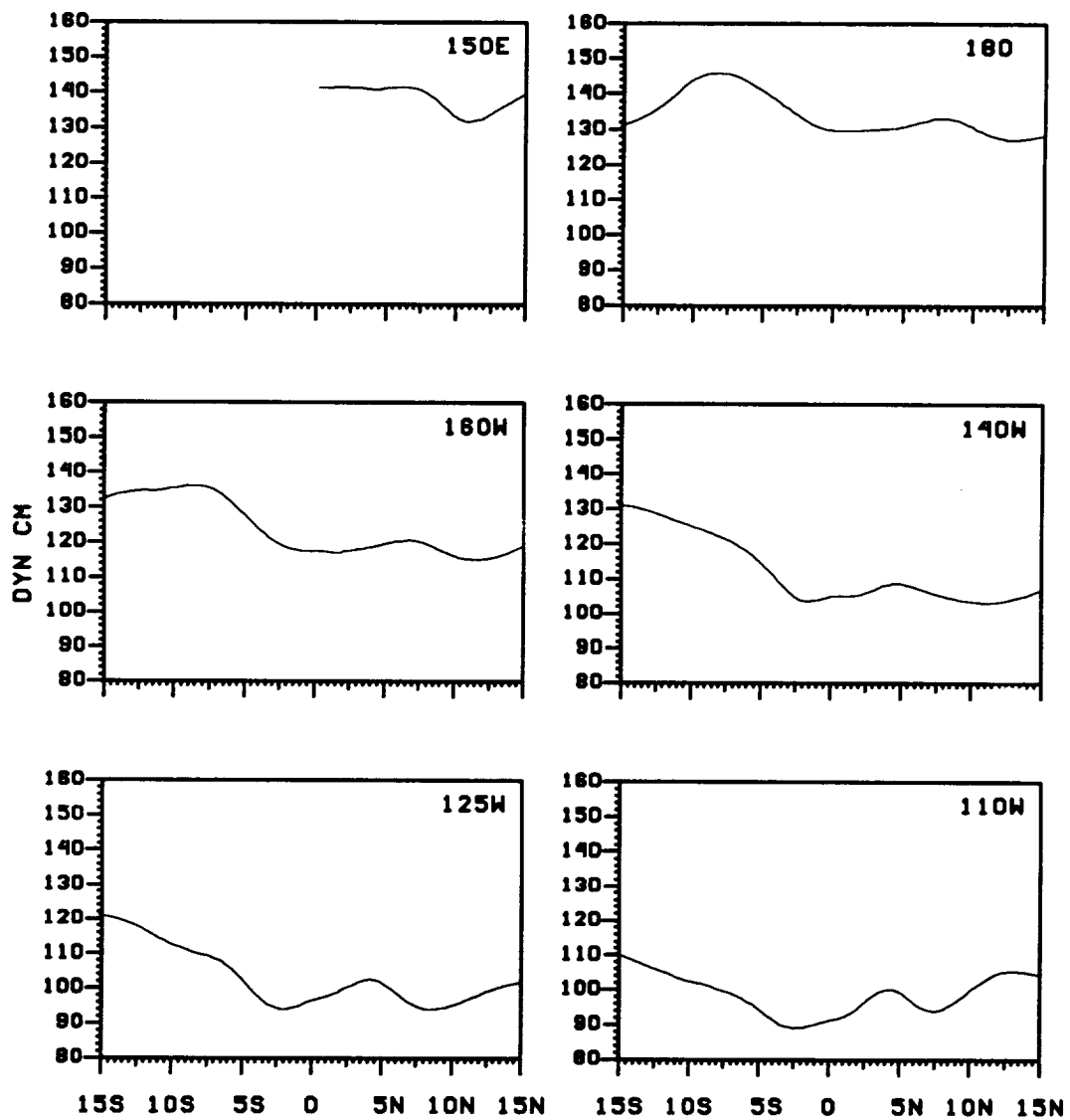


Figure C.4

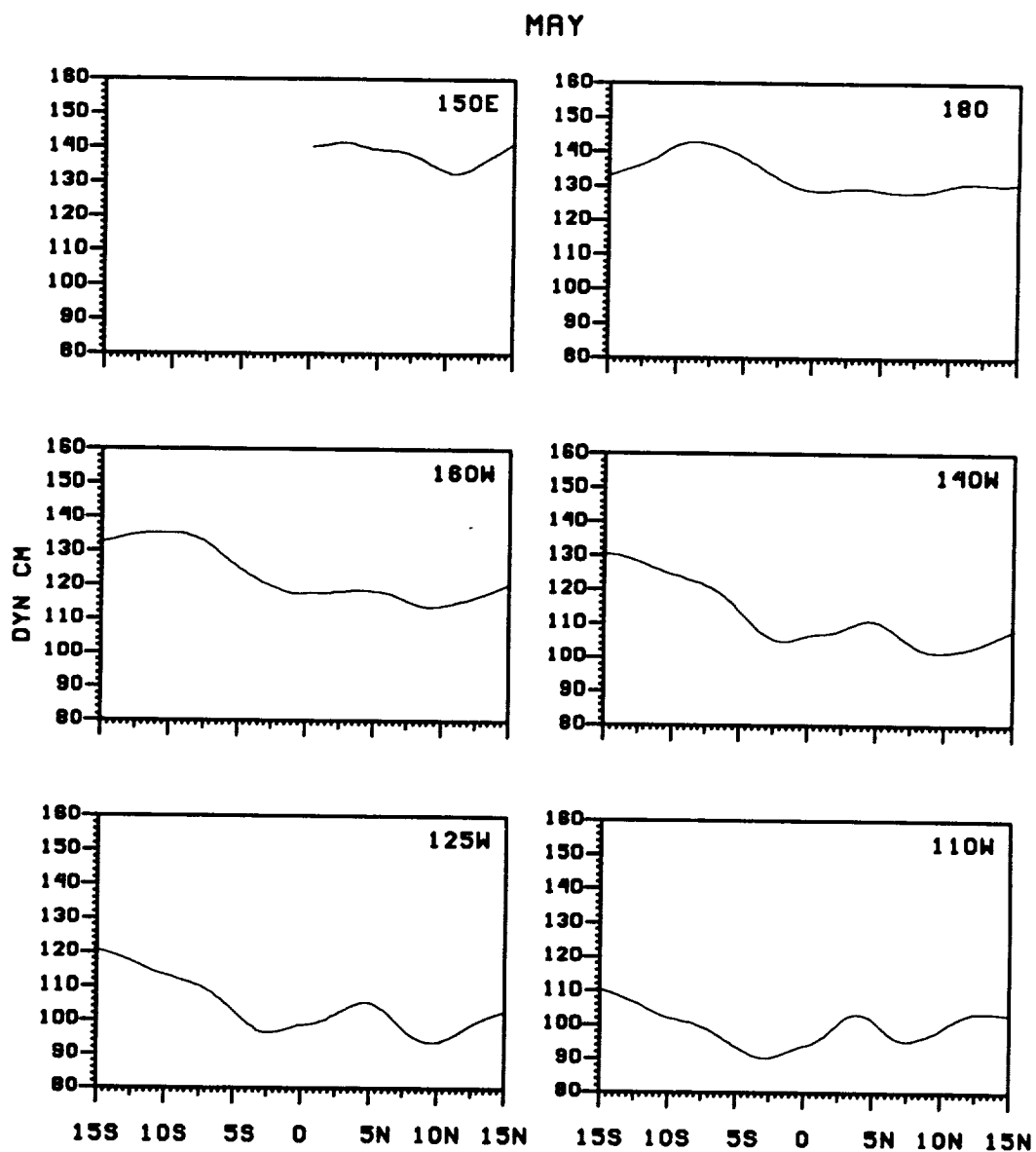


Figure C.4

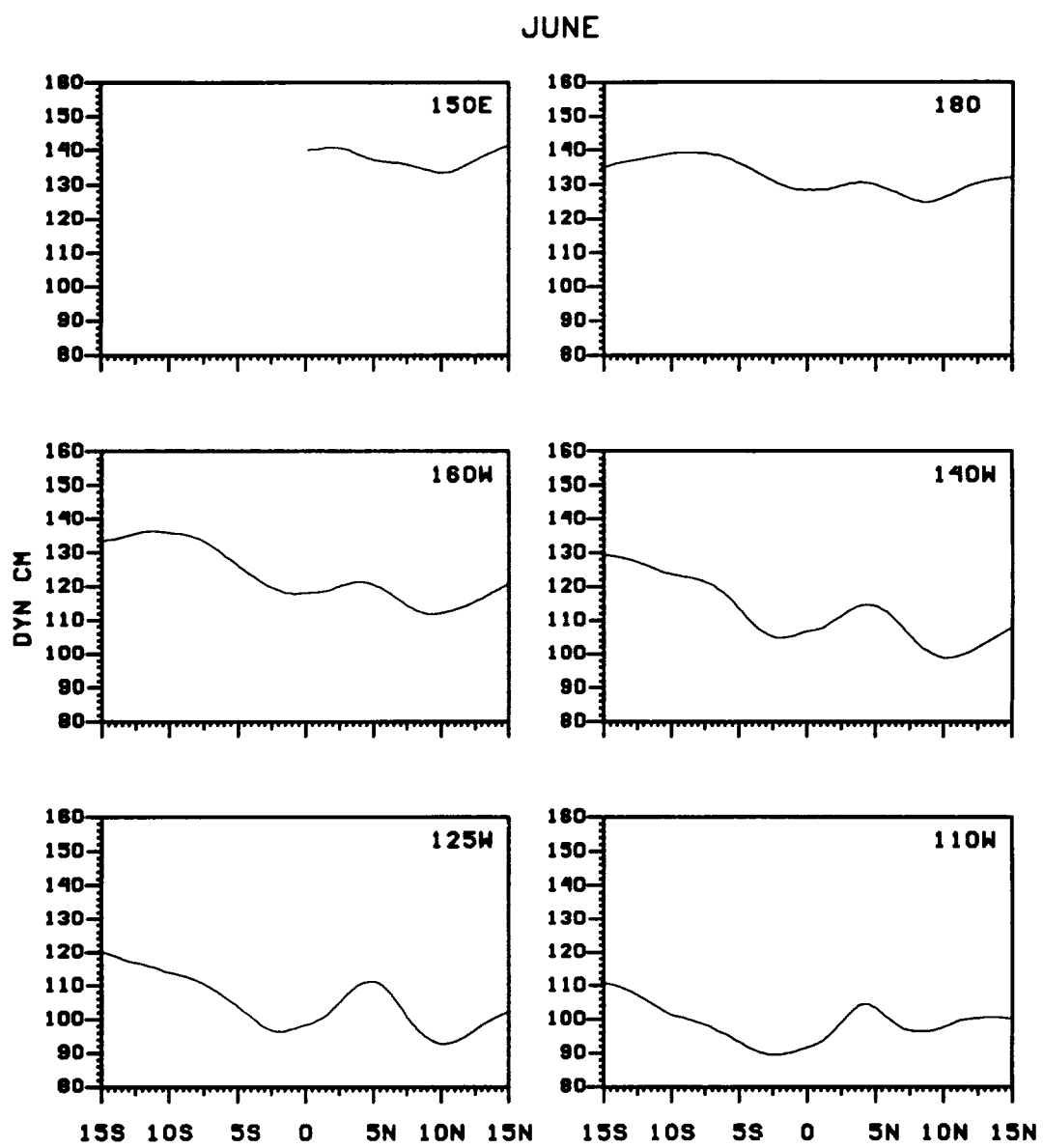


Figure C.4

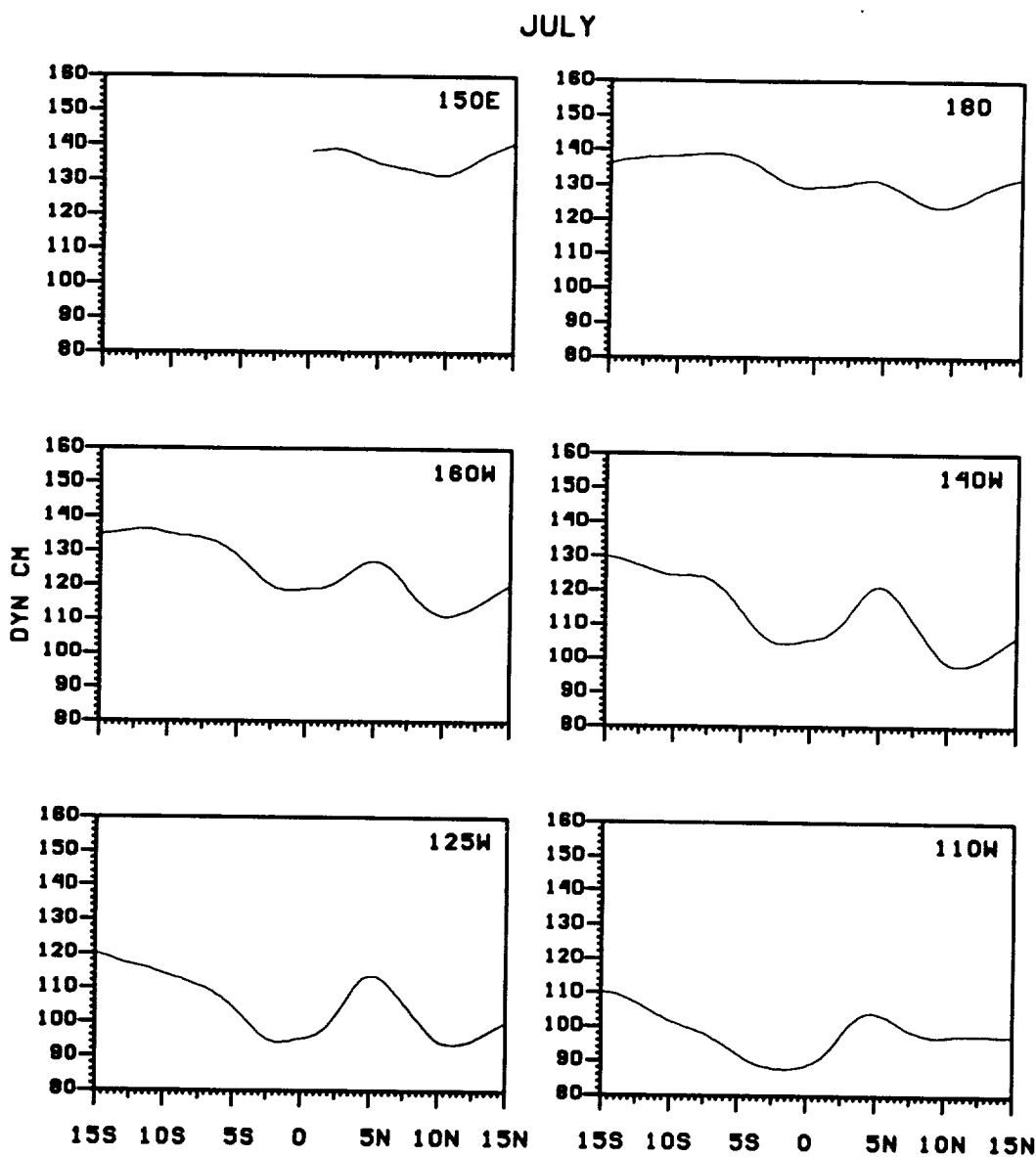


Figure C.4

AUGUST

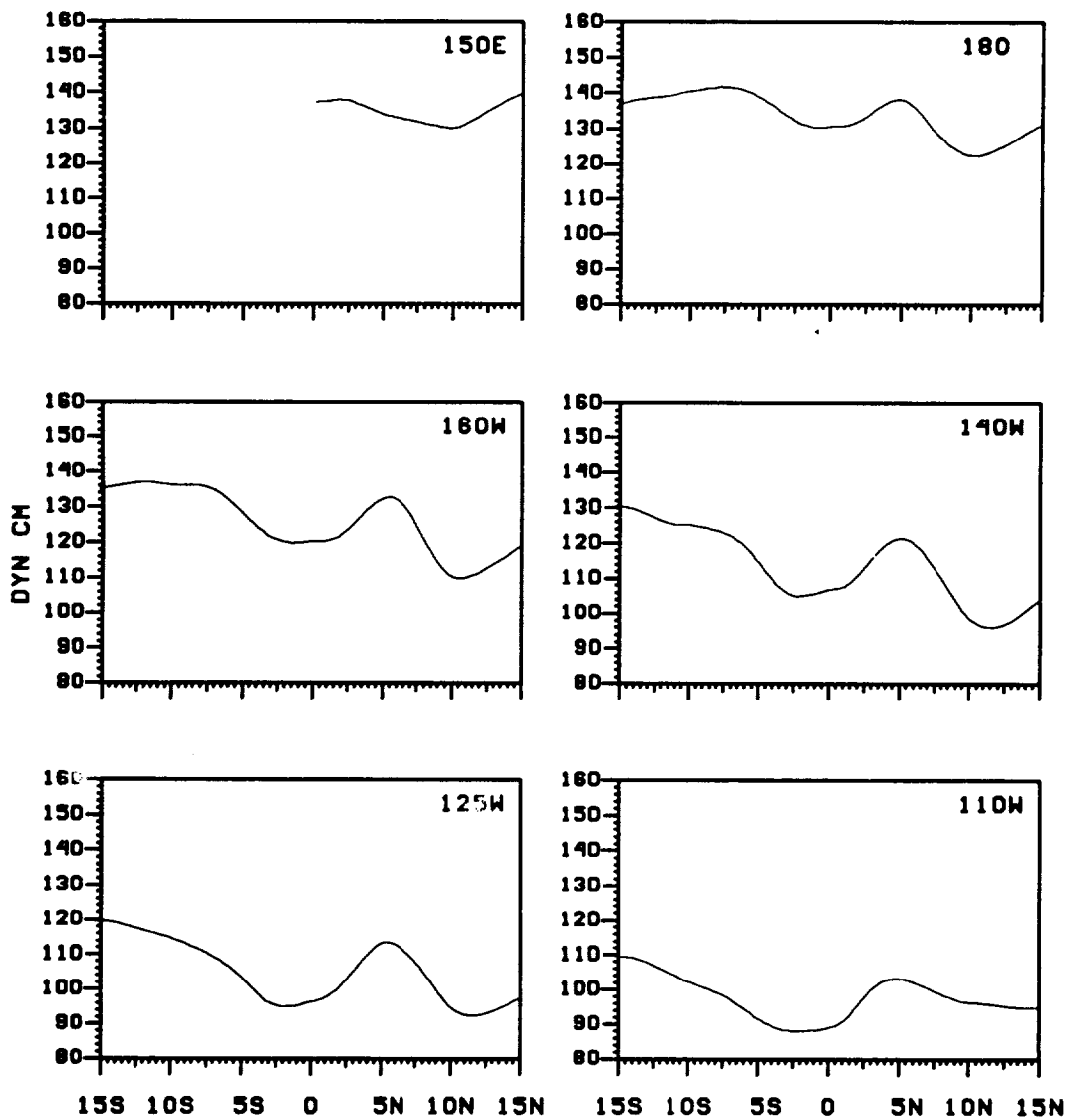


Figure C.4

SEPTEMBER

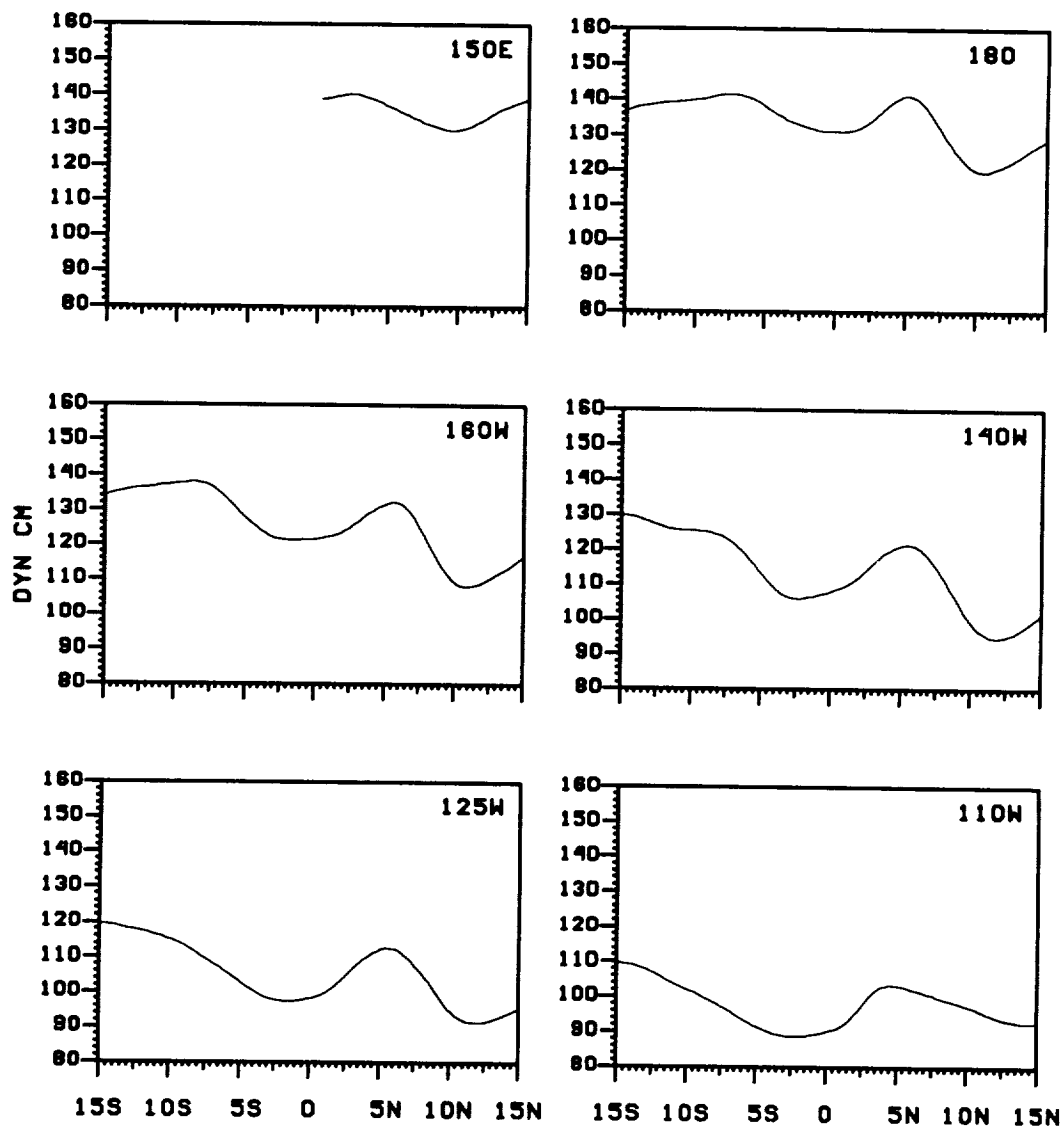


Figure C.4

OCTOBER

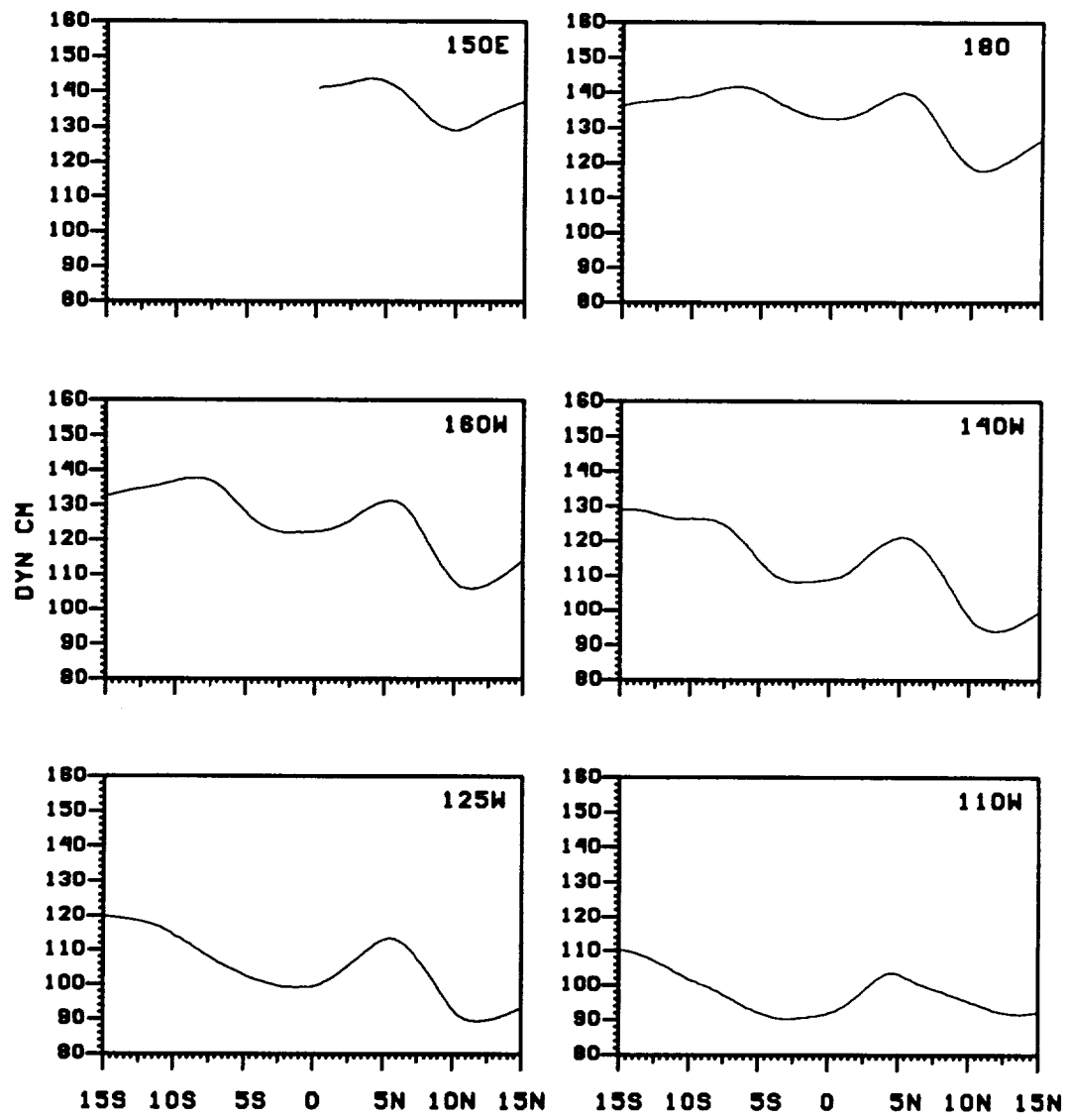


Figure C.4

NOVEMBER

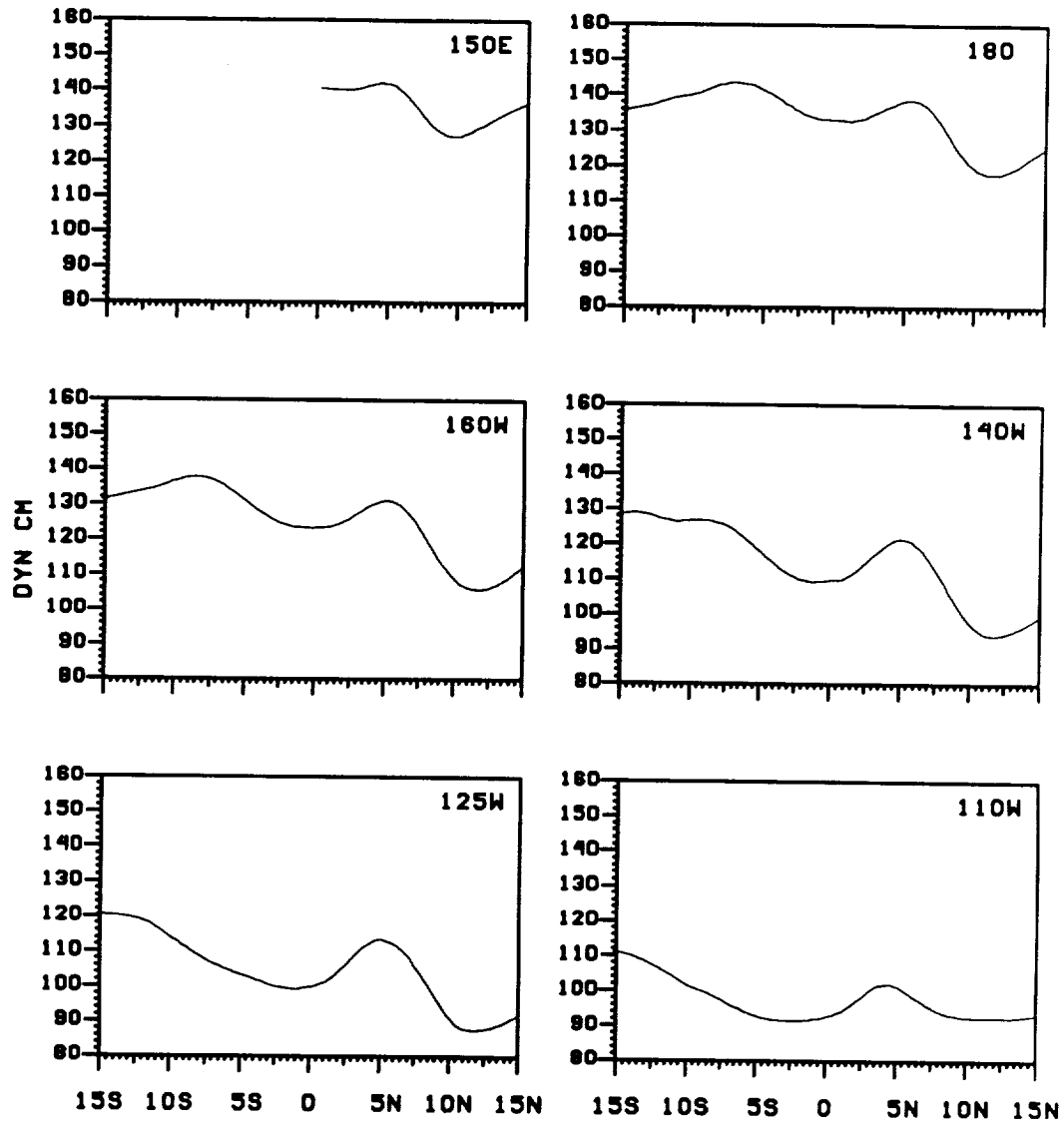


Figure C.4

DECEMBER

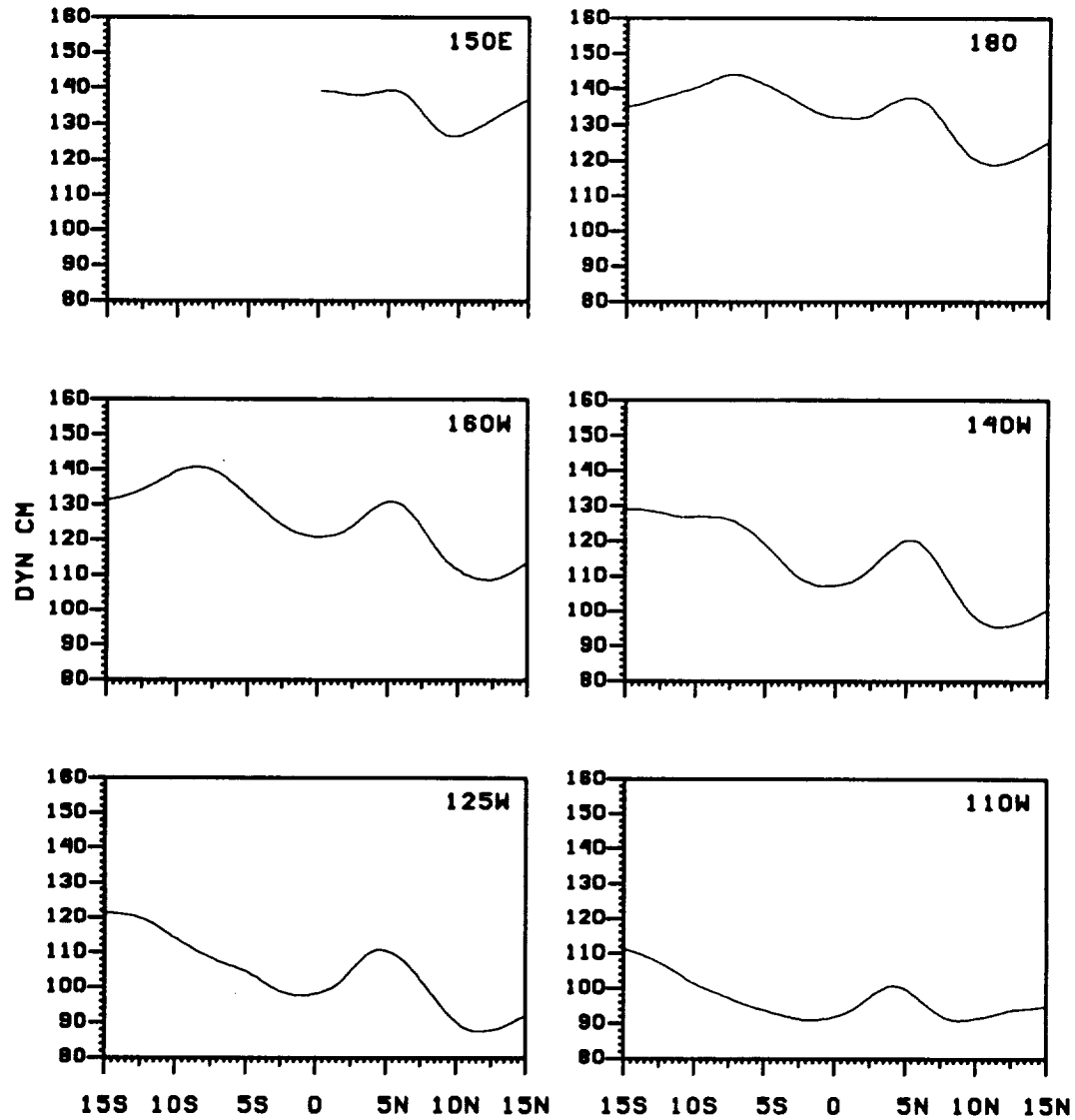


Figure C.4

C.5

Temperature profiles in °C

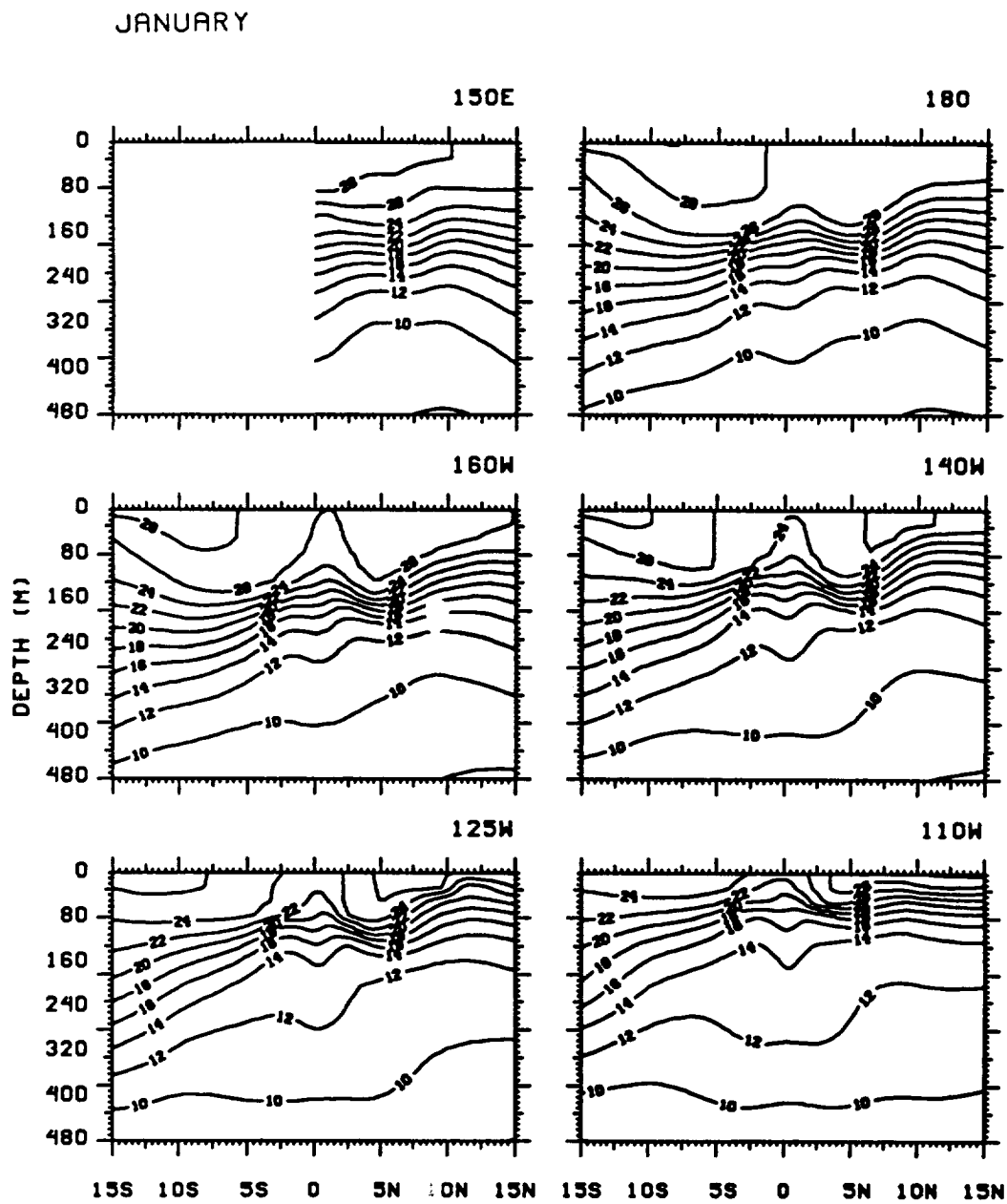


Figure C.5

FEBRUARY

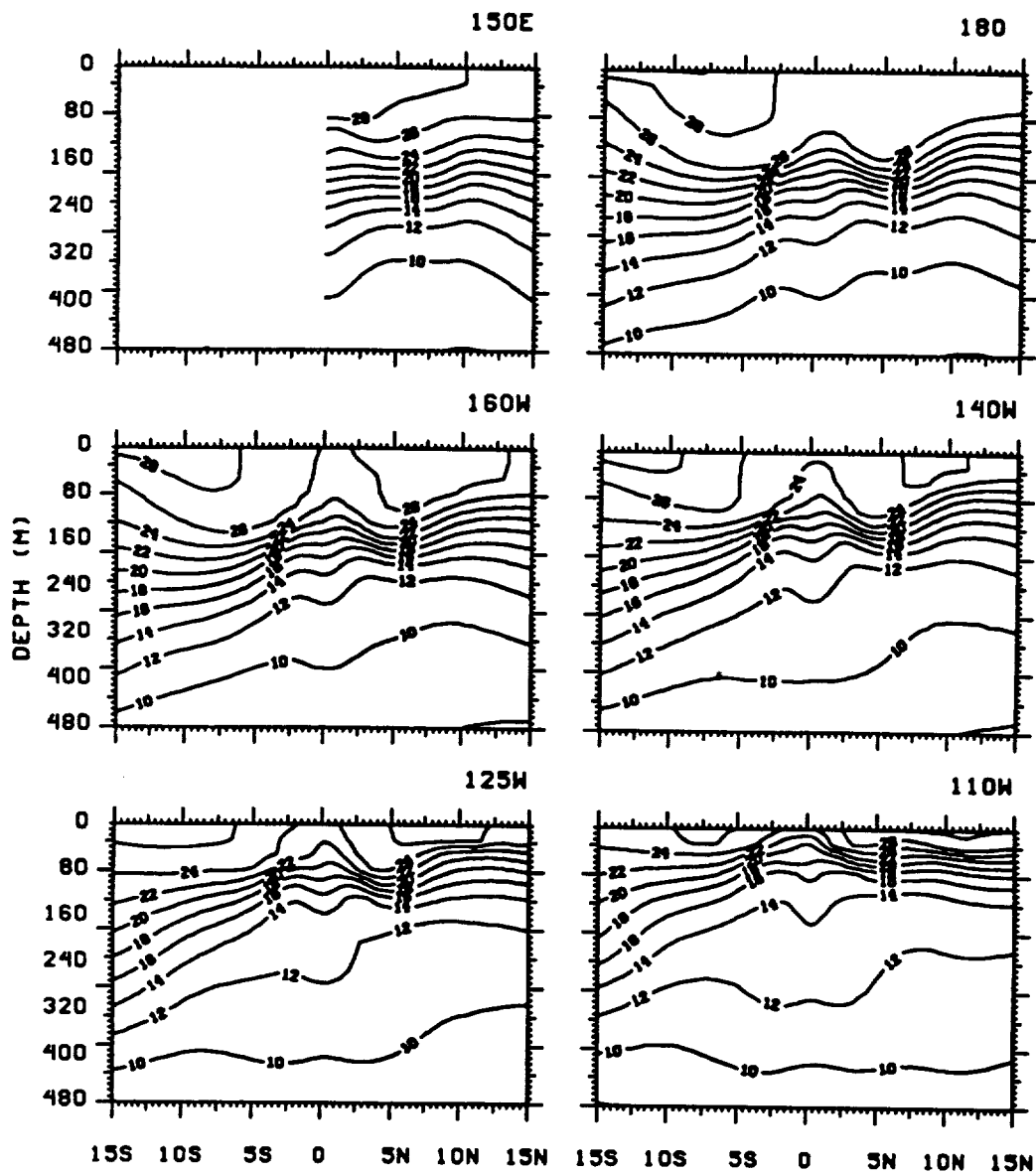


Figure C.5

MARCH

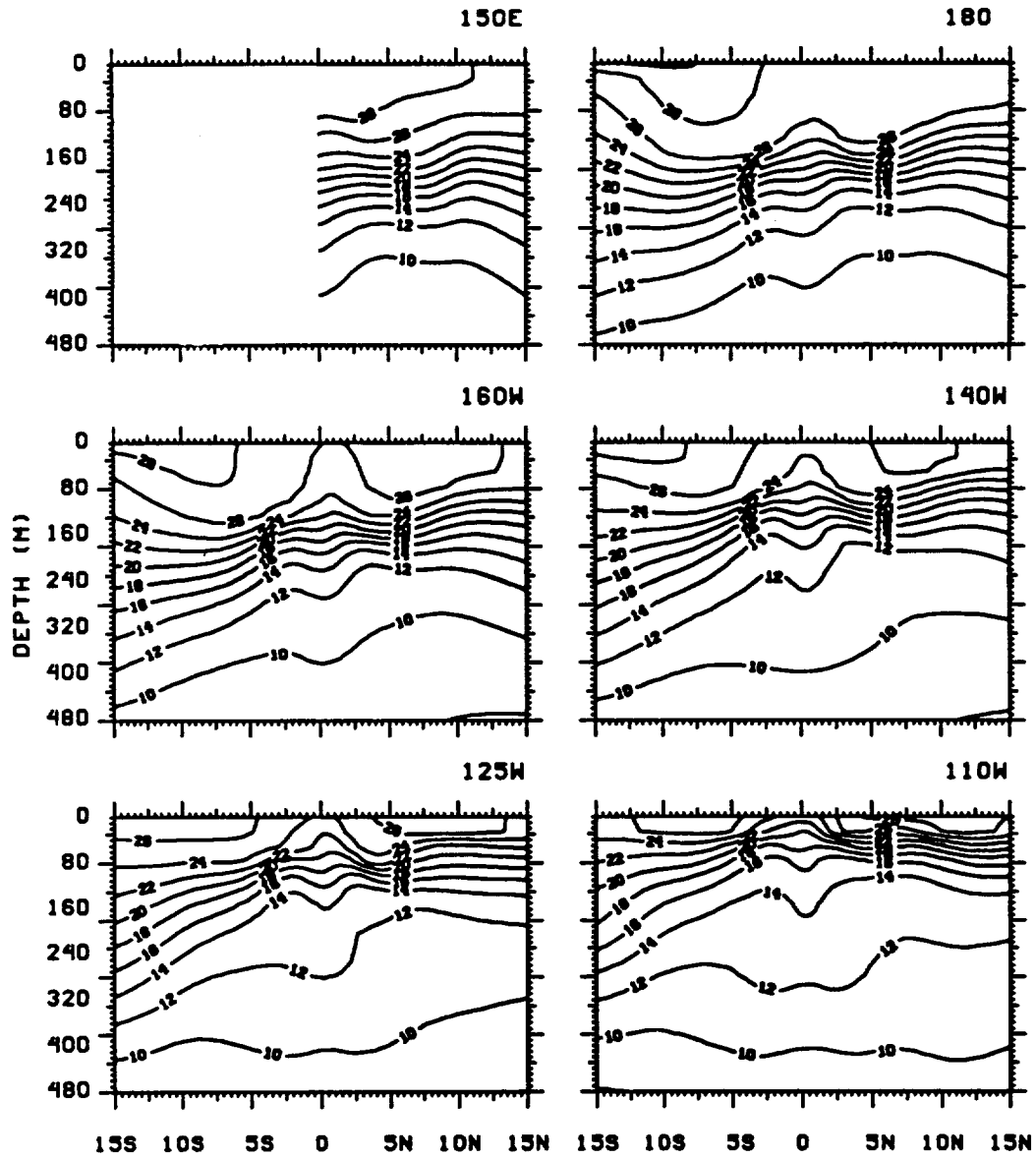


Figure C.5

APRIL

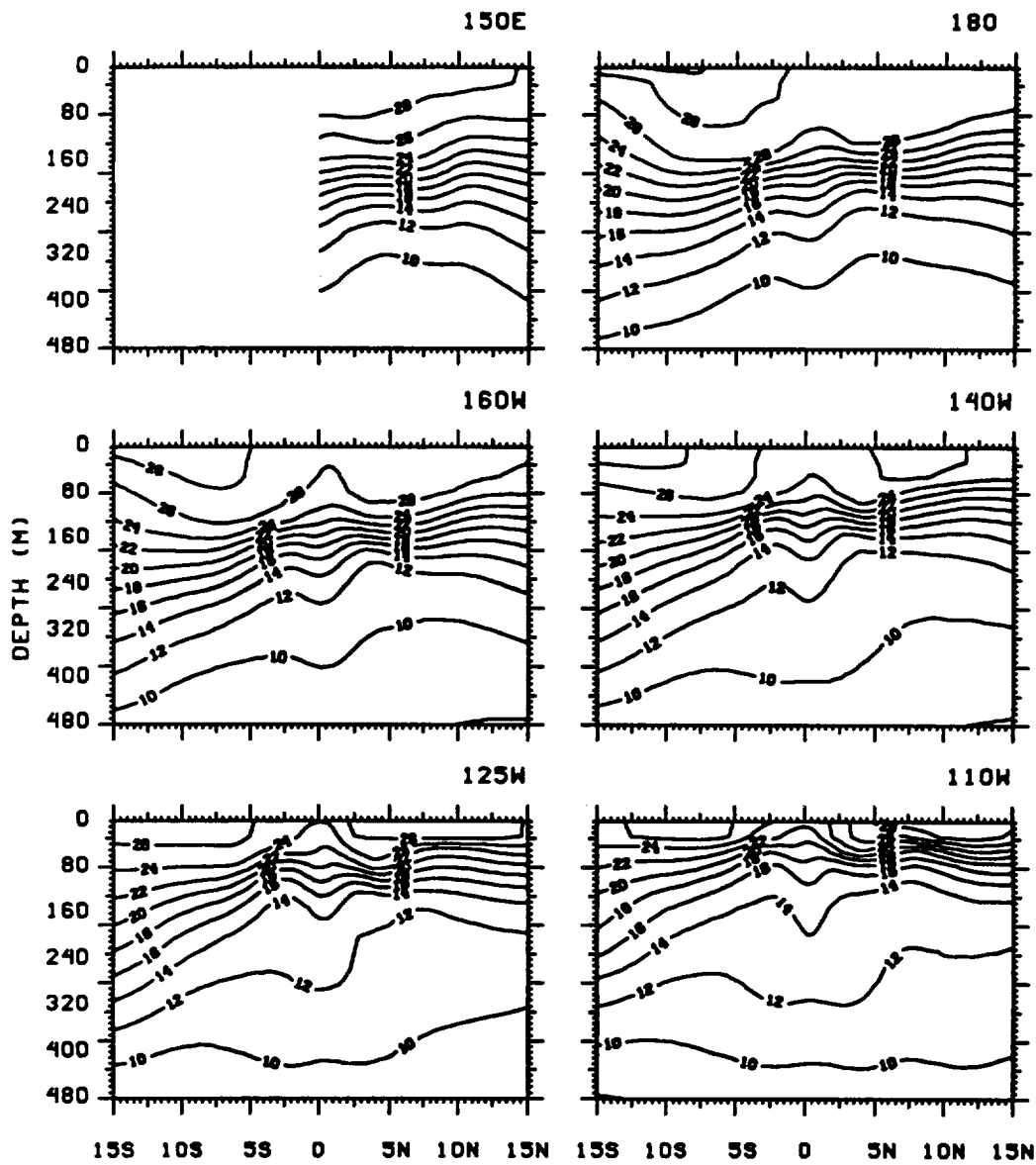


Figure C.5

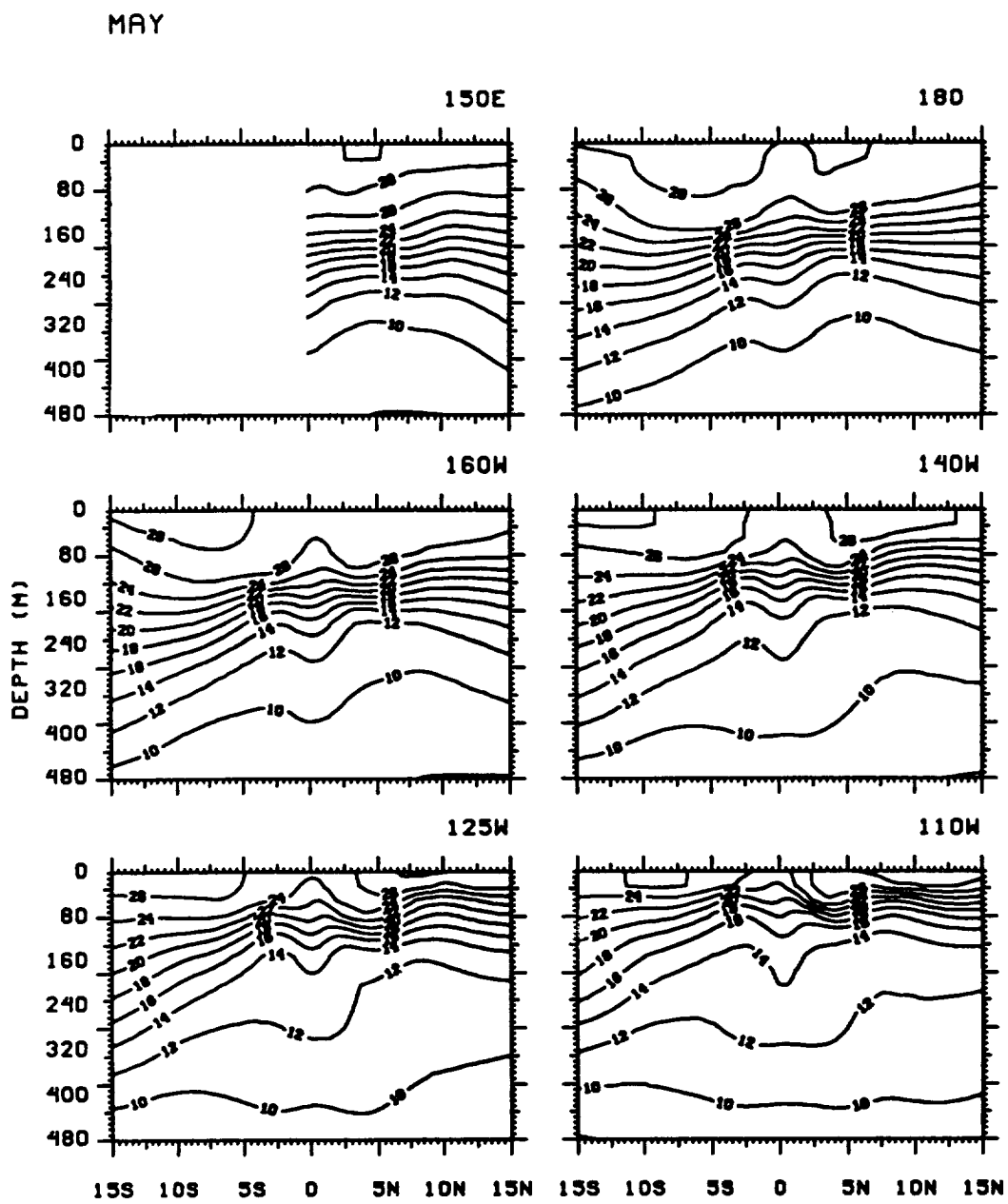


Figure C.5

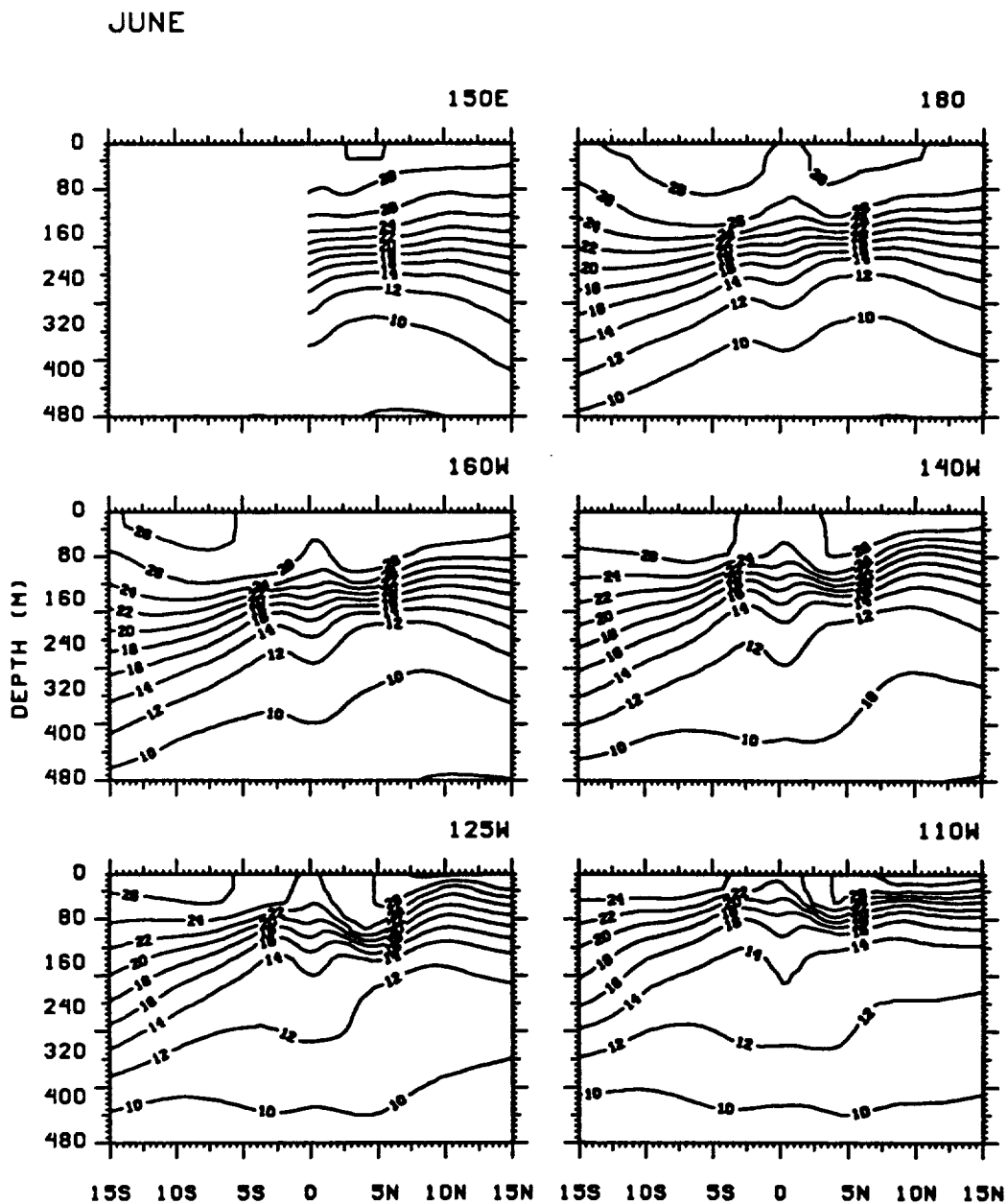


Figure C.5

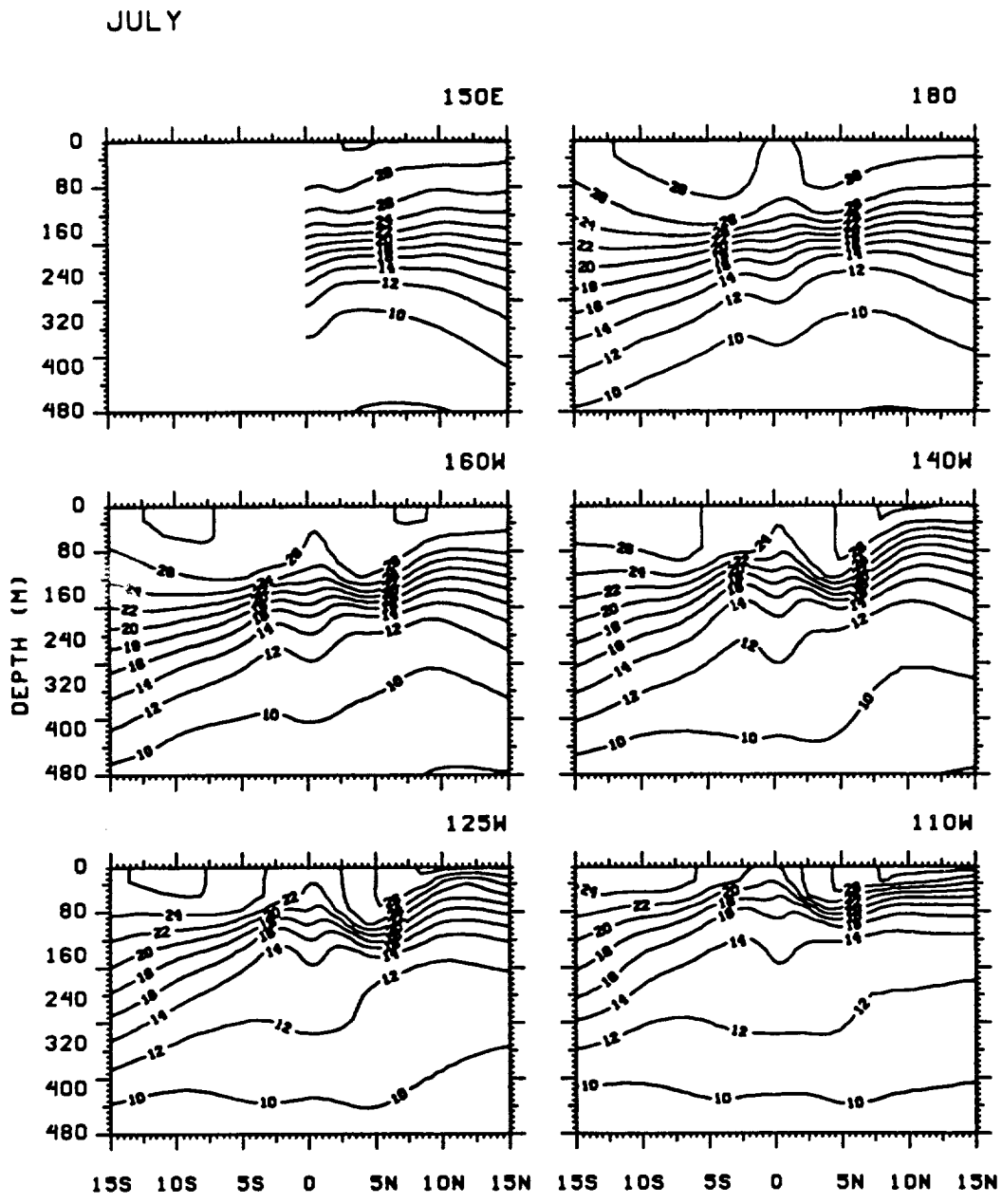


Figure C.5

AUGUST

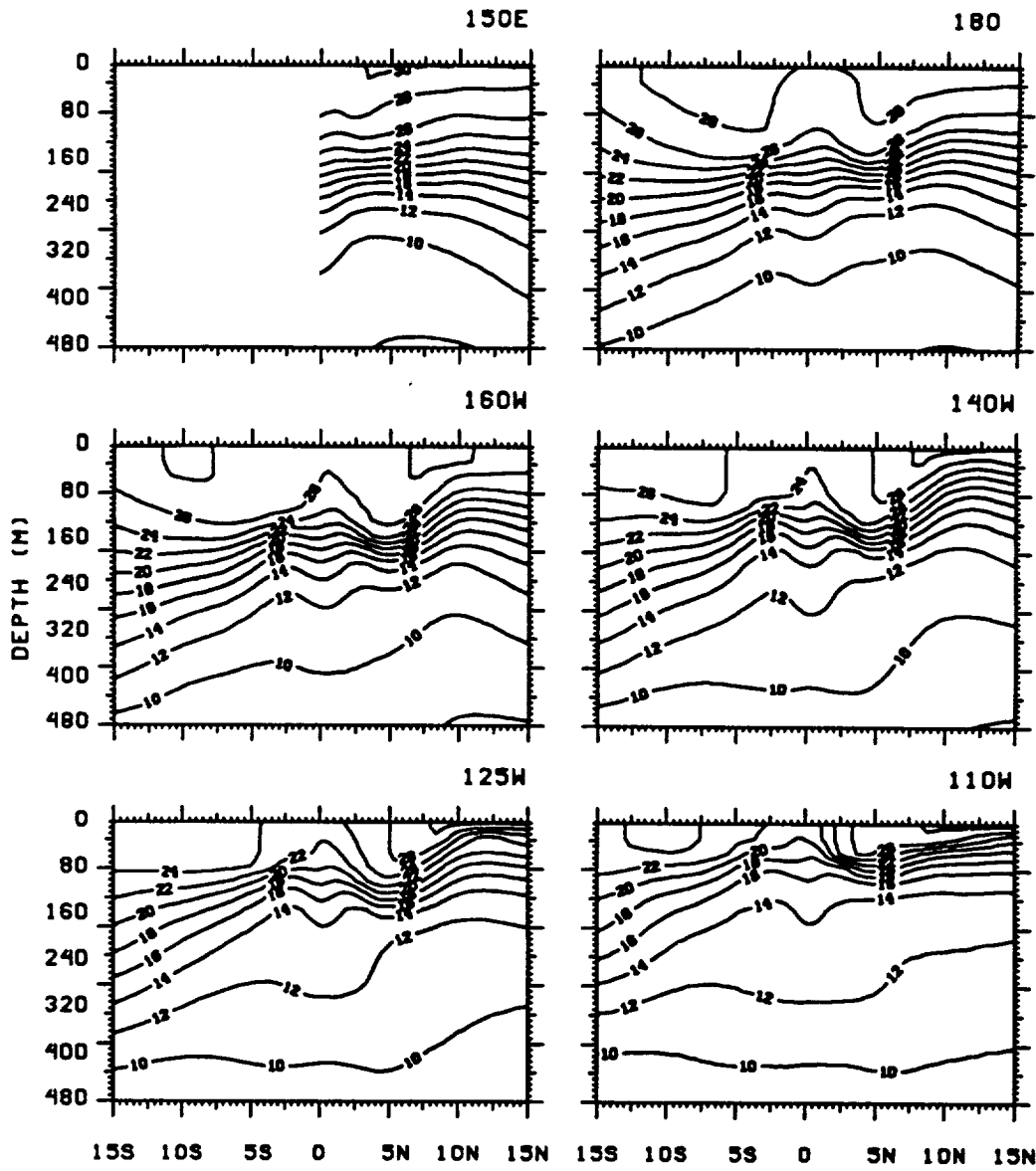


Figure C.5

SEPTEMBER

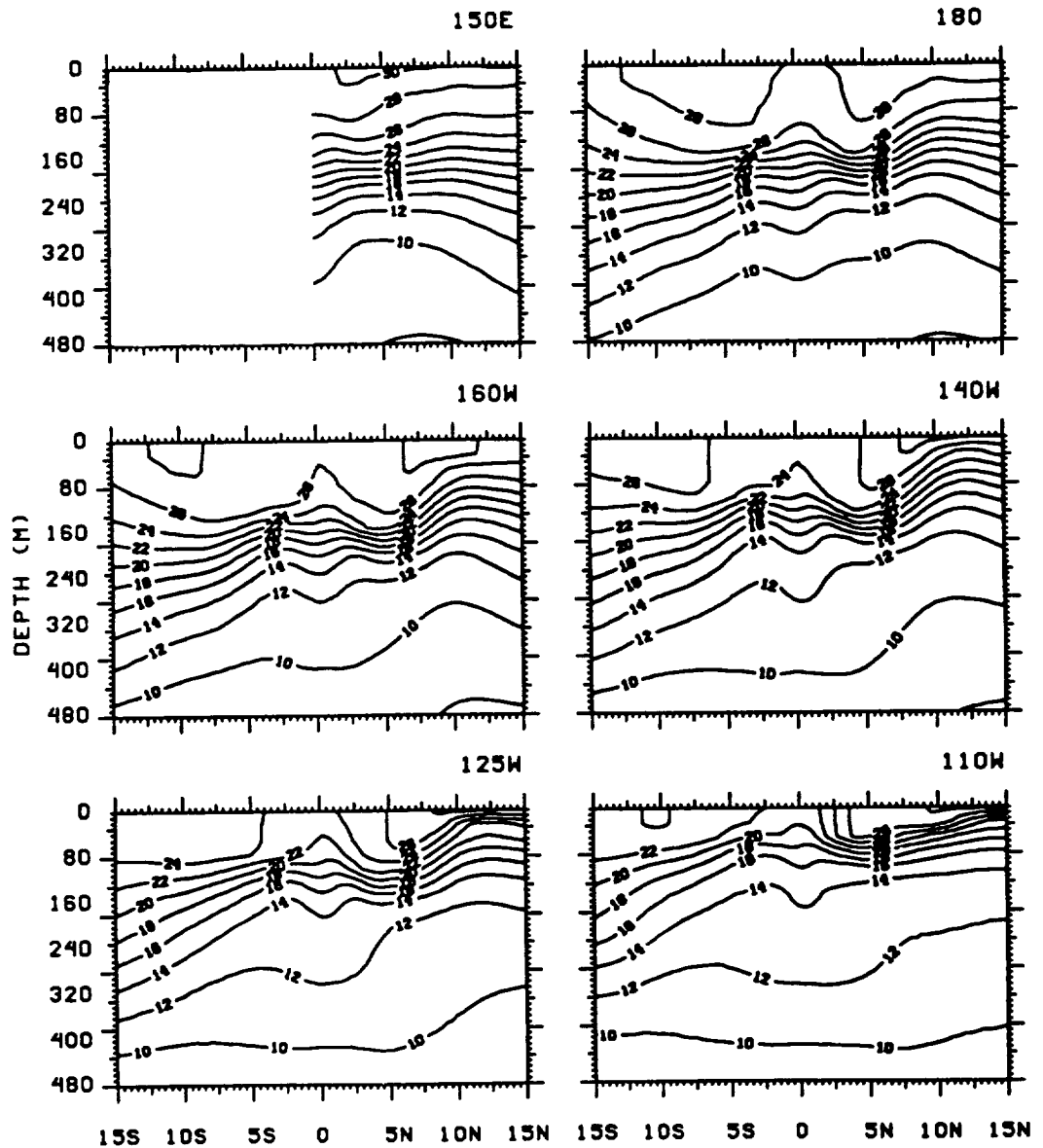


Figure C.5

OCTOBER

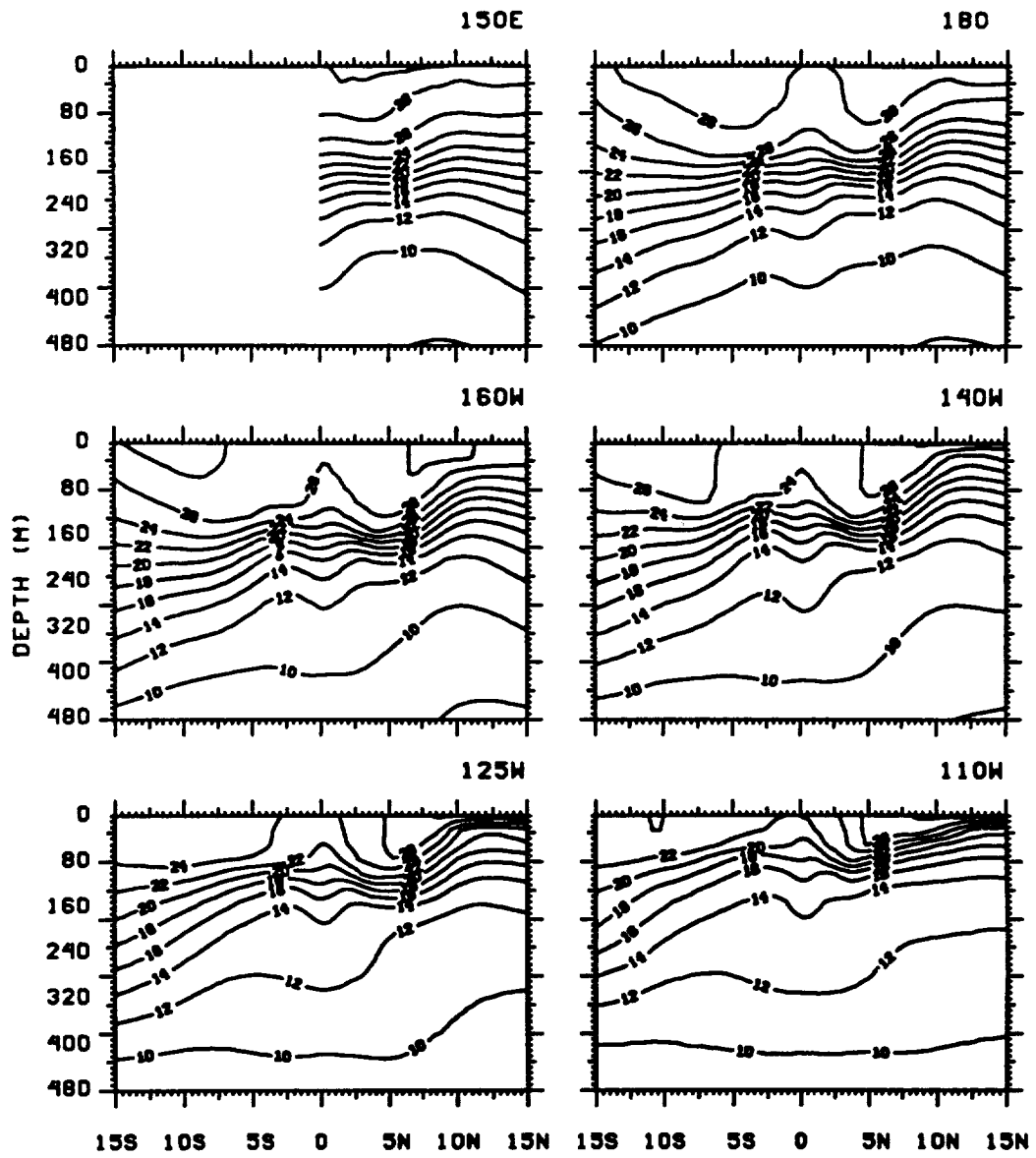


Figure C.5

NOVEMBER

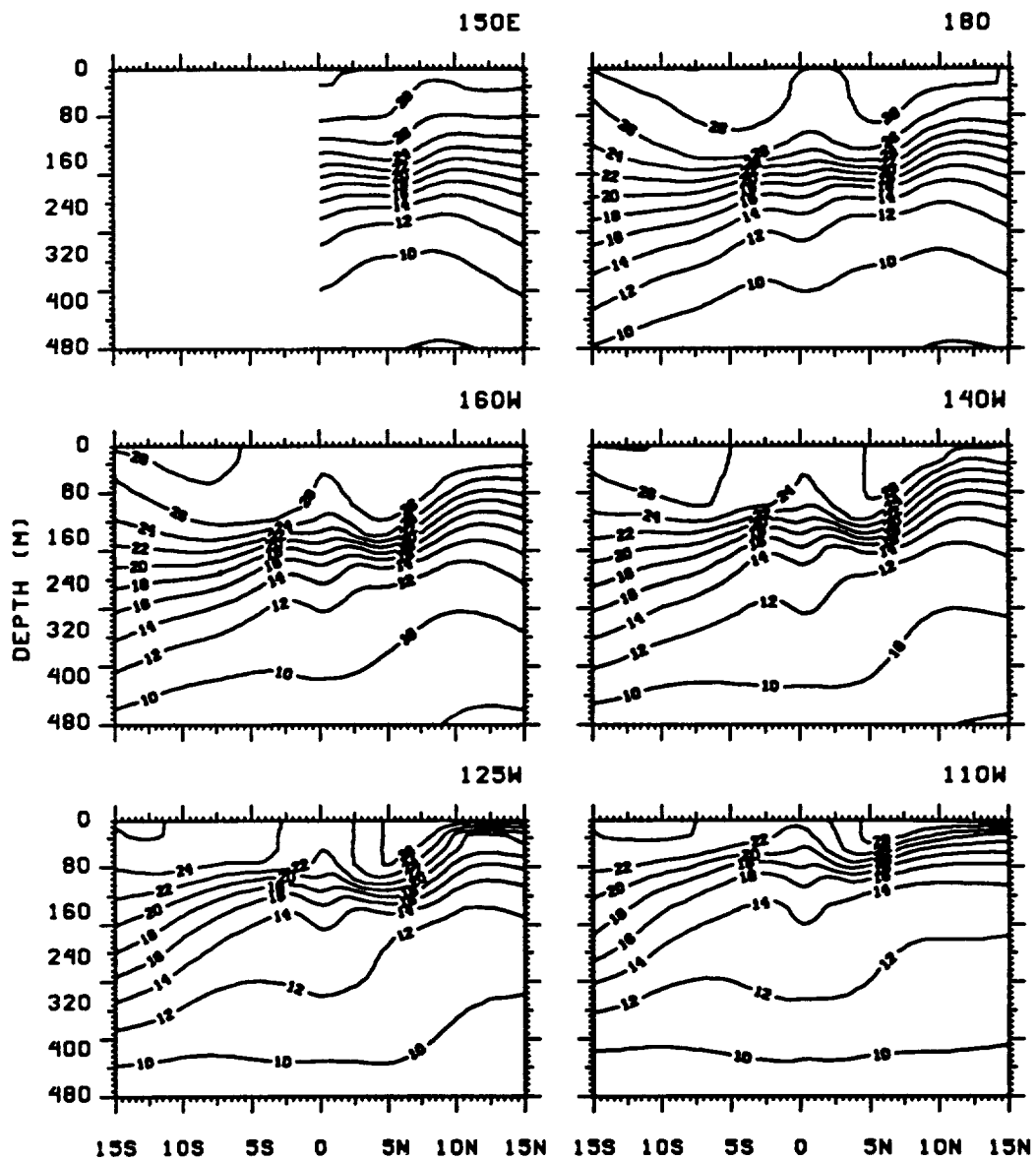


Figure C.5

DECEMBER

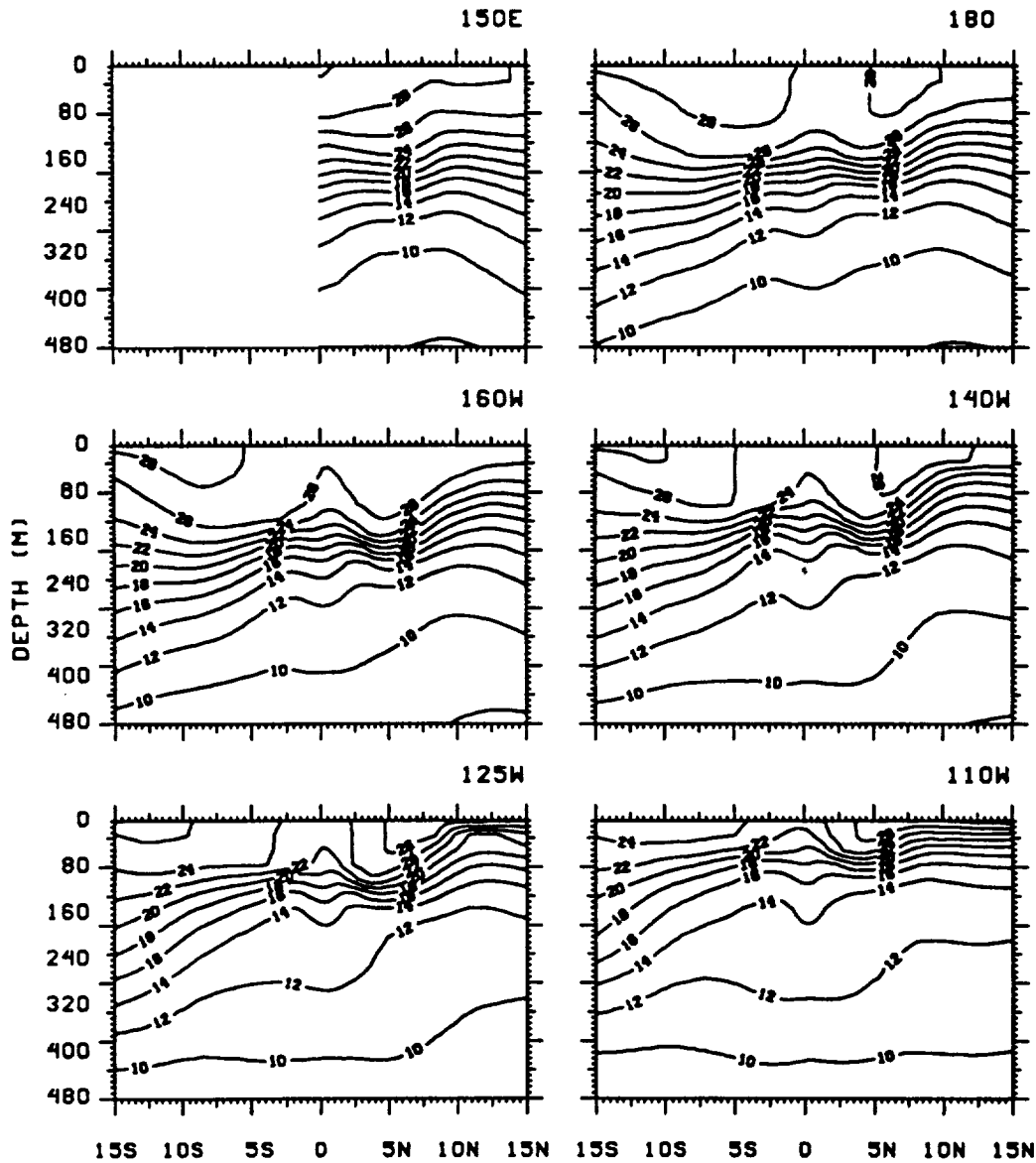


Figure C.5

References

- Barnett, T. P., and W. C. Patzert, 1980: Scales of thermal variability in the tropical Pacific. *J. Phys. Oceanogr.*, **10**, 529-540.
- Bryan, K., 1969: A numerical method for the study of the world ocean. *J. of Comp. Phys.*, **4**, 347-376.
- Bunker, A. F., 1976: Computations of surface energy flux and annual air-sea interaction cycles of the north Atlantic ocean. *Mon. Wea. Rew.*, **104**, 1122-1140.
- Chao, Y., 1990: Seasonal and interannual variability in the tropical Pacific ocean. Ph.D. Dissertation, Princeton University, Princeton, 131 pp.
- Chao, Y., D. Halpern and C. R. Mechoso, 1991: A Pacific ocean general circulation model for satellite data assimilation. JPL Report, 91-9, Jet Propulsion Lab., Pasadena, 32 pp.
- Cox, M. D. 1984: A primitive, 3-dimensional model of the ocean. GFDL Ocean Group Technical Report No. 1, Geophysical Fluid Dynamics Laboratory, Princeton University, Princeton, 143 pp.
- _____, 1980: Generation and propagation of 30-day waves in a numerical model of the Pacific. *J. Phys. Oceanogr.*, **10**, 1168-1186.
- Ekman V. W., 1905: On the influence of the earth's rotation on ocean currents. *Arkiv för Matematik, Astronomi och Fysik*, **2**, No. 11.
- Gill, A. E. 1982: *Atmosphere-Ocean Dynamics*, Academic Press, 662 pp.
- Halpern, D. 1991: Variability of the North Equatorial Countercurrent along 150°W during November 1977 - March 1978. Unpublished.
- _____, 1980: A Pacific equatorial temperature section from 172°E to 110°W during winter and spring 1979. *Deep-Sea Res.*, **27**, 931-940.
- Harrison, D. E., 1989: On climatological monthly mean wind stress and wind stress curl fields over the world oceans. *J. Climate*, **2**, 57-70.
- _____, W. S. Kessler, and B. S. Giese, 1989: Ocean circulation model hindcasts of the 1982-83 El Nino: Thermal variability along the Ship-of-Opportunity tracks. *J. Phys. Oceanogr.*, **19**, 397-418.
- Hellerman, S., and M. Rosenstein, 1983: Normal monthly wind stress over the world ocean with error estimates. *J. Phys. Oceanogr.*, **13**, 1093-1104.

- Johnson, E. S., L. A. Regier and R. A. Knox, 1988: A study of geostrophy in tropical Pacific ocean currents during the NORPAX Tahiti Shuttle using a shipboard acoustic current profiler. *J. Phys. Oceanogr.*, **18**, 708-723.
- Knauss, J. A., 1961: The structure of the Pacific Equatorial Countercurrent. *J. Geophys. Res.*, **66**, 143-155.
- Large, W. G., and S. Pond, 1982: Sensible and latent heat flux measurements over the oceans. *J. Phys. Oceanogr.*, **12**, 464-482.
- Legeckis, R., 1986: Long waves in the equatorial Pacific and Atlantic oceans during 1983. *Ocean-Air Int.*, **1**, 1-10.
- _____, 1977: Long waves in the equatorial Pacific Ocean: A view from a geostationary satellite. *Science*, **197**, 1179-1181.
- Levitus, S. 1982: Climatological atlas of the world ocean. NOAA Professional Paper No. 13, U. S. Government Printing Office, Washington, 173 pp., 17 fiche.
- Lukas, R., E. Firing, P. Hacker, P. L. Richardson, C. A. Collins, R. Fine and R. Gammon, 1991: Observations of the Mindanao Current during the Western Equatorial Pacific Ocean Circulation Study (WEPOCS). *J. Geophys. Res.*, in press.
- Meyers, G., 1980: Do Sverdrup transports account for the North Equatorial Pacific Countercurrent? *J. Geophys. Res.*, **85**, 1073-1075.
- _____, 1975: Seasonal variation in transport of the Pacific North Equatorial Current relative to the wind field. *J. Phys. Oceanogr.*, **5**, 442-449.
- _____, and G. L Donguy, 1984: The North Equatorial Countercurrent and heat storage in the western Pacific ocean during 1982-83. *Nature*, **312**, 258-260.
- Millero, F. J., and A. Poisson, 1981: International one-atmosphere equation of state of seawater. *Deep-Sea Res.*, **28**, 625-629.
- _____, C.-T. Chen, A. Bradshaw and K. Schleicher, 1980: A new high pressure equation of state for seawater. *Deep-Sea Res.*, **25**, 255-264.
- Pacanowski, R. C. and S. G. H. Philander, 1981: Parameterization of vertical mixing in numerical models of the tropical oceans. *J. Phys. Oceanogr.*, **11**, 1443-1451.
- Philander, S. G. H., 1978: Instabilities of zonal currents, Part 2. *J. Geophys. Res.*, **83**, 3679-3682.
- _____, W. J. Hurlin and A. D. Seigel, 1987: Simulation of the seasonal cycle of the tropical Pacific Ocean. *J. Phys. Oceanogr.*, **17**, 1986-2002.
- _____, and R. C. Pacanowski, 1986: A model of the seasonal cycle in the tropical Atlantic ocean. *J. Geophys. Res.*, **91**, 14192-14206.

- _____, W. J. Hurlin and R. C. Pacanowski, 1986: Properties of long equatorial waves in models of the seasonal cycle in the tropical Atlantic and Pacific oceans. *J. Geophys. Res.*, **91**, 14207-14211.
- _____, and A. D. Seigel, 1985: Simulation of El Niño of 1982-83, in *Proceedings of the 16th International Liege Colloquium on Ocean Hydrodynamics*, edited by J. Nihoul. Elsevier, New York, 517-541.
- Pond, S., and G. L. Pickard. 1987: *Introductory Dynamical Oceanography*, 2nd Ed., Pergamon, 329 pp.
- Spillane, M., and P. P. Niiler, 1975: On the theory of strong, midlatitude wind-driven ocean circulation, I, The North Equatorial Countercurrent as a quasi-geostrophic jet. *Geophys. Fluid Dyn.*, **7**, 43-66.
- Stommel, H., 1965: *The Gulf Stream*. University of California Press. 2 Edition, 248 pp.
- Sverdrup, H. U., 1947: Wind-driven currents in a baroclinic ocean; with application to the equatorial currents of the eastern Pacific. *Proc. Natl. Acad. Sci. U. S.*, **33**, 318-326.
- _____, M. W. Johnson and R. H. Fleming, 1942: *The Oceans, their Physics, Chemistry and General Biology*, Prentice-Hall, p. 1087.
- Trenberth, K. E., J. G. Olson and W. G. Large, 1989: A global ocean wind stress climatology based on ECMWF analyses. *NCAR Tech. Note*. NCAR/TN-338+str. 83 pp.
- Umatani, S., and T. Yamagata, 1991: Response of the eastern tropical Pacific to meridional migration of the ITCZ: The generation of the Costa Rica dome. *J. Phys. Oceanogr.*, **21**, 346-363.
- Wyrki, K., 1974a: Sea level and the seasonal fluctuations of the equatorial currents in the western Pacific ocean. *J. Phys. Oceanogr.*, **4**, 91-103.
- _____, 1974b: Equatorial currents in the Pacific 1950 to 1970 and their relations to the trade winds. *J. Phys. Oceanogr.*, **4**, 372-380.
- _____, and B. Kilonsky, 1984: Mean water and current structure during the Hawaii-to-Tahiti Shuttle Experiment. *J. Phys. Oceanogr.*, **14**, 242-254.
- _____, E. Firing, D. Halpern, R. Knox, G. J. McNally, W. C. Patzert, E. D. Stroup, B. A. Taft and R. Williams, 1981: The Hawaii-to-Tahiti Shuttle Experiment. *Science*, **211**, 22-28.
- _____, and R. Kendall, 1967: Transports of the Pacific Equatorial Countercurrent. *J. Geophys. Res.*, **72**, 2073-2076.
- Yoshida, K. 1955: An example of variations in oceanic circulation in response to the variations in wind field. *J. Oceanogr. Soc. Japan*, **11**, 103-108.

